

Smoothed particle hydrodynamics for solid dynamics

Dong Wu

Vollständiger Abdruck der von der TUM School of Engineering and Design der
Technischen Universität München zur Erlangung eines

Doktors der Ingenieurwissenschaften (Dr.-Ing.)

genehmigten Dissertation.

Vorsitz: Prof. Dr.-Ing. Christoph Meier
Prüfende der Dissertation: 1. Priv.-Doz. Dr.-Ing. Xiangyu Hu
2. Prof. Dr.-Ing. Oskar J. Haidn

Die Dissertation wurde am 13.11.2024 bei der Technischen Universität München
eingereicht und durch die TUM School of Engineering and Design am 28.02.2025
angenommen.

Declaration of Authorship

I hereby declare that except where specific reference is made to the work of others, the contents of this dissertation are original and have not been submitted in whole or in part for consideration for any other degree or qualification in this, or any other university. This dissertation is my own work and contains nothing which is the outcome of work done in collaboration with others, except as specified in the text and Acknowledgements.

Dong Wu
April 16, 2025

© Dong Wu, 2025
dong.wu@tum.de

All rights reserved. No part of this publication may be reproduced, modified, re-written, or distributed in any form or by any means, without the prior written permission of the author.

Released April 16, 2025
Typesetting \LaTeX

Abstract

This dissertation presents a series of advancements in Smoothed Particle Hydrodynamics (SPH) aimed at improving the modeling of solid dynamics, particularly in addressing hourglass instabilities, and the simulation of thin structures, plates and shells, under large deformations. The research is structured in three major phases to create a robust framework for accurate, stable, and efficient simulations of solid materials.

The Total Lagrangian SPH (TLSPH) method for elastic solid dynamics suffers from hourglass modes, which can grow and lead to simulation failure, particularly in cases involving large deformations. In the first phase of this dissertation, we address this long-standing issue for the full-dimensional, or volume-particle, SPH method by proposing an essentially non-hourglass formulation based on volumetric and deviatoric stress decomposition. Recognizing that nonphysical zigzag particle distributions, induced by hourglass modes, are primarily characterized by shear deformation, and drawing inspiration from the standard SPH discretization of the viscous term in the Navier-Stokes (NS) equation, our formulation computes the action of shear stress directly through the Laplacian of displacement rather than the divergence of shear stress. A comprehensive set of challenging benchmark tests demonstrate that, while improving both accuracy and computational efficiency, this formulation essentially suppresses hourglass modes and achieves excellent numerical stability with a single general effective parameter. Additionally, the deformation of a practically relevant stent structure is simulated to highlight the potential application of the present method in biomechanics.

However, existing hourglass control methods have been effective only for a limited range of material models. A comprehensive solution capable of addressing hourglass issues across a wide spectrum of materials—encompassing elasticity, plasticity, and anisotropy—has remained elusive. In the second phase of our research, we introduce a unified TLSPH formulation based on volumetric-deviatoric stress decomposition, aimed at fundamentally mitigating hourglass modes in general simulations. In contrast to previous approaches that rely on stress points or additional viscous or hourglass-control stresses within the momentum equation, our formulation uses a weighted average of the standard, hourglass-prone formulation and the non-hourglass formulation developed in the first phase, employing a single limiter to dynamically adjust the balance between the two. This dimensionless characteristic allows seamless integration with complex material models. To validate the formulation, simulations across a range of benchmark cases involving elastic, plastic, and anisotropic materials are conducted. To demonstrate its versatility, we also apply the formulation to simulate a complex scenario involving a viscous plastic Oobleck material, contacts, and very large deformations. This unified formulation addresses a critical gap in TLSPH simulations by providing a comprehensive solution to mitigate hourglass modes, enhancing the reliability and accuracy of simulations across diverse material models and complex scenarios.

For plate and shell structures, the traditional full-dimensional SPH method is computationally inefficient. To address this, we propose a reduced-dimensional,

surface-particle SPH formulation based on mid-surface reconstruction. This formulation is tailored for both quasi-static and dynamic analyses of plate and shell structures undergoing finite deformations and large rotations. Leveraging Uflyand–Mindlin plate theory, the surface-particle formulation resolves thin structures using only one layer of particles at the mid-surface. To account for geometric non-linearity and capture finite deformations and large rotations, two reduced dimensional linear-reproducing correction matrices are introduced, alongside weighted non-singular transformations between the rotation angle and pseudo-normal. Additionally, a new anisotropic Kelvin-Voigt damping mechanism is specifically developed for thin and moderately thick plate and shell structures to enhance numerical stability. To further improve robustness, a shear-scaled momentum-conserving hourglass control algorithm with an adaptive limiter is incorporated to mitigate discrepancies between particle positions, pseudo-normal and those predicted by the deformation gradient. A series of benchmark problems, for which analytical solutions or numerical results from literature or traditional volume-particle SPH methods are available for quantitative and qualitative comparison, are examined to demonstrate the accuracy and stability of the proposed method.

In conclusion, the advancements presented in this dissertation mark a significant step forward in the development of SPH for solid dynamics. The novel formulations provide a robust and reliable toolset for addressing complex deformation problems, offering valuable insights into material behavior under extreme conditions and opening new possibilities for the practical application of SPH in real-world engineering scenarios.

Acknowledgements

First and foremost, I would like to express my deepest gratitude to my supervisor, PD Dr. Xiangyu Hu, for his unwavering support, patience, and continuous guidance throughout my PhD journey. His invaluable suggestions, insightful feedback, and warm encouragement have been instrumental in shaping this work. I am particularly thankful for his thorough advice, which inspired new ideas and provided motivation during moments of frustration. I greatly appreciate his detailed feedback during our weekly group meetings, his careful revision of our papers, and his exceptional ability to guide research progress. His broad vision, passion for science, and deep understanding of solid dynamics and Smoothed Particle Hydrodynamics (SPH) have been truly inspiring.

I also extend my sincere gratitude to Prof. Nikolaus A. Adams, Director of the Chair of Aerodynamics and Fluid Mechanics at the Technical University of Munich, apl. Prof. Christian Stemmer, and my mentor, Prof. Oskar J. Haidn, for providing an excellent research environment. I am grateful to have had the opportunity to work alongside such dedicated individuals and to benefit from their support and resources.

I would like to acknowledge my collaborators at the Chair, including Chi Zhang, Massoud Rezavand, Yujie Zhu, Bo Zhang, Shuoguo Zhang, Feng Wang, Yaru Ren, Shuaihao Zhang and Haitao Li, and beyond the Chair, including Yongchuan Yu, Hao Ma, Xiaojing Tang, Zhentong Wang, Mai Ye, Zhenxi Zhao, Yuan Jia, Junwei Jiang, Abdella Mohamed, Ibraheem Nasser, and Nicolò Salis. It has been a privilege to collaborate with such talented individuals, and I have thoroughly enjoyed the stimulating discussions and camaraderie throughout my PhD journey.

I am also grateful to other members of the Chair for their support, interesting discussions, and companionship, including Yiqi Feng, Wenbin Zhang, Yu Fan, Dr. Wanli Wang, Dr. Yazhou Wang, Jingyu Wang, Yu Jiao, Youjie Xu, and many others. A special thanks to our staff members, Angela Grygier and Hua Liu, for their kind assistance and support throughout my time at the Chair.

I am deeply thankful to the Chinese Scholarship Council and the German Research Foundation (DFG) for their financial support, which made this research possible at the Technical University of Munich.

A heartfelt acknowledgment goes to Prof. Guilin Wen and Prof. Hanfeng Yin, my master's supervisors at Hunan University, Changsha, China. I am forever grateful for their encouragement to pursue computational dynamics and for their guidance during my Master's thesis, which ignited my passion for scientific research.

Lastly, I would like to express my profound gratitude to my parents and my older sister, to whom I dedicate this dissertation. Without their boundless love, encouragement, and unwavering support, this thesis would not have been possible.

Contents

Declaration of Authorship	iii
Abstract	v
Acknowledgements	vii
1 Introduction	1
1.1 Review of SPH	1
1.2 State of art	2
1.2.1 Hourglass modes	2
1.2.2 Reduced-dimensional model	4
1.3 Aims and objectives	5
1.4 Outline	6
2 Fundamentals and modeling approaches in solid dynamics	7
2.1 Kinematics and governing equations	7
2.2 Material models	8
2.2.1 Linear elastic material	8
2.2.2 Neo-Hookean elastic material	8
2.2.3 Plastic material	9
2.2.4 Holzapfel-Odgen material	11
2.2.5 Electrophysiologically induced active stress model	11
2.3 Theoretical model of thin structures	12
2.3.1 3D plate model	12
Kinematics	13
Stress correction	14
Conservation equations	14
2.3.2 3D shell model	16
Kinematics	16
Stress correction and conservation equation	17
2.3.3 2D plate/shell model	17
2.4 Theory and fundamentals of the SPH method	18
2.4.1 Integral interpolation and particle approximation	18
2.4.2 The smoothing kernel	19
2.5 SPH method of solid dynamics	20
2.5.1 SPH discretization	20
2.5.2 Time integration scheme	21
2.6 Summary	21
3 Summaries of publications	23
3.1 An essentially non-hourglass formulation for total Lagrangian smoothed particle hydrodynamics	23
3.1.1 Summary of the publication	23

3.1.2	Individual contributions of the candidate	25
3.2	Unified non-hourglass formulation for total Lagrangian SPH solid dynamics	26
3.2.1	Summary of the publication	26
3.2.2	Individual contributions of the candidate	28
3.3	An SPH formulation for general plate and shell structures with finite deformation and large rotation	29
3.3.1	Summary of the publication	29
3.3.2	Individual contributions of the candidate	30
4	Conclusions and outlooks	31
4.1	Conclusions	31
4.2	Outlooks	32
	Bibliography	35
A	Original journal papers	43
A.1	Paper I	45
A.2	Paper II	75
A.3	Paper III	111

Chapter 1

Introduction

1.1 Review of SPH

Smoothed Particle Hydrodynamics (SPH), a fully Lagrangian, mesh-free method, was originally developed for astrophysical simulations and fluid dynamics [1, 2]. Over the past few decades, SPH has garnered increasing attention and has been widely adopted in various fields [3, 4, 5, 6, 7, 8]. In SPH, the continuum is represented by a set of particles, with each particle carrying fundamental physical properties such as mass and velocity. The governing equations are discretized by replacing their integral forms with finite summations over the corresponding values of neighboring particles within a defined support domain. This is achieved through the use of a Gaussian-like kernel function, which serves as the weighting function for particle interactions [9, 10, 11], as illustrated in Figure 1.1. For a more detailed explanation of the SPH method theory and fundamentals, we refer to Section 2.4. The particle approximation is recalculated at every time step, ensuring that the method dynamically adapts to the local distribution of particles. This characteristic enables SPH to naturally handle large deformations and complex geometries, making it a versatile tool in computational mechanics.

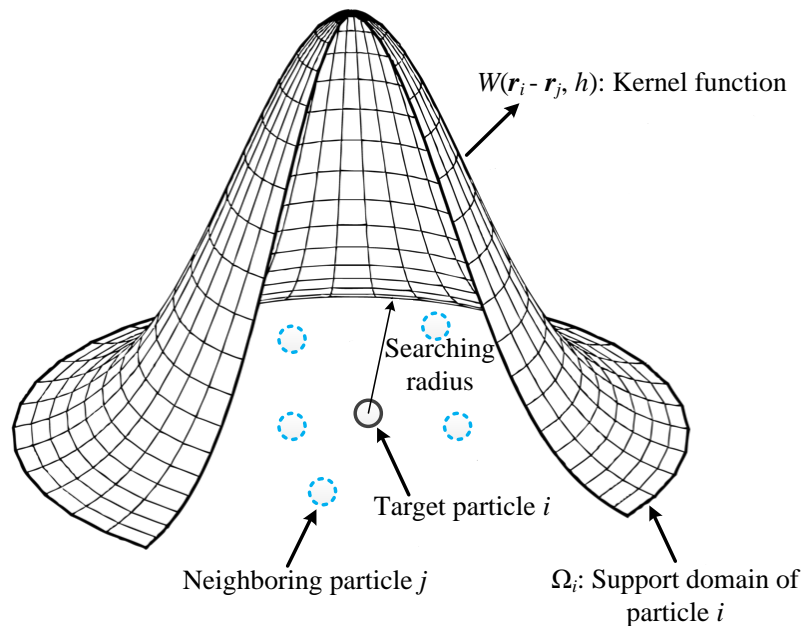


FIGURE 1.1: Particle interaction and the kernel function.

Since many common abstractions, which are intrinsically linked to numerous physical systems, can be modeled through particle interactions, the SPH method

provides a versatile approach to discretizing multi-physics equations within a unified computational framework [12]. This allows for shared algorithms, such as neighboring particle search and time stepping, simplifying parallel computation and significantly improving computational efficiency [13]. More importantly, the unified computational framework facilitates monolithic and strong coupling, which is seamless, spatio-temporally localized, and conservative both locally and globally [14, 15]. The SPH method has proven successful in addressing multi-physics problems within a unified framework [12, 13], including fluid-structure interaction (FSI) [16, 17, 18, 19, 20], cardiac electrophysiology [21, 22], laser beam welding [23, 24], porous media [25, 26, 27], and other domains. FSI, in particular, represents a typical multi-physics system where fluid and solid dynamics are tightly coupled. Unlike partition-based FSI solvers, where solid dynamics are discretized using the Finite Element Method (FEM) [28, 29] and fluid dynamics using SPH, the unified computational framework based solely on the SPH method [16, 17, 19] requires that solid dynamics equations, especially those involving large strain, are also discretized using the SPH method.

Despite its promising achievements, early studies revealed that the original SPH method for solid dynamics could be unstable and inaccurate due to three primary deficiencies: linear inconsistency, tensile instability, and hourglass modes. The first issue arises from incomplete kernel support at domain boundaries or with irregular particle distributions [10]. Several solutions have been proposed to address this, including the normalized smoothing approach [30], kernel gradient correction [3, 31], and the finite particle method (FPM) [32]. Tensile instability, characterized by nonphysical fractures and the formation of voids or particle clustering in solid [33] and fluid simulations [34], respectively, arises due to the zero-order inconsistency in particle discretization [35]. While this deficiency can generally be alleviated using artificial stress techniques [36, 37, 38] or the generalized transport-velocity formulation [39, 40], it can be completely eliminated by the Total Lagrangian SPH (TLSPH) method, where the kernel function is evaluated once in the initial undeformed reference configuration [41], unlike the traditional Updated Lagrangian SPH (ULSPH) method, which requires no additional correction terms [42, 31]. Since its development, the TLSPH method has been successfully applied to numerous solid dynamics simulations, including electromagnetically driven rings [43], thermomechanical deformations [44], shell models [45, 46, 47], and biomechanics [21].

1.2 State of art

The problem of numerical instability caused by hourglass modes continues to pose challenges in TLSPH solid dynamics. Additionally, the traditional full-dimensional, or volume-particle, SPH method (referred to as the volume SPH method) becomes computationally inefficient when applied to plate and shell structures. This dissertation tackles both of these issues, concentrating on the elimination of hourglass modes and the development of a reduced-dimensional, surface-particle SPH method (referred to as the shell SPH method) to improve computational efficiency for thin-walled structures.

1.2.1 Hourglass modes

In modeling solid dynamics using SPH, hourglass instabilities can result in spurious, non-physical deformations, especially in cases involving large deformations

and highly strained material behavior, as illustrated in Figure 1.2. The artifact of

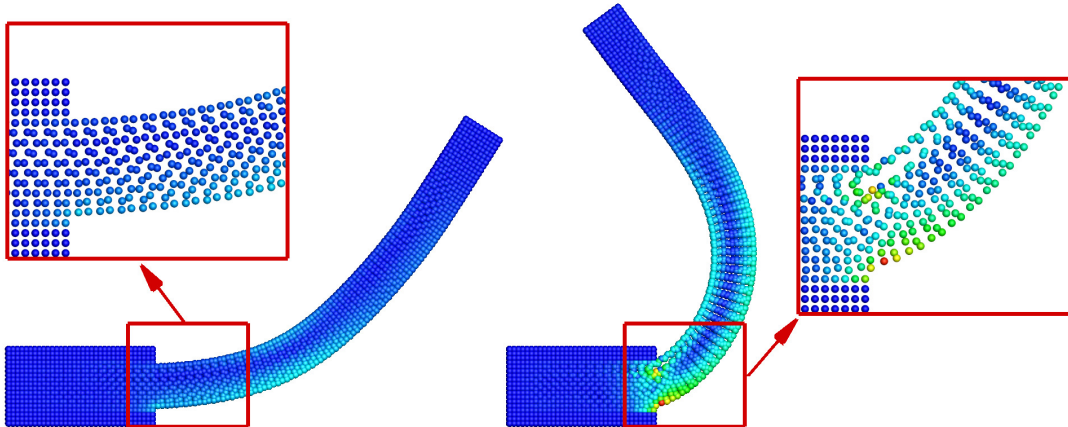


FIGURE 1.2: Hourglass modes exist when 2D plate oscillating [48].

hourglass modes was first observed in FEM simulations and is characterized by a zigzag mesh and field pattern [49, 50]. Similar to FEM, hourglass modes in SPH occur when the deformation gradient remains unchanged as particles shift into a non-physical zigzag pattern, resulting in zero-energy modes [51, 52, 53]. To address this issue in the ULSPH method, Beissel and Belytschko [54] introduced a stabilization term to the potential energy function, while Vidal et al. [55] proposed an artificial viscosity term by minimizing a local measure of the Laplacian of the deformation field. Although both schemes have been successfully applied to various benchmark cases, they rely on empirical, case-dependent parameters [56]. A more robust approach is to introduce additional integration or stress points between the original particles to represent the stress field [51, 41, 57, 45, 53]. While this approach effectively eliminates hourglass modes, it increases algorithmic complexity, computational overhead, and suffers from the lack of a clear rule for determining the optimal placement of stress points [58].

In the TLSPH method, it has been found that introducing artificial viscosity, similar to that used in computational fluid dynamics (CFD), can effectively reduce hourglass modes in dynamic simulations [59, 60]. However, since these artificial viscosity formulations rely on the particle velocity gradient, their effectiveness becomes questionable when the velocity field is flat or insignificant. More recently, Kondo et al. [61], Ganzenmüller [62], and Shimizu et al. [63] introduced artificial force or stress methods to correct the inconsistencies caused by the zigzag pattern between the local displacement field and the linear prediction from the deformation gradient. While these methods are both effective and computationally efficient, they may suppress the non-linear components of the displacement field due to excessive artificial stiffness [64, 65]. Furthermore, they often require case-dependent, empirically tuned parameters to achieve physically meaningful results [56].

Aside from introducing additional stress points [58], a common feature among these schemes is their integration into the momentum equation as corrective or stabilizing terms [54, 61], similar to the hourglass-control stress terms used in many FEM [66, 67]. These methods typically rely on basic material parameters, such as sound speed [38, 59, 60] or Young's modulus [54, 61, 62]. The dependence on material parameters implies that the correction terms are tied to the physical characteristics of the material, despite being aimed at mitigating a purely numerical instability. This leads to challenges in generalizing these solutions for more complex material models. For instance, determining optimal parameters becomes difficult when dealing

with non-isotropic contributions in the material model, or deciding the appropriate correction magnitude for plastic materials exhibiting complex yielding and hardening behaviors. As a result, these parameters are often non-generalized and require case-specific or material model-specific tuning to avoid either insufficient or excessive correction [64, 65, 56, 68, 69]. Thus far, a comprehensive solution that effectively addresses hourglass issues across a broad range of material models—encompassing elasticity, plasticity, and anisotropy—remains elusive.

1.2.2 Reduced-dimensional model

In the case of plate and shell structures—common thin structures in scientific and engineering fields such as shipbuilding [70, 71], aerospace [72], and medical treatment [73]—the traditional volume SPH method is computationally inefficient [74]. Given the availability of well-established and mature reduced-dimensional theories, such as Kirchhoff-Love [75] and Uflyand-Mindlin (or Mindlin-Reissner) [76, 77, 78, 79], which are based on mid-surface reconstruction for plate and shell structures, it is anticipated that a much more efficient shell SPH method can be developed using only a single layer of particles. As shown in Figure 1.3, the shell model requires significantly fewer particles to simulate plate problems compared to the volume model, offering considerable computational savings.

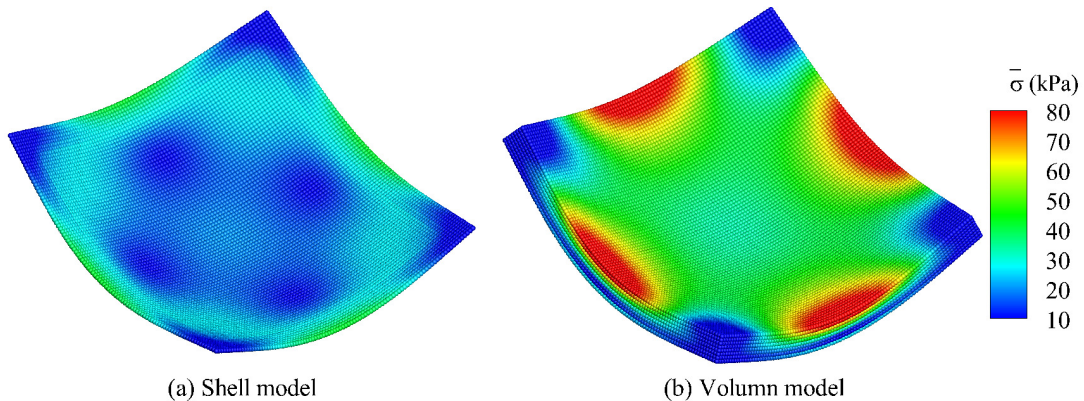


FIGURE 1.3: 3D square plate: Particles colored by von Mises stress $\bar{\sigma}$ obtained by the shell (left) and volume (right) methods. Note that the left panel shows the stress $\bar{\sigma}$ of the plate mid-surface [80].

Early meshless methods for plates and shells were primarily based on Petrov or element-free Galerkin formulations [81, 82, 83, 84, 85], or the reproducing kernel particle method [86, 87, 47], which have been applied to problems involving plastic deformation and material failure [85]. In the context of SPH, Maurel and Combescure [45] were the first to develop a shell SPH method for total Lagrangian quasi-static and dynamic analyses of moderately thick plates and shells, based on the Uflyand-Mindlin theory and assuming small deformations. In their work, an artificial viscosity term was introduced to mitigate numerical instability issues, while a stress point method was employed to address hourglass or zero-energy modes. While the use of stress points is effective in preventing zero-energy modes, it introduces several issues [62, 88] as mentioned in Section 1.2.1. Nonetheless, this method was later extended for large deformation analyses by Ming et al. [89] and for dynamic damage-fracture analyses by Caleyron et al. [90]. Lin et al. [46] developed a similar method for quasi-static analyses, incorporating an artificial viscosity term based on membrane and shearing decomposition. Ming et al. [91] were the first to consider

finite deformation by accounting for all strain components, using Gauss-Legendre quadrature to more accurately capture non-linear stress. Since the introduction of the SPH shell model, it has been successfully applied in several engineering fields, including composite plate and shell structures [92, 93], explosion analysis [94], and ship simulations [71].

1.3 Aims and objectives

The primary goal of this dissertation is to develop and improve SPH formulations for solid dynamics, with a particular emphasis on addressing the hourglass instabilities and extending the applicability of SPH to plate and shell structures.

The first objective is to develop a *Non-Hourglass Formulation for TLSPH elastic dynamics*. This formulation is designed to eliminate the non-physical deformations that commonly arise in traditional SPH simulations due to hourglass instabilities. By introducing a novel formulation, this objective seeks to enhance the accuracy and stability of TLSPH in handling elastic dynamics problems, particularly in scenarios involving large deformations and complex stress conditions. The work addressing this objective is presented in detail in Paper I [88]

- Wu, D., Zhang, C., Tang, X. and Hu, X., 2023. An essentially non-hourglass formulation for total Lagrangian smoothed particle hydrodynamics. *Computer Methods in Applied Mechanics and Engineering*, 407, p.115915.

which has been attached in Appendix A.1.

The second objective is to create a *Unified Non-Hourglass TLSPH Formulation*. This formulation builds on the first objective, extending the approach to a broader range of materials and deformation scenarios. The unified formulation aims to provide a comprehensive solution for both elastic, plastic and anisotropic deformations, offering improved computational robustness across various solid dynamics applications. This work is detailed in Paper II [48]

- Wu, D., Tang, X., Zhang, S. and Hu, X., 2024. A generalized essentially non-hourglass total Lagrangian SPH solid dynamics. *Computational Mechanics*, pp.1-33.

which is attached in Appendix A.2.

The last but not least objective of the dissertation is to extend the SPH method to handle *General Plate and Shell Structures*. These structures, which are common in engineering applications, present unique challenges due to their thin geometries and susceptibility to large deformations and rotations. The goal is to develop a specialized SPH formulation capable of accurately simulating the complex behavior of plates and shells, ensuring that SPH can be applied to a wider range of solid dynamics problems. This work is detailed in Paper III [80]

- Wu, D., Zhang, C. and Hu, X., 2024. An SPH formulation for general plate and shell structures with finite deformation and large rotation. *Journal of Computational Physics*, 510, p.113113.

which is attached in Appendix A.3.

1.4 Outline

The structure of this dissertation is as follows. Chapter 1 introduces the SPH method, reviews the state of the art regarding hourglass modes and reduced-dimensional models in SPH, and outlines the aims and objectives of this dissertation. Fundamentals and modeling approaches in solid dynamics are described in Chapter 2, covering the kinematics and governing equations, various material models, the theoretical model for plates, the theory and fundamentals of the SPH method, and its application to solid dynamics. As summarized in Chapter 3, this dissertation introduces an essentially non-hourglass formulation for TLSPH elastic dynamics, further develops a unified non-hourglass formulation capable of addressing a wide array of material behaviors, and proposes a collocated reduced-dimensional SPH formulation for total Lagrangian quasi-static and dynamic analyses of general plate or shell structures, involving finite deformation or/and large rotation. Finally, in Chapter 4 the conclusions are summarized and recommendations for future work are given.

Chapter 2

Fundamentals and modeling approaches in solid dynamics

This chapter provides a comprehensive overview of the fundamental concepts and methods used for modeling solid dynamics. It begins with a discussion of kinematics and governing equations, which form the foundation for understanding the motion and deformation of solid materials within the total Lagrangian framework. The chapter then examines constitutive relations, which describe the behavior of various materials under loading conditions. Following this, a theoretical model for thin structures is introduced, outlining the principles for modeling thin structures subjected to large deformations. The chapter also reviews the theory of SPH, covering the key principles of this mesh-free method. Lastly, the application of the SPH method to solid dynamics is explored in detail.

2.1 Kinematics and governing equations

In the context of continuum mechanics within the total Lagrangian framework, the kinematics and governing equations are formulated with respect to the initial, undeformed reference configuration, $\Omega^0 \subset \mathbb{R}^D$, where D represents the spatial dimension. A deformation map φ is used to describe the transformation between the initial configuration Ω^0 and the current deformed configuration $\Omega = \varphi(\Omega^0)$. This map characterizes the deformation of the body at any given time t as

$$\mathbf{r} = \varphi(\mathbf{r}^0, t), \quad (2.1)$$

where \mathbf{r}^0 and \mathbf{r} denote the initial and current positions of a material point, respectively. The deformation gradient tensor \mathbb{F} is then defined as

$$\mathbb{F} = \nabla^0 \mathbf{r} = \nabla^0 \mathbf{u} + \mathbb{I}, \quad (2.2)$$

where $\mathbf{u} = \mathbf{r} - \mathbf{r}^0$ is the displacement, $\nabla^0 \equiv \frac{\partial}{\partial \mathbf{r}^0}$ the gradient operator with respect to the initial configuration Ω^0 and \mathbb{I} the identity matrix.

The conservation equations for mass and momentum in the total Lagrangian formulation are expressed as

$$\begin{cases} \rho = J^{-1} \rho^0 \\ \rho^0 \ddot{\mathbf{u}} = \nabla^0 \cdot \mathbb{P}^T, \end{cases} \quad (2.3)$$

where ρ^0 and ρ are the initial and current densities, respectively, $J = \det(\mathbb{F})$, $\ddot{\mathbf{u}}$ the acceleration, \mathbb{P} the first Piola-Kirchhoff stress tensor, and T the matrix transposition

operator. \mathbb{P} can be obtained by

$$\mathbb{P} = \mathbb{F}\mathbb{S}, \quad (2.4)$$

where \mathbb{S} is the second Piola-Kirchhoff stress tensor, and \mathbb{P} can also be obtained by the alternative Kirchhoff or Cauchy stress as

$$\mathbb{P} = \boldsymbol{\tau}\mathbb{F}^{-\text{T}} = J\boldsymbol{\sigma}\mathbb{F}^{-\text{T}}. \quad (2.5)$$

2.2 Material models

A range of material models is included in this section, covering elastic, plastic (perfect, linear, and non-linear hardening, viscous), anisotropic materials with fiber direction, and electrophysiologically induced active stress models.

2.2.1 Linear elastic material

Using the deformation gradient tensor \mathbb{F} , the Green-Lagrangian strain tensor \mathbb{E} is obtained as

$$\mathbb{E} = \frac{1}{2} (\mathbb{F}^{\text{T}}\mathbb{F} - \mathbb{I}) = \frac{1}{2} (\mathbb{C} - \mathbb{I}), \quad (2.6)$$

where \mathbb{C} is the right Cauchy deformation gradient tensor. The Eulerian Almansi strain $\boldsymbol{\varepsilon}$ can be converted from \mathbb{E} as

$$\boldsymbol{\varepsilon} = \mathbb{F}^{-\text{T}} \cdot \mathbb{E} \cdot \mathbb{F}^{-1} = \frac{1}{2} (\mathbb{I} - \mathbb{F}^{-\text{T}}\mathbb{F}^{-1}). \quad (2.7)$$

When the material is linear and isotropic, the second Piola-Kirchhoff stress \mathbb{S} reads

$$\begin{aligned} \mathbb{S} &= K \operatorname{tr}(\mathbb{E}) \mathbb{I} + 2G \left(\mathbb{E} - \frac{1}{3} \operatorname{tr}(\mathbb{E}) \mathbb{I} \right) \\ &= \lambda \operatorname{tr}(\mathbb{E}) \mathbb{I} + 2\mu \mathbb{E}, \end{aligned} \quad (2.8)$$

and the Cauchy stress $\boldsymbol{\sigma}$ is

$$\boldsymbol{\sigma} = \lambda \operatorname{tr}(\boldsymbol{\varepsilon}) \mathbb{I} + 2\mu \boldsymbol{\varepsilon}, \quad (2.9)$$

where λ and μ are the Lamé constants, $K = \lambda + 2\mu/3$ the bulk modulus and $G = \mu$ the shear modulus. The relationship between the two moduli is given by

$$E = 2G(1 + \nu) = 3K(1 - 2\nu), \quad (2.10)$$

where E denotes the Young's modulus and ν the Poisson's ratio.

2.2.2 Neo-Hookean elastic material

The Kirchhoff stress $\boldsymbol{\tau}$ for the neo-Hookean elastic material can be derived from the strain energy function [95]

$$\mathfrak{W}_e = \mathfrak{W}_v(J) + \mathfrak{W}_s(\bar{\boldsymbol{b}}). \quad (2.11)$$

Here, the volume-preserving left Cauchy-Green deformation gradient tensor is denoted by $\bar{\boldsymbol{b}} = |\boldsymbol{b}|^{-\frac{1}{d}} \boldsymbol{b}$. The volume-dependent strain energy $\mathfrak{W}_v(J)$, with the bulk

modulus K , can be written as

$$\mathfrak{W}_v(J) = \frac{1}{2}K \left[\frac{1}{2}(J^2 - 1) - \ln J \right]. \quad (2.12)$$

The shear-dependent strain energy $\mathfrak{W}_s(\bar{\mathbf{b}})$ can be expressed as [96]

$$\mathfrak{W}_s(\bar{\mathbf{b}}) = \frac{1}{2}G (\text{tr}(\bar{\mathbf{b}}) - D). \quad (2.13)$$

The Kirchhoff stress tensor $\boldsymbol{\tau}$ is then derived by partially differentiating the strain energy function with respect to the deformation gradient \mathbf{F} as

$$\boldsymbol{\tau} = \frac{\partial \mathfrak{W}_e}{\partial \mathbf{F}} \mathbf{F}^T = \frac{K}{2}(J^2 - 1) \mathbf{I} + G \text{dev}(\bar{\mathbf{b}}), \quad (2.14)$$

where

$$\text{dev}(\bar{\mathbf{b}}) = \bar{\mathbf{b}} - \frac{1}{D} \text{tr}(\bar{\mathbf{b}}) \mathbf{I} = |\mathbf{b}|^{-\frac{1}{D}} \left[\mathbf{b} - \frac{1}{D} \text{tr}(\mathbf{b}) \mathbf{I} \right] \quad (2.15)$$

returns the trace-free part of $\bar{\mathbf{b}}$, i.e., $\text{tr}(\text{dev}(\bar{\mathbf{b}})) = 0$.

2.2.3 Plastic material

Four distinct plastic models are introduced, including perfect plasticity, linear hardening, non-linear hardening, and viscous plastic models. To describe the stress-strain evolution in plasticity, we employ the classical J_2 flow theory [97]. According to this theory, the deformation gradient tensor \mathbf{F} is decomposed into an elastic volumetric part \mathbf{F}_e and a plastic deviatoric part \mathbf{F}_p as [95]

$$\mathbf{F} = \mathbf{F}_e \mathbf{F}_p. \quad (2.16)$$

The elastic part of left Cauchy-Green tensor \mathbf{b}_e is defined as $\mathbf{b} = \mathbf{F}_e \mathbf{F}_e^T$. For plasticity analysis, the plastic right Cauchy deformation gradient tensor \mathbf{C}_p is introduced as

$$\mathbf{C}_p = \mathbf{F}_p^T \mathbf{F}_p. \quad (2.17)$$

The relationship between \mathbf{b}_e and \mathbf{C}_p is described as

$$\mathbf{b}_e = \mathbf{F} \mathbf{C}_p^{-1} \mathbf{F}^T. \quad (2.18)$$

The plastic behavior is governed by the deviatoric component of the Kirchhoff stress, denoted as $\boldsymbol{\tau}_{de} = G \text{dev}(\bar{\mathbf{b}})$. To model plasticity, a scalar yield function $f(\boldsymbol{\tau}_{de})$ is introduced. When $f(\boldsymbol{\tau}_{de}) > 0$, indicating that the material has entered the plastic regime, $\boldsymbol{\tau}_{de}$ is mapped back to the yield surface—a boundary separating elastic and plastic regions—via a return mapping process, resulting in $\boldsymbol{\tau}_{de}^e$.

While detailed descriptions of the non-linear hardening plastic model can be found in our previous work [98], and further insights into the viscous plastic model are available in Ref. [96], we will focus primarily on the perfect and linear hardening plastic models in the following discussion. It is important to note that the main differences among these four plastic models lie in the return mapping process. The scalar yield function $f(\boldsymbol{\tau}_{de})$ for both the perfect and linear hardening plastic models can be expressed as

$$f(\boldsymbol{\tau}_{de}) = \|\boldsymbol{\tau}_{de}\|_F - \sqrt{\frac{2}{3}} (\kappa \xi + \tau_y), \quad (2.19)$$

Algorithm 1: Algorithm for J_2 flow theory with linear isotropic hardening.

- 1 Update deformation tensor $\mathbb{F}^{n+\frac{1}{2}}$
- 2 Compute elastic predictor (Note that $\mathbb{C}_p^0 = \mathbb{I}$)

$$\mathbb{b}_e^{trial, n+\frac{1}{2}} = \mathbb{F}^{n+\frac{1}{2}} \left(\mathbb{C}_p^{n-\frac{1}{2}} \right)^{-1} \left(\mathbb{F}^{n+\frac{1}{2}} \right)^T,$$

$$\boldsymbol{\tau}_{de}^{trial, n+\frac{1}{2}} = G \operatorname{dev} \left(\mathbb{b}_e^{trial, n+\frac{1}{2}} \right).$$

- 3 Check for plastic loading (Note that $\zeta^0 = 0$)

$$f^{trial, n+\frac{1}{2}} = \|\boldsymbol{\tau}_{de}^{trial, n+\frac{1}{2}}\|_F - \sqrt{\frac{2}{3}} \left(\kappa \zeta^{n-\frac{1}{2}} + \tau_y \right).$$

- 4 **if** $f^{trial, n+\frac{1}{2}} \leq 0$ **then**

- 5 | Elastic state, set $(\bullet)^{n+\frac{1}{2}} = (\bullet)^{trial, n+\frac{1}{2}}$, and $\left(\mathbb{C}_p^{n+\frac{1}{2}} \right)^{-1} = \left(\mathbb{C}_p^{n-\frac{1}{2}} \right)^{-1}$.

- 6 **else**

- 7 | Plastic state, and perform 9 (the return mapping)

- 8 **end**

- 9 Compute normalized shear modulus

$$\tilde{G} = \frac{1}{d} \operatorname{tr} \left(\mathbb{b}_e^{trial, n+\frac{1}{2}} \right) G.$$

Compute increment of hardening factor

$$\zeta^{inc, n+\frac{1}{2}} = \frac{0.5 f^{trial, n+\frac{1}{2}}}{\tilde{G} + \kappa/3.0}.$$

Update hardening factor

$$\zeta^{n+\frac{1}{2}} = \zeta^{n-\frac{1}{2}} + \sqrt{\frac{2}{3}} \zeta^{inc, n+\frac{1}{2}}.$$

Update stress and deformation gradient

$$\boldsymbol{\tau}_{de}^{n+\frac{1}{2}} = \boldsymbol{\tau}_{de}^{trial, n+\frac{1}{2}} - 2\tilde{G}\zeta^{inc, n+\frac{1}{2}} \boldsymbol{\tau}_{de}^{trial, n+\frac{1}{2}} / \|\boldsymbol{\tau}_{de}^{trial, n+\frac{1}{2}}\|_F,$$

$$\mathbb{b}_e^{n+\frac{1}{2}} = \frac{1}{G} \boldsymbol{\tau}_{de}^{n+\frac{1}{2}} + \frac{1}{d} \operatorname{tr} \left(\mathbb{b}_e^{trial, n+\frac{1}{2}} \right) \mathbb{I},$$

$$\left(\mathbb{C}_p^{n+\frac{1}{2}} \right)^{-1} = \left(\mathbb{F}^{n+\frac{1}{2}} \right)^{-1} \mathbb{b}_e^{n+\frac{1}{2}} \left(\mathbb{F}^{n+\frac{1}{2}} \right)^{-T}.$$

where κ is the hardening modulus, ζ the hardening factor which is 0 for perfect plasticity, and τ_y the initial flow stress, also called yield stress. Note that $\|\bullet\|_F$ denotes a Frobenius norm of a tensor variable. The detailed algorithm of the linear hardening plastic model from Ref. [95] is presented in Algorithm 1. The superscript $(\bullet)^{trial}$ denotes quantities related to a trial elastic state, which is evaluated to determine if it exceeds the elastic limit. The time-stepping algorithm is applied in the elastoplastic material description. It is noteworthy that the plasticity algorithm operates at the mid point of the n -th time step, i.e., parameters are denoted as $(\bullet)^{n+\frac{1}{2}}$. Additionally, it should be emphasized that the updated \mathbb{b}_e obtained through the return mapping process can be substituted into Eq. (2.14) to calculate the Kirchhoff stress $\boldsymbol{\tau}$ for plastic materials by replacing \mathbb{b} .

2.2.4 Holzapfel-Ogden material

The Holzapfel-Ogden model [99] accounts for the anisotropic properties of muscle tissue, such as the myocardium. As outlined in Ref. [21], the strain energy function is expressed as

$$\begin{aligned} \mathfrak{W} = & \frac{a}{2b} \exp [b(I_1 - 3)] - a \ln J + \frac{\lambda}{2} (\ln J)^2 \\ & + \sum_{i=f,s} \frac{a_i}{2b_i} \{ \exp [b_i (I_{ii} - 1)^2] - 1 \} \\ & + \frac{a_{fs}}{2b_{fs}} \{ \exp [b_{fs} I_{fs}^2] - 1 \}, \end{aligned} \quad (2.20)$$

where $a, b, a_f, b_f, a_s, b_s, a_{fs}$ and b_{fs} represent eight positive material constants. The series of parameters a have units of stress, while b are dimensionless. Here, the principle invariants are defined as

$$I_1 = \text{tr } \mathbf{C}, \quad I_2 = \frac{1}{2} [I_1^2 - \text{tr}(\mathbf{C}^2)], \quad I_3 = \det(\mathbf{C}) = J^2, \quad (2.21)$$

where the left Cauchy-Green deformation tensor $\mathbf{C} = \mathbf{F}^T \mathbf{F}$, and three other independent invariants associated with directional preferences are given by

$$I_{ff} = \mathbf{C} : \mathbf{f}^0 \otimes \mathbf{f}^0, \quad I_{ss} = \mathbf{C} : \mathbf{s}^0 \otimes \mathbf{s}^0, \quad I_{fs} = \mathbf{C} : \mathbf{f}^0 \otimes \mathbf{s}^0, \quad (2.22)$$

where \mathbf{f}^0 and \mathbf{s}^0 are the undeformed muscle fiber and sheet unit direction, respectively.

The second Piola-Kirchhoff stress \mathbf{S} is derived by

$$\mathbf{S} = 2 \frac{\partial \mathfrak{W}}{\partial \mathbf{C}} - p \mathbf{C}^{-1} = 2 \sum_j \frac{\partial \mathfrak{W}}{\partial I_j} \frac{\partial I_j}{\partial \mathbf{C}} - p \mathbf{C}^{-1} \quad j = 1, ff, ss, fs, \quad (2.23)$$

where

$$\frac{\partial I_1}{\partial \mathbf{C}} = \mathbb{I}, \quad \frac{\partial I_{ff}}{\partial \mathbf{C}} = \mathbf{f}_0 \otimes \mathbf{f}_0, \quad \frac{\partial I_{ss}}{\partial \mathbf{C}} = \mathbf{f}_0 \otimes \mathbf{f}_0, \quad \frac{\partial I_{fs}}{\partial \mathbf{C}} = \mathbf{f}_0 \otimes \mathbf{s}_0 + \mathbf{s}_0 \otimes \mathbf{f}_0, \quad (2.24)$$

and $p = \frac{\partial \mathfrak{W}}{\partial J}$ serves as the Lagrange multiplier introduced to enforce incompressibility. Substituting Eqs. (2.20) and (2.24) into Eq.(2.23) and applying $\boldsymbol{\tau} = \mathbf{F} \mathbf{S} \mathbf{F}^T$, the Kirchhoff stress $\boldsymbol{\tau}$ is obtained as

$$\begin{aligned} \boldsymbol{\tau} = & \{ \lambda \ln J - a \} \mathbb{I} + a \exp [b (I_1 - 3)] \mathbb{b} \\ & + 2a_f (I_f - 1) \exp [b_f (I_f - 1)^2] \mathbf{F}(\mathbf{f}_0 \otimes \mathbf{f}_0) \mathbf{F}^T \\ & + 2a_s (I_s - 1) \exp [b_s (I_s - 1)^2] \mathbf{F}(\mathbf{s}_0 \otimes \mathbf{s}_0) \mathbf{F}^T \\ & + a_{fs} I_{fs} \exp [b_{fs} (I_{fs})^2] \mathbf{F}(\mathbf{f}_0 \otimes \mathbf{s}_0 + \mathbf{s}_0 \otimes \mathbf{f}_0) \mathbf{F}^T. \end{aligned} \quad (2.25)$$

2.2.5 Electrophysiologically induced active stress model

Building on the methodology presented in Refs. [100, 21], we incorporate the stress tensor with the transmembrane potential V_m using the active stress approach. This

approach decomposes the Kirchhoff stress τ into passive and active components as

$$\tau = \tau_{passive} + \tau_{active}, \quad (2.26)$$

where the passive component $\tau_{passive}$ represents the stress required to achieve a given passive muscle deformation, and is modeled using the previously mentioned Holzapfel-Odgen material. The active component τ_{active} denotes the tension activated by the depolarization of the propagating transmembrane potential. Following the active stress approach proposed in Ref. [100], the active component is determined as

$$\tau_{active} = T_a \mathbb{F} f_0 \otimes f_0 \mathbb{F}^T, \quad (2.27)$$

where T_a represents the active muscle contraction stress.

2.3 Theoretical model of thin structures

We first introduce the theoretical mode of 3D plate, and then that of 3D shell in which material points may possess different initial normal directions leading to different initial local coordinate systems. After that, we briefly describe the 2D plate and shell models, which resolve the plane strain problem, as a simplification of the 3D counterparts.

2.3.1 3D plate model

We adopt the Uflyand–Mindlin plate theory [76, 77] to account for transverse shear stress, which is particularly important for moderately thick plates. According to this theory, the behavior of the plate can be represented by a single layer of material points located at its mid-surface, as illustrated in Figure 2.1.

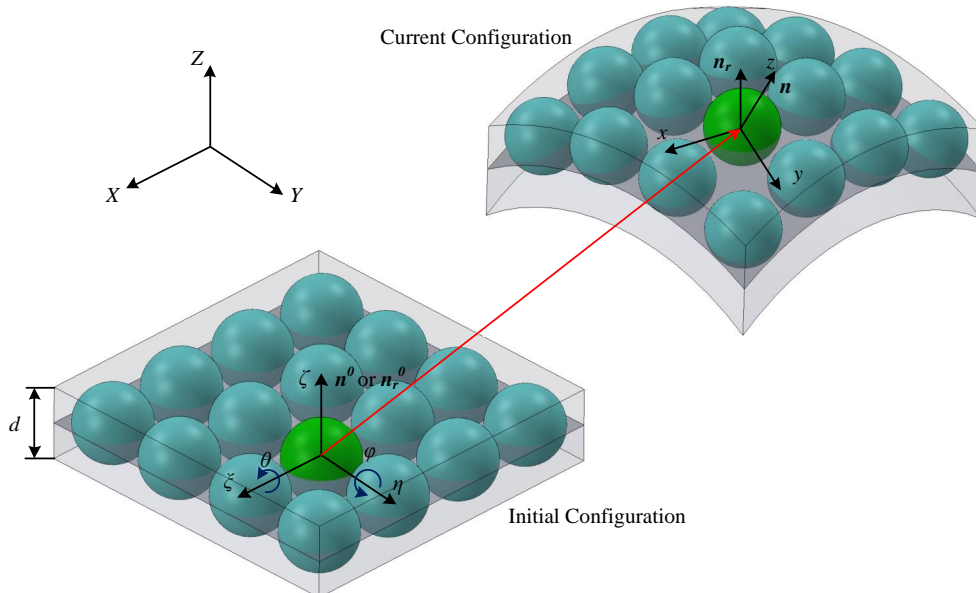


FIGURE 2.1: Schematic of a 3D plate model [80]. Note that while the shell domain is discretized by spheres herein, it is important to clarify that a sphere or particle domain is actually a cube.

Kinematics

We introduce $\mathbf{X} = (X, Y, Z)$ to represent the global coordinate system, and $\boldsymbol{\xi} = (\xi, \eta, \zeta)$ and $\mathbf{x} = (x, y, z)$, associated with so-called pseudo-normal vector \mathbf{n} , to denote the initial and current local coordinate systems, respectively. Note that the initial local coordinate system is same with the global one for plate. Each material point possesses five degrees of freedom, viz., three translations $\mathbf{u} = \{u, v, w\}^T$ and two rotations $\boldsymbol{\theta} = \{\theta, \varphi\}^T$ expressed in the global coordinates. Positive values of θ and φ indicate that the plate is rotated anticlockwise around the coordinate axis when the axis points toward the observer and the coordinate system is right-handed. The two rotations are used to update the pseudo-normal $\mathbf{n} = \{n_1, n_2, n_3\}^T$ which is also defined in the global coordinate system and remains straight but is not necessarily perpendicular to the mid-surface, i.e., the pseudo normal may be different with the real normal \mathbf{n}_r , as shown in Figure 2.1. Note that $\mathbf{n}^0 = \{0, 0, 1\}^T$ denotes the pseudo-normal in the initial configuration with the superscript $(\bullet)^0$ denoting the initial configuration. Additionally, it is worth clarifying that although the plate domain is discretized using spheres in Figure 2.1, which is a common practice in particle methods, it is essential to understand that a sphere or particle domain is actually a cubic shape.

For a plate, the position \mathbf{r} of a material point at a distance χ away from the mid-surface along the pseudo normal \mathbf{n} can be expressed as

$$\mathbf{r}(\xi, \eta, \chi, t) = \mathbf{r}_m(\xi, \eta, t) + \chi \mathbf{n}(\xi, \eta, t), \quad \chi \in [-d/2, d/2], \quad (2.28)$$

where d is the thickness, \mathbf{r}_m the position of the material point at the mid-surface with the subscript $(\bullet)_m$ denoting the mid-surface. Note that since the thickness is assumed to be constant during deformation and the pseudo normal \mathbf{n} represents the plate thickness direction, the distance χ is always between $-d/2$ and $d/2$. Therefore, the displacement \mathbf{u} of the material point can be determined by

$$\mathbf{u}(\xi, \eta, \chi, t) = \mathbf{u}_m(\xi, \eta, t) + \chi \Delta \mathbf{n}(\xi, \eta, t), \quad (2.29)$$

where $\Delta \mathbf{n} = \mathbf{n} - \mathbf{n}^0$. Then we can define the deformation gradient tensor as

$$\mathbb{F} = \nabla^0 \mathbf{r} = \nabla^0 \mathbf{u} + \mathbb{I} = (\mathbf{a}_1, \mathbf{a}_2, \mathbf{a}_3), \quad (2.30)$$

where $\nabla^0 \equiv \partial/\partial \boldsymbol{\xi}$ is the gradient operator with respect to the initial configuration, \mathbb{I} the identity matrix, and $\mathbf{a}_1, \mathbf{a}_2, \mathbf{a}_3$ are specified by

$$\begin{cases} \mathbf{a}_1 = \mathbf{r}_{m,\xi} + \chi \mathbf{n}_\xi \\ \mathbf{a}_2 = \mathbf{r}_{m,\eta} + \chi \mathbf{n}_\eta \\ \mathbf{a}_3 = \mathbf{n} \end{cases} \quad (2.31)$$

with $\nabla^0 \mathbf{r}_m \equiv (\mathbf{r}_{m,\xi}, \mathbf{r}_{m,\eta})^T$ and $\nabla^0 \mathbf{n} \equiv (\mathbf{n}_\xi, \mathbf{n}_\eta)^T$. The deformation gradient tensor can be decomposed into two components as

$$\mathbb{F} = \mathbb{F}_m + \chi \mathbb{F}_n, \quad (2.32)$$

where $\mathbb{F}_m = (\mathbf{r}_{m,\xi}^T, \mathbf{r}_{m,\eta}^T, \mathbf{n}^T)$ and $\mathbb{F}_n = (\mathbf{n}_\xi^T, \mathbf{n}_\eta^T, 0)$. The change rate of this deformation gradient is expressed as

$$\dot{\mathbb{F}} = \nabla^0 \dot{\mathbf{u}} = \nabla^0 \dot{\mathbf{u}}_m + \chi \nabla^0 \dot{\mathbf{n}}, \quad (2.33)$$

where $\dot{\mathbf{u}}_m$ and $\dot{\mathbf{n}}$ denote the velocity and change rate of pseudo-normal, respectively. Furthermore, the real normal \mathbf{n}_r is given as

$$\mathbf{n}_r = \frac{\mathbf{r}_{m,\xi} \times \mathbf{r}_{m,\eta}}{|\mathbf{r}_{m,\xi} \times \mathbf{r}_{m,\eta}|}. \quad (2.34)$$

Stress correction

As the thickness is significantly less than the length and width of plate, the following boundary conditions hold when the plate is free from external forces on its surfaces where $\chi = \pm \frac{d}{2}$ or $z = \pm \frac{d}{2}$

$$\sigma_{xz}^l \Big|_{z=\pm \frac{d}{2}} = 0, \quad \sigma_{yz}^l \Big|_{z=\pm \frac{d}{2}} = 0, \quad (2.35)$$

$$\sigma_{zz}^l \Big|_{z \in [-\frac{d}{2}, \frac{d}{2}]} = 0, \quad (2.36)$$

with the superscript $(\bullet)^l$ denoting the current local coordinates. Taking the boundary condition Eq. (2.36) and constitutive Eq. (2.9) into account, the following relation of strains holds [86]

$$\bar{\epsilon}_{zz}^l = \frac{-\nu (\epsilon_{xx}^l + \epsilon_{yy}^l)}{1 - \nu}, \quad (2.37)$$

where the current local strain \mathcal{E}^l is obtained by

$$\mathcal{E}^l = \mathbf{Q} \mathcal{E} \mathbf{Q}^T. \quad (2.38)$$

Here, \mathbf{Q} is the orthogonal transformation matrix from the global to current local coordinates. Following Batoz and Dhatt [101], \mathbf{Q} can be given as

$$\mathbf{Q} = \begin{bmatrix} n_3 + \frac{(n_2)^2}{1+n_3} & -\frac{n_1 n_2}{1+n_3} & -n_1 \\ -\frac{n_1 n_2}{1+n_3} & n_3 + \frac{(n_1)^2}{1+n_3} & -n_2 \\ n_1 & n_2 & n_3 \end{bmatrix}. \quad (2.39)$$

To satisfy the boundary conditions of Eq. (2.35), the transverse shear stress should be corrected as [102]

$$\bar{\sigma}_{xz}^l = \bar{\sigma}_{zx}^l = \beta \sigma_{xz}^l, \quad \bar{\sigma}_{yz}^l = \bar{\sigma}_{zy}^l = \beta \sigma_{yz}^l, \quad (2.40)$$

where β denotes the shear correction factor which is typically set to 5/6 for the rectangular section of the isotropic plate. Taking the corrected strain $\bar{\mathcal{E}}^l$ into constitutive Eq. (2.9) and then applying Eq. (2.40), the corrected current local Cauchy stress $\bar{\boldsymbol{\sigma}}^l$ is obtained.

Conservation equations

The mass conservation equation can be written as

$$\rho = J_m^{-1} \rho^0, \quad (2.41)$$

where $J_m = \det(\mathbb{F}_m)$, ρ^0 and ρ represent the initial and current densities, respectively. The momentum conservation equation is

$$\rho \dot{\mathbf{i}}^l = \nabla \cdot (\bar{\boldsymbol{\sigma}}^l)^T \quad (2.42)$$

or

$$\rho \begin{bmatrix} \dot{u}^l \\ \dot{v}^l \\ \dot{w}^l \end{bmatrix} = \begin{bmatrix} \frac{\partial \bar{\sigma}_{xx}^l}{\partial x} + \frac{\partial \bar{\sigma}_{xy}^l}{\partial y} + \frac{\partial \bar{\sigma}_{xz}^l}{\partial z} \\ \frac{\partial \bar{\sigma}_{yx}^l}{\partial x} + \frac{\partial \bar{\sigma}_{yy}^l}{\partial y} + \frac{\partial \bar{\sigma}_{yz}^l}{\partial z} \\ \frac{\partial \bar{\sigma}_{zx}^l}{\partial x} + \frac{\partial \bar{\sigma}_{zy}^l}{\partial y} + \frac{\partial \bar{\sigma}_{zz}^l}{\partial z} \end{bmatrix}. \quad (2.43)$$

With Eqs. (2.35) and (2.36), we can integrate Eq. (2.43) along χ or $z \in [-d/2, d/2]$ as

$$d\rho \begin{bmatrix} \dot{u}_m^l \\ \dot{v}_m^l \\ \dot{w}_m^l \end{bmatrix} = \begin{bmatrix} \frac{\partial N_{xx}^l}{\partial x} + \frac{\partial N_{xy}^l}{\partial y} \\ \frac{\partial N_{yx}^l}{\partial x} + \frac{\partial N_{yy}^l}{\partial y} \\ \frac{\partial N_{zx}^l}{\partial x} + \frac{\partial N_{zy}^l}{\partial y} \end{bmatrix}, \quad (2.44)$$

where the stress resultant \mathbb{N}^l is calculated by the Gauss–Legendre quadrature rule as

$$\mathbb{N}^l = \int_{-d/2}^{d/2} \bar{\boldsymbol{\sigma}}^l(z) dz = \sum_{ip=1}^N \bar{\boldsymbol{\sigma}}^l(z_{ip}) A_{ip}. \quad (2.45)$$

Here, z_{ip} is the integral point, A_{ip} the weight, and N the number of the integral point. Since the quadrature rule is conducted to yield an exact result for polynomials of degree $2N - 1$ or lower [103], N is determined by the applied constitutive relation.

By multiplying both sides of Eq. (2.42) by z and integrating along $z \in [-d/2, d/2]$, the angular momentum conservation equation can be obtained as

$$\frac{d^3}{12} \rho \begin{bmatrix} \dot{n}_1^l \\ \dot{n}_2^l \\ \dot{n}_3^l \end{bmatrix} = \begin{bmatrix} \frac{\partial M_{xx}^l}{\partial x} + \frac{\partial M_{xy}^l}{\partial y} \\ \frac{\partial M_{yx}^l}{\partial x} + \frac{\partial M_{yy}^l}{\partial y} \\ \frac{\partial M_{zx}^l}{\partial x} + \frac{\partial M_{zy}^l}{\partial y} \end{bmatrix} + \begin{bmatrix} -N_{xz}^l \\ -N_{yz}^l \\ 0 \end{bmatrix}, \quad (2.46)$$

where the moment resultant \mathbb{M}^l is calculated as

$$\mathbb{M}^l = \int_{-d/2}^{d/2} z \bar{\boldsymbol{\sigma}}^l(z) dz = \sum_{ip=1}^N z_{ip} \bar{\boldsymbol{\sigma}}^l(z_{ip}) A_{ip}. \quad (2.47)$$

Note that

$$\int_{-d/2}^{d/2} z \frac{\partial \bar{\sigma}_{xz}^l}{\partial z} dz = \left[z \bar{\sigma}_{xz}^l \right]_{-d/2}^{d/2} - \int_{-d/2}^{d/2} \bar{\sigma}_{xz}^l dz = -N_{xz}^l. \quad (2.48)$$

Therefore, the two governing equations, including the evolution of mid-surface displacement and pseudo normal, respectively, for the 3D plate can be described as

$$\begin{cases} d\rho \dot{\mathbf{i}}_m^l = \nabla^l \cdot (\mathbb{N}^l)^T \\ \frac{d^3}{12} \rho \dot{\mathbf{n}}^l = \nabla^l \cdot (\mathbb{M}^l)^T + \mathbf{Q}^l, \end{cases} \quad (2.49)$$

where

$$\mathbb{N}^l = \begin{bmatrix} N_{xx}^l & N_{xy}^l & 0 \\ N_{yx}^l & N_{yy}^l & 0 \\ N_{zx}^l & N_{zy}^l & 0 \end{bmatrix}, \mathbb{M}^l = \begin{bmatrix} M_{xx}^l & M_{xy}^l & 0 \\ M_{yx}^l & M_{yy}^l & 0 \\ M_{zx}^l & M_{zy}^l & 0 \end{bmatrix}, \mathbf{Q}^l = \begin{bmatrix} -N_{xz}^l \\ -N_{yz}^l \\ 0 \end{bmatrix}. \quad (2.50)$$

In total Lagrangian formulation, the conservation equations above are converted into

$$\begin{cases} d\rho^0 \dot{\mathbf{u}}_m = (\mathbb{F}_m)^{-T} \nabla^0 \cdot (J_m \mathbb{N}^T) \\ \frac{d^3}{12} \rho^0 \dot{\mathbf{n}} = (\mathbb{F}_m)^{-T} \nabla^0 \cdot (J_m \mathbb{M}^T) + J_m \mathbf{Q}^T \mathbf{Q}^l, \end{cases} \quad (2.51)$$

where $\mathbb{N} = \mathbf{Q}^T \mathbb{N}^l \mathbf{Q}$ and $\mathbb{M} = \mathbf{Q}^T \mathbb{M}^l \mathbf{Q}$ are the stress and moment resultants, respectively, in global coordinates.

2.3.2 3D shell model

Based on the 3D plate model, the 3D shell model is obtained by introducing the initial local coordinate system and the transformation matrix from the global to initial local coordinate system. As the transformation matrix is a unit matrix for plates, both plates and shells can be constructed in their initial local coordinates, allowing for a unified model for both structures.

Kinematics

The kinematics of shell can be constructed in the initial local coordinates denoted with the superscript $(\bullet)^L$. Each material point possesses five degrees of freedom, viz., three translations $\mathbf{u}^L = \{u^L, v^L, w^L\}^T$ and two rotations $\boldsymbol{\theta}^L = \{\theta^L, \varphi^L\}^T$ as shown in Figure 2.2. The pseudo-normal vector is also presented in initial local coordinates by $\mathbf{n}^L = \{n_1^L, n_2^L, n_3^L\}^T$, especially denoted by $\mathbf{n}^{0,L} = \{0, 0, 1\}^T$ in the initial local configuration. The local position \mathbf{r}^L of a material point can be expressed

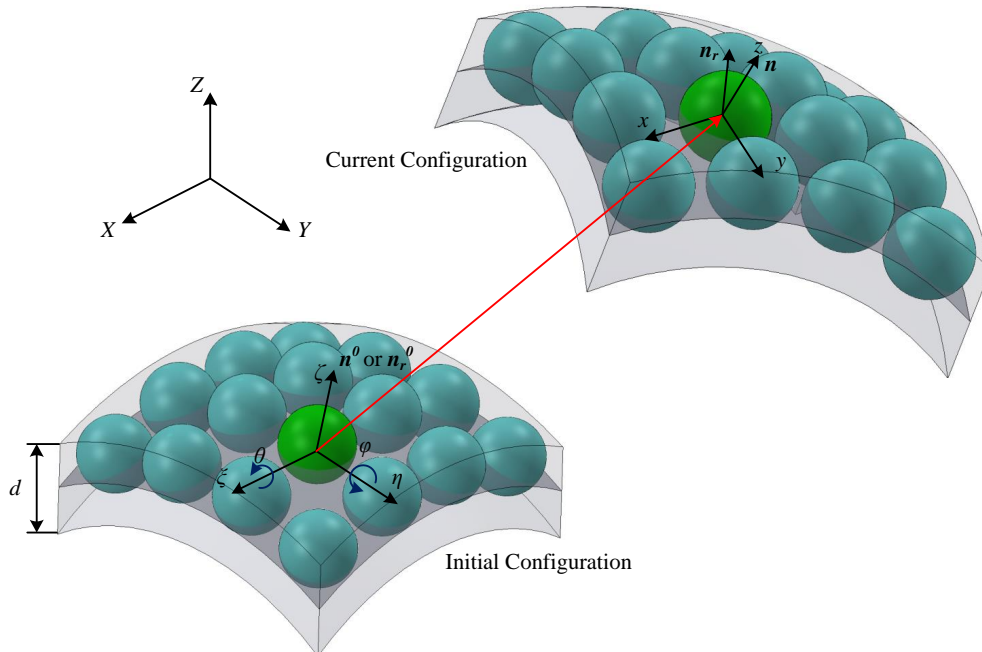


FIGURE 2.2: Schematic of a 3D shell model [80].

as

$$\mathbf{r}^L(\xi, \eta, \chi, t) = \mathbf{r}_m^L(\xi, \eta, t) + \chi \mathbf{n}^L(\xi, \eta, t), \quad \chi \in [-d/2, d/2]. \quad (2.52)$$

The local displacement \mathbf{u}^L can thus be obtained by

$$\mathbf{u}^L(\xi, \eta, \chi, t) = \mathbf{u}_m^L(\xi, \eta, t) + \chi \Delta \mathbf{n}^L(\xi, \eta, t), \quad (2.53)$$

where $\Delta \mathbf{n}^L = \mathbf{n}^L - \mathbf{n}^{0,L}$. Similar to 3D plates, the local deformation gradient tensor of 3D shells can be defined as

$$\mathbb{F}^L = \nabla^{0,L} \mathbf{r}^L + \nabla^{0,L} \mathbf{n}^L - \nabla^{0,L} \mathbf{n}^{0,L} = (\mathbf{a}_1^L, \mathbf{a}_2^L, \mathbf{a}_3^L), \quad (2.54)$$

where $\nabla^{0,L} \equiv \partial / \partial \xi$ is the gradient operators defined in the initial local configuration, and $\mathbf{a}_1^L, \mathbf{a}_2^L, \mathbf{a}_3^L$ are detailed by

$$\begin{cases} \mathbf{a}_1^L = \mathbf{r}_{m,\xi}^L + \chi \mathbf{n}_{\xi}^L - \chi \mathbf{n}_{\xi}^{0,L} \\ \mathbf{a}_2^L = \mathbf{r}_{m,\eta}^L + \chi \mathbf{n}_{\eta}^L - \chi \mathbf{n}_{\eta}^{0,L} \\ \mathbf{a}_3^L = \mathbf{n}^L. \end{cases} \quad (2.55)$$

Stress correction and conservation equation

With the local deformation gradient tensor \mathbb{F}^L , the local Eulerian Almansi strain \mathbb{E}^L can be calculated by the Eq. (2.7). After that, the current local \mathbb{E}^l is obtained according to the coordinate transformation as

$$\mathbb{E}^l = \mathbf{Q} (\mathbf{Q}^0)^T \mathbb{E}^L \mathbf{Q}^0 \mathbf{Q}^T, \quad (2.56)$$

where \mathbf{Q}^0 , the orthogonal transformation matrix from the global to initial local coordinates, is calculated from Eq. (2.39) while the current pseudo normal \mathbf{n} is replaced by the initial one \mathbf{n}^0 . And then the corrected strain $\bar{\mathbb{E}}^l$ is estimated by applying Eq. (2.37). After getting the current local Cauchy stress $\bar{\sigma}^l$ by Eq. (2.9), the corrected one $\bar{\sigma}^l$ is obtained by Eq. (2.40).

Note that the total Lagrangian conservation equations of a 3D shell has the same form as Eqs. (2.51) with $\mathbb{F}_m = (\mathbf{Q}^0)^T \mathbb{F}_m^L \mathbf{Q}^0$.

2.3.3 2D plate/shell model

If a plate/shell is assumed to be a strip that is very long and has a finite width, and the transverse load is assumed to be uniform along the length, the analysis can be simplified at any cross section as a plane strain problem [104].

The kinematics of 2D plate and shell can also be built in initial local coordinates. The 2D model is in the global X-Z plane, and each material point possesses three degrees of freedom, viz., two translations $\mathbf{u}^L = \{u^L, w^L\}^T$ and one rotation $\boldsymbol{\theta}^L = \{\varphi^L\}^T$ expressed in the initial local coordinates. The pseudo-normal vector is presented in the initial local coordinates by $\mathbf{n}^L = \{n_1^L, n_3^L\}^T$, especially denoted by $\mathbf{n}^{0,L} = \{0, 1\}^T$ in the initial local configuration. Similar to 3D model, the local position \mathbf{r}^L of a material point can be expressed as

$$\mathbf{r}^L(\xi, \chi, t) = \mathbf{r}_m^L(\xi, t) + \chi \mathbf{n}^L(\xi, t), \quad \chi \in [-d/2, d/2], \quad (2.57)$$

the local displacement \mathbf{u}^L can be evaluated as

$$\mathbf{u}^L(\xi, \chi, t) = \mathbf{u}_m^L(\xi, t) + \chi \Delta \mathbf{n}^L(\xi, t). \quad (2.58)$$

and the local deformation gradient tensor is written as

$$\mathbb{F}^L = \nabla^{0,L} \mathbf{r}^L + \nabla^{0,L} \mathbf{n}^L - \nabla^{0,L} \mathbf{n}^{0,L} = (\mathbf{a}_1^L, \mathbf{a}_3^L), \quad (2.59)$$

where \mathbf{a}_1^L and \mathbf{a}_3^L are given by

$$\begin{cases} \mathbf{a}_1^L = \mathbf{r}_{m,\xi}^L + \zeta \mathbf{n}_\xi^L - \zeta \mathbf{n}_\xi^{0,L} \\ \mathbf{a}_3^L = \mathbf{n}^L. \end{cases} \quad (2.60)$$

The coordinate transformation matrix \mathbf{Q} from global to current local coordinates is simplified from Eqs. (2.39) as

$$\mathbf{Q} = \begin{bmatrix} n_3 & -n_1 \\ n_1 & n_3 \end{bmatrix}, \quad (2.61)$$

and the 2D transformation matrix \mathbf{Q}^0 from global to initial local coordinates can also be calculated by Eq. (2.61) while the current pseudo normal \mathbf{n} is replaced by the initial one \mathbf{n}^0 . The corrected relation of strains is simplified from Eq. (2.37) as

$$\bar{\epsilon}_{zz}^l = \frac{-\nu \epsilon_{xx}^l}{1 - \nu}. \quad (2.62)$$

Finally, the 2D conservation equation is identical to 3D Eq. (2.51) with

$$\mathbb{N}^l = \begin{bmatrix} N_{xx}^l & 0 \\ N_{zx}^l & 0 \end{bmatrix}, \mathbb{M}^l = \begin{bmatrix} M_{xx}^l & 0 \\ M_{zx}^l & 0 \end{bmatrix}, \mathbf{Q}^l = \begin{bmatrix} -N_{xz}^l \\ 0 \end{bmatrix}. \quad (2.63)$$

2.4 Theory and fundamentals of the SPH method

Before introducing the discretizations of the governing equations, we first summarize the theory and fundamentals of the SPH method.

2.4.1 Integral interpolation and particle approximation

In the SPH method, the continuum media is discretized into a finite number of Lagrangian particles, whose interactions are governed by a compact-support kernel function, typically a Gaussian-like function, which approximates the spatial differential operators. Each particle i , located at the position vector \mathbf{r}_i and moving with the material velocity $\dot{\mathbf{u}}_i$, carries particle-average field variables, such as mass m_i , density ρ_i , volume V_i , etc. The discretization of a variable field $f(\mathbf{r})$ can then be written as

$$f_i = \int f(\mathbf{r}) W(\mathbf{r}_i - \mathbf{r}, h) d\mathbf{r}, \quad (2.64)$$

where the kernel function $W(\mathbf{r}_i - \mathbf{r}, h)$ is radially symmetric with respect to \mathbf{r}_i and h the smoothing length. By introducing particle summation, this variable field can be

approximated by

$$f_i \approx \sum_j V_j W(\mathbf{r}_i - \mathbf{r}_j, h) f_j = \sum_j \frac{m_j}{\rho_j} W(\mathbf{r}_i - \mathbf{r}_j, h) f_j, \quad (2.65)$$

where the summation is conducted over all the neighboring particles j in the support domain of the particle i .

Following Ref. [9], the original SPH approximation of the spatial derivative operator of the variable field $f(\mathbf{r})$ at particle i can be obtained by

$$\begin{aligned} \nabla f_i &= \int_{\Omega} \nabla f(\mathbf{r}) W(\mathbf{r}_i - \mathbf{r}, h) dV \\ &= - \int_{\Omega} f(\mathbf{r}) \nabla W(\mathbf{r}_i - \mathbf{r}, h) dV \approx - \sum_j V_j \nabla_i W_{ij} f_j, \end{aligned} \quad (2.66)$$

where $\nabla_i W_{ij} = \frac{\partial W(\mathbf{r}_{ij}, h)}{\partial \mathbf{r}_{ij}} \mathbf{e}_{ij}$ is the derivative of the kernel function with r_{ij} denoting the particle distance and \mathbf{e}_{ij} the unit vector pointing from particle j to particle i . Following Ref. [6], we can modify Eq. (2.66) into a strong form as

$$\nabla f_i = \nabla f_i - f_i \nabla 1 \approx - \sum_j V_j \nabla_i W_{ij} f_{ij}, \quad (2.67)$$

where $f_{ij} = f_i - f_j$ is the interparticle difference value. This strong-form approximation of the spatial derivative is useful for computing the local structure of a field. And Eq. (2.66) can also be rewritten into a weak form as

$$\nabla f_i = f_i \nabla 1 + \nabla f_i \approx 2 \sum_j V_j \nabla W_{ij} \tilde{f}_{ij}, \quad (2.68)$$

where $\tilde{f}_{ij} = (f_i + f_j) / 2$ denotes the interparticle average value. This weak-form approximation of the derivative is applied to determine the surface integration with respect to a variable for solving the conservation law. Due to the anti-symmetric property of the derivative of the kernel function, i.e., $\nabla_i W_{ij} = -\nabla_j W_{ji}$, the momentum conservation of the particle system is achieved with Eq. (2.68).

2.4.2 The smoothing kernel

In the SPH method, the smoothing kernel plays a critical role in determining the consistency and accuracy of both kernel and particle approximations. Therefore, selecting an appropriate kernel function is essential for ensuring reliable results in SPH simulations. As highlighted by Liu and Liu [105] and Monaghan [9], the smoothing kernel must be normalized over its support domain, expressed as

$$\int_{\Omega} W(\mathbf{r}_i - \mathbf{r}, h) d\mathbf{r} = 1, \quad (2.69)$$

and also should be compactly supported as

$$W(\mathbf{r}_i - \mathbf{r}) = 0, \quad \text{for } |\mathbf{r}_i - \mathbf{r}| > kh. \quad (2.70)$$

Here, k is the smoothing factor, $|\mathbf{r}_i - \mathbf{r}| \leq kh$ defines the support domain. Additionally, the smoothing kernel must satisfy the symmetry condition, which is essential

for ensuring conservation properties, and it should approximate a delta function as the smoothing length approaches zero. For further details, refer to Ref. [106].

Various smoothing kernels have been proposed for SPH method [1, 2, 107, 108, 9, 106, 105]. A fifth-order Wendland kernel [109] reads

$$W(\mathbf{r}_i - \mathbf{r}, h) = \alpha \begin{cases} (1 + 2q)(2 - q)^4 & \text{if } 0 \leq q \leq 2 \\ 0 & \text{if } 2 \leq q \end{cases}, \quad (2.71)$$

where $q = |\mathbf{r}_i - \mathbf{r}|/h$ the constant α is $\frac{7}{64\pi h^2}$ for 2D problems and $\frac{21}{256\pi h^3}$ for 3D problems. For thin structure modeling, a reduced-dimensional kernel is applied, and thus α is $\frac{3}{4h}$ for 2D thin structures and $\frac{7}{4\pi h^2}$ for 3D thin structures according to Eq. (2.69).

2.5 SPH method of solid dynamics

2.5.1 SPH discretization

Following Refs. [9, 6], the momentum conservation Eq. (2.3) is discretized in the weak-form SPH approximation of the spatial derivative as

$$\rho_i^0 \dot{\mathbf{u}}_i = \sum_j \left(\mathbb{F}_i \mathbb{B}_i^{0T} + \mathbb{F}_j \mathbb{B}_j^{0T} \right) \nabla_i^0 W_{ij} V_j^0, \quad (2.72)$$

where $\nabla_i^0 W_{ij} = \frac{\partial W(r_{ij}^0, h)}{\partial r_{ij}^0} \mathbf{e}_{ij}^0$ denotes the gradient of the kernel function evaluated at the initial reference configuration with r_{ij}^0 representing the initial particle distance and \mathbf{e}_{ij}^0 the initial unit vector pointing from particle j to particle i . Additionally, ρ_i^0 is the initial density of particle i , and V_j^0 is the initial volume of particle j . Here, the superscript $(\bullet)^0$ is introduced to represent variables defined at the initial reference configuration. The kernel gradient correction (KGC) correction matrix \mathbb{B}^0 is adopted to ensure first-order completeness as [3, 110, 111, 31, 53]

$$\mathbb{B}_i^0 = \left(\sum_j V_j^0 (\mathbf{r}_j^0 - \mathbf{r}_i^0) \otimes \nabla_i^0 W_{ij} \right)^{-1}. \quad (2.73)$$

The deformation tensor \mathbb{F} is updated based on its rate of change, which is approximated in the strong-form discretization of the spatial derivative [9, 6] as

$$\frac{d\mathbb{F}_i}{dt} = \dot{\mathbb{F}}_i = \nabla^0 \dot{\mathbf{u}}_i = \sum_j V_j^0 (\dot{\mathbf{u}}_j - \dot{\mathbf{u}}_i) \otimes \nabla_i^0 W_{ij} \mathbb{B}_i^0. \quad (2.74)$$

In total Lagrangian framework, this is equivalent to directly calculating $\mathbb{F} = \nabla^0 \mathbf{r}$. It is worth noting that, due to the KGC correction matrix employed in Eq. (2.74) for computing $\dot{\mathbb{F}}_i$ [3, 110, 111, 31, 53], the rotational motion is accurately captured [110], objectivity is preserved and the ghost or artificial forces due to rigid-body rotation are eliminated [112].

Following the approach in Ref. [60], we introduce an artificial damping stress \mathbb{T}_d based on the Kelvin-Voigt type damper when calculating the Kirchhoff stress \mathbb{T} as

$$\mathbb{T}_d = \frac{\chi}{2} \frac{d\mathbb{b}}{dt}, \quad (2.75)$$

where the artificial viscosity factor $\chi = \rho Ch/2$ with $C = \sqrt{K/\rho}$, where K is bulk modules, and h denoting the smoothing length. Here, $\mathbb{b} = \mathbb{F}\mathbb{F}^T$ denotes the the left Cauchy-Green deformation gradient tensor, and its change rate can be obtained directly as

$$\frac{d\mathbb{b}}{dt} = \left[\frac{d\mathbb{F}}{dt} \mathbb{F}^T + \mathbb{F} \left(\frac{d\mathbb{F}}{dt} \right)^T \right]. \quad (2.76)$$

Note that the artificial damping stress in Eq. (2.75) is proportional to the smoothing length h . As the resolution increases or static equilibrium reaches, the effect of this numerical dissipation diminishes. Also note that the numerical dissipation of Eq. (2.75) plays the main role to ensure non-increasing of total energy.

2.5.2 Time integration scheme

In accordance with Ref. [113], the position-based Verlet scheme is employed for time integration. Initially, the deformation gradient tensor, density, and particle position are updated to the midpoint of n -th time step as

$$\begin{cases} \mathbb{F}^{n+\frac{1}{2}} = \mathbb{F}^n + \frac{1}{2}\Delta t \dot{\mathbb{F}}^n \\ \rho^{n+\frac{1}{2}} = \rho^0 \frac{1}{J} \\ \mathbf{r}^{n+\frac{1}{2}} = \mathbf{r}^n + \frac{1}{2}\Delta t \dot{\mathbf{u}}^n. \end{cases} \quad (2.77)$$

Upon calculating the Kirchhoff stress $\boldsymbol{\tau}^n$ based on the applied constitutive relation and the artificial damping stress $\boldsymbol{\tau}_d^n = \frac{\chi}{2} \left[\dot{\mathbb{F}}^n \mathbb{F}^{n+\frac{1}{2},T} + \mathbb{F}^{n+\frac{1}{2}} \dot{\mathbb{F}}^{n,T} \right]$ and subsequently obtaining particle acceleration using Eq. (2.72), the velocity is updated through

$$\dot{\mathbf{u}}^{n+1} = \dot{\mathbf{u}}^n + \Delta t \ddot{\mathbf{u}}^{n+1}. \quad (2.78)$$

After that, the rate of change of the deformation gradient tensor $\dot{\mathbb{F}}^{n+1}$ is computed using Eq. (2.74). Finally, the deformation gradient tensor and particle positions are updated to a new time step with

$$\begin{cases} \mathbb{F}^{n+1} = \mathbb{F}^{n+\frac{1}{2}} + \frac{1}{2}\Delta t \dot{\mathbb{F}}^{n+1} \\ \rho^{n+1} = \rho^0 \frac{1}{J} \\ \mathbf{r}^{n+1} = \mathbf{r}^{n+\frac{1}{2}} + \frac{1}{2}\Delta t \dot{\mathbf{u}}^{n+1}. \end{cases} \quad (2.79)$$

Adhering to the Courant-Friedrichs-Lewy (CFL) condition and the limit under external force as referenced in Refs. [114, 115, 116, 108, 105], the time step size is given as

$$\Delta t = \text{CFL} \min \left(\frac{h}{C + |\dot{\mathbf{u}}|_{\max}}, \sqrt{\frac{h}{|\ddot{\mathbf{u}}|_{\max}}} \right), \quad (2.80)$$

where the CFL number is set to 0.6, as recommended in Refs. [117, 12].

2.6 Summary

In this chapter, we explored the governing equations and kinematics of solid dynamics, which form the foundational basis for modeling the behavior of solid materials under various conditions. The constitutive relations were then examined to describe

material responses, followed by the introduction of a theoretical model for thin structures. The SPH method was presented as an effective mesh-free approach, adaptable to both general and thin-structured solids. Finally, the SPH for solid dynamics was discussed.

stress directly by discretizing the Laplacian operator on the displacement field (analogous to velocity in the NS equation) to capture shear deformation directly, rather than relying on the deformation gradient and first Piola-Kirchhoff stress tensor. The acceleration due to shear stress in the proposed framework is expressed as

$$\ddot{\mathbf{u}}_{si} = \zeta G \sum_j \left(J_i^{-\frac{2}{d}} + J_j^{-\frac{2}{d}} \right) \frac{\mathbf{r}_{ij}}{r_{ij}^0} \frac{\partial W(r_{ij}^0, h)}{\partial r_{ij}^0} \frac{V_j^0}{\rho_i^0}, \quad (3.1)$$

where the parameter ζ deviates slightly from unity due to numerical errors in kernel summation and is influenced by the smoothing length h and the choice of kernel function [120]. It should be noted that ζ is not necessary to be changed in accordance with the specific constitutive relation. The flowcharts for both the original and the proposed SPH formulations are presented in Figure 3.2.

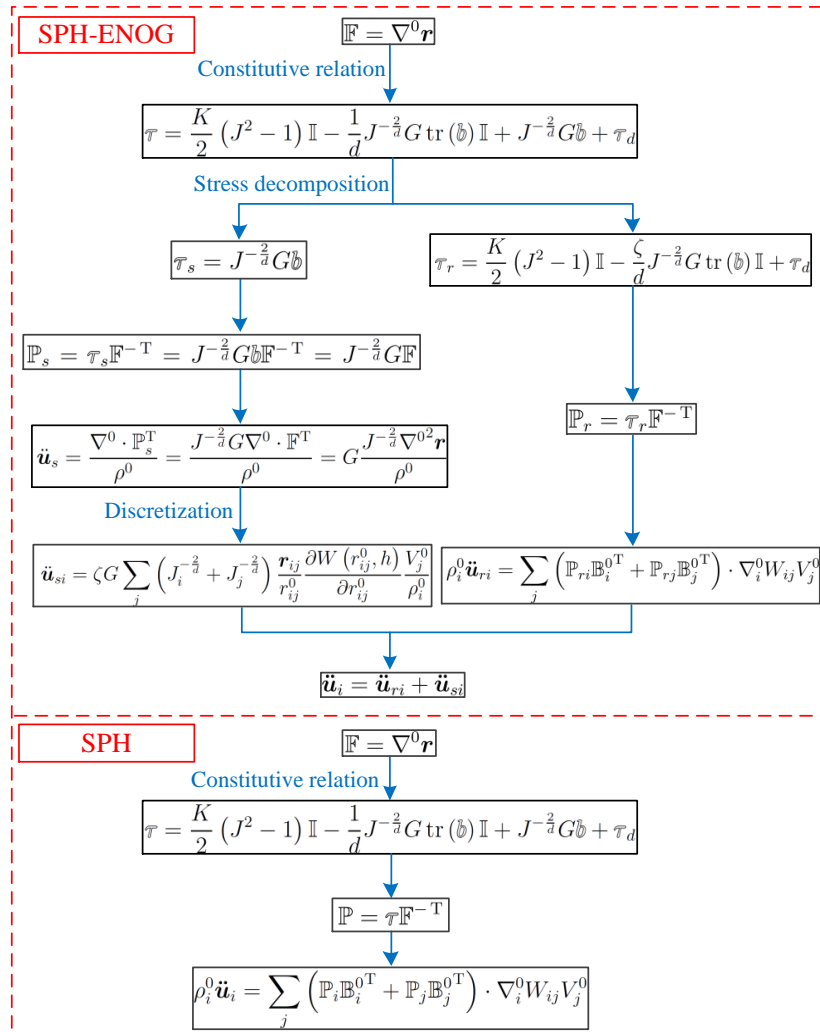


FIGURE 3.2: Flowcharts of the original total Lagrangian SPH (denoted as SPH) in Ref. [17] and present (denoted as SPH-ENOG) formulations.

A comprehensive set of challenging benchmark cases has been simulated to demonstrate that the proposed formulation not only improves accuracy and computational

efficiency but also effectively suppresses hourglass modes, achieving excellent numerical stability with a single general effective parameter. Additionally, the deformation of a stent structure, relevant to practical applications, is simulated to showcase the potential of this method in biomechanics. Figure 3.3 illustrates the comparison of deformed particle configurations during 2D plate oscillation.

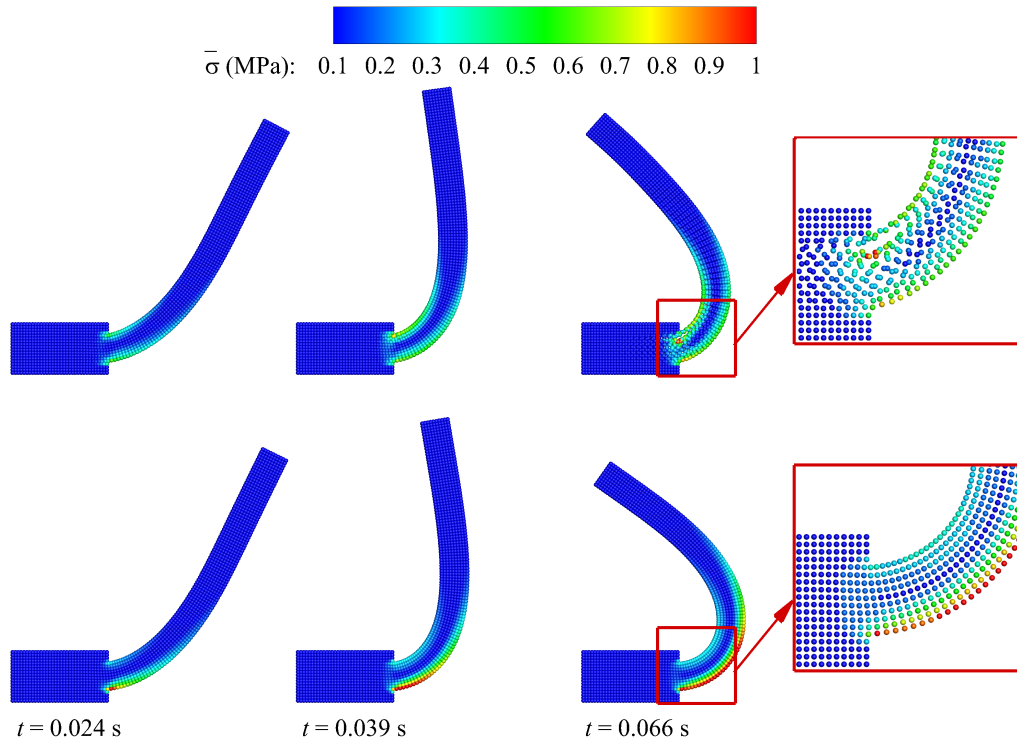


FIGURE 3.3: 2D oscillating plate: Comparison of the deformed configuration colored by von Mises stress $\bar{\sigma}$ at serial time instants obtained by the SPH (top panel) and the SPH-ENOG (bottom panel) [88].

3.1.2 Individual contributions of the candidate

This article [88] was published in the international peer-reviewed journal *Computer Methods in Applied Mechanics and Engineering*. My contribution to this work was the development of the method and the corresponding computer code for its implementation. I have performed simulations, analyzed the results, and wrote the manuscript for the publication.

3.2 Unified non-hourglass formulation for total Lagrangian SPH solid dynamics

D. Wu, X. J. Tang, S. H. Zhang and X. Y. Hu

3.2.1 Summary of the publication

Hourglass modes remain a significant source of numerical instability in TLSPH solid dynamics, especially under large deformations, regardless of material properties. While some methods, such as introducing additional stress points [51, 41, 57, 45], increase computational complexity, most existing hourglass control methods rely on material parameters like sound speed [38, 59, 60] or Young's modulus [54, 61, 62]. This dependence on material properties suggests the physical relevance of the correction terms in mitigating a pure numerical instability, and thus often requires tuning on a case-by-case basis to avoid inadequate or excessive correction [64, 65, 56, 68, 69]. As a result, finding a comprehensive solution that can effectively address hourglass issues across a wide range of material models—encompassing elasticity, plasticity, and anisotropy—remains a challenge.

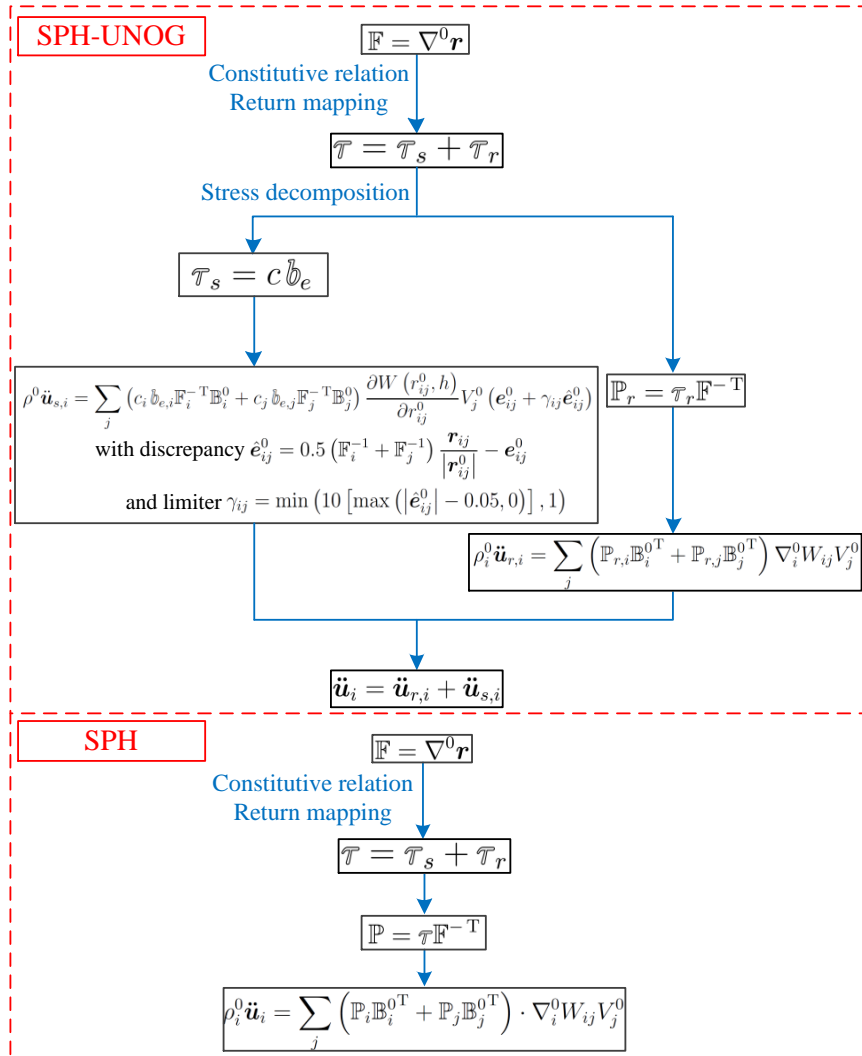


FIGURE 3.4: Flowcharts of the original total Lagrangian SPH (denoted as SPH) in Ref. [17] and present (denoted as SPH-UNOG) formulations.

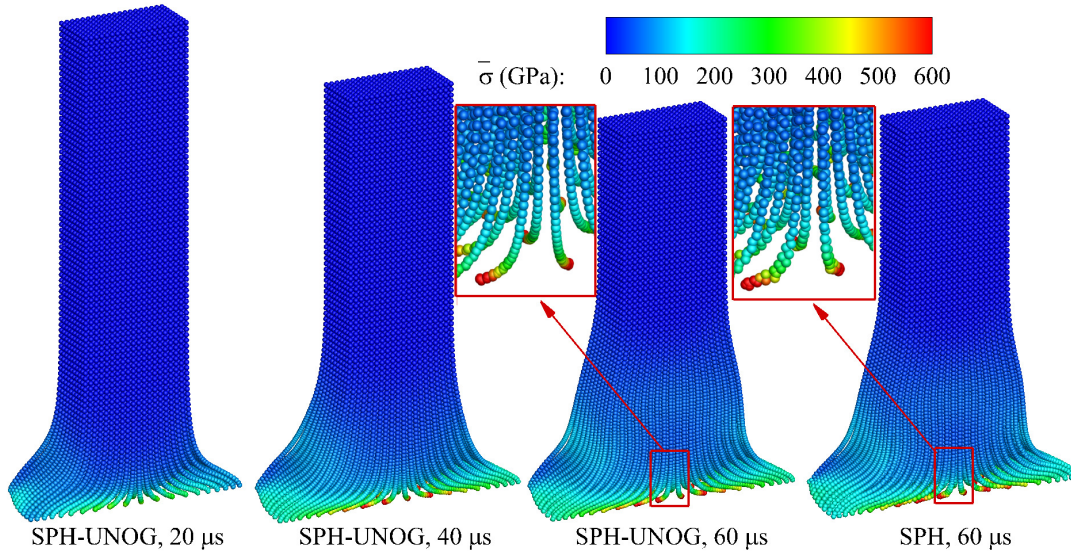


FIGURE 3.5: 3D Taylor bar: Deformed configuration colored by von Mises stress $\bar{\sigma}$ at serial temporal instants obtained by SPH-UNOG, and its comparison with that of SPH. The material is modeled by isotropic hardening elastic-plasticity.

In this study, we present a unified non-hourglass TLSPH formulation based on volumetric-deviatoric stress decomposition, capable of addressing a wide range of material behaviors, including elasticity, plasticity, anisotropy, and more. Unlike approaches that use staggered formulations or additional stress points, this method is built on the standard collocated TLSPH formulation. By comparing the standard SPH formulation with the Laplacian operator introduced in our previous work [88] for resolving hourglass issues in elasticity, we introduce a correction in the shear stress discretization. This correction relies solely on the dimensionless discrepancy produced by tracing back the initial inter-particle direction from the current deformation gradient. Compared to the method in Ref. [62], the proposed formulation integrates naturally with the standard SPH divergence operator, and its dimensionless nature enables seamless handling of complex material models. Rather than introducing extra hourglass-control or viscous stress, as seen in previous FEM, meshless, or SPH methods [66, 67, 38, 59, 60, 54, 61, 62], this formulation conceptually represents a weighted average of two SPH formulations: one being the standard, hourglass-prone version, and the other an essentially non-hourglass formulation for elastic dynamics [88], without adding extra stresses.

Flowcharts for the original and current SPH formulations are shown in Figure 3.4. By employing a limiter with a single set of dimensionless parameters to adaptively adjust the weighting, extensive benchmark tests are conducted to validate the stability and accuracy of this formulation for elastic, plastic, and anisotropic materials. A complex scenario involving viscous plastic Oobleck material, contact, and large deformations is also simulated to demonstrate the versatility of the proposed method. Figure 3.5 illustrates a comparison of deformed particle configurations during a 3D Taylor bar collision. Our approach addresses a critical gap in TLSPH simulations by offering a unified solution for mitigating hourglass modes, enhancing the reliability and accuracy of simulations across various material models and complex scenarios.

3.2.2 Individual contributions of the candidate

This article [48] was published in the international peer-reviewed journal *Computational Mechanics*. My contribution to this work was the development of the method and the corresponding computer code for its implementation. I have performed simulations, analyzed the results, and wrote the manuscript for the publication.

3.3 An SPH formulation for general plate and shell structures with finite deformation and large rotation

D. Wu, C. Zhang and X. Y. Hu

3.3.1 Summary of the publication

For plate and shell structures, the traditional full-dimensional, or volume-particle, SPH method is not computationally efficient [74]. Furthermore, well-established reduced-dimensional theories, such as Kirchhoff-Love [75] and Uflyand-Mindlin (or Mindlin-Reissner) [76, 77, 78, 79], based on mid-surface reconstruction, provide a foundation for more efficient modeling of these structures. Therefore, it is expected that a reduced-dimensional or surface-particle SPH method, utilizing only a single layer of particles, can offer a much more computationally efficient alternative.

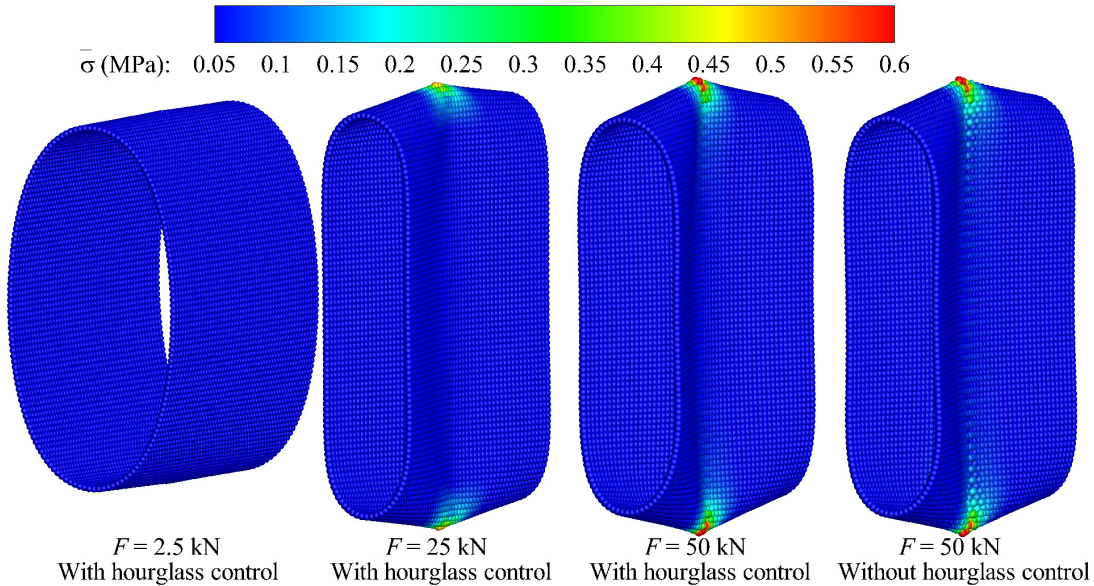


FIGURE 3.6: Pulled-out cylindrical shell: Particles colored by the von Mises stress $\bar{\sigma}$ of the mid-surface under 3 point force magnitudes, and its comparison with the results obtained without hourglass control applied.

In this work, we propose a collocated surface-particle SPH formulation for total Lagrangian quasi-static and dynamic analyses of general plate and shell structures, which may be thin or moderately thick, involving finite deformations and/or large rotations. First, to better capture the geometric non-linearity induced by finite deformations and large rotations, two new reduced-dimensional correction matrices for linearly reproducing position and normal direction are introduced, along with a weighted conversion algorithm that ensures non-singularity under large rotations. Second, a new non-isotropic Kelvin-Voigt damping mechanism, based on Ref. [60], is proposed to achieve numerical stability for both thin and moderately thick plate and shell structures. Third, to address hourglass modes using only collocated particles—without the need for additional stress points—we draw inspiration from Refs. [61, 62] and develop a shear-scaled momentum-conserving formulation with an adaptive limiter.

A series of numerical examples involving quasi-static and dynamic analyses of both thin and moderately thick plate and shell structures are provided. The results

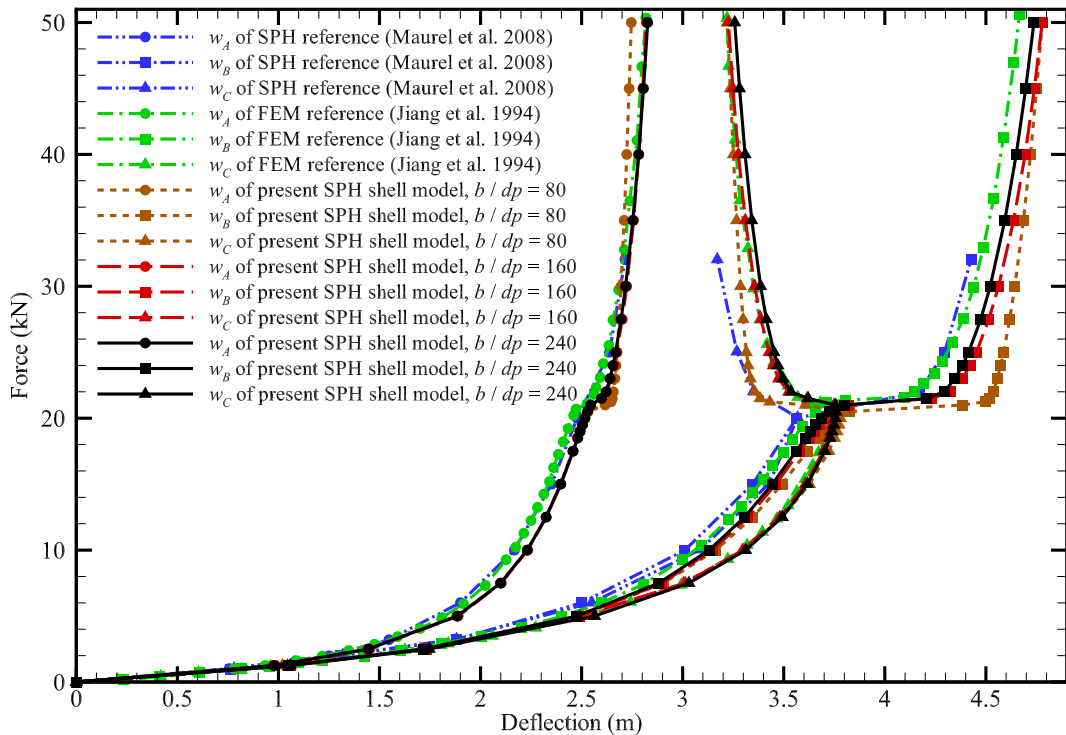


FIGURE 3.7: Pulled-out cylindrical shell: Curves of radical displacements as a function of the point force magnitude and spatial resolution, and their comparison with those of Maurel and Combescure [45] and Jiang et al. [121].

are compared with analytical and numerical solutions from the literature, as well as those obtained using the volume-particle SPH method, to demonstrate the accuracy and stability of the proposed approach. Figure 3.6 illustrates the distribution of von Mises stress at the mid-surface under varying force magnitudes when a cylindrical shell is pulled by a pair of point forces. Figure 3.7 shows the quantitative analysis and convergence study.

3.3.2 Individual contributions of the candidate

This article [80] was published in the international peer-reviewed journal *Journal of Computational Physics*. My contribution to this work was the development of the method and the corresponding computer code for its implementation. I have performed simulations, analyzed the results, and wrote the manuscript for the publication.

Chapter 4

Conclusions and outlooks

4.1 Conclusions

The research presented in this publication-based dissertation addresses several critical challenges in the field of SPH for solid dynamics, with a particular emphasis on mitigating hourglass instabilities in the full-dimensional (volume-particle) SPH method and extending its applicability to thin structures, plates and shells. Throughout the three phases of this work, significant advancements have been made that substantially improve the stability, accuracy, and applicability of SPH methods for a wide range of solid dynamics applications.

To address the artifact of hourglass modes in elastic solid dynamics, we have developed an efficient, robust, and essentially non-hourglass formulation without the need for case-dependent tuning parameters or additional computational effort in the TLSPH method. This formulation effectively suppresses the long-standing issue of hourglass modes and demonstrates robustness in simulations involving large strain dynamics. Additionally, the deformation of complex stent structures has been studied, showcasing the versatility of this formulation and paving the way for practical applications in biomechanics.

While the above non-hourglass formulation is focused on elastic structural responses, we have also developed a unified non-hourglass formulation to address hourglass issues across a wide range of material models. This comprehensive approach closes a critical gap in TLSPH simulations by enhancing the reliability and accuracy of simulations for diverse material models and complex scenarios. Through extensive validation using benchmark cases and a single set of modeling parameters, we have demonstrated the robustness and accuracy of this formulation. Moreover, the successful simulation of the large deformation of Oobleck material highlights the potential of this approach for real-world applications.

For plate and shell structures, the traditional full-dimensional SPH method is computationally inefficient. To address this, we have developed a reduced-dimensional SPH method based on mid-surface reconstruction, using only a single layer of particles for more efficient quasi-static and dynamic analyses of both thin and moderately thick plate and shell structures. By introducing two reduced-dimensional linear-reproducing correction matrices, this method accurately reproduces linear gradients of the position and pseudo-normal. Finite deformations are accounted for by considering all strain components, aided by Gauss-Legendre quadrature along the thickness. To handle large rotations, a weighted non-singularity conversion is introduced between the rotation angles and pseudo-normal. Additionally, a non-isotropic Kelvin-Voigt damping mechanism and a momentum-conserving hourglass control algorithm with a limiter are proposed to enhance numerical stability and suppress hourglass modes. An extensive set of numerical examples has been conducted, demonstrating the accuracy and robustness of the proposed method.

Overall, the advancements made in this dissertation significantly contribute to the field of SPH for solid dynamics. By resolving the long-standing issue of hour-glass instabilities and extending the applicability of SPH to plates and shells, these developments enhance the practicality and effectiveness of SPH as a valuable tool for real-world engineering applications.

4.2 Outlooks

The present work can be further enhanced in several potential directions, related to numerical features and/or physical modeling. Several possibilities for future research include:

- Although the proposed non-hourglass formulation is designed for a wide range of material models, it could be extended to model damage and fracture, where similar volumetric and deviatoric decompositions are often applied [95].
- While the proposed non-hourglass formulation has been developed for TL-SPH, it is expected that a similar idea can be applied to updated Lagrangian SPH solid dynamics, as a future work, for situations where latter is preferred.
- Beyond hourglass modes, another numerical stability issue involves the non-positivity of the deformation gradient determinant under large anisotropic stretch or compression [122]. Addressing this problem offers another promising area for future research.
- The current SPH formulation for general plate and shell structures assumes constant thickness, a straight pseudo-normal, and particles with two rotational degrees of freedom. Future research could explore models that account for variable thickness and particles with additional drilling rotation.
- The proposed thin-structure formulation currently applies only to isotropic and linear elastic material models. Future extensions could include nonlinear elastic, plastic, anisotropic, and fracture material models.
- The formulation is currently limited to simulating a whole piece of thin structure. Another promising direction is to simulate more complex structures, such as I-beams, which are composed of several pieces of thin structures.
- A comprehensive stability analysis, particularly concerning spatial and temporal discretization, is also planned as part of future research efforts.
- The simulation results for the pinched hemispherical shell still exhibit hour-glass modes. Future work will focus on developing a modified or new non-hourglass formulation. One potential approach is to explore methods similar to those used in traditional mesh-based techniques, where concentrated particle stress is redistributed to surrounding particles using a specific distribution function. Additionally, we plan to apply the non-hourglass formulation from our previous work [88, 48] to address hourglass issues by calculating the acceleration induced by shear stress through a Laplacian operator.
- We have observed that the traction-free boundary conditions are not strictly maintained in our current thin-structure formulation, and addressing this issue is another priority for future research.

-
- The present thin-structure formulation, initially developed for plate and shell structures with moderate to high moduli, could be extended to handle soft thin structures, such as membranes.
 - Future work could also involve developing SPH methods for fluid-structure interactions, especially within a unified computational framework for multi-physics modeling, focusing on interactions between fluids and thin structures.

Bibliography

- [1] L. B. Lucy. “A Numerical Approach to the Testing of the Fission Hypothesis”. In: *The astronomical journal* 82 (1977), pp. 1013–1024.
- [2] R. A. Gingold and J. J. Monaghan. “Smoothed particle hydrodynamics: theory and application to non-spherical stars”. In: *Monthly notices of the royal astronomical society* 181.3 (1977), pp. 375–389.
- [3] P. W. Randles and L. D. Libersky. “Smoothed particle hydrodynamics: some recent improvements and applications”. In: *Computer Methods in Applied Mechanics and Engineering* 139.1 (1996), pp. 375–408.
- [4] M. Luo, A. Khayyer, and P. Lin. “Particle methods in ocean and coastal engineering”. In: *Applied Ocean Research* 114 (2021), p. 102734.
- [5] A. Khayyer, H. Gotoh, and Y. Shimizu. “On systematic development of FSI solvers in the context of particle methods”. In: *Journal of Hydrodynamics* (2022), pp. 1–13.
- [6] C. Zhang et al. “Smoothed particle hydrodynamics: Methodology development and recent achievement”. In: *Journal of Hydrodynamics* 34.5 (2022), pp. 767–805.
- [7] F. Xu et al. “On methodology and application of smoothed particle hydrodynamics in fluid, solid and biomechanics”. In: *Acta Mechanica Sinica* 39.2 (2023), p. 722185.
- [8] A. Khayyer et al. “Preface: Latest advances in SPH for fluid mechanics”. In: *European Journal of Mechanics B Fluids* 98 (2023), pp. 208–210.
- [9] J. J. Monaghan. “Smoothed Particle Hydrodynamics”. In: *Reports on Progress in Physics* 68.8 (2005), p. 1703.
- [10] M. B. Liu and G. R. Liu. “Smoothed particle hydrodynamics (SPH): an overview and recent developments”. In: *Archives of Computational Methods in Engineering* 17.1 (2010), pp. 25–76.
- [11] J. J. Monaghan. “Smoothed particle hydrodynamics and its diverse applications”. In: *Annual Review of Fluid Mechanics* 44 (2012), pp. 323–346.
- [12] C. Zhang et al. “SPHinXsys: An open-source multi-physics and multi-resolution library based on smoothed particle hydrodynamics”. In: *Computer Physics Communications* (2021), p. 108066.
- [13] P. N. Sun et al. “An accurate FSI-SPH modeling of challenging fluid-structure interaction problems in two and three dimensions”. In: *Ocean Engineering* 221 (2021), p. 108552.
- [14] H. G. Matthies and J. Steindorf. “Partitioned strong coupling algorithms for fluid–structure interaction”. In: *Computers & structures* 81.8-11 (2003), pp. 805–812.

- [15] H. G. Matthies, R. Niekamp, and J. Steindorf. "Algorithms for strong coupling procedures". In: *Computer Methods in Applied Mechanics and Engineering* 195.17-18 (2006), pp. 2028–2049.
- [16] C. Antoci, M. Gallati, and S. Sibilla. "Numerical simulation of fluid–structure interaction by SPH". In: *Computers & Structures* 85.11 (2007), pp. 879–890.
- [17] L. Han and X. Hu. "SPH modeling of fluid-structure interaction". In: *Journal of Hydrodynamics* 30.1 (2018), pp. 62–69.
- [18] A. Khayyer et al. "An enhanced ISPH–SPH coupled method for simulation of incompressible fluid–elastic structure interactions". In: *Computer Physics Communications* 232 (2018), pp. 139–164.
- [19] M. Liu and Z. Zhang. "Smoothed particle hydrodynamics (SPH) for modeling fluid-structure interactions". In: *Science China Physics, Mechanics & Astronomy* 62.8 (2019), pp. 1–38.
- [20] J. M. Pearl, C. D. Raskin, and J. M. Owen. *SPH formulation and fluid-solid interface model for the fully compressible interaction of dissimilar materials*. Tech. rep. Lawrence Livermore National Lab.(LLNL), Livermore, CA (United States), 2021.
- [21] C. Zhang et al. "An integrative smoothed particle hydrodynamics method for modeling cardiac function". In: *Computer Methods in Applied Mechanics and Engineering* 381 (2021), p. 113847.
- [22] C. Zhang, H. Gao, and X. Hu. "A multi-order smoothed particle hydrodynamics method for cardiac electromechanics with the Purkinje network". In: *Computer Methods in Applied Mechanics and Engineering* 407 (2023), p. 115885.
- [23] C. Bierwisch et al. "Particle-based simulation, dimensional analysis and experimental validation of laser absorption and thermo-viscous flow during sintering of polymers". In: *Procedia Cirp* 94 (2020), pp. 74–79.
- [24] D. Sollich et al. "An improved recoil pressure boundary condition for the simulation of deep penetration laser beam welding using the SPH method". In: *European Journal of Mechanics-B/Fluids* 96 (2022), pp. 26–38.
- [25] G. Ma et al. "A five-phase approach, SPH framework and applications for predictions of seepage-induced internal erosion and failure in unsaturated/saturated porous media". In: *Computer Methods in Applied Mechanics and Engineering* 401 (2022), p. 115614.
- [26] Y. Lian et al. "An effective and stabilised (u- pl) SPH framework for large deformation and failure analysis of saturated porous media". In: *Computer Methods in Applied Mechanics and Engineering* 408 (2023), p. 115967.
- [27] R. Feng et al. "A general smoothed particle hydrodynamics (SPH) formulation for coupled liquid flow and solid deformation in porous media". In: *Computer Methods in Applied Mechanics and Engineering* 419 (2024), p. 116581.
- [28] Q. Yang, V. Jones, and L. McCue. "Free-surface flow interactions with deformable structures using an SPH–FEM model". In: *Ocean Engineering* 55 (2012), pp. 136–147.
- [29] C. Hermange et al. "A 3D SPH–FE coupling for FSI problems and its application to tire hydroplaning simulations on rough ground". In: *Computer Methods in Applied Mechanics and Engineering* 355 (2019), pp. 558–590.

- [30] G. R. Johnson, R. A. Stryk, and S. R. Beissel. "SPH for high velocity impact computations". In: *Computer Methods in Applied Mechanics and Engineering* 139.1-4 (1996), pp. 347–373.
- [31] R. Vignjevic, J. R. Reveles, and J. Campbell. "SPH in a total Lagrangian formalism". In: *CMC-Tech Science Press- 4.3* (2006), p. 181.
- [32] M. B. Liu and G. R. Liu. "Restoring particle consistency in smoothed particle hydrodynamics". In: *Applied numerical mathematics* 56.1 (2006), pp. 19–36.
- [33] J. W. Swegle, D. L. Hicks, and S. W. Attaway. "Smoothed Particle Hydrodynamics stability analysis". In: *Journal of computational physics* 116.1 (1995), pp. 123–134.
- [34] S. J. Lind, B. D. Rogers, and P. K. Stansby. "Review of smoothed particle hydrodynamics: towards converged Lagrangian flow modelling". In: *Proceedings of the Royal Society A* 476.2241 (2020), p. 20190801.
- [35] T. Rabczuk, T. Belytschko, and S. P. Xiao. "Stable particle methods based on Lagrangian kernels". In: *Computer Methods in Applied Mechanics and Engineering* 193.12-14 (2004), pp. 1035–1063.
- [36] J. J. Monaghan. "SPH without a tensile instability". In: *Journal of Computational Physics* 159.2 (2000), pp. 290–311.
- [37] J. P. Gray, J. J. Monaghan, and R. P. Swift. "SPH elastic dynamics". In: *Computer Methods in Applied Mechanics and Engineering* 190.49 (2001), pp. 6641–6662.
- [38] J. M. Owen. "A tensor artificial viscosity for SPH". In: *Journal of Computational Physics* 201.2 (2004), pp. 601–629.
- [39] C. Zhang, X. Hu, and N. A. Adams. "A generalized transport-velocity formulation for smoothed particle hydrodynamics". In: *Journal of Computational Physics* 337 (2017), pp. 216–232.
- [40] Y. Zhu, C. Zhang, and X. Hu. "A consistency-driven particle-advection formulation for weakly-compressible smoothed particle hydrodynamics". In: *Computers & Fluids* 230 (2021), p. 105140.
- [41] T. Belytschko et al. "A unified stability analysis of meshless particle methods". In: *International Journal for Numerical Methods in Engineering* 48.9 (2000), pp. 1359–1400.
- [42] J. Bonet and S. Kulasegaram. "Alternative total Lagrangian formulations for corrected smooth particle hydrodynamics (CSPH) methods in large strain dynamic problems". In: *Revue Européenne des Éléments Finis* 11.7-8 (2002), pp. 893–912.
- [43] T. De Vuyst and R. Vignjevic. "Total Lagrangian SPH modelling of necking and fracture in electromagnetically driven rings". In: *International Journal of Fracture* 180.1 (2013), pp. 53–70.
- [44] K. Ba and A. Gakwaya. "Thermomechanical total Lagrangian SPH formulation for solid mechanics in large deformation problems". In: *Computer Methods in Applied Mechanics and Engineering* 342 (2018), pp. 458–473.
- [45] B. Maurel and A. Combescure. "An SPH shell formulation for plasticity and fracture analysis in explicit dynamics". In: *International Journal for Numerical Methods in Engineering* 76.7 (2008), pp. 949–971.

- [46] J. Lin et al. "Efficient meshless SPH method for the numerical modeling of thick shell structures undergoing large deformations". In: *International Journal of Non-Linear Mechanics* 65 (2014), pp. 1–13.
- [47] Y. Peng, A. Zhang, and F. Ming. "A thick shell model based on reproducing kernel particle method and its application in geometrically nonlinear analysis". In: *Computational Mechanics* 62.3 (2018), pp. 309–321.
- [48] D. Wu et al. "Unified non-hourglass formulation for total Lagrangian SPH solid dynamics." In: *Computational Mechanics* (2024).
- [49] D. P. Flanagan and T. Belytschko. "A uniform strain hexahedron and quadrilateral with orthogonal hourglass control". In: *International Journal for Numerical Methods in Engineering* 17.5 (1981), pp. 679–706.
- [50] O. P. Jacquotte and J. T. Oden. "Analysis of hourglass instabilities and control in underintegrated finite element methods". In: *Computer Methods in Applied Mechanics and Engineering* 44.3 (1984), pp. 339–363.
- [51] C. T. Dyka, P. W. Randles, and R. P. Ingel. "Stress points for tension instability in SPH". In: *International Journal for Numerical Methods in Engineering* 40.13 (1997), pp. 2325–2341.
- [52] R. Vignjevic, J. Campbell, and L. Libersky. "A treatment of zero-energy modes in the smoothed particle hydrodynamics method". In: *Computer Methods in Applied Mechanics and Engineering* 184.1 (2000), pp. 67–85.
- [53] R. Vignjevic and J. Campbell. "Review of development of the smooth particle hydrodynamics (SPH) method". In: *Predictive Modeling of Dynamic Processes*. Springer, 2009, pp. 367–396.
- [54] S. Beissel and T. Belytschko. "Nodal integration of the element-free Galerkin method". In: *Computer Methods in Applied Mechanics and Engineering* 139.1-4 (1996), pp. 49–74.
- [55] Y. Vidal, J. Bonet, and A. Huerta. "Stabilized updated Lagrangian corrected SPH for explicit dynamic problems". In: *International Journal for Numerical Methods in Engineering* 69.13 (2007), pp. 2687–2710.
- [56] J. O'Connor and B. D. Rogers. "A fluid–structure interaction model for free-surface flows and flexible structures using smoothed particle hydrodynamics on a GPU". In: *Journal of Fluids and Structures* 104 (2021), p. 103312.
- [57] P. W. Randles and L. D. Libersky. "Normalized SPH with stress points". In: *International Journal for Numerical Methods in Engineering* 48.10 (2000), pp. 1445–1462.
- [58] M. R. I. Islam and C. Peng. "A stabilized total-Lagrangian SPH method for large deformation and failure in geomaterials". In: *arXiv preprint arXiv:1907.06990* (2019).
- [59] C. H. Lee et al. "A new Jameson–Schmidt–Tukel smooth particle hydrodynamics algorithm for large strain explicit fast dynamics". In: *Computer Methods in Applied Mechanics and Engineering* 311 (2016), pp. 71–111.
- [60] C. Zhang et al. "An artificial damping method for total Lagrangian SPH method with application in biomechanics". In: *Engineering Analysis with Boundary Elements* 143 (2022), pp. 1–13.
- [61] M. Kondo, Y. Suzuki, and S. Koshizuka. "Suppressing local particle oscillations in the Hamiltonian particle method for elasticity". In: *International Journal for Numerical Methods in Engineering* 81.12 (2010), pp. 1514–1528.

- [62] G. C. Ganzenmüller. "An hourglass control algorithm for Lagrangian smooth particle hydrodynamics". In: *Computer Methods in Applied Mechanics and Engineering* 286 (2015), pp. 87–106.
- [63] Y. Shimizu, A. Khayyer, and H. Gotoh. "An implicit SPH-based structure model for accurate Fluid–Structure Interaction simulations with hourglass control scheme". In: *European Journal of Mechanics-B/Fluids* 96 (2022), pp. 122–145.
- [64] T. Belytschko. "Correction of article by DP Flanagan and T. Belytschko". In: *International Journal for Numerical Methods in Engineering* 19.3 (1983), pp. 467–468.
- [65] L. Stainier and J. P. Ponthot. "An improved one-point integration method for large strain elastoplastic analysis". In: *Computer Methods in Applied Mechanics and Engineering* 118.1-2 (1994), pp. 163–177.
- [66] T. Belytschko et al. "Hourglass control in linear and nonlinear problems". In: *Computer Methods in Applied Mechanics and Engineering* 43.3 (1984), pp. 251–276.
- [67] W. Liu, J. S. J. Ong, and R. A. Uras. "Finite element stabilization matrices-a unification approach". In: *Computer Methods in Applied Mechanics and Engineering* 53.1 (1985), pp. 13–46.
- [68] P. R. R. de Campos et al. "A New Updated Reference Lagrangian Smooth Particle Hydrodynamics algorithm for isothermal elasticity and elasto-plasticity". In: *Computer Methods in Applied Mechanics and Engineering* 392 (2022), p. 114680.
- [69] C. H. Lee et al. "An entropy-stable updated reference Lagrangian smoothed particle hydrodynamics algorithm for thermo-elasticity and thermo-viscoplasticity". In: *Computational Particle Mechanics* (2023), pp. 1–39.
- [70] B. C. Cerik et al. "Simulation of ship collision and grounding damage using Hosford-Coulomb fracture model for shell elements". In: *Ocean Engineering* 173 (2019), pp. 415–432.
- [71] Y. Peng et al. "A meshfree framework for the numerical simulation of elasto-plasticity deformation of ship structure". In: *Ocean Engineering* 192 (2019), p. 106507.
- [72] G. Totaro and Z. Gürdal. "Optimal design of composite lattice shell structures for aerospace applications". In: *Aerospace Science and Technology* 13.4-5 (2009), pp. 157–164.
- [73] J. D. Laubrie, J. S. Mousavi, and S. Avril. "A new finite-element shell model for arterial growth and remodeling after stent implantation". In: *International Journal for Numerical Methods in Biomedical Engineering* 36.1 (2020), e3282.
- [74] P. W. Cleary. "Modelling confined multi-material heat and mass flows using SPH". In: *Applied Mathematical Modelling* 22.12 (1998), pp. 981–993.
- [75] A. E. Love. "H.: The Small Free Vibrations and Deformation of a Thin Elastic Shell". In: *Proceedings of the Royal Society of London Series I* 43 (1887), pp. 352–353.
- [76] Y. S. Uflyand. "Wave Propagation by Transverse Vibrations of Beams and Plates". In: *PMM: Journal of Applied Mathematics and Mechanics* 12 (1948), pp. 287–300.
- [77] R. D. Mindlin. "Influence of rotatory inertia and shear on flexural motions of isotropic, elastic plates". In: *Journal of Applied Mechanics* 18 (1951), pp. 31–38.

- [78] I. Elishakoff, F. Hache, and N. Challamel. "Vibrations of asymptotically and variationally based Uflyand–Mindlin plate models". In: *International Journal of Engineering Science* 116 (2017), pp. 58–73.
- [79] I. Elishakoff. *Handbook on Timoshenko-Ehrenfest beam and Uflyand-Mindlin plate theories*. World Scientific, 2020.
- [80] D. Wu, C. Zhang, and X. Hu. "An SPH formulation for general plate and shell structures with finite deformation and large rotation". In: *Journal of Computational Physics* 510 (2024), p. 113113.
- [81] P. Krysl and T. Belytschko. "Analysis of thin shells by the element-free Galerkin method". In: *International Journal of Solids and Structures* 33.20-22 (1996), pp. 3057–3080.
- [82] S. Li, W. Hao, and W. K. Liu. "Numerical simulations of large deformation of thin shell structures using meshfree methods". In: *Computational Mechanics* 25 (2000), pp. 102–116.
- [83] T. Rabczuk, P. M. A. Areias, and T. Belytschko. "A meshfree thin shell method for non-linear dynamic fracture". In: *International Journal for Numerical Methods in Engineering* 72.5 (2007), pp. 524–548.
- [84] D. Li, Z. Lin, and S. Li. "Numerical analysis of Mindlin shell by meshless local Petrov-Galerkin method". In: *Acta Mechanica Solida Sinica* 21.2 (2008), pp. 160–169.
- [85] T. Rabczuk et al. "Immersed particle method for fluid–structure interaction". In: *International Journal for Numerical Methods in Engineering* 81.1 (2010), pp. 48–71.
- [86] B. M. Donning and W. K. Liu. "Meshless methods for shear-deformable beams and plates". In: *Computer Methods in Applied Mechanics and Engineering* 152.1-2 (1998), pp. 47–71.
- [87] J. S. Chen and D. Wang. "A constrained reproducing kernel particle formulation for shear deformable shell in Cartesian coordinates". In: *International Journal for Numerical Methods in Engineering* 68.2 (2006), pp. 151–172.
- [88] D. Wu et al. "An essentially non-hourglass formulation for total Lagrangian smoothed particle hydrodynamics". In: *Computer Methods in Applied Mechanics and Engineering* 407 (2023), p. 115915.
- [89] F. Ming, A. Zhang, and X. Cao. "A robust shell element in meshfree SPH method". In: *Acta Mechanica Sinica* 29.2 (2013), pp. 241–255.
- [90] F. Caleyron et al. "Dynamic simulation of damage-fracture transition in smoothed particles hydrodynamics shells". In: *International Journal for Numerical Methods in Engineering* 90.6 (2012), pp. 707–738.
- [91] F. Ming, A. Zhang, and S. Wang. "Smoothed particle hydrodynamics for the linear and nonlinear analyses of elastoplastic damage and fracture of shell". In: *International Journal of Applied Mechanics* 7.02 (2015), p. 1550032.
- [92] J. Lin et al. "On the implementation of a nonlinear shell-based SPH method for thin multilayered structures". In: *Composite Structures* 108 (2014), pp. 905–914.
- [93] J. Lin et al. "Numerical modeling of the low-velocity impact of composite plates using a shell-based SPH method". In: *Meccanica* 50.10 (2015), pp. 2649–2660.

- [94] Y. Peng, A. Zhang, and F. Ming. "Numerical simulation of structural damage subjected to the near-field underwater explosion based on SPH and RKPM". In: *Ocean Engineering* 222 (2021), p. 108576.
- [95] J. C. Simo and T. J. R. Hughes. *Computational inelasticity*. Vol. 7. Springer Science & Business Media, 2006.
- [96] Y. Yue et al. "Continuum foam: A material point method for shear-dependent flows". In: *ACM Transactions on Graphics (TOG)* 34.5 (2015), pp. 1–20.
- [97] R. Mises. "Mechanik der festen Körper im plastisch-deformablen Zustand". In: *Nachrichten von der Gesellschaft der Wissenschaften zu Göttingen, Mathematisch-Physikalische Klasse* 1913 (1913), pp. 582–592.
- [98] X. Tang et al. "An explicit multi-time stepping algorithm for multi-time scale coupling problems in SPH". In: *arXiv preprint arXiv:2309.04010* (2023).
- [99] G. A. Holzapfel and R. W. Ogden. "Constitutive modelling of passive myocardium: a structurally based framework for material characterization". In: *Philosophical Transactions of the Royal Society A: Mathematical, Physical and Engineering Sciences* 367.1902 (2009), pp. 3445–3475.
- [100] M. P. Nash and A. V. Panfilov. "Electromechanical model of excitable tissue to study reentrant cardiac arrhythmias". In: *Progress in Biophysics and Molecular Biology* 85 (2004), pp. 501–522.
- [101] J. L. Batoz and G. Dhatt. *Modélisation des structures par éléments finis: Solides élastiques*. Presses Université Laval, 1990.
- [102] K. Wisniewski. *Finite rotation shells: Basic equations and finite elements for Reissner kinematics*. CIMNE-Springer, 2010.
- [103] A. Gil, J. Segura, and N. M. Temme. *Numerical methods for special functions*. SIAM, 2007.
- [104] J. N. Reddy. *Theory and analysis of elastic plates and shells*. CRC press, 2006.
- [105] G. R. Liu and M. B. Liu. *Smoothed particle hydrodynamics: a meshfree particle method*. World Scientific, 2003.
- [106] M. B. Liu, G. R. Liu, and K. Y. Lam. "Constructing smoothing functions in smoothed particle hydrodynamics with applications". In: *Journal of Computational and Applied Mathematics* 155.2 (2003), pp. 263–284.
- [107] J. J. Monaghan and J. C. Lattanzio. "A refined particle method for astrophysical problems". In: *Astronomy and astrophysics* 149 (1985), pp. 135–143.
- [108] J. J. Monaghan. "Smoothed particle hydrodynamics". In: *Annual review of astronomy and astrophysics* 30.1 (1992), pp. 543–574.
- [109] H. Wendland. "Piecewise polynomial, positive definite and compactly supported radial functions of minimal degree". In: *Advances in Computational Mathematics* 4.1 (1995), pp. 389–396.
- [110] J. Bonet and T. S. L. Lok. "Variational and momentum preservation aspects of smooth particle hydrodynamic formulations". In: *Computer Methods in Applied Mechanics and Engineering* 180.1-2 (1999), pp. 97–115.
- [111] J. Bonet and S. Kulasegaram. "A simplified approach to enhance the performance of smooth particle hydrodynamics methods". In: *Applied Mathematics and Computation* 126.2-3 (2002), pp. 133–155.

- [112] L. Westhofen, S. Jeske, and J. Bender. "A comparison of linear consistent correction methods for first-order SPH derivatives". In: *Proceedings of the ACM on Computer Graphics and Interactive Techniques* 6.3 (2023), pp. 1–20.
- [113] C. Zhang, M. Rezavand, and X. Hu. "A multi-resolution SPH method for fluid-structure interactions". In: *Journal of Computational Physics* 429 (2021), p. 110028.
- [114] C. Hirsch. *Numerical Calculation of Internal and External Flows*. Vol. 1 and 2. Wiley, 1988.
- [115] J. D. Anderson and J. Wendt. *Computational fluid dynamics*. Vol. 206. Springer, 1995.
- [116] J. J. Monaghan. "Why particle methods work". In: *SIAM Journal on Scientific and Statistical Computing* 3.4 (1982), pp. 422–433.
- [117] C. Zhang, M. Rezavand, and X. Hu. "A multi-resolution SPH method for fluid-structure interactions". In: *Journal of Computational Physics* 429 (2021), p. 110028.
- [118] J. P. Morris, P. J. Fox, and Y. Zhu. "Modeling low Reynolds number incompressible flows using SPH". In: *Journal of Computational Physics* 136.1 (1997), pp. 214–226.
- [119] X. Hu and N. A. Adams. "A multi-phase SPH method for macroscopic and mesoscopic flows". In: *Journal of Computational Physics* 213.2 (2006), pp. 844–861.
- [120] X. Hu and N. A. Adams. "Angular-momentum conservative smoothed particle dynamics for incompressible viscous flows". In: *Physics of Fluids* 18.10 (2006), p. 101702.
- [121] L. Jiang, M. W. Chernuka, and N. G. Pegg. "A co-rotational, updated Lagrangian formulation for geometrically nonlinear finite element analysis of shell structures". In: *Finite Elements in Analysis and design* 18.1-3 (1994), pp. 129–140.
- [122] B. Smith, F. D. Goes, and T. Kim. "Stable neo-hookean flesh simulation". In: *ACM Transactions on Graphics (TOG)* 37.2 (2018), pp. 1–15.

Appendix A

Original journal papers

Here, the peer-reviewed journal publications of the present work are attached.

A.1 Paper I

Dong Wu, Chi Zhang, Xiaojing Tang, Xiangyu Hu

An essentially non-hourglass formulation for total Lagrangian smoothed particle hydrodynamics

In *Computer Methods in Applied Mechanics and Engineering*, Volume 407, 2023, p. 115915,
DOI: <https://doi.org/10.1016/j.cma.2023.115915>.

Copyright © 2023 Elsevier. Reprinted with permission.

Contribution: My contribution to this work was the development of the method and the corresponding computer code for its implementation. I performed simulations and analyzed the results, and wrote the manuscript for the publication.



ELSEVIER



Available online at www.sciencedirect.com

ScienceDirect

Comput. Methods Appl. Mech. Engrg. 407 (2023) 115915

**Computer methods
in applied
mechanics and
engineering**

www.elsevier.com/locate/cma

An essentially non-hourglass formulation for total Lagrangian smoothed particle hydrodynamics

Dong Wu, Chi Zhang, Xiaojing Tang, Xiangyu Hu*

TUM School of Engineering and Design, Technical University of Munich, 85748 Garching, Germany

Received 14 October 2022; received in revised form 18 January 2023; accepted 23 January 2023

Available online xxxx

Abstract

The total Lagrangian smoothed particle hydrodynamics (TL-SPH) for elastic solid dynamics suffers from hourglass modes which can grow and lead to the failure of simulation for problems with large deformation. To address this long-standing issue, we present an essentially non-hourglass formulation based on volumetric-deviatoric stress decomposition. Inspired by the fact that the artifact of nonphysical zigzag particle distribution induced by the hourglass modes is mainly characterized by shear deformation and the standard SPH discretization for the viscous term in the Navier–Stokes (NS) equation, the present formulation computes the action of shear stress directly through the Laplacian of displacement other than from the divergence of shear stress. A comprehensive set of challenging benchmark cases are simulated to demonstrate that, while improving accuracy and computational efficiency, the present formulation is able to essentially suppress the hourglass modes and achieves very good numerical stability with a single general effective parameter. In addition, the deformation of a practically relevant stent structure is simulated to demonstrate the potential of the present method in the field of biomechanics.

© 2023 Published by Elsevier B.V.

Keywords: Hourglass modes; Zero-energy modes; Kirchhoff stress; Smoothed particle hydrodynamics; Total Lagrangian formulation

1. Introduction

Smoothed particle hydrodynamics (SPH), a fully Lagrangian mesh-free method and originally developed for the astrophysical simulation and fluid dynamics [1,2], has attracted more and more interest over the past decades [3–6]. In SPH method, the continuum is represented by particles, where the physical properties of the system, e.g. mass and velocity, are located, and the discretization of the governing equation is achieved through the particle interactions with the help of a Gaussian-like kernel function [7–9]. Since a significant number of common abstractions, which are intrinsically related to numerous physical systems, are realized through particle interactions, SPH method can be used to discretize the multi-physics equations within a unified computational framework [10], so that the algorithms, such as neighboring particle search and time stepping, can be shared, parallel computation can be simplified and efficiency can be greatly improved [11]. More importantly, the unified computational framework permits monolithic and strong coupling, which is seamless, spatio-temporal local and conservative locally and globally [12,13]. The

* Corresponding author.

E-mail addresses: dong.wu@tum.de (D. Wu), c.zhang@tum.de (C. Zhang), xiaojing.tang@tum.de (X. Tang), xiangyu.hu@tum.de (X. Hu).

fluid–structure interaction (FSI) represents a typical multi-physical system in which fluid and solid dynamics are coupled. Unlike the partition-based coupling for the FSI solver, where solid dynamics equations are discretized by the finite element method (FEM) [14,15] and fluid dynamics equations by SPH method, the unified computational framework based on SPH method [16–18] requires that solid dynamics equations, particularly those associated with large elastic strain, are also discretized by SPH method.

Notwithstanding its promising achievement, early attempts indicated that the original SPH method for solid dynamics may be unstable and not accurate due to three deficiencies: linear inconsistency, tensile instability and hourglass modes. The first deficiency is caused by incomplete kernel support at domain boundary or with irregular particle distributions [8]. As the cure for this problem, several algorithms have been proposed in the literature, such as the normalized smoothing approach [19], the kernel gradient correction [3,20] and the finite particle method (FPM) [21]. Tensile instability, which is characterized by nonphysical fractures and void region or particle clustering in solid [22] and fluid simulations [23], respectively, arises due to the zero-order inconsistency of the particle discretization [24]. While this deficiency can be generally alleviated by the artificial stress [25–27] and the generalized transport-velocity formulation [28,29], it can be completely eliminated by the total Lagrangian SPH (TL-SPH) method, in which the kernel function is only evaluated once in the initial undeformed reference configuration [30] unlike the traditional updated Lagrangian SPH (UL-SPH) method, without introducing additional correction term [20,31]. Since its inception, the TL-SPH method has been successfully applied in many simulations of elastic solid dynamics, such as electromagnetically driven rings [32], thermomechanical deformations [33], shell models [34–36], FSI [18,37,38], biomechanics [39], etc.

The artifact of hourglass modes was first observed in FEM simulations, and is characterized by the zigzag mesh and field pattern [40,41]. Similar to FEM, the hourglass modes in SPH are caused by the deformation gradient remaining unchanged when the particles move to the nonphysical zigzag pattern, i.e., the zero-energy modes [42–44]. To address this issue in the UL-SPH method, Beissel and Belytschko [45] introduced a stabilization term to the potential energy function and Vidal et al. [46] an artificial viscosity term by minimizing a local measure of the Laplacian of the deformation field. Both schemes have been successfully applied in some benchmark cases, however, with empirical case-dependent parameters [47]. A more robust approach is to introduce additional integration or stress points between the original particles to present the stress field [44,48]. While this approach removes the hourglass modes effectively, it increases the complexity of algorithm and computational overhead, and suffers from the lack of a rule on determining the location of stress points [49].

In the TL-SPH method, it is found that introducing artificial viscosity similar to that used in computational fluid dynamics (CFD) can effectively decrease hourglass modes for the simulation of dynamical problems [50,51]. Since these artificial viscosity formulations rely on the particle velocity gradient, their validity is questionable when the velocity field becomes flat or less significant. More recently, Kondo et al. [52], Ganzenmüller [53] and Shimizu et al. [54] introduced artificial force or stress methods to correct the inconsistency due to the zigzag pattern between the local displacement field and that linearly predicted from the deformation gradient. While effective and computationally efficient, these schemes may suppress non-linear part of the displacement field with excessive artificial stiffness [55,56] and, again, require the empirical case-dependent tuning parameter to obtain physically meaningful results [47].

In this paper, an essentially non-hourglass formulation without case-dependent tuning parameter is developed for the TL-SPH method to simulate elastic solid dynamics. Inspired by the fact that the zigzag particle distribution is mainly characterized by shear deformation and the standard SPH discretization of Laplacian operator for the viscous force in the Navier–Stokes (NS) equation [7,57,58], we propose a simple and computationally efficient discretization for shear deformation and stress based on volumetric and deviatoric decomposition [59]. The present formulation is implemented in the TL-SPH method with a general effective correction parameter for the error introduced by the kernel summation. A set of benchmark cases are first studied to validate the stability, accuracy and efficiency of the present formulation. Then, a bio-mechanical application, i.e., the deformation of a stent structure, is used to demonstrate its potential in the field of bio-mechanics. The remainder of this paper is organized as follows. Section 2 introduces the governing equations of solid dynamics together with volumetric and deviatoric decomposition. The details of the present formulation are described in Section 3. Numerical examples are provided and discussed in Section 4, and then the concluding remarks are presented in Section 5. For better comparison and future in-depth studies, all the computational codes for this study are released in the SPHinXsys repository [10,60] at <https://www.sphinxsys.org> and <https://github.com/Xiangyu-Hu/SPHinXsys>.

2. Kinematics and governing equations

Considering continuum mechanics in the total Lagrangian framework, the kinematics and dynamic equations are expressed in terms of the initial, undeformed reference configuration $\Omega^0 \subset \mathbb{R}^d$ with d denoting the dimension. A deformation map φ between the initial configuration Ω^0 and current deformed configuration $\Omega = \varphi(\Omega^0)$ describes the body deformation at time t as

$$\mathbf{r} = \varphi(\mathbf{r}^0, t), \tag{1}$$

where \mathbf{r}^0 and \mathbf{r} are the initial and current positions of a material point, respectively. Subsequently, the deformation gradient tensor \mathbb{F} is given by

$$\mathbb{F} = \nabla^0 \mathbf{r} = \nabla^0 \mathbf{u} + \mathbb{I}, \tag{2}$$

where $\mathbf{u} = \mathbf{r} - \mathbf{r}^0$ is the displacement, $\nabla^0 \equiv \frac{\partial}{\partial \mathbf{r}^0}$ the gradient operator with respect to the initial configuration Ω^0 and \mathbb{I} the identity matrix.

The conservation equations for mass and momentum in the total Lagrangian formulation can be expressed as

$$\begin{cases} \rho = J^{-1} \rho^0 \\ \rho^0 \ddot{\mathbf{u}} = \nabla^0 \cdot \mathbb{P}^T, \end{cases} \tag{3}$$

where ρ^0 and ρ are the initial and current densities, respectively, $J = \det(\mathbb{F})$, $\ddot{\mathbf{u}}$ the acceleration, \mathbb{P} the first Piola–Kirchhoff stress tensor, and T the matrix transposition operator. While \mathbb{P} can be obtained directly by

$$\mathbb{P} = \mathbb{F}\mathbb{S}, \tag{4}$$

where \mathbb{S} is the second Piola–Kirchhoff stress tensor, \mathbb{P} is obtained by the alternative Kirchhoff-stress approach in this work as

$$\mathbb{P} = \tau \mathbb{F}^{-T}. \tag{5}$$

Here, the Kirchhoff stress τ is decomposed into volumetric and deviatoric components, and can be derived from the following strain energy function [59]

$$\mathfrak{W}_e = \mathfrak{W}_v(J) + \mathfrak{W}_s(\bar{\mathbf{b}}). \tag{6}$$

Here, the volume-preserving left Cauchy–Green deformation gradient tensor $\bar{\mathbf{b}} = J^{-\frac{2}{d}} \mathbf{b} = |\mathbf{b}|^{-\frac{1}{d}} \mathbf{b}$ with $\mathbf{b} = \mathbb{F}\mathbb{F}^T$. For neo-Hookean materials, the volume-dependent strain energy $\mathfrak{W}_v(J)$ weighted by the bulk modulus K can be expressed as

$$\mathfrak{W}_v(J) = \frac{1}{2} K \left[\frac{1}{2} (J^2 - 1) - \ln J \right], \tag{7}$$

whereas the shear-dependent strain energy $\mathfrak{W}_s(\bar{\mathbf{b}})$ weighted by the shear modulus G [61] is given by

$$\mathfrak{W}_s(\bar{\mathbf{b}}) = \frac{1}{2} G (\text{tr}(\bar{\mathbf{b}}) - d). \tag{8}$$

Then, the Kirchhoff stress tensor τ can be derived as

$$\tau = \frac{\partial \mathfrak{W}_e}{\partial \mathbb{F}} \mathbb{F}^T = \frac{K}{2} (J^2 - 1) \mathbb{I} + G \text{dev}(\bar{\mathbf{b}}), \tag{9}$$

where

$$\text{dev}(\bar{\mathbf{b}}) = \bar{\mathbf{b}} - \frac{1}{d} \text{tr}(\bar{\mathbf{b}}) \mathbb{I} = J^{-\frac{2}{d}} \left[\mathbf{b} - \frac{1}{d} \text{tr}(\mathbf{b}) \mathbb{I} \right]. \tag{10}$$

The deviatoric operator $\text{dev}(\bar{\mathbf{b}})$ returns the trace-free part of $\bar{\mathbf{b}}$, i.e., $\text{tr}(\text{dev}(\bar{\mathbf{b}}))$ is equal to zero. Note that while the volumetric component of the constitutive Eq. (9) can be modified depending on the material property and all counterparts are appropriate for this study, only the Eq. (9) is utilized in this study.

3. Methodology

3.1. Fundamentals of SPH method

In SPH method, the continuum media is discretized by a finite number of Lagrangian particles whose interactions are realized by a compact-support kernel function, usually a Gaussian-like function, to approximate the spatial differential operators. Each particle i , located at the position vector \mathbf{r}_i and moving with the material velocity $\dot{\mathbf{u}}_i$, carries particle-average field variables, such as mass m_i , density ρ_i , volume V_i , etc. Then, the discretization for a variable field $f(\mathbf{r})$ can be written as

$$f_i = \int f(\mathbf{r})W(\mathbf{r}_i - \mathbf{r}, h)d\mathbf{r}, \quad (11)$$

where the kernel function $W(\mathbf{r}_i - \mathbf{r}, h)$ is radially symmetric with respect to \mathbf{r}_i and h the smoothing length. By introducing particle summation, this variable field can be approximated by

$$f_i \approx \sum_j V_j W(\mathbf{r}_i - \mathbf{r}_j, h)f_j = \sum_j \frac{m_j}{\rho_j} W(\mathbf{r}_i - \mathbf{r}_j, h)f_j, \quad (12)$$

where the summation is conducted over all the neighboring particles j in the support domain of the particle i .

Following Ref. [7], the original SPH approximation of the spatial derivative operator of the variable field $f(\mathbf{r})$ at particle i can be obtained by

$$\begin{aligned} \nabla f_i &= \int_{\Omega} \nabla f(\mathbf{r})W(\mathbf{r}_i - \mathbf{r}, h)dV \\ &= - \int_{\Omega} f(\mathbf{r})\nabla W(\mathbf{r}_i - \mathbf{r}, h)dV \approx - \sum_j V_j \nabla_i W_{ij} f_j, \end{aligned} \quad (13)$$

where $\nabla_i W_{ij} = \frac{\partial W(r_{ij}, h)}{\partial r_{ij}} \mathbf{e}_{ij}$ is the derivative of the kernel function with r_{ij} denoting the particle distance and \mathbf{e}_{ij} the unit vector pointing from particle j to particle i . Following Ref. [6], we can modify Eq. (13) into a strong form as

$$\nabla f_i = \nabla f_i - f_i \nabla 1 \approx - \sum_j V_j \nabla_i W_{ij} f_{ij}, \quad (14)$$

where $f_{ij} = f_i - f_j$ is the interparticle difference value. This strong-form approximation of the spatial derivative is useful for computing the local structure of a field. And Eq. (13) can also be rewritten into a weak form as

$$\nabla f_i = f_i \nabla 1 + \nabla f_i \approx 2 \sum_j V_j \nabla W_{ij} \tilde{f}_{ij}, \quad (15)$$

where $\tilde{f}_{ij} = (f_i + f_j)/2$ denotes the interparticle average value. This weak-form approximation of the derivative is applied to determine the surface integration with respect to a variable for solving the conservation law. Due to the anti-symmetric property of the derivative of the kernel function, i.e., $\nabla_i W_{ij} = -\nabla_j W_{ji}$, the momentum conservation of the particle system is achieved with Eq. (15).

3.2. Total Lagrangian SPH

With Eq. (15) in hand, the momentum conservation Eq. (3) is discretized in the TL-SPH formulation as

$$\rho_i^0 \dot{\mathbf{u}}_i = \sum_j \left(\mathbb{P}_i \mathbb{B}_i^{0T} + \mathbb{P}_j \mathbb{B}_j^{0T} \right) \cdot \nabla_i^0 W_{ij} V_j^0, \quad (16)$$

where $\nabla_i^0 W_{ij} = \frac{\partial W(\mathbf{r}_{ij}^0, h)}{\partial \mathbf{r}_{ij}^0} \mathbf{e}_{ij}^0$ denotes the gradient of the kernel function evaluated at the initial reference configuration. Here, we introduce the superscript $(\bullet)^0$ to represent the variable defined at the initial reference configuration. The correction matrix \mathbb{B}^0 is adopted to fulfill first-order completeness as [3,44,62]

$$\mathbb{B}_i^0 = \left(\sum_j V_j^0 (\mathbf{r}_j^0 - \mathbf{r}_i^0) \otimes \nabla_i^0 W_{ij} \right)^{-1}. \quad (17)$$

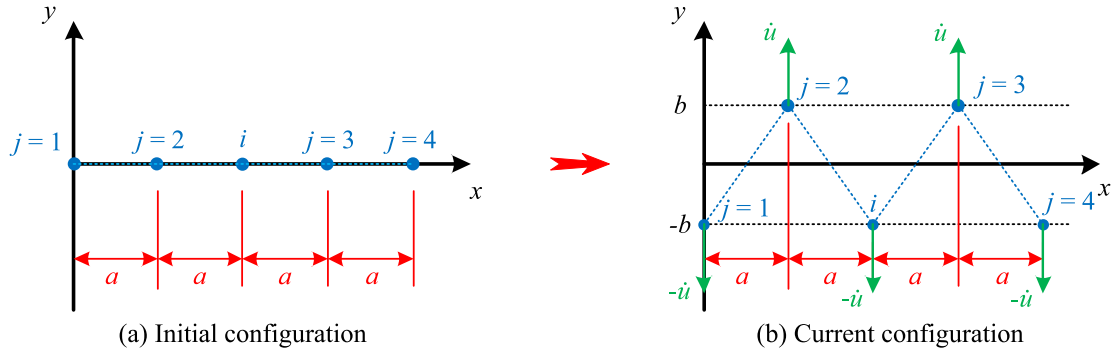


Fig. 1. Schematic of zero-energy modes by considering the simple case where a single row of particles is uniformly distributed along the x -axis in the initial configuration. Note that, when applying Eq. (18), the deformation gradient tensor remains unchanged under the action of shearing.

Note that the correction matrix in the TL-SPH formulation is symmetric and computed only once. The deformation tensor \mathbb{F} is updated by its change rate approximated by using Eq. (14) as

$$\frac{d\mathbb{F}_i}{dt} = \dot{\mathbb{F}}_i = \sum_j V_j^0 (\dot{\mathbf{u}}_j - \dot{\mathbf{u}}_i) \otimes \nabla_i^0 W_{ij} \mathbb{B}_i^0, \tag{18}$$

Following Ref. [51], an artificial damping stress τ_d based on the Kelvin–Voigt type damper is introduced when calculating Kirchhoff stress τ as

$$\tau_d = \frac{\gamma}{2} \cdot \frac{d\mathbb{b}}{dt}, \tag{19}$$

where the artificial viscosity factor $\gamma = \rho ch/2$ with $c = \sqrt{K/\rho}$ and the change rate of the left Cauchy–Green deformation gradient tensor

$$\frac{d\mathbb{b}}{dt} = \left[\frac{d\mathbb{F}}{dt} \cdot \mathbb{F}^T + \mathbb{F} \cdot \left(\frac{d\mathbb{F}}{dt} \right)^T \right]. \tag{20}$$

3.3. Essentially non-hourglass formulation

Although the aforementioned TL-SPH formulation guarantees the first-order consistency and avoids the tensile instability, the deficiency of hourglass modes still persists often when there is large strain or deformation [30]. More specifically, the gradient operator in Eq. (18) averages the relative velocities respected to all neighboring particles, leading to a smeared-out mean field at the particle center. This mean approximation may result in an underestimated deformation gradient and subsequently a wrong stress field when there is a zigzag particle distribution, as shown in Fig. 1, which actually indicates very large local, especially shear, deformations.

Based on the observation that the zigzag particle distribution exhibits large shear deformation, one may consider a more robust formulation in which such shear deformation can be captured directly without using Eq. (18). On the other hand, one may notice that, in a standard SPH formulation of the viscous force [7,57,58] in weakly compressible NS equation, the Laplacian operator is directly discretized with the velocity field rather than first computing the shear rate and stress tensors, and from them computing shear force by applying divergence operation [63]. Baring these in mind, one may try to find an essentially non-hourglass formulation in which the shear force is obtained by the discretization of the Laplacian operator on the displacement (analog to velocity in NS equation) field to capture the shear deformation directly, other than from the deformation gradient and first Piola–Kirchhoff stress tensor. Actually, it is shown later that such discretization can be achieved with the help of Kirchhoff stress decomposition.

We first rewrite the Kirchhoff stress by combining the Eqs. (9), (10) and (19) as

$$\tau = \frac{K}{2} (J^2 - 1) \mathbb{I} - \frac{1}{d} J^{-\frac{2}{d}} G \text{tr}(\mathbb{b}) \mathbb{I} + J^{-\frac{2}{d}} G \mathbb{b} + \tau_d, \tag{21}$$

where the first term of the right-hand side is the Kirchhoff volumetric stress term, the second and third terms together give the Kirchhoff deviatoric stress and the fourth is the numerical damping term. Since the second term

is the component of the elements on the primary diagonal of the Kirchhoff stress tensor, the separated third term, denoted as τ_s , actually contains all the shear stress components. For the shear part of the first Piola–Kirchhoff stress $\mathbb{P}_s = \tau_s \mathbb{F}^{-T} = J^{-\frac{2}{d}} G \mathbb{b} \mathbb{F}^{-T} = J^{-\frac{2}{d}} G \mathbb{F}$, the particle acceleration induced by the τ_s , together with Eq. (2) and the weakly-compressible assumption, can be derived as

$$\ddot{\mathbf{u}}_s = \frac{\nabla^0 \cdot \mathbb{P}_s^T}{\rho^0} = \frac{J^{-\frac{2}{d}} G \nabla^0 \cdot \mathbb{F}^T}{\rho^0} = G \frac{J^{-\frac{2}{d}} \nabla^{0^2} \mathbf{r}}{\rho^0}, \quad (22)$$

where the acceleration due to τ_s is calculated directly from the Laplacian operator of the current position vector.

Inspired by the standard SPH discretization of the viscous term in the NS equation [57], and other similar formulations for heat condition [7] and pressure projection [64], we discretize $\ddot{\mathbf{u}}_s$ in the total Lagrangian formulation as

$$\ddot{\mathbf{u}}_{si} = \zeta G \sum_j \left(J_i^{-\frac{2}{d}} + J_j^{-\frac{2}{d}} \right) \frac{\mathbf{r}_{ij}}{r_{ij}^0} \frac{\partial W(r_{ij}^0, h)}{\partial r_{ij}^0} \frac{V_j^0}{\rho_i^0}, \quad (23)$$

where the parameter ζ is slightly different from unit due to the numerical error of kernel summation, and relevant to the smoothing length h and the choice of kernel function [65], and not necessary to be changed in accordance with the specific constitutive relation. As will be shown in the numerical examples, ζ is general effective and therefore remained constant in this work. Furthermore, applying the Laplacian operator to the shear deformation underlies that the shear stress is diffused accordingly, implying no shear stress concentration. Thanks to the anti-symmetric form [7], the present formulation also preserves momentum conservative property.

To demonstrate that the present formulation ensures non-increasing of elastic energy, we can construct a shear strain energy of the system as

$$\mathfrak{W}_s = - \sum_i V_i^0 \sum_j \frac{1}{2} G \frac{\mathbf{r}_{ij} \cdot \mathbf{r}_{ij}}{r_{ij}^0} \frac{\partial W(r_{ij}^0, h)}{\partial r_{ij}^0} V_j^0 \geq 0. \quad (24)$$

Note that the negative sign is due to the non-positive derivative of the kernel function. Applying the differential operator on both sides of Eq. (24), we obtain the variation of the shear strain energy as follow

$$d\mathfrak{W}_s = - \sum_i V_i^0 \sum_j G \frac{\mathbf{r}_{ij} \cdot d\mathbf{r}_{ij}}{r_{ij}^0} \frac{\partial W(r_{ij}^0, h)}{\partial r_{ij}^0} V_j^0. \quad (25)$$

With Eq. (23) in hand, it is straightforward to derive for a particle pair that

$$G \frac{\mathbf{r}_{ij}}{r_{ij}^0} \frac{\partial W(r_{ij}^0, h)}{\partial r_{ij}^0} V_j^0 \cdot d\mathbf{r}_i \geq 0, \quad (26)$$

and

$$G \frac{\mathbf{r}_{ij}}{r_{ij}^0} \frac{\partial W(r_{ij}^0, h)}{\partial r_{ij}^0} V_j^0 \cdot d\mathbf{r}_j \leq 0, \quad (27)$$

where $d\mathbf{r}_i$ and $d\mathbf{r}_j$, respectively, are the position change of particles i and j acted by the inter-particle shear force. Subtracting Eq. (27) from Eq. (26) yields the following inequality

$$G \frac{\mathbf{r}_{ij}}{r_{ij}^0} \frac{\partial W(r_{ij}^0, h)}{\partial r_{ij}^0} V_j^0 \cdot d\mathbf{r}_{ij} \geq 0, \quad (28)$$

implying that $d\mathfrak{W}_s \leq 0$ as given by Eq. (25). This confirms that Eq. (23) decreases the shear strain energy as it should. Note that, since elastic shear force is non-dissipative, the decreased shear strain energy actually is transformed to kinetic energy of the system, other than to thermal energy as the viscous shear force in fluid. See also the discussion in Section 4.2 and Fig. 8.

It is worth noting that Eq. (23) does not guarantee the first order consistency without introducing the kernel gradient correction, particularly for the truncated support domain and irregular particle distribution. Particles with

incomplete support domains are typically surface particles or those located at the constrained boundary. For the former, the truncated support domain provides a implicit way of imposing free stress boundary condition, similar with the free surface particle in the SPH simulation of free-surface flows. For the later, the support domain is typically supplemented by extending several layers of particles, imposing the constrained boundary condition. As for the irregular particle distributions, the introduction of the kernel gradient correction can improve the accuracy. However, this improvement for regular or homogeneous particle distributions is negligible, which is the case for the numerical examples examined in the present study. When the particles are generated, as for all test cases in this work, either from lattice positions or by the body-fitted particle generator [66], regular or homogeneous distributions can be ensured.

Besides the shear stress τ_s , the remaining Kirchhoff stress, denoted as τ_r , is expressed as

$$\tau_r = \frac{K}{2} (J^2 - 1) \mathbb{I} - \frac{\zeta}{d} J^{-\frac{2}{d}} G \text{tr}(\mathbb{b}) \mathbb{I} + \tau_d. \quad (29)$$

Note that the correction factor ζ is also applied in the second term to fulfill the consistency of the Kirchhoff shear stress. With the $\mathbb{P}_r = \tau_r \mathbb{F}^{-T}$ in hand, the acceleration $\ddot{\mathbf{u}}_{ri}$ of particle i , induced by the τ_{ri} , is calculated by using the Eq. (16) while substituting \mathbb{P}_r for \mathbb{P} . Finally, the acceleration of the particle i is given as

$$\ddot{\mathbf{u}}_i = \ddot{\mathbf{u}}_{ri} + \ddot{\mathbf{u}}_{si}. \quad (30)$$

For clarity, the flowcharts for the original and present SPH formulations are given, respectively, in Fig. 2. Note that Eq. (21) is also applied to calculate τ , which is later converted into \mathbb{P} , in the original formulation for direct comparison.

3.4. Time integration scheme

Following Ref. [38], the position-based Verlet scheme is applied for the time integration. First, the deformation gradient tensor, density and particle position are updated to the midpoint as

$$\begin{cases} \mathbb{F}^{n+\frac{1}{2}} = \mathbb{F}^n + \frac{1}{2} \Delta t \dot{\mathbb{F}}^n \\ \rho^{n+\frac{1}{2}} = \rho^0 \frac{1}{J} \\ \mathbf{r}^{n+\frac{1}{2}} = \mathbf{r}^n + \frac{1}{2} \Delta t \dot{\mathbf{u}}^n. \end{cases} \quad (31)$$

After the calculation of the particle acceleration with Eq. (30), the velocity is updated by

$$\dot{\mathbf{u}}^{n+1} = \dot{\mathbf{u}}^n + \Delta t \ddot{\mathbf{u}}. \quad (32)$$

Finally, the change rate of deformation gradient tensor $\dot{\mathbb{F}}^{n+1}$ with Eq. (18) is calculated and the deformation gradient tensor and position of particles are updated to a new time step with

$$\begin{cases} \mathbb{F}^{n+1} = \mathbb{F}^{n+\frac{1}{2}} + \frac{1}{2} \Delta t \dot{\mathbb{F}}^{n+1} \\ \rho^{n+1} = \rho^0 \frac{1}{J} \\ \mathbf{r}^{n+1} = \mathbf{r}^{n+\frac{1}{2}} + \frac{1}{2} \Delta t \dot{\mathbf{u}}^{n+1}. \end{cases} \quad (33)$$

To maintain the numerical stability, the time step Δt is given as

$$\Delta t = \text{CFL} \min \left(\frac{h}{c_v + |\dot{\mathbf{u}}|_{\max}}, \sqrt{\frac{h}{|\ddot{\mathbf{u}}|_{\max}}} \right). \quad (34)$$

Note that the present Courant–Friedrichs–Lewy (CFL) number is set as 0.6.

4. Numerical examples

In this part, a set of benchmark tests where analytical or numerical reference data in literature are available for qualitative and quantitative comparison are studied to demonstrate the accuracy and efficiency of the present essentially non-hourglass formulation (SPH-ENOG). For comparison, the original formulation, SPH, and the artificial stress method in Ref. [53] (denoted as SPH-GM) are considered. Having the validation, the deformation of a complex stent structure is studied to demonstrate the versatility of the presented formulation. The 5th-order

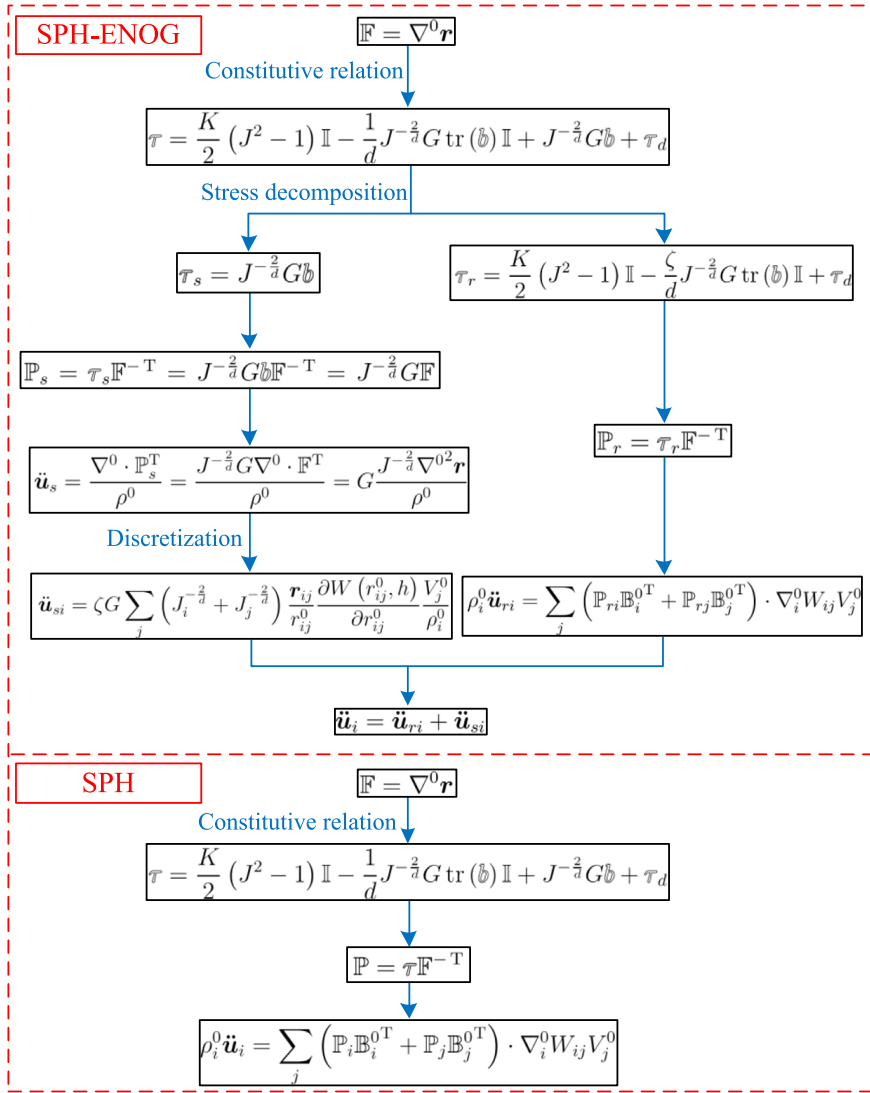


Fig. 2. Flowcharts of the original total Lagrangian SPH (denoted as SPH) in Ref. [17] and present (denoted as SPH-ENOG) formulations.

Wendland kernel [67] with a smoothing length of $h = 1.15 dp$, where dp is the initial particle spacing, and a cut-off radius of $2.3 dp$ is employed. After the kernel function and smoothing length are selected, the parameter ζ is set as 1.07 according to numerical experiments and remains constant throughout this work.

4.1. 2D oscillating plate

In this part, we consider the oscillation of a thin plate with one edge fixed and the others free, which has been theoretically [68] and numerically [26,28] studied in the literature. This plane strain problem can be modeled by a 2D plate strip of length L , perpendicular to the fixed edge, and thickness H . Following the Refs. [26,28], the plate strip is clamped between several layers of constrained SPH particles, as shown in Fig. 3. The initial velocity v_y , perpendicular to the plate strip, is given by

$$v_y(x) = v_f c \frac{f(x)}{f(L)}, \tag{35}$$

where v_f is a constant that varies with different cases, and

$$f(x) = (\sin(kL) + \sinh(kL)) (\cos(kx) - \cosh(kx)) - (\cos(kL) + \cosh(kL)) (\sin(kx) - \sinh(kx)) \tag{36}$$

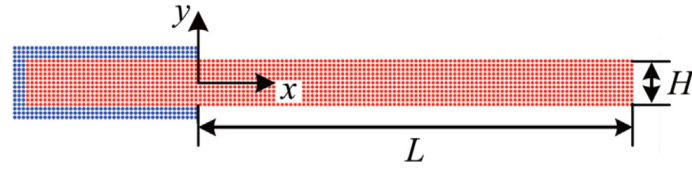


Fig. 3. 2D oscillating plate: Initial configuration.

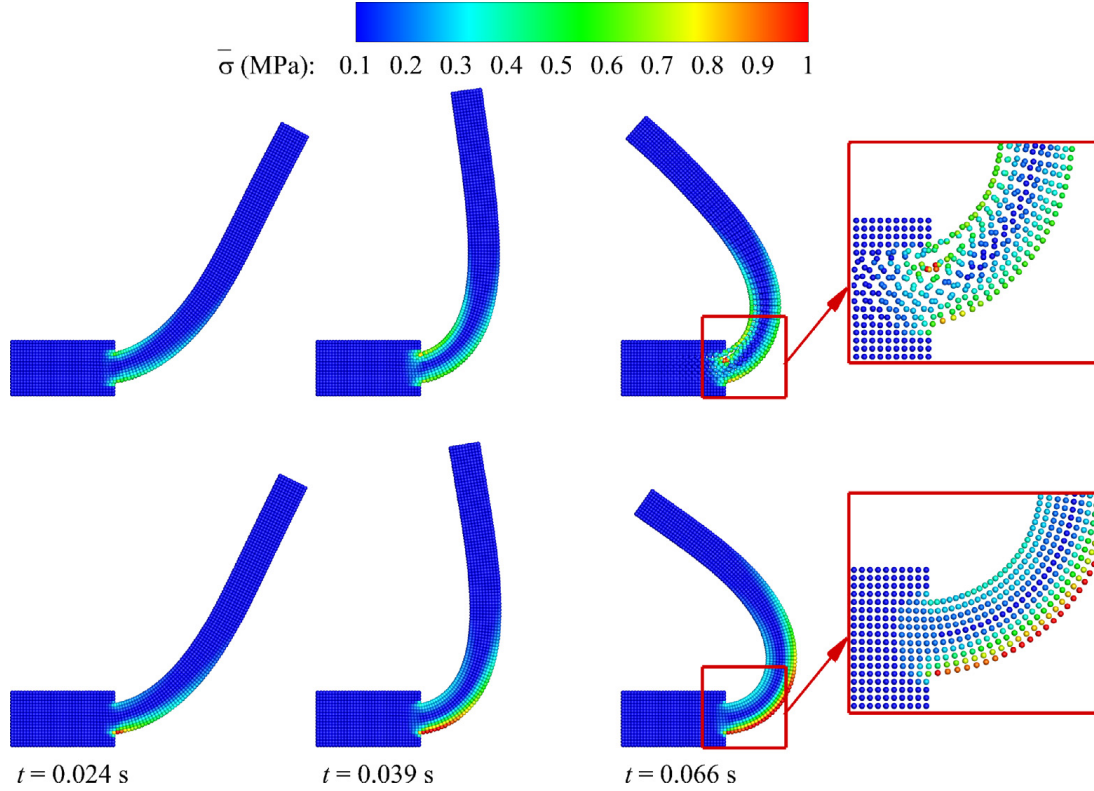


Fig. 4. 2D oscillating plate: Comparison of the deformed configuration colored by von Mises stress $\bar{\sigma}$ at serial time instants obtained by the SPH (top panel) and the SPH-ENOG (bottom panel) with the length $L = 0.2$ m, height $H = 0.02$ m, $v_f = 0.15$, and spatial particle discretization $H/dp = 10$. The material is modeled with density $\rho_0 = 1000.0$ kg/m³, Young’s modulus $E = 2.0$ MPa, and Poisson’s ratio $\nu = 0.3975$. (For interpretation of the references to color in this figure legend, the reader is referred to the web version of this article.)

with k determined by

$$\cos(kL) \cosh(kL) = -1 \tag{37}$$

and $kL = 1.875$. The material properties are set as follows: density $\rho_0 = 1000.0$ kg/m³, Young’s modulus $E = 2.0$ MPa and Poisson’s ratio ν varies for different cases. The frequency ω of the oscillating plate is theoretically given by

$$\omega^2 = \frac{EH^2k^4}{12\rho(1-\nu^2)}. \tag{38}$$

Fig. 4 shows the deformed particle configuration with von Mises stress $\bar{\sigma}$ contour obtained by the SPH and SPH-ENOG for the case of $L = 0.2$ m, $H = 0.02$ m, $v_f = 0.15$, $\nu = 0.3975$ and the initial particle spacing $dp = H/10 = 0.002$ m. It can be noted that, while SPH is able to preserve uniform particle distribution for this problem when the deformation is moderate as in Ref. [17], its results exhibit particle disorder when the deformation is large, as shown in top panel of Fig. 4, especially near the region of maximum displacement and stress. The larger the deformation of the plate strip is, the more pairs of particles stick together, which is consistent with that reported

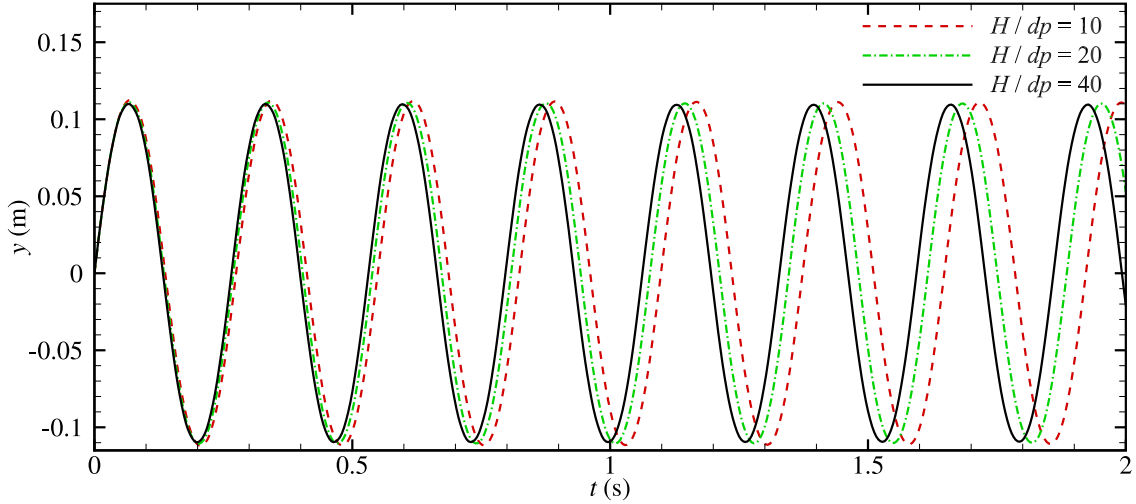


Fig. 5. 2D oscillating plate: Time history of the vertical position y observed at the midpoint of the plate strip end obtained by the SPH-ENOG in the long term with the length $L = 0.2$ m, height $H = 0.02$ m and $v_f = 0.05$. The material is modeled with density $\rho_0 = 1000.0$ kg/m³, Young's modulus $E = 2.0$ MPa and Poisson's ratio $\nu = 0.3975$. Note that dp is the initial particle spacing.

in Ref. [53] for a static problem (see their Fig. 6). On the contrary, the SPH-ENOG, similar to SPH-GM, suppresses such phenomenon and features smooth deformation and stress fields.

A convergence study and the comparisons between numerical and theoretical solutions are performed to demonstrate the accuracy of the present formulation. The convergence study tests three different spatial resolutions: $H/dp = 10$, $H/dp = 20$, and $H/dp = 40$. Fig. 5 shows the time history of vertical position y of the midpoint at the end of the strip with $v_f = 0.05$. It can be observed that the differences between different solutions are decreasing, as the spatial resolution increases, similar with those of Refs. [26,28]. Also, a long-term simulation is conducted herein to demonstrate the numerical stability of the proposed formulation. For quantitative validation, Table 1 reports the oscillation period T obtained by the present SPH-ENOG with the spatial particle resolution $H/dp = 40$ and its comparison with the theoretical solution for a wide range of v_f and ν . The error is about 9.00% for $\nu = 0.22$ and decreases to about 5.00% when the Poisson's ratio is increased to 0.4. As the thickness is assumed to be very small in the analytical theory, Table 2 shows the comparison when the length L remains the same and thickness H is half of its previous value. A significantly better agreement is obtained with the maximum error decreasing to 2.29% with $\nu = 0.4$. It should be noted that when $v_f = 0.15$ and $\nu = 0.4$, the deformation is too large and the plate is in contact with the constrained base, so the period of the plate is not informative.

4.2. 3D oscillating plate

In this section, we further consider the oscillation of a 3D thin plate with a simple support boundary condition for all lateral edges. Following Refs. [69–71], a square plate with length and width $L = W = 0.4$ m and height $H = 0.01$ m, as shown in Fig. 6(a), is considered. The simple support boundary condition is imposed on the center line of lateral faces, viz., the corresponding particles are fixed in z direction. The initial vertical velocity v_z is given by

$$v_z(x, y) = \sin \frac{m\pi x}{L} \sin \frac{n\pi y}{W}, \quad (39)$$

where m and n are integers controlling the x - and y -directional vibration modes, respectively. The material properties are set as follows: density $\rho_0 = 1000.0$ kg/m³, Young's modulus $E = 100.0$ MPa and Poisson's ratio $\nu = 0.3$. The theoretical vibration period of the plate is given by

$$T = \frac{2}{\pi} \left[\left(\frac{m}{L} \right)^2 + \left(\frac{n}{W} \right)^2 \right]^{-1} \sqrt{\frac{\rho_0 H}{D}}, \quad (40)$$

Table 1

2D oscillating plate: Quantitative validation of the oscillation period for $L = 0.2$ m and $H = 0.02$ m with various v_f and ν .

v_f	ν	$T_{\text{SPH-ENOG}}$	$T_{\text{Theoretical}}$	Error
0.01	0.22	0.29439	0.27009	9.00%
0.05	0.22	0.29428	0.27009	8.96%
0.1	0.22	0.29373	0.27009	8.75%
0.15	0.22	0.29374	0.27009	8.76%
0.01	0.30	0.28197	0.26412	6.76%
0.05	0.30	0.28166	0.26412	6.64%
0.1	0.30	0.28096	0.26412	6.38%
0.15	0.30	0.28126	0.26412	6.50%
0.01	0.40	0.26534	0.25376	4.56%
0.05	0.40	0.26473	0.25376	4.32%
0.1	0.40	0.26382	0.25376	3.96%
0.15	0.40	0.26656	0.25376	5.04%

Table 2

2D oscillating plate: Quantitative validation of the oscillation period for $L = 0.2$ m and $H = 0.01$ m with various v_f and ν .

v_f	ν	$T_{\text{SPH-ENOG}}$	$T_{\text{Theoretical}}$	Error
0.01	0.22	0.57670	0.54018	6.76%
0.05	0.22	0.57205	0.54018	5.90%
0.1	0.22	0.56458	0.54018	4.52%
0.15	0.22	0.56677	0.54018	4.92%
0.01	0.30	0.55414	0.52824	4.90%
0.05	0.30	0.54638	0.52824	3.43%
0.1	0.30	0.53971	0.52824	2.17%
0.15	0.30	0.54027	0.52824	2.28%
0.01	0.40	0.51914	0.50752	2.29%
0.05	0.40	0.51074	0.50752	0.63%
0.1	0.40	0.50808	0.50752	0.11%
0.15	0.40	–	–	–

where

$$D = \frac{EH^3}{12(1-\nu^2)} \quad (41)$$

denotes the flexural rigidity.

Fig. 6(b–d) shows the deformed particle configuration with von Mises stress contour obtained by the SPH-ENOG for the vibration modes of $(m, n) = (1, 1), (2, 1)$ and $(2, 2)$ with the spatial resolution $H/dp = 9$. With the same setup, Fig. 7 shows the deformed particle configuration colored by pressure for the vibration modes of $(m, n) = (1, 1)$ and $(2, 2)$. For all cases, the SPH-ENOG captures smooth deformation and stress fields, indicating its numerical stability and robustness. Fig. 8 shows kinetic, elastic strain and total energy for the vibration modes of $(m, n) = (1, 1)$ and $(2, 2)$, and the former is compared with that of the theoretical solution. It can be noted that the SPH-ENOG provides a well estimation of kinetic energy profile for the vibration mode of $(m, n) = (1, 1)$ in the long term, and exhibits only a 3.4% reduction in oscillation amplitude after 7 periods for the case of $(m, n) = (2, 2)$. Due to the smeared-out and underestimated deformation gradient field which is prone for hourglass modes in the original formulation, it is not out of expectation that the amplitude of the present elastic strain energy evaluated from the deformation gradient is apparently smaller than that of kinetic energy for both vibration modes. In Fig. 8(b), we also show the kinetic energy obtained by SPH. Compared with SPH, SPH-ENOG shows improved accuracy in predicting vibration period and does not introduce extra numerical dissipation, indicating that the numerical dissipation is primarily due to the utilized numerical damping term, i.e., Eq. (19). Given that the plate in the theoretical solution is assumed to be thin enough to ignore the shear deformation [69], the numerical periods are

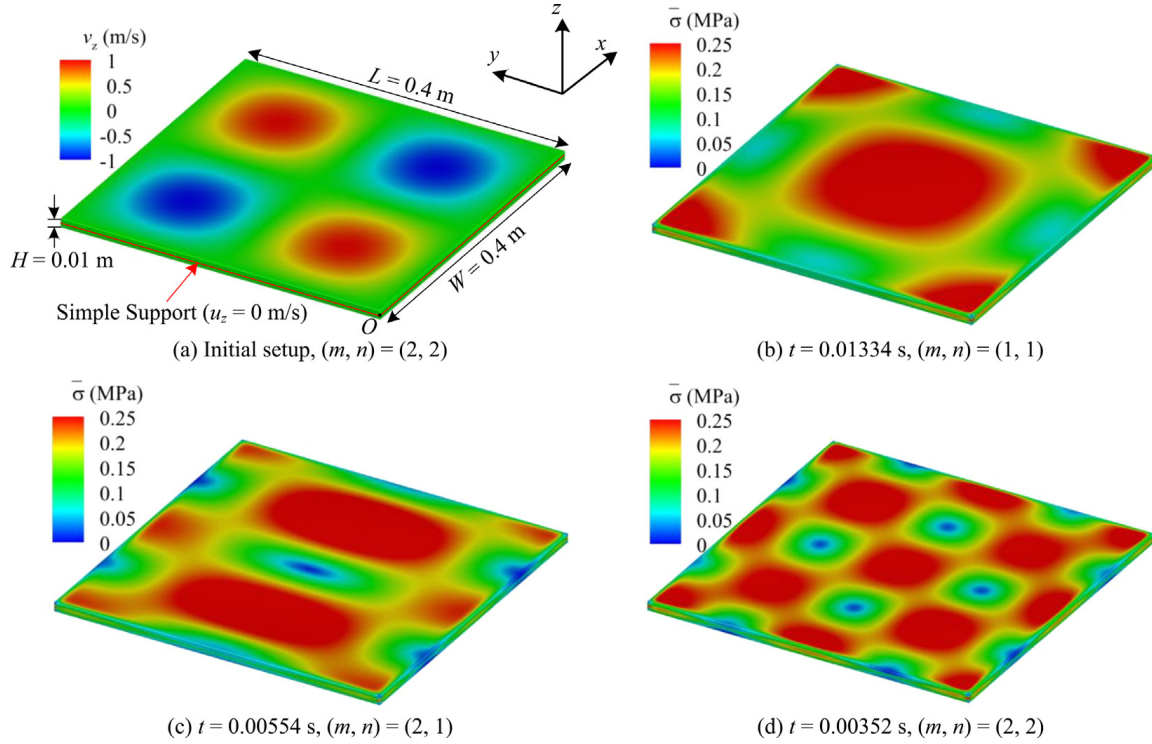


Fig. 6. 3D oscillating plate: (a) Schematic of initial setup for the case of $(m, n) = (2, 2)$, (b–d) deformed configuration colored by von Mises stress $\bar{\sigma}$ for the vibration modes of $(m, n) = (1, 1)$, $(2, 1)$ and $(2, 2)$ at the quarter-period time point obtained by the SPH-ENOG with the length and width $L = W = 0.4$ m, height $H = 0.01$ m, and spatial particle discretization $H/dp = 9$. The material is modeled with density $\rho_0 = 1000.0$ kg/m³, Young’s modulus $E = 100.0$ MPa and Poisson’s ratio $\nu = 0.3$. (For interpretation of the references to color in this figure legend, the reader is referred to the web version of this article.)

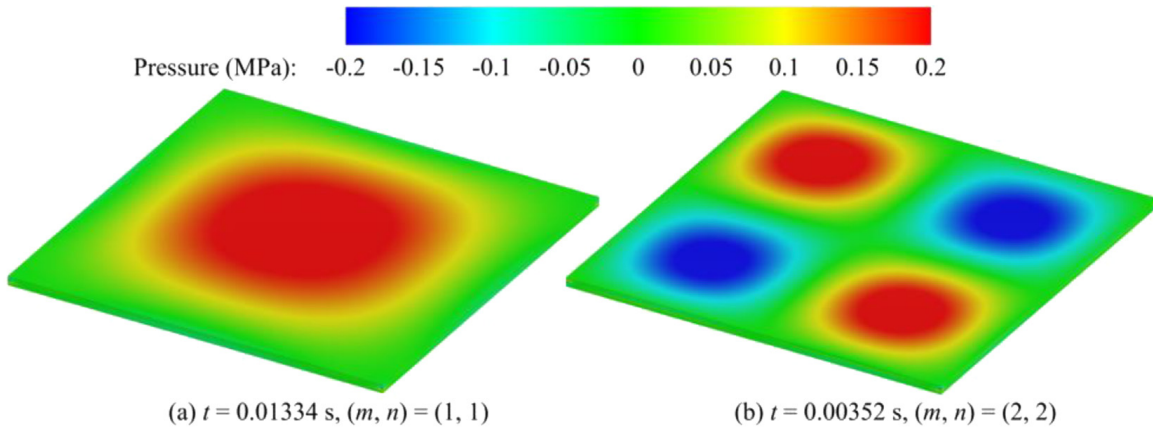


Fig. 7. 3D oscillating plate: Deformed configuration colored by pressure for the vibration modes of $(m, n) = (1, 1)$ and $(2, 2)$ at the quarter-period time point obtained by the SPH-ENOG with the length and width $L = W = 0.4$ m, height $H = 0.01$ m, and spatial particle discretization $H/dp = 9$. The material is modeled with density $\rho_0 = 1000.0$ kg/m³, Young’s modulus $E = 100.0$ MPa and Poisson’s ratio $\nu = 0.3$. (For interpretation of the references to color in this figure legend, the reader is referred to the web version of this article.)

estimated with acceptable phase error in comparison to the theoretical solutions, as is the case in Ref. [70] (see their Fig. 3(b)) and the numerical results of the 2D oscillating plate.

Furthermore, a convergence study and a quantitative validation are performed to demonstrate the accuracy of the present formulation. The convergence study tests three different spatial resolutions, i.e., $H/dp = 3$, $H/dp = 5$, and $H/dp = 9$, for the vibration modes of $(m, n) = (1, 1)$, $(2, 1)$ and $(2, 2)$. Table 3 shows the periods of the oscillations converge rapidly with increasing resolution and are in good agreements with the theoretical ones. The

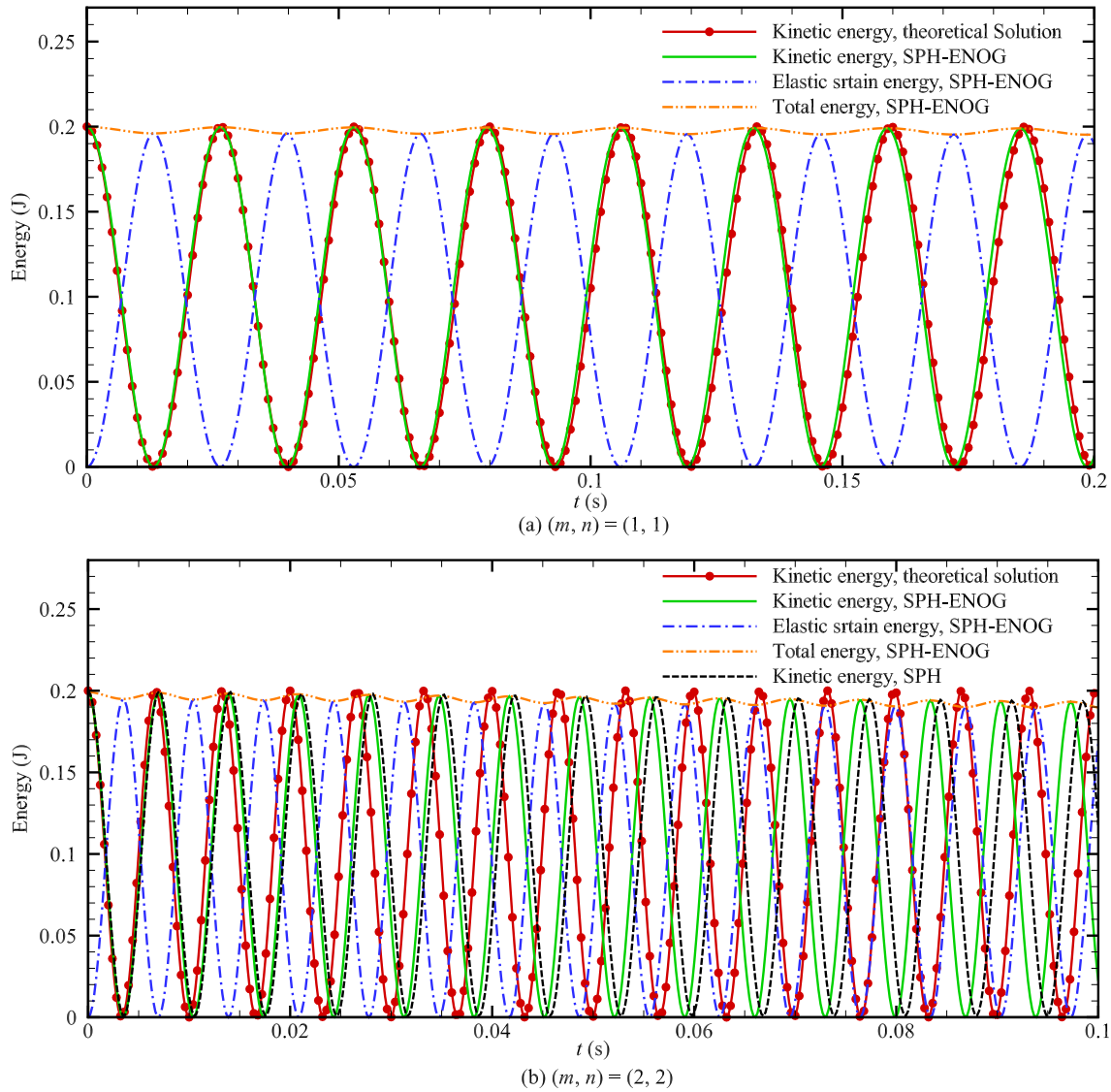


Fig. 8. 3D oscillating plate: Time history of the kinetic, elastic strain and total energy for the vibration mode of $(m, n) = (1, 1)$ and $(2, 2)$ obtained by the SPH-ENOG in the long term with the length and width $L = W = 0.4$ m, height $H = 0.01$ m, spatial particle discretization $H/dp = 9$, and the kinetic energy is compared with that of the theoretical solution for both modes and SPH for the mode of $(m, n) = (2, 2)$. The material is modeled with density $\rho_0 = 1000.0$ kg/m³, Young’s modulus $E = 100.0$ MPa and Poisson’s ratio $\nu = 0.3$.

Table 3

3D Oscillating plate: Quantitative validation of the oscillation period for vibration modes of $(m, n) = (1, 1)$, $(2, 1)$ and $(2, 2)$ with three different spatial resolutions.

SPH-ENOG	$H/dp = 3$	$H/dp = 5$	$H/dp = 9$	Theoretical
$(m, n) = (1, 1)$	0.0541881	0.0532965	0.0528678	0.0532208
$(m, n) = (2, 1)$	0.0226420	0.0223003	0.0221520	0.0212883
$(m, n) = (2, 2)$	0.0142465	0.0140275	0.0138464	0.0133052

total CPU wall-clock times required by the SPH and SPH-ENOG with the spatial resolution of $H/dp = 9$ and physical time of 1 s are approximately 8.73 h and 8.57 h, respectively. The computations in present study are all performed on an Intel Core i7-9700F 3.0 GHz 8-core desktop computer. In comparison to the Hamiltonian MPS (moving particle semi-implicit) method in Ref. [70], SPH-ENOG achieves the comparable accuracy in terms of the estimated period, but with much less CPU wall-clock time, which suggests higher computational efficiency of the present SPH method.

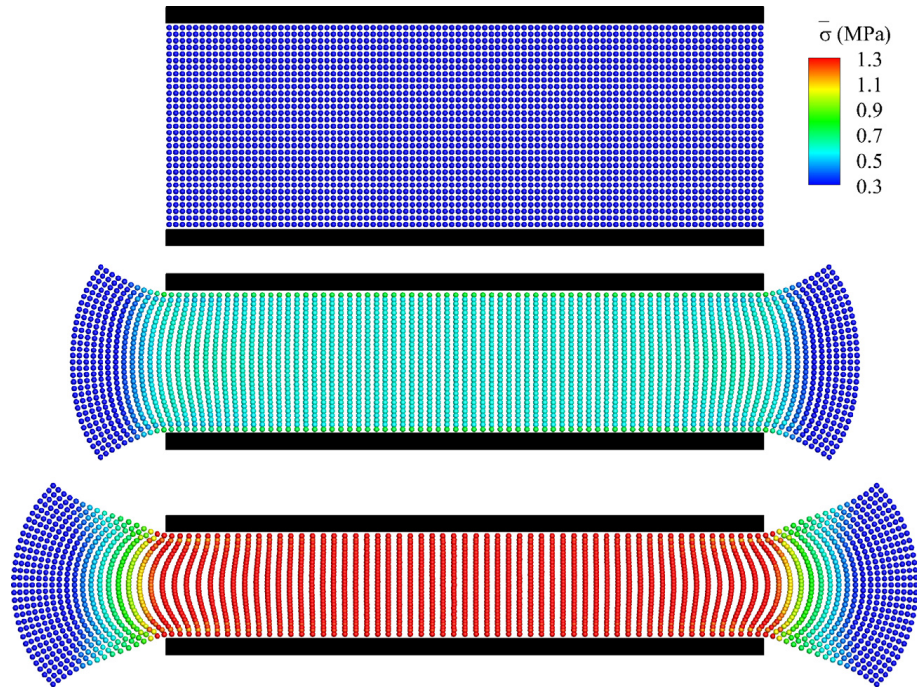


Fig. 9. Punching strip: Vertical compression states of 0%, 25%, and 50% with rubber particles colored by von Mises stress $\bar{\sigma}$. The rubber strip is modeled with the length $L = 9$ mm, height $H = 3$ mm and spatial particle discretization $H/dp = 30$, and its material is set as density $\rho_0 = 1100$ kg/m³, Young's modulus $E = 1.0$ GPa and Poisson's ratio $\nu = 0.45$. (For interpretation of the references to color in this figure legend, the reader is referred to the web version of this article.)

4.3. Punching strip

In this section, we consider the example of punched rubber where a rubber strip is compressed by punch tools. This example is a classic challenging test [53] not only for meshless methods [72] but also for FEM [73] due to the large deformation. The rubber strip is defined by a rectangular block of length $L = 9$ mm and height $H = 3$ mm, and its material is modeled with density $\rho_0 = 1100$ kg/m³, Young's modulus $E = 1.0$ GPa and Poisson's ratio $\nu = 0.45$. The punch tools are modeled as rigid rectangular blocks with the dimension 9 mm \times 0.3 mm, discretized by the same particle spacing with the strip, and initialized with a punch velocity of 2 mm/s until the vertical compression ratio of 50% is reached. A splitting random-choice dynamic relaxation method [74] is applied to obtain the quasi-steady solution.

Fig. 9 shows the initial and deformed configuration colored by von Mises stress $\bar{\sigma}$ obtained by the present SPH-ENOG with the spatial particle discretization $H/dp = 30$. As the punch tools compress, the rubber strip experiences imposed deformation and the material expands outward towards the open sides. The very smooth particle distribution and stress fields are observed even near the sharp corners of the punch tools where the largest deformation exists, demonstrating the effectiveness and robustness of the proposed formulation. The present deformed configuration is of the volume preservation, in contrast to the outcome of SPH-GM stated in Ref. [53] (see their Fig. 7), which is reflected in the high Poisson's ratios $\nu \in [0.45, 0.5)$ [75]. Fig. 10 shows the convergence study with particle refinement. It can be observed that both the deformation pattern and von Mises stress $\bar{\sigma}$ exhibit good convergence properties.

4.4. Pulling test

In this section, the 2D pulling rubber strip [53,72] and 3D pulling rubber cylinder [76] are considered to investigate the robustness and versatility of the proposed formulation. Following Ref. [53,72], the 2D rubber strip is of a square with the side length $L = 2$ mm, and its rubber material properties are the same as the previous punching strip test. The tensile deformation is initialized by imposing the velocity of $v = (0, \pm 0.1$ mm/s) to

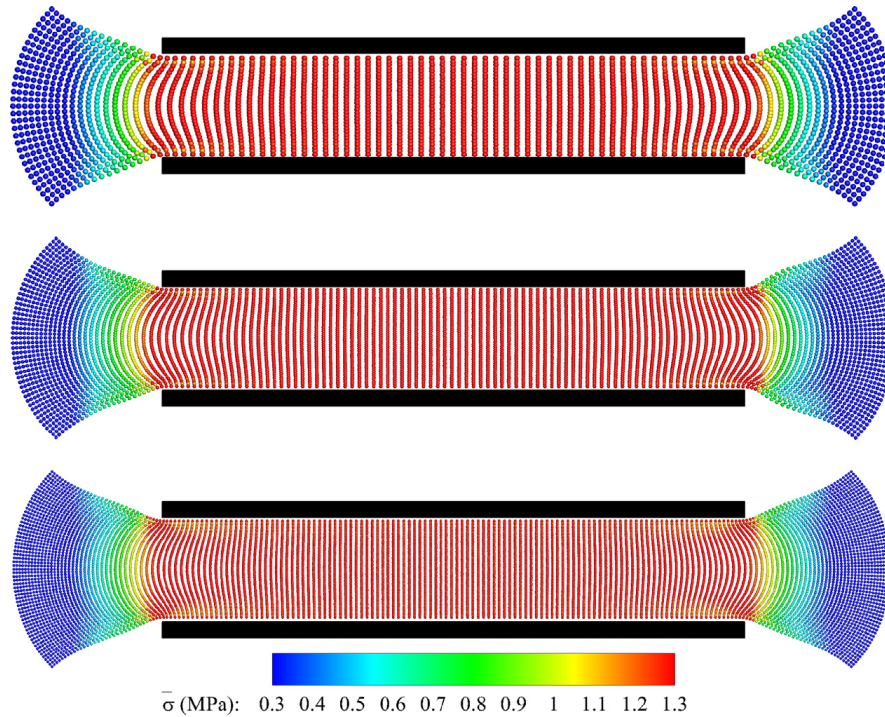


Fig. 10. Punching strip: A sequence of particle refinement analyses using the present SPH-ENOG. Three different spatial resolutions, $H/dp = 30$, $H/dp = 45$ and $H/dp = 60$, are applied. The material is modeled with density $\rho_0 = 1100 \text{ kg/m}^3$, Young's modulus $E = 1.0 \text{ GPa}$ and Poisson's ratio $\nu = 0.45$.

the top and bottom rows of particles, respectively. The initial particle spacing $dp = L/30$ is applied to discretize the system, and the splitting random-choice dynamic relaxation method [74] is applied to obtain the quasi-static elongation. Fig. 11(a) and (b) respectively show the particle configuration with von Mises stress contour obtained by the SPH and SPH-ENOG when the 500% tension is reached, i.e., the length of the strip is increased to 12 mm. The SPH is unstable and its result exhibits particle disorder in the rows of particles, and the disorder phenomenon is more obvious near the top and bottom boundaries. As expected, the present SPH-ENOG formulation is able to stably predict the large tensile deformation. Different with the unrealistic result of SPH-GM reported in Ref. [53] (see their Fig. 8), the present deformed configuration is of the typical I-shaped cross section of I-beam, which is consistent with that of Ref. [72] (see their Fig. 7), although slight discrepancy is exhibited near the top and bottom boundaries due to the large stress gradient. The robustness of the SPH-ENOG is further demonstrated for a even more challenging case by increasing the stretch to 1000% in tension, as shown in Fig. 11(c).

The 2D pulling test can be extended to 3D by considering the initial configuration of a cylinder with the radius $R = 1 \text{ mm}$ and height $H = 2 \text{ mm}$. The Poisson's ratio is changed to $\nu = 0.49$ following the Ref. [76], and the initial particle spacing $dp = 0.1 \text{ mm}$. The body-fitted particle generator [66] is applied to generate initial particle distribution. Fig. 12(a) and (b) respectively show the deformed configuration colored with von Mises stress obtained by the SPH and SPH-ENOG when the 240% tension is reached. Again the deformed configuration is of the typical I-shape and is in good agreement with the results from a mesh-based method as in Ref. [76] (see their Fig. 5). Some particles near the top and bottom boundaries run away in the SPH result, while the smooth particle and stress distributions are observed in the SPH-ENOG result. Fig. 12(c) shows the particle distribution and von Mises stress field for a even more challenging case with 480% tension.

4.5. Bending column

To further investigate the robustness and accuracy of the present formulation, we consider a bending-dominated problem where the numerical solution is available in literature [77] for quantitative validation. Following Ref. [39], a rubber-like material column spanning the length $L = 6 \text{ m}$ and square cross section (height $H = 1 \text{ m}$) is clamped

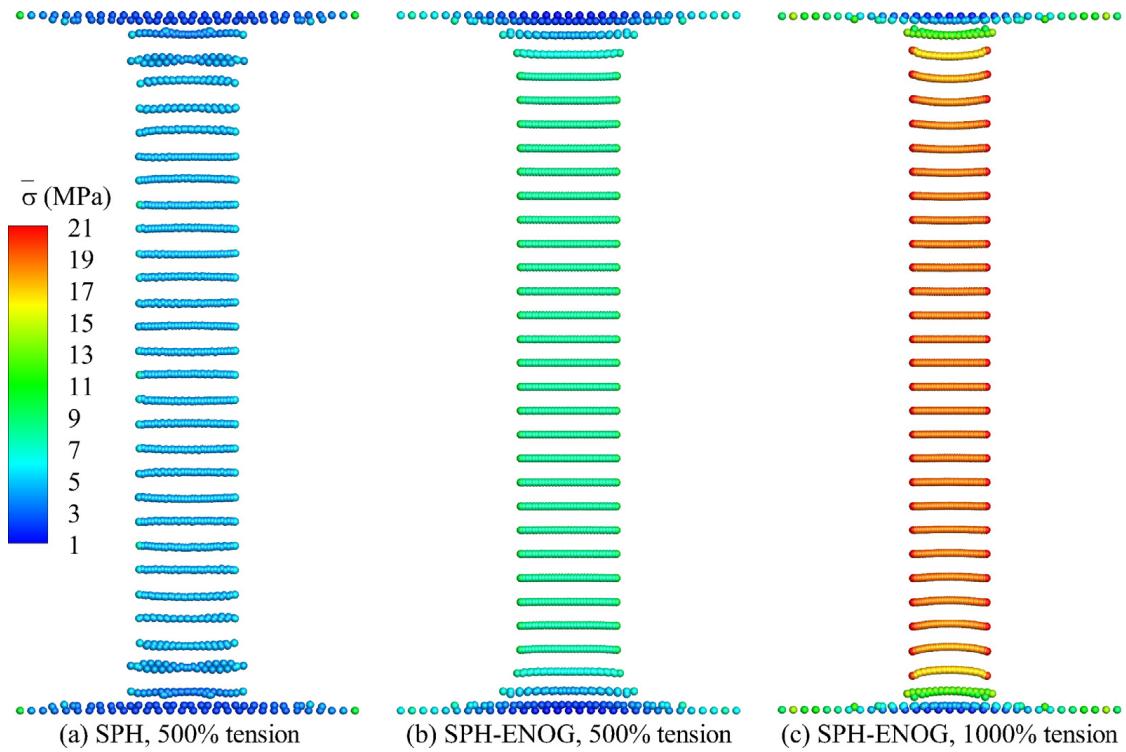


Fig. 11. 2D pulling rubber square strip: Deformed configuration plotted with von Mises stress $\bar{\sigma}$ and scaled in the vertical direction for clarity. The material parameters are of density $\rho_0 = 1100 \text{ kg/m}^3$, Young’s modulus $E = 1.0 \text{ GPa}$ and Poisson’s ratio $\nu = 0.45$, and the spatial particle discretization is set as $L/dp = 20$.

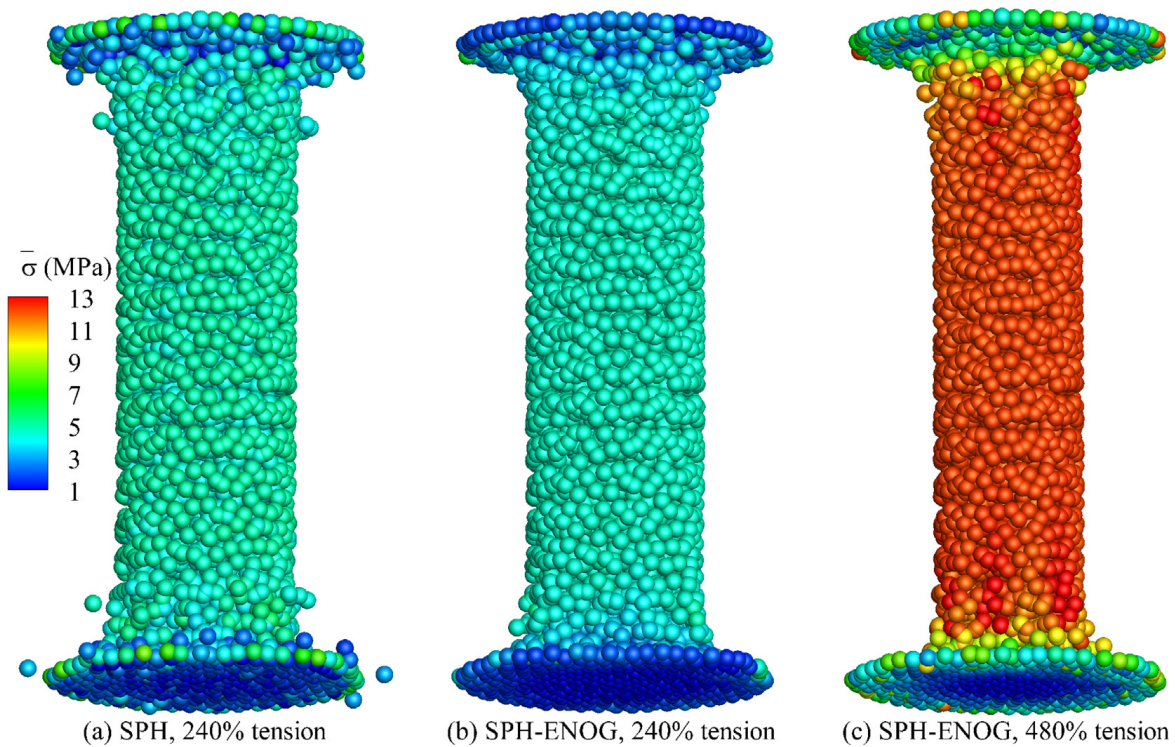


Fig. 12. 3D pulling rubber cylinder: Deformed configuration plotted with von Mises stress $\bar{\sigma}$ and scaled in the vertical direction for clarity. The material parameters are of density $\rho_0 = 1100 \text{ kg/m}^3$, Young’s modulus $E = 1.0 \text{ GPa}$ and Poisson’s ratio $\nu = 0.49$, and the spatial particle discretization is set as $H/dp = 20$. (For interpretation of the references to color in this figure legend, the reader is referred to the web version of this article.)

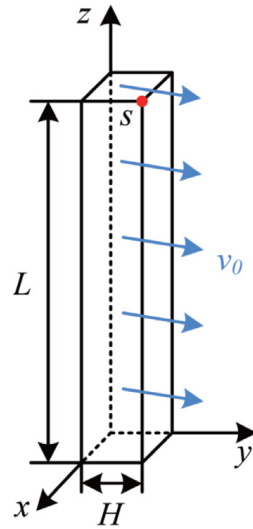


Fig. 13. Bending column: Initial configuration.

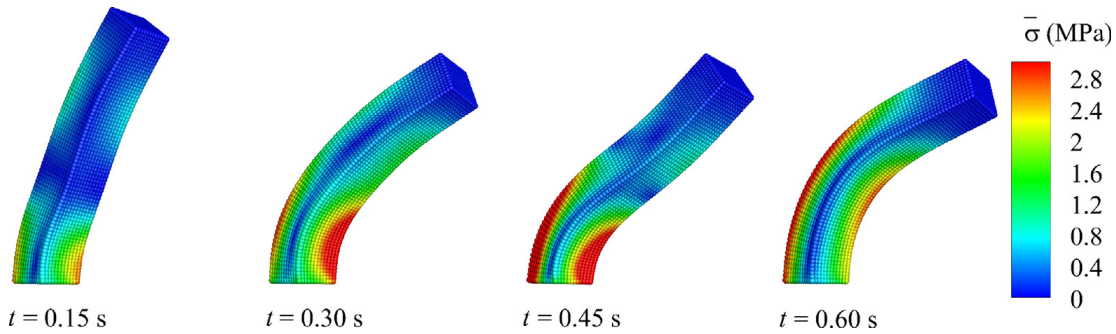


Fig. 14. Bending column: Deformed configuration colored by von Mises stress $\bar{\sigma}$ at serial temporal instants obtained by the present SPH-ENOG with initial uniform velocity $\mathbf{v}_0 = 10 \left(\frac{\sqrt{3}}{2}, \frac{1}{2}, 0 \right)^T$ m/s. The material is modeled with density $\rho_0 = 1100$ kg/m³, Young’s modulus $E = 17$ MPa and Poisson’s ratio $\nu = 0.45$, and spatial particle discretization is set as $H/dp = 12$ with H denoting the height of the column and dp the initial particle spacing. (For interpretation of the references to color in this figure legend, the reader is referred to the web version of this article.)

on its bottom and oscillates freely by imposing an initial uniform velocity $\mathbf{v}_0 = 10 \left(\frac{\sqrt{3}}{2}, \frac{1}{2}, 0 \right)^T$ m/s as shown in Fig. 13. The neo-Hookean material model is applied with density $\rho_0 = 1100$ kg/m³, Young’s modulus $E = 17$ MPa and Poisson’s ratio $\nu = 0.45$.

Fig. 14 shows the time evolution of the deformed configuration colored by von Mises stress contour obtained by the present formulation. The well-ordered particle distribution and smooth stress field are observed in the present result. For quantitative validation, Fig. 15 reports the time history of the z -axis position of point S , given in Fig. 13, with different resolutions, $H/dp = 6$, $H/dp = 12$, and $H/dp = 24$, and its comparison with the reference result reported by Aguirre et al. [77]. It can be observed that a good agreement is achieved as the increase of the spatial resolution. As shown in Fig. 16, compared with the original SPH, the present SPH-ENOG shows better agreement with the reference especially in the long run (after 1.5 s), implying its robustness in the large time scale simulation.

To evaluate the computational performance, we also analyze the total CPU time of the SPH and SPH-ENOG for simulating the bending column with physical time of 3 s. Table 4 summarizes the CPU wall-clock time with the corresponding total particle number, which shows the cost of calculation is reduced by about 2% when using the SPH-ENOG.

A more challenging problem is studied to show the outperformance of the present formulation by increasing the initial velocity to $\mathbf{v}_0 = 20 \left(\frac{\sqrt{3}}{2}, \frac{1}{2}, 0 \right)^T$ m/s. As shown in Fig. 17, the simulation result of the SPH exhibits

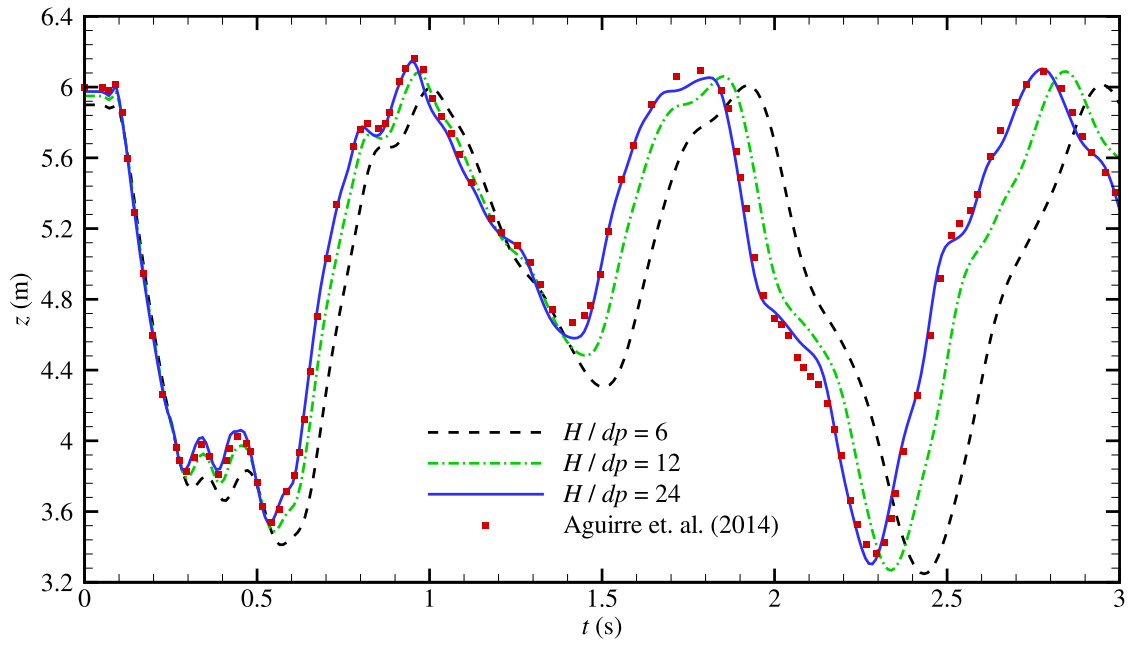


Fig. 15. Bending column: Time history of the vertical position z observed at node S obtained by the SPH-ENOG with three different spatial resolutions and the initial uniform velocity $\mathbf{v}_0 = 10 \left(\frac{\sqrt{3}}{2}, \frac{1}{2}, 0 \right)^T$ m/s, and its comparison with that of Aguirre et al. [77]. The material is modeled with density $\rho_0 = 1100$ kg/m³, Young’s modulus $E = 17$ MPa, and Poisson’s ratio $\nu = 0.45$. Note that H is the height of the column and dp the initial particle spacing.

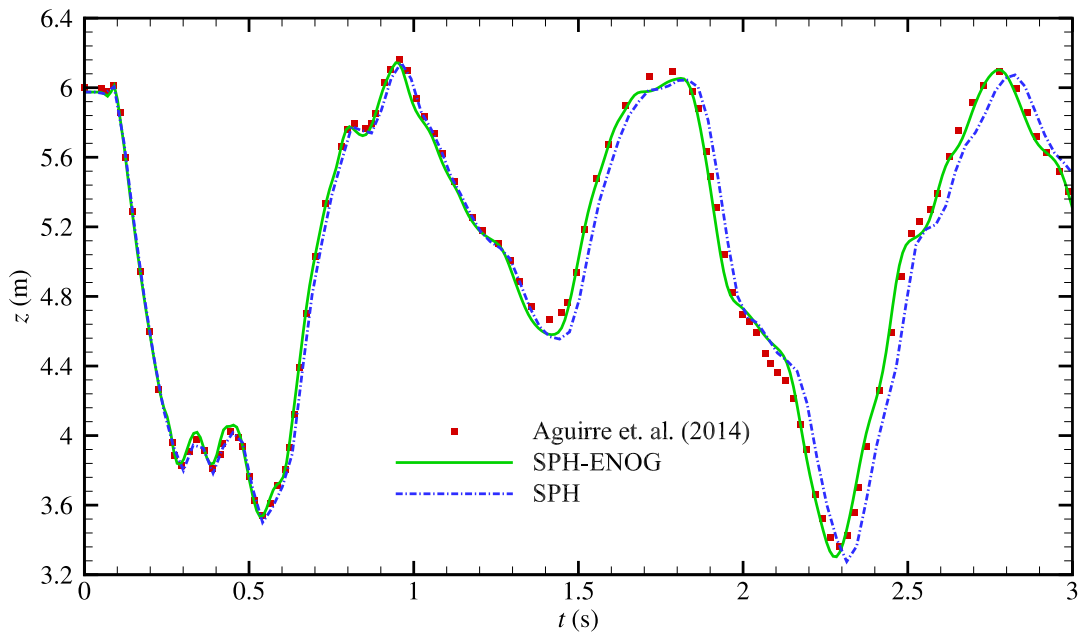


Fig. 16. Bending column: Time history of the vertical position z observed at node S obtained by the SPH-ENOG and SPH with initial uniform velocity $\mathbf{v}_0 = 10 \left(\frac{\sqrt{3}}{2}, \frac{1}{2}, 0 \right)^T$ m/s, and its comparison with that of Aguirre et al. [77]. The material is modeled with density $\rho_0 = 1100$ kg/m³, Young’s modulus $E = 17$ MPa Poisson’s ratio $\nu = 0.45$, and the spatial particle discretization is $H/dp = 24$ with H denoting the height of the column and dp the initial particle spacing.

Table 4

Computational efficiency for the SPH and SPH-ENOG with different spatial resolutions.

Model	Resolution	CPU wall-clock time (s)
SPH	1296	5.10
SPH-ENOG	1296	4.98
SPH	10,368	103.89
SPH-ENOG	10,368	99.74
SPH	82,944	1777.46
SPH-ENOG	82,944	1746.83

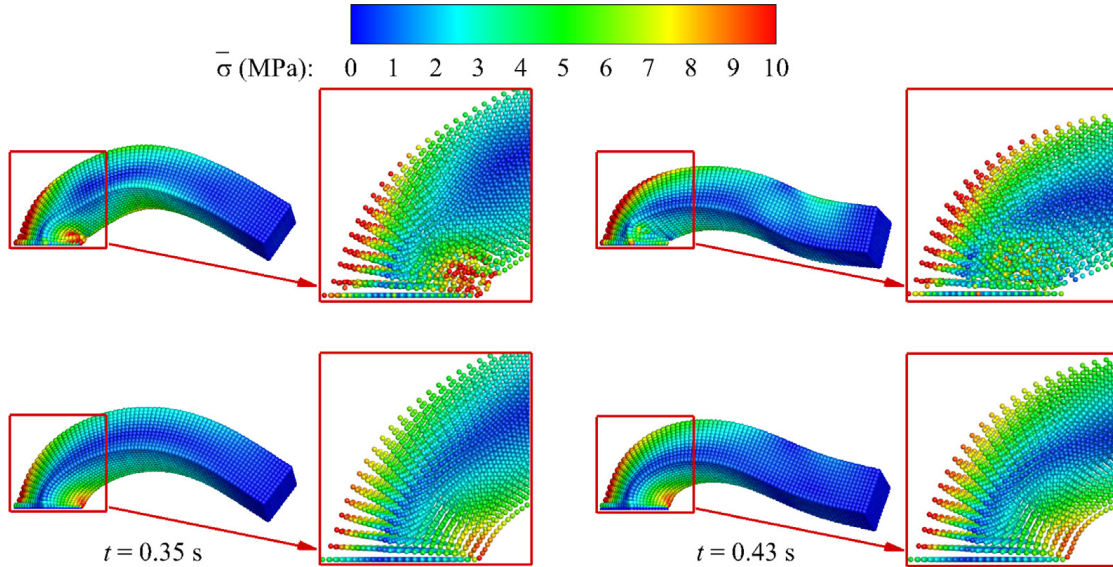


Fig. 17. Bending column: Deformed configuration colored by von Mises stress at two temporal instants obtained by the SPH (top panel) and SPH-ENOG (bottom panel) with initial uniform velocity $\mathbf{v}_0 = 20 \left(\frac{\sqrt{3}}{2}, \frac{1}{2}, 0 \right)^T$ m/s. The material is modeled with density $\rho_0 = 1100$ kg/m³, Young’s modulus $E = 17$ MPa and Poisson’s ratio $\nu = 0.45$, and the spatial particle discretization is $H/dp = 12$ with H denoting the height of the column and dp the initial particle spacing. (For interpretation of the references to color in this figure legend, the reader is referred to the web version of this article.)

noticeable particle disorder, especially near the clamped bottom where the maximum von Mises stress exists, while the present SPH-ENOG captures the very regular particle distribution and smooth stress field, further demonstrating the robustness of the proposed formulation.

4.6. Twisting column

In this section, the bending column is extended to a twisting column in line with Refs. [50,51,78]. As shown in Fig. 18, the twisting is initialized with a sinusoidal rotational velocity field of $\boldsymbol{\omega} = [0, \Omega_0 \sin(\pi y_0/2L), 0]$ with $\Omega_0 = 105$ rad/s. The column is considered as being nearly incompressible material, modeled of density $\rho_0 = 1100$ kg/m³, Young’s modulus $E = 17$ MPa and Poisson’s ratio $\nu = 0.499$.

Fig. 19 shows the deformed configuration at different time instants with von Mises stress contour obtained by the SPH and SPH-ENOG. Both simulations perform well and produce very similar results in terms of deformation patterns compared with those in the literature (see Fig. 28 in Ref. [50]), except small fluctuation of stress near the bottom constrained surface produced by SPH. A significantly more challenging problem is studied by increasing the initial angular velocity to $\Omega_0 = 300$ rad/s with $\nu = 0.49$. As shown in Fig. 20, a stable simulation by applying the proposed formulation is demonstrated. The unstabilized results of the SPH show obvious particle disorder, especially between the second and third spiral lines from the bottom. On the contrary, the results calculated by the SPH-ENOG exhibit the very ordered particle distribution and smooth stress field. Note that similar test has been simulated in Ref. [51] (see their Fig. 10) by an artificial viscosity formulation but with a very critical Poisson’s ratio

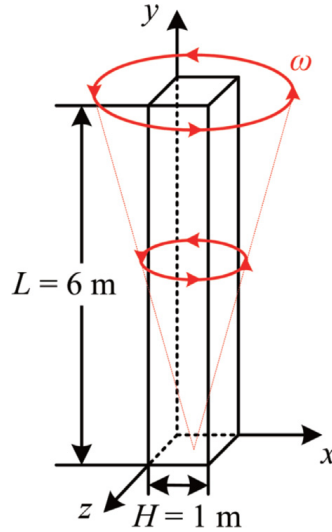


Fig. 18. Twisting column: Initial configuration.

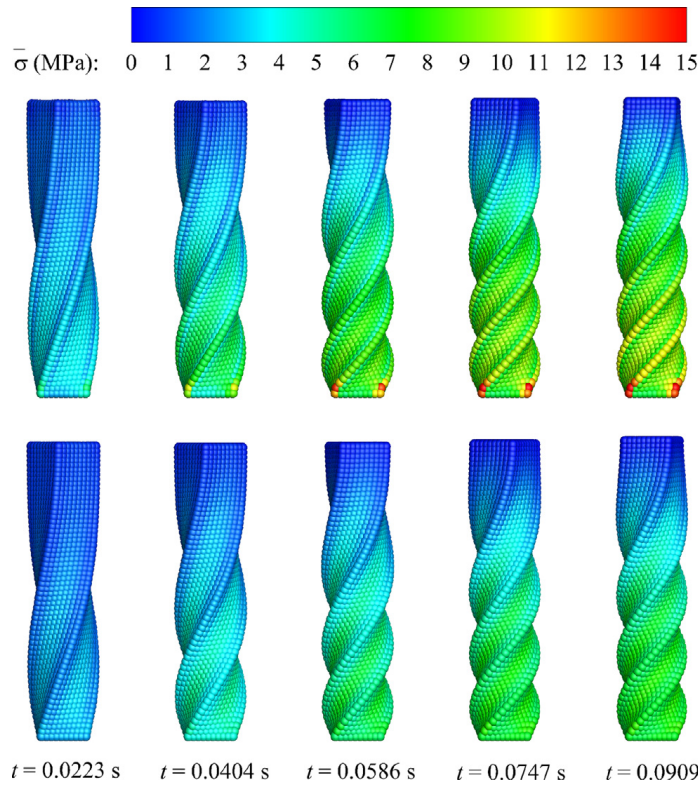


Fig. 19. Twisting column: Deformed configuration colored by von Mises stress at different time instants for the SPH (top panel) and SPH-ENOG (bottom panel) with initial rotational velocity $\omega = [0, \Omega_0 \sin(\pi y_0/2L), 0]$ with $\Omega_0 = 105$ rad/s. The material is modeled with density $\rho_0 = 1100$ kg/m³, Young’s modulus $E = 17$ MPa and Poisson’s ratio $\nu = 0.499$, and the spatial particle discretization is set as $H/dp = 10$ with H denoting the height of the column and dp the initial particle spacing. (For interpretation of the references to color in this figure legend, the reader is referred to the web version of this article.)

$\nu = 0.49995$ to avoid the hourglass modes. In the present study, we apply $\nu = 0.49$, indicating much large time steps can be used, and obtain stable simulation without exhibiting particle disorder. Also note that, the artificial viscosity formulation may face further difficulties when the velocity field becomes flat or less significant as the static test cases in this work. A convergence study is also carried out by sequentially refining the spatial resolution from $H/dp = 4$ to $H/dp = 8$ and $H/dp = 12$. As shown in Fig. 21, both the deformation and von Mises stress $\bar{\sigma}$ exhibit good convergence properties.

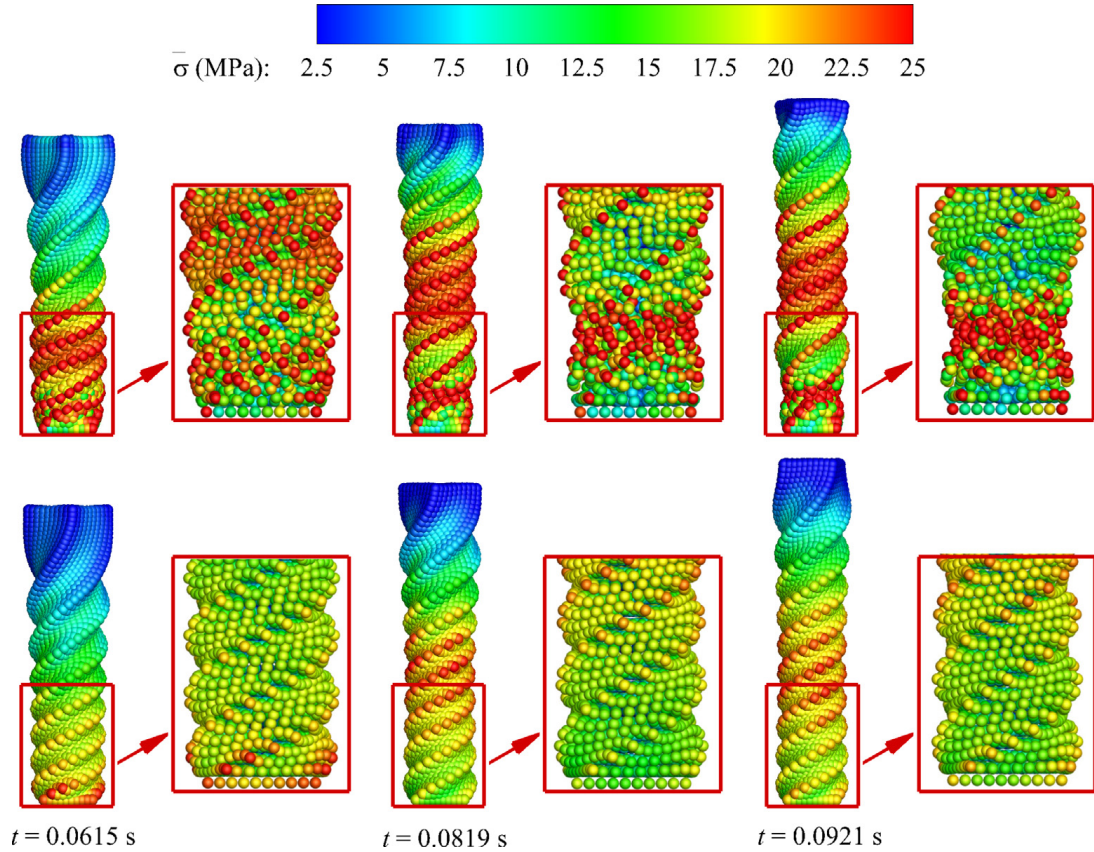


Fig. 20. Twisting column: Deformed configuration colored by von Mises stress at different time instants for the SPH (top panel) and SPH-ENOG (bottom panel) with initial sinusoidal rotational velocity $\Omega_0 = 300$ rad/s. The material is modeled with density $\rho_0 = 1100$ kg/m³, Young’s modulus $E = 17$ MPa and Poisson’s ratio $\nu = 0.49$, and the spatial particle discretization is set as $H/dp = 10$ with H denoting the height of the column and dp the initial particle spacing. (For interpretation of the references to color in this figure legend, the reader is referred to the web version of this article.)

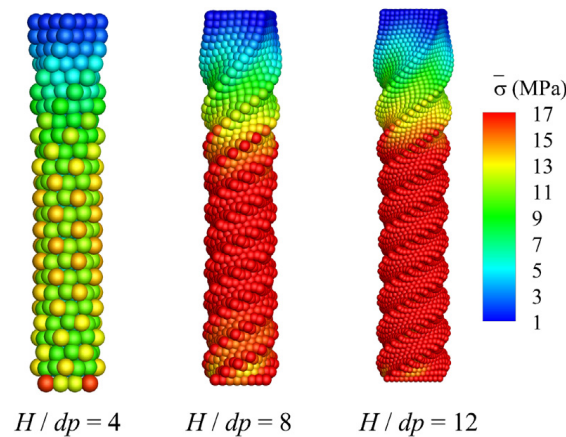


Fig. 21. Twisting column: A sequence of particle refinement analyses using the SPH-ENOG with the initial sinusoidal rotational velocity $\Omega_0 = 300$ rad/s. The material is modeled with density $\rho_0 = 1100$ kg/m³, Young’s modulus $E = 17$ MPa and Poisson’s ratio $\nu = 0.49$. Note that H is the height of the column and dp the initial particle spacing.

Finally, the robustness of the present formulation is further examined by increasing the initial angular velocity to $\Omega_0 = 400$ rad/s. Fig. 22 shows the deformed configuration with different time instants. The extremely large deformations of the whole twisting process, including the recovery process and reverse rotation, are well captured as expected.

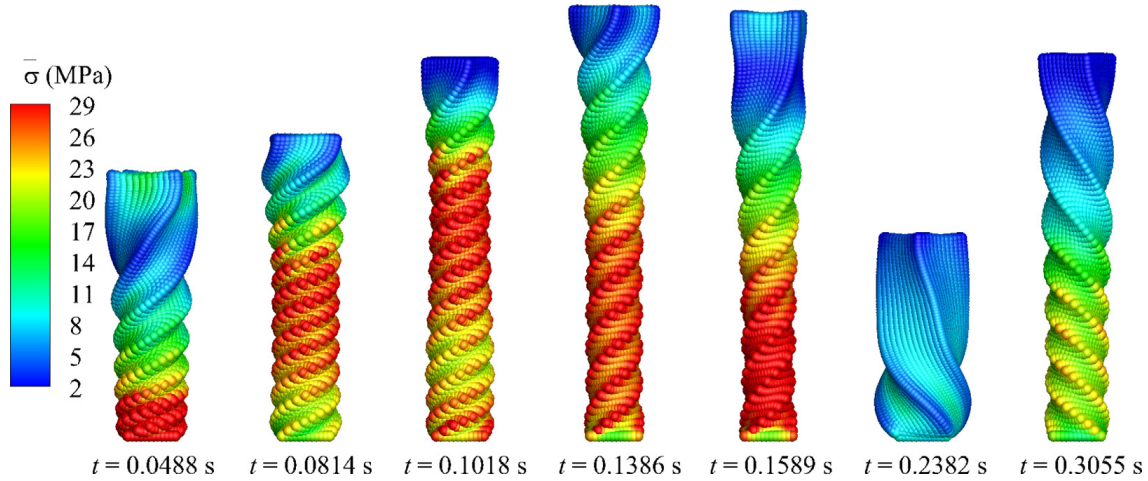


Fig. 22. Twisting column: Deformed configuration plotted with von Mises stress at serial time instants obtained by the SPH-ENOG with the initial sinusoidal rotational velocity $\Omega_0 = 400$ rad/s. The material is modeled with density $\rho_0 = 1100$ kg/m³, Young’s modulus $E = 17$ MPa and Poisson’s ratio $\nu = 0.49$, and the spatial particle discretization is set as $H/dp = 12$ with H denoting the height of the column and dp the initial particle spacing.

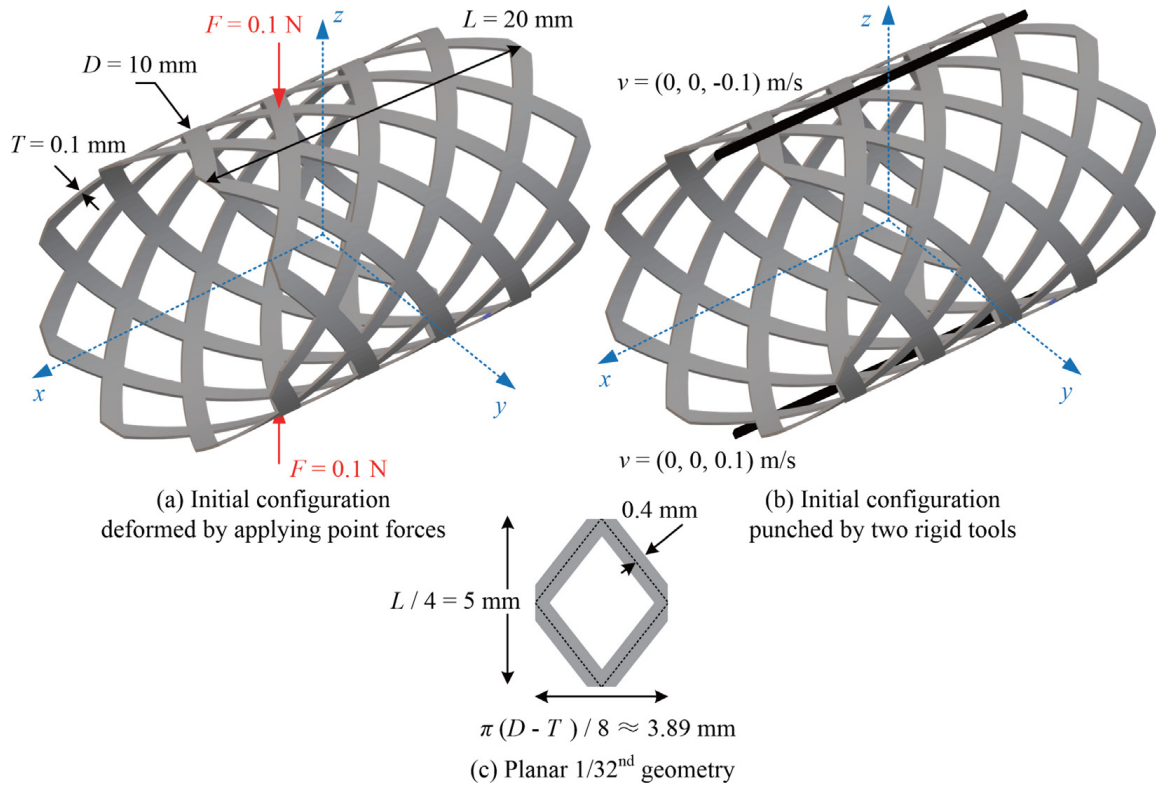


Fig. 23. Stent structure: Problem setup. The corresponding computer-aided design (CAD) file in STL format can be downloaded from our code repository or GrabCAD.

4.7. Stent structure

A realistic cardiovascular stent, widely used in biomedical applications, is investigated in this section to demonstrate the robustness and versatility of the SPH-ENOG. As shown in Fig. 23, a Palmaz-Schatz shaped stent with the length of $L = 20$ mm, outer diameter $D = 10$ mm and thickness $T = 0.1$ mm is considered herein. One of the element structures on the planar surface is also shown on the bottom panel of Fig. 23. The material properties are

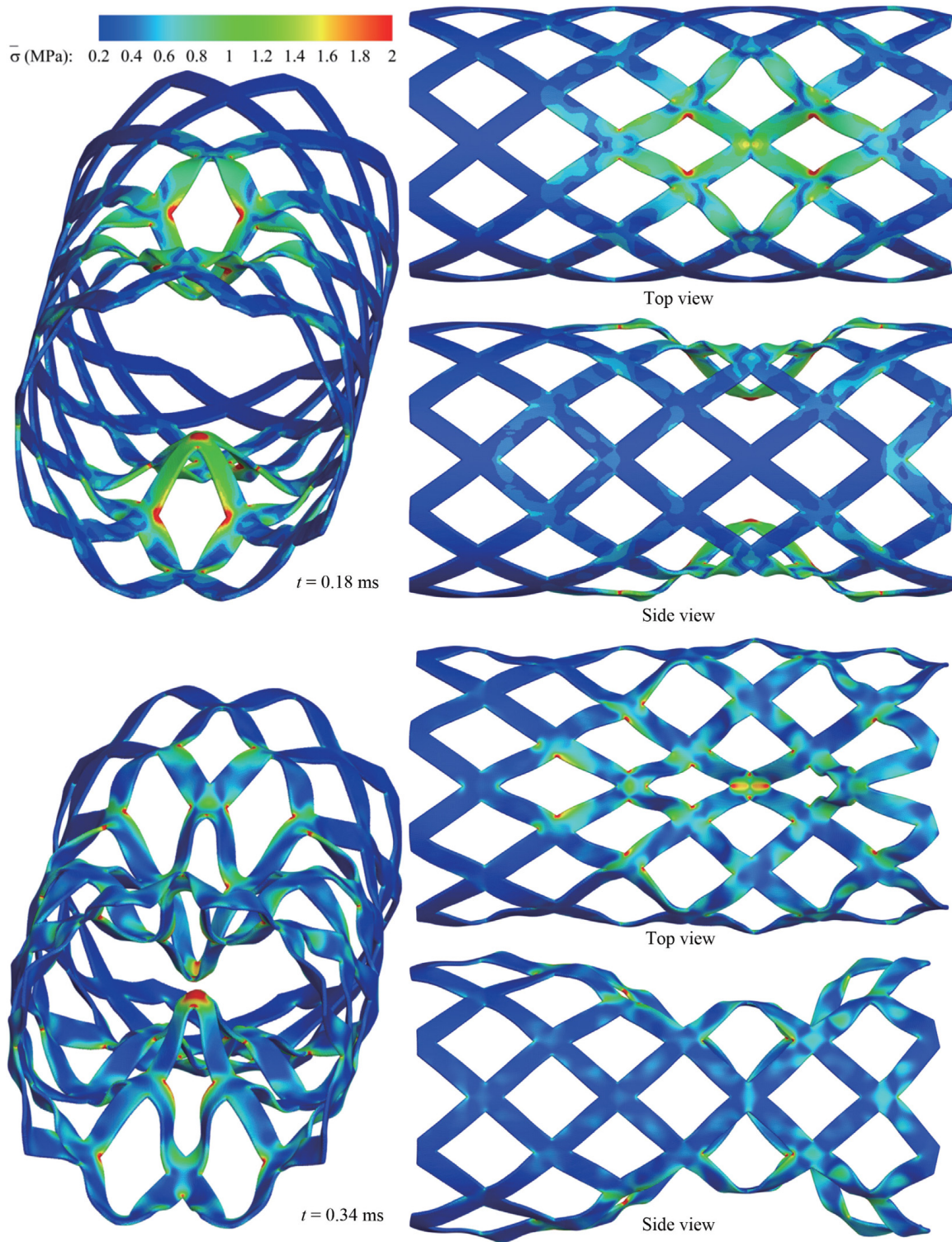


Fig. 24. Stent structure: Deformed configuration under two diametrically opposed point forces $F = 0.1$ N colored by von Mises stress at $t = 0.18$ ms and $t = 0.34$ ms. The neo-Hookean material is applied with density $\rho_0 = 1100$ kg/m³, Young's modulus $E = 17$ MPa and Poisson's ratio $\nu = 0.45$. (For interpretation of the references to color in this figure legend, the reader is referred to the web version of this article.)

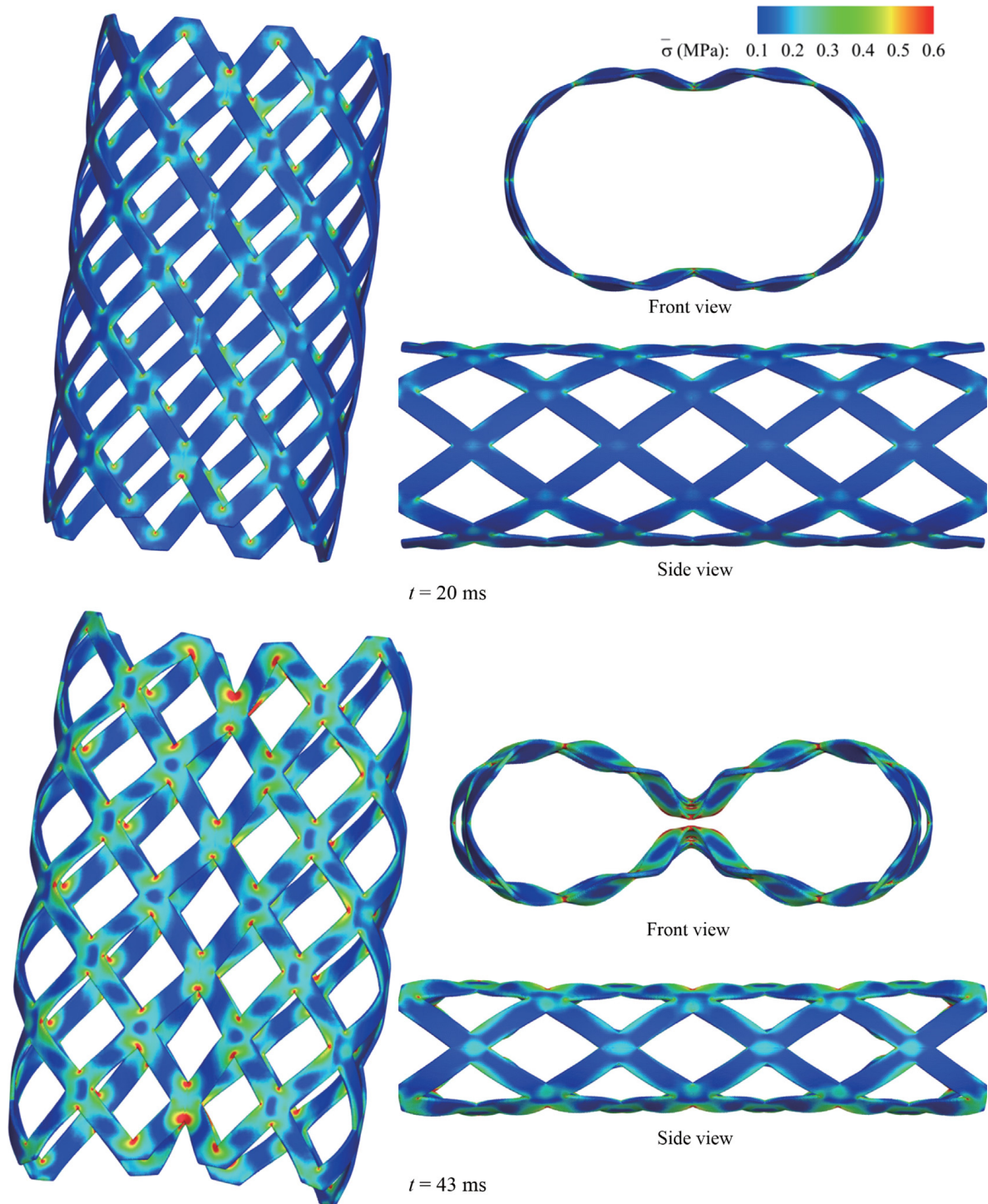


Fig. 25. Stent structure: Deformed configuration under punching setup colored by von Mises stress at $t = 0.18$ ms and $t = 0.34$ ms. The neo-Hookean material is applied with density $\rho_0 = 1100$ kg/m³, Young’s modulus $E = 17$ MPa and Poisson’s ratio $\nu = 0.45$. (For interpretation of the references to color in this figure legend, the reader is referred to the web version of this article.)

$\rho_0 = 1100$ kg/m³, Young’s modulus $E = 17$ MPa and Poisson’s ratio $\nu = 0.45$. Also, the initial particle distribution is generated by the body-fitted particle generator [66] with initial particle spacing $dp = T/3$. Two diametrically opposed point forces $F = 0.1$ N are applied on the stent to active the deformation as shown in Fig. 23(a), and the stent is also punched by two rigid tools modeled as cuboids with dimensions $20 \times 0.15 \times 0.15$ mm³ with the punch velocity of 0.1 m/s as shown in Fig. 23(b) to further examine the robustness of the present formulation.

Fig. 24 shows the overall deformation of the stent structure under point forces at time instants $t = 0.18$ ms and $t = 0.34$ ms colored by the von Mises stress. The deformation pattern and smooth stress field of this complex thin structure are well captured, especially around the points of applying forces and sharp corners of the stent where the maximum stress exists. Fig. 25 shows the compressed stent colored by von Mises stress at different time instants. It is remarkable that the extremely large deformation is well captured, paving the way of realistic cardiovascular applications.

5. Concluding remarks

In this paper, we present an efficient, robust and essentially non-hourglass formulation without introducing case-dependent tuning parameter and extra computational effort for the TL-SPH method. The proposed formulation demonstrates its capability of suppressing the long standing issues of the hourglass modes and shows its robustness in the simulation of large strain dynamics. Last but not least, the deformation of complex stent structures is studied to demonstrate the versatility of the presented formulation, representing a stepping stone to practical applications in the field of biomechanics. Note that, although the present formulation is proposed for elastic structural responses, it may be extended for modeling elastic–plastic and damage/fracture, in which the same volumetric and deviatoric decomposition is often applied [59].

CRedit authorship contribution statement

Dong Wu: Conceptualization, Methodology, Investigation, Visualization, Validation, Formal analysis, Writing – original draft, Writing – review & editing. **Chi Zhang:** Investigation, Methodology, Formal analysis, Writing – review & editing. **Xiaojing Tang:** Investigation, Writing – review & editing. **Xiangyu Hu:** Supervision, Methodology, Investigation, Writing – review & editing.

Declaration of competing interest

The authors declare that they have no known competing financial interests or personal relationships that could have appeared to influence the work reported in this paper.

Data availability

The code and data will be publish in Github.

Acknowledgments

D. Wu is partially supported by the China Scholarship Council (No. 201906130189). C. Zhang and X.Y. Hu would like to express their gratitude to the German Research Foundation (DFG) for their sponsorship of this research under grant number DFG HU1527/12-4.

References

- [1] L.B. Lucy, A numerical approach to the testing of the fission hypothesis, *Astron. J.* 82 (1977) 1013–1024.
- [2] R.A. Gingold, J.J. Monaghan, Smoothed particle hydrodynamics: theory and application to non-spherical stars, *Mon. Not. R. Astron. Soc.* 181 (3) (1977) 375–389.
- [3] P. Randles, L.D. Libersky, Smoothed particle hydrodynamics: some recent improvements and applications, *Comput. Methods Appl. Mech. Engrg.* 139 (1–4) (1996) 375–408.
- [4] M. Luo, A. Khayyer, P. Lin, Particle methods in ocean and coastal engineering, *Appl. Ocean Res.* 114 (2021) 102734.
- [5] A. Khayyer, H. Gotoh, Y. Shimizu, On systematic development of FSI solvers in the context of particle methods, *J. Hydrodyn.* (2022) 1–13.
- [6] C. Zhang, Y.-j. Zhu, D. Wu, N.A. Adams, X. Hu, Smoothed particle hydrodynamics: Methodology development and recent achievement, *J. Hydrodyn.* 34 (5) (2022) 767–805.
- [7] J.J. Monaghan, Smoothed particle hydrodynamics, *Rep. Progr. Phys.* 68 (8) (2005) 1703.
- [8] M. Liu, G. Liu, Smoothed particle hydrodynamics (SPH): an overview and recent developments, *Arch. Comput. Methods Eng.* 17 (1) (2010) 25–76.
- [9] J.J. Monaghan, Smoothed particle hydrodynamics and its diverse applications, *Annu. Rev. Fluid Mech.* 44 (2012) 323–346.
- [10] C. Zhang, M. Rezavand, Y. Zhu, Y. Yu, D. Wu, W. Zhang, J. Wang, X. Hu, SPHinXsys: An open-source multi-physics and multi-resolution library based on smoothed particle hydrodynamics, *Comput. Phys. Comm.* (2021) 108066.

- [11] P.-N. Sun, D. Le Touze, G. Oger, A.-M. Zhang, An accurate FSI-SPH modeling of challenging fluid-structure interaction problems in two and three dimensions, *Ocean Eng.* 221 (2021) 108552.
- [12] H.G. Matthies, J. Steindorf, Partitioned strong coupling algorithms for fluid-structure interaction, *Comput. Struct.* 81 (8–11) (2003) 805–812.
- [13] H.G. Matthies, R. Niekamp, J. Steindorf, Algorithms for strong coupling procedures, *Comput. Methods Appl. Mech. Engrg.* 195 (17–18) (2006) 2028–2049.
- [14] Q. Yang, V. Jones, L. McCue, Free-surface flow interactions with deformable structures using an SPH-FEM model, *Ocean Eng.* 55 (2012) 136–147.
- [15] C. Hermange, G. Oger, Y. Le Chenadec, D. Le Touzé, A 3D SPH-FE coupling for FSI problems and its application to tire hydroplaning simulations on rough ground, *Comput. Methods Appl. Mech. Engrg.* 355 (2019) 558–590.
- [16] C. Antoci, M. Gallati, S. Sibilla, Numerical simulation of fluid-structure interaction by SPH, *Comput. Struct.* 85 (11–14) (2007) 879–890.
- [17] L. Han, X. Hu, SPH modeling of fluid-structure interaction, *J. Hydrodyn.* 30 (1) (2018) 62–69.
- [18] M. Liu, Z. Zhang, Smoothed particle hydrodynamics (SPH) for modeling fluid-structure interactions, *Sci. China Phys. Mech. Astron.* 62 (8) (2019) 1–38.
- [19] G.R. Johnson, R.A. Stryk, S.R. Beissel, SPH for high velocity impact computations, *Comput. Methods Appl. Mech. Engrg.* 139 (1–4) (1996) 347–373.
- [20] R. Vignjevic, J.R. Reveles, J. Campbell, SPH in a total Lagrangian formalism, *CMC-Tech Science Press-* 4 (3) (2006) 181.
- [21] M. Liu, G.-R. Liu, Restoring particle consistency in smoothed particle hydrodynamics, *Appl. Numer. Math.* 56 (1) (2006) 19–36.
- [22] J.W. Swegle, D.L. Hicks, S.W. Attaway, Smoothed particle hydrodynamics stability analysis, *J. Comput. Phys.* 116 (1) (1995) 123–134.
- [23] S.J. Lind, B.D. Rogers, P.K. Stansby, Review of smoothed particle hydrodynamics: towards converged Lagrangian flow modelling, *Proc. R. Soc. Lond. Ser. A Math. Phys. Eng. Sci.* 476 (2241) (2020) 20190801.
- [24] T. Rabczuk, T. Belytschko, S. Xiao, Stable particle methods based on Lagrangian kernels, *Comput. Methods Appl. Mech. Engrg.* 193 (12–14) (2004) 1035–1063.
- [25] J.J. Monaghan, SPH without a tensile instability, *J. Comput. Phys.* 159 (2) (2000) 290–311.
- [26] J.P. Gray, J.J. Monaghan, R. Swift, SPH elastic dynamics, *Comput. Methods Appl. Mech. Engrg.* 190 (49–50) (2001) 6641–6662.
- [27] J.M. Owen, A tensor artificial viscosity for SPH, *J. Comput. Phys.* 201 (2) (2004) 601–629.
- [28] C. Zhang, X.Y. Hu, N.A. Adams, A generalized transport-velocity formulation for smoothed particle hydrodynamics, *J. Comput. Phys.* 337 (2017) 216–232.
- [29] Y. Zhu, C. Zhang, X. Hu, A consistency-driven particle-advection formulation for weakly-compressible smoothed particle hydrodynamics, *Comput. & Fluids* 230 (2021) 105140.
- [30] T. Belytschko, Y. Guo, W. Kam Liu, S. Ping Xiao, A unified stability analysis of meshless particle methods, *Internat. J. Numer. Methods Engrg.* 48 (9) (2000) 1359–1400.
- [31] J. Bonet, S. Kulasegaram, Alternative total Lagrangian formulations for corrected smooth particle hydrodynamics (CSPH) methods in large strain dynamic problems, *Rev. Eur. Élé. Finis* 11 (7–8) (2002) 893–912.
- [32] T. De Vuyst, R. Vignjevic, Total Lagrangian SPH modelling of necking and fracture in electromagnetically driven rings, *Int. J. Fract.* 180 (1) (2013) 53–70.
- [33] K. Ba, A. Gakwaya, Thermomechanical total Lagrangian SPH formulation for solid mechanics in large deformation problems, *Comput. Methods Appl. Mech. Engrg.* 342 (2018) 458–473.
- [34] B. Maurel, A. Combescure, An SPH shell formulation for plasticity and fracture analysis in explicit dynamics, *Internat. J. Numer. Methods Engrg.* 76 (7) (2008) 949–971.
- [35] J. Lin, H. Naceur, D. Coutellier, A. Laksimi, Efficient meshless SPH method for the numerical modeling of thick shell structures undergoing large deformations, *Int. J. Non-Linear Mech.* 65 (2014) 1–13.
- [36] Y. Peng, A. Zhang, F. Ming, A thick shell model based on reproducing kernel particle method and its application in geometrically nonlinear analysis, *Comput. Mech.* 62 (3) (2018) 309–321.
- [37] A. Khayyer, H. Gotoh, H. Falahaty, Y. Shimizu, An enhanced ISPH-SPH coupled method for simulation of incompressible fluid-elastic structure interactions, *Comput. Phys. Comm.* 232 (2018) 139–164.
- [38] C. Zhang, M. Rezavand, X. Hu, A multi-resolution SPH method for fluid-structure interactions, *J. Comput. Phys.* 429 (2021) 110028.
- [39] C. Zhang, J. Wang, M. Rezavand, D. Wu, X. Hu, An integrative smoothed particle hydrodynamics method for modeling cardiac function, *Comput. Methods Appl. Mech. Engrg.* 381 (2021) 113847.
- [40] D. Flanagan, T. Belytschko, A uniform strain hexahedron and quadrilateral with orthogonal hourglass control, *Internat. J. Numer. Methods Engrg.* 17 (5) (1981) 679–706.
- [41] O.-P. Jacquotte, J.T. Oden, Analysis of hourglass instabilities and control in underintegrated finite element methods, *Comput. Methods Appl. Mech. Engrg.* 44 (3) (1984) 339–363.
- [42] C. Dyka, P. Randles, R. Ingel, Stress points for tension instability in SPH, *Internat. J. Numer. Methods Engrg.* 40 (13) (1997) 2325–2341.
- [43] R. Vignjevic, J. Campbell, L. Libersky, A treatment of zero-energy modes in the smoothed particle hydrodynamics method, *Comput. Methods Appl. Mech. Engrg.* 184 (1) (2000) 67–85.
- [44] R. Vignjevic, J. Campbell, Review of development of the smooth particle hydrodynamics (SPH) method, in: *Predictive Modeling of Dynamic Processes*, Springer, 2009, pp. 367–396.
- [45] S. Beissel, T. Belytschko, Nodal integration of the element-free Galerkin method, *Comput. Methods Appl. Mech. Engrg.* 139 (1–4) (1996) 49–74.

- [46] Y. Vidal, J. Bonet, A. Huerta, Stabilized updated Lagrangian corrected SPH for explicit dynamic problems, *Internat. J. Numer. Methods Engrg.* 69 (13) (2007) 2687–2710.
- [47] J. O'Connor, B.D. Rogers, A fluid–structure interaction model for free-surface flows and flexible structures using smoothed particle hydrodynamics on a GPU, *J. Fluids Struct.* 104 (2021) 103312.
- [48] P. Randles, L. Libersky, Normalized SPH with stress points, *Internat. J. Numer. Methods Engrg.* 48 (10) (2000) 1445–1462.
- [49] M.R.I. Islam, C. Peng, A stabilized total-Lagrangian SPH method for large deformation and failure in geomaterials, 2019, arXiv preprint arXiv:1907.06990.
- [50] C.H. Lee, A.J. Gil, G. Greto, S. Kulasegaram, J. Bonet, A new Jameson–Schmidt–Turkel smooth particle hydrodynamics algorithm for large strain explicit fast dynamics, *Comput. Methods Appl. Mech. Engrg.* 311 (2016) 71–111.
- [51] C. Zhang, Y. Zhu, Y. Yu, D. Wu, M. Rezavand, S. Shao, X. Hu, An artificial damping method for total Lagrangian SPH method with application in biomechanics, *Eng. Anal. Bound. Elem.* 143 (2022) 1–13.
- [52] M. Kondo, Y. Suzuki, S. Koshizuka, Suppressing local particle oscillations in the Hamiltonian particle method for elasticity, *Internat. J. Numer. Methods Engrg.* 81 (12) (2010) 1514–1528.
- [53] G.C. Ganzenmüller, An hourglass control algorithm for Lagrangian smooth particle hydrodynamics, *Comput. Methods Appl. Mech. Engrg.* 286 (2015) 87–106.
- [54] Y. Shimizu, A. Khayyer, H. Gotoh, An implicit SPH-based structure model for accurate Fluid–Structure Interaction simulations with hourglass control scheme, *Eur. J. Mech. B Fluids* 96 (2022) 122–145.
- [55] T. Belytschko, Correction of article by DP Flanagan and T. Belytschko, *Internat. J. Numer. Methods Engrg.* 19 (3) (1983) 467–468.
- [56] L. Stainier, J.P. Ponthot, An improved one-point integration method for large strain elastoplastic analysis, *Comput. Methods Appl. Mech. Engrg.* 118 (1–2) (1994) 163–177.
- [57] J.P. Morris, P.J. Fox, Y. Zhu, Modeling low Reynolds number incompressible flows using SPH, *J. Comput. Phys.* 136 (1) (1997) 214–226.
- [58] X.Y. Hu, N.A. Adams, A multi-phase SPH method for macroscopic and mesoscopic flows, *J. Comput. Phys.* 213 (2) (2006) 844–861.
- [59] J.C. Simo, T.J. Hughes, *Computational Inelasticity*, Vol. 7, Springer Science & Business Media, 2006.
- [60] C. Zhang, M. Rezavand, Y. Zhu, Y. Yu, D. Wu, W. Zhang, S. Zhang, J. Wang, X. Hu, SPHinXsys: An open-source meshless, multi-resolution and multi-physics library, *Softw. Impacts* 6 (2020) 100033.
- [61] Y. Yue, B. Smith, C. Batty, C. Zheng, E. Grinspun, Continuum foam: A material point method for shear-dependent flows, *ACM Trans. Graph.* 34 (5) (2015) 1–20.
- [62] J. Bonet, S. Kulasegaram, A simplified approach to enhance the performance of smooth particle hydrodynamics methods, *Appl. Math. Comput.* 126 (2–3) (2002) 133–155.
- [63] H. Takeda, S.M. Miyama, M. Sekiya, Numerical simulation of viscous flow by smoothed particle hydrodynamics, *Progr. Theoret. Phys.* 92 (5) (1994) 939–960.
- [64] S.J. Cummins, M. Rudman, An SPH projection method, *J. Comput. Phys.* 152 (2) (1999) 584–607.
- [65] X. Hu, N. Adams, Angular-momentum conservative smoothed particle dynamics for incompressible viscous flows, *Phys. Fluids* 18 (10) (2006) 101702.
- [66] Y. Zhu, C. Zhang, Y. Yu, X. Hu, A CAD-compatible body-fitted particle generator for arbitrarily complex geometry and its application to wave-structure interaction, *J. Hydrodyn.* 33 (2) (2021) 195–206.
- [67] H. Wendland, Piecewise polynomial, positive definite and compactly supported radial functions of minimal degree, *Adv. Comput. Math.* 4 (1) (1995) 389–396.
- [68] L.D. Landau, E.M. Lifchits, *Course of Theoretical Physics: Theory of Elasticity*, Butterworth-Heinemann, 1986.
- [69] A.W. Leissa, *Vibration of Plates*, Vol. 160, Scientific and Technical Information Division, National Aeronautics and Space Administration, 1969.
- [70] A. Khayyer, H. Gotoh, Y. Shimizu, Y. Nishijima, A 3D Lagrangian meshfree projection-based solver for hydroelastic Fluid–Structure Interactions, *J. Fluids Struct.* 105 (2021) 103342.
- [71] A. Khayyer, Y. Shimizu, H. Gotoh, S. Hattori, A 3D SPH-based entirely Lagrangian meshfree hydroelastic FSI solver for anisotropic composite structures, *Appl. Math. Model.* 112 (2022) 560–613.
- [72] J.S. Chen, C. Pan, C.T. Wu, W.K. Liu, Reproducing kernel particle methods for large deformation analysis of non-linear structures, *Comput. Methods Appl. Mech. Engrg.* 139 (1–4) (1996) 195–227.
- [73] J.S. Chen, C.T. Wu, C. Pan, A pressure projection method for nearly incompressible rubber hyperelasticity, part II: Applications, *J. Appl. Mech.* 63 (1996) 869–876.
- [74] Y. Zhu, C. Zhang, X. Hu, A dynamic relaxation method with operator splitting and random-choice strategy for SPH, *J. Comput. Phys.* (2022) 111105.
- [75] G.N. Greaves, A.L. Greer, R.S. Lakes, T. Rouxel, Poisson's ratio and modern materials, *Nature Mater.* 10 (11) (2011) 823–837.
- [76] B. Smith, F.D. Goes, T. Kim, Stable neo-hookean flesh simulation, *ACM Trans. Graph.* 37 (2) (2018) 1–15.
- [77] M. Aguirre, A.J. Gil, J. Bonet, A.A. Carreño, A vertex centred finite volume Jameson–Schmidt–Turkel (JST) algorithm for a mixed conservation formulation in solid dynamics, *J. Comput. Phys.* 259 (2014) 672–699.
- [78] C.H. Lee, A.J. Gil, A. Ghavamian, J. Bonet, A total Lagrangian upwind smooth particle hydrodynamics algorithm for large strain explicit solid dynamics, *Comput. Methods Appl. Mech. Engrg.* 344 (2019) 209–250.

A.2 Paper II

Dong Wu, Xiaojing Tang, Shuaihao Zhang, Xiangyu Hu

Unified non-hourglass formulation for total Lagrangian SPH solid dynamics

In *Computational Mechanics*, 2024, pp. 1-33, DOI: <https://doi.org/10.1007/s00466-024-02552-7>.

Copyright © 2024 Springer. Reprinted with permission.

Contribution: My contribution to this work was the development of the method and the corresponding computer code for its implementation. I performed simulations and analyzed the results, and wrote the manuscript for the publication.



Unified non-hourglass formulation for total Lagrangian SPH solid dynamics

Dong Wu¹ · Xiaojing Tang² · Shuaihao Zhang³ · Xiangyu Hu¹

Received: 10 April 2024 / Accepted: 4 September 2024
© The Author(s) 2024

Abstract

The persistence of hourglass modes poses a significant numerical instability issue in total Lagrangian smoothed particle hydrodynamics (TLSPH) solid dynamics, especially when dealing with substantial deformations, regardless of material properties. However, existing hourglass control methods have shown effectiveness only within limited applications. Thus far, a comprehensive solution capable of addressing hourglass issues across a wide range of material models, including elasticity, plasticity, and anisotropy, remains elusive. In this study, we introduce a unified TLSPH formulation grounded in volumetric-deviatoric stress decomposition, aimed at fundamentally mitigating hourglass modes in general simulations. Different conceptually from previous approaches using stress points or extra viscous or hourglass-control stresses within the momentum equation, our formulation is based on the weighted average of a standard but hourglass-prone formulation and an essentially non-hourglass formulation for elastic materials, employing a single limiter to dynamically adjust the weighting between the two formulations. Crucially, the dimensionless characteristic of the formulation enables seamless handling of complex material models. To validate the effectiveness of our formulation, we conduct simulations across a range of benchmark cases involving elastic, plastic, and anisotropic materials. To illustrate its versatility, we apply the formulation to simulate a complex scenario involving viscous plastic Oobleck material, contacts, and very large deformation. Our work addresses a critical gap in TLSPH simulations by offering a unified approach to mitigate hourglass modes, enhancing the reliability and accuracy of simulations across diverse material models and complex scenarios.

Keywords Hourglass modes · Elasticity · Plasticity · Anisotropy · Smoothed particle hydrodynamics · Total Lagrangian formulation

1 Introduction

Smoothed particle hydrodynamics (SPH), a fully Lagrangian mesh-free method, has attracted escalating interest in recent decades [1–5]. In SPH, the continuum is represented by particles, and the governing equations are discretized through particle interactions based on a Gaussian-like kernel function [6–8]. As numerous fundamental abstractions, intrinsically linked to various physical systems, can be effectively represented through particle interactions, SPH method has succeeded in addressing multi-physics problems within a unified computational framework [9, 10], including fluid–structure interaction [11–14], cardiac electrophysiology [15, 16], laser beam welding [17, 18], porous media [19–21], and various other domains. In such unified computational framework, the total Lagrangian SPH (TLSPH) formulation [22, 23] is often used to model solid dynamics.

Xiangyu Hu
xiangyu.hu@tum.de

Dong Wu
dong.wu@tum.de

Xiaojing Tang
xiaojing.tang@tum.de

Shuaihao Zhang
szhang07@connect.hku.hk

- ¹ Chair of Aerodynamics and Fluid Mechanics, Technical University of Munich, 85748 Garching, Germany
- ² Chair of Space Propulsion and Mobility, Technical University of Munich, 85521 Ottobrunn, Germany
- ³ Department of Civil Engineering, The University of Hong Kong, Pokfulam, Hong Kong SAR, China

However, the numerical instability issue of hourglass modes persists in TLSPH solid dynamics, arising from vanishing deformation gradient as particles move to a non-physical zigzag pattern, i.e., the zero-energy modes [22, 24]. Initial attempts to address the issue involve a staggered formulation, introducing extra integration or stress points [25–28]. Since the inherent complexity and the undefined methodology for the placement of these additional stress points [29] greatly limit the practical application of this staggered formulation for general problems, more recent efforts focus on enhancing the traditional SPH framework with corrective or stabilizing terms [30, 31].

A shared attribute among these terms is their integration into the momentum equation as additional force, similar to the hourglass-control stress terms in many finite element methods (FEM) [32, 33], relying on dimensional and basic material parameters, such as sound speed [34–36] or Young's modulus [30, 31, 37]. The inclusion of material parameters implies the physical relevance of the correction terms in mitigating a pure numerical instability, thereby leading to the issue of generalizing these solutions for more complex material models. For example, challenges may arise in determining optimal parameters for the presence of non-isotropic contributions in the material model, or in deciding the appropriate correction magnitude for plastic materials exhibiting complex yielding and hardening behaviors. Consequently, parameters are non-generalized, and frequently needed to be tuned on a case-by-case or material model-specific basis to avoid inadequate or excessive correction [38–42]. Thus far, a comprehensive solution capable of effectively addressing hourglass issues across a wide range of material models, including elasticity, plasticity, and anisotropy, remains elusive.

In this study, based on volumetric-deviatoric stress decomposition, we present a unified non-hourglass TLSPH formulation capable of addressing a wide array of material behaviors, from elasticity and plasticity to anisotropy and beyond. Different from the approaches using staggered formulation or extra stress points, the present method is based on standard collocation TLSPH formulation. By comparing the standard SPH formulation with the original Laplacian operator applied in our previous work [43] to handle the hourglass issues for standard elasticity, we introduce a correction in the discretization of shear stress, relying only on the dimensionless discrepancy produced by a tracing-back prediction of the initial inter-particle direction from the current deformation gradient. Compared with the one in Ref. [37], the present formulation is naturally incorporated with the standard SPH divergence operator and its dimensionless characteristic enables seamless handling of complex material models. Note that, other than introducing extra hourglass-control or viscous stress as in previous FEM, meshless or SPH methods, the present formulation is conceptually a

weighted average of two previous SPH formulations: one standard but prone to hourglass effects, and the other is from an essentially non-hourglass formulation of elastic dynamics [43], without additional stresses. By employing a limiter with a single set of dimensionless parameters to adaptively adjust the weighting, extensive benchmark examples are tested to validate the stability and accuracy of the present formulation for elastic, plastic and anisotropic materials. A complex problem, involving viscous plastic Oobleck material, contacts and very large deformation, is also simulated to illustrate the versatility of the proposed formulation.

The structure of this paper is as follows. Section 2 describes the TLSPH formulation of solid dynamics. A variety of material models applied in this study are outlined in Sect. 3, and the present formulation are detailed in Sect. 4. Numerical examples are presented and discussed in Sect. 5. In Sect. 6, brief concluding remarks are offered. To foster future in-depth investigations, all computational codes utilized in this study [9, 44] are publicly available via the SPHinXsys project website at <https://www.sphinxsys.org>.

2 Total Lagrangian SPH

In the context of the total Lagrangian framework, the kinematics and governing equations for describing the deformation of a solid body are formulated with respect to the initial, undeformed reference configuration. Subsequently, the discretization of these equations for TLSPH is detailed, and the time integration scheme is introduced.

2.1 Kinematics and governing equations

The deformation gradient tensor \mathbb{F} is given by

$$\mathbb{F} = \nabla^0 \mathbf{r} = \nabla^0 \mathbf{u} + \mathbb{I}, \quad (1)$$

where $\mathbf{u} = \mathbf{r} - \mathbf{r}^0$ is the displacement with \mathbf{r}^0 and \mathbf{r} denoting the initial and current positions of a material point, respectively, $\nabla^0 \equiv \frac{\partial}{\partial \mathbf{r}^0}$ the material gradient operator with respect to the initial configuration and \mathbb{I} the identity matrix.

The governing equations in total Lagrangian formulation can be expressed as

$$\begin{cases} \rho = J^{-1} \rho^0 \\ \rho^0 \ddot{\mathbf{u}} = \nabla^0 \cdot \mathbb{P}^T, \end{cases} \quad (2)$$

where ρ^0 and ρ are the initial and current densities, respectively, $J = \det(\mathbb{F})$, $\ddot{\mathbf{u}}$ the acceleration, \mathbb{P} the first Piola–Kirchhoff stress tensor, and \mathbb{T} the matrix transposition operator. Note that the mass continuity equation is implicitly satisfied in total Lagrangian formulation. \mathbb{P} can be obtained by the Kirchhoff stress $\boldsymbol{\tau}$ as

$$\mathbb{P} = \mathbb{F}^{-T}. \tag{3}$$

2.2 SPH discretization

Following Refs. [3, 6], the momentum conservation Eq. (2) is discretized in the weak-form SPH approximation of the spatial derivative as

$$\rho_i^0 \ddot{\mathbf{u}}_i = \sum_j \left(\mathbb{P}_i \mathbb{B}_i^{0T} + \mathbb{P}_j \mathbb{B}_j^{0T} \right) \nabla_i^0 W_{ij} V_j^0, \tag{4}$$

where $\nabla_i^0 W_{ij} = \frac{\partial W(r_{ij}^0, h)}{\partial r_{ij}^0} \mathbf{e}_{ij}^0$ denotes the gradient of the kernel function evaluated at the initial reference configuration with r_{ij}^0 representing the initial particle distance and \mathbf{e}_{ij}^0 the initial unit vector pointing from particle j to particle i . Additionally, ρ_i^0 is the initial density of particle i , and V_j^0 is the initial volume of particle j . Here, the superscript $(\cdot)^0$ is introduced to represent variables defined at the initial reference configuration. The kernel gradient correction (KGC) correction matrix \mathbb{B}^0 is adopted to ensure first-order completeness as [1, 24, 45–47]

$$\mathbb{B}_i^0 = \left(\sum_j V_j^0 (\mathbf{r}_j^0 - \mathbf{r}_i^0) \otimes \nabla_i^0 W_{ij} \right)^{-1}. \tag{5}$$

The deformation tensor \mathbb{F} is updated based on its rate of change, which is approximated in the strong-form discretization of the spatial derivative [3, 6] as

$$\frac{d\mathbb{F}_i}{dt} = \dot{\mathbb{F}}_i = \nabla^0 \dot{\mathbf{u}}_i = \sum_j V_j^0 (\dot{\mathbf{u}}_j - \dot{\mathbf{u}}_i) \otimes \nabla_i^0 W_{ij} \mathbb{B}_i^0. \tag{6}$$

In total Lagrangian framework, this is equivalent to directly calculating $\mathbb{F} = \nabla^0 \mathbf{r}$. It is worth noting that, due to the KGC correction matrix employed in Eq. (6) for computing $\dot{\mathbb{F}}_i$ [1, 24, 45–47], the rotational motion is accurately captured [45], objectivity is preserved and the ghost or artificial forces due to rigid-body rotation are eliminated [48].

Following the approach in Ref. [36], we introduce an artificial damping stress \mathbb{T}_d based on the Kelvin–Voigt type damper when calculating the Kirchhoff stress \mathbb{T} as

$$\mathbb{T}_d = \frac{\chi}{2} \frac{d\mathbb{b}}{dt}, \tag{7}$$

where the artificial viscosity factor $\chi = \rho Ch/2$ with $C = \sqrt{K/\rho}$, where K is bulk modulus, as obtained from the material models in Sect. 3, and h denoting the smoothing length. Here, $\mathbb{b} = \mathbb{F}\mathbb{F}^T$ denotes the the left Cauchy-Green deformation gradient tensor, and its change rate can be obtained directly as

$$\frac{d\mathbb{b}}{dt} = \left[\frac{d\mathbb{F}}{dt} \mathbb{F}^T + \mathbb{F} \left(\frac{d\mathbb{F}}{dt} \right)^T \right]. \tag{8}$$

Note that the artificial damping stress in Eq. (7) is proportional to the smoothing length h . As the resolution increases or static equilibrium reaches, the effect of this numerical dissipation vanishes. Also note that, since the present non-hourglass formulation presented in Sect. 4 is non-dissipative, the numerical dissipation of Eq. (7) plays the main role to ensure non-increasing of total energy.

2.3 Time integration scheme

In accordance with Ref. [23], the position-based Verlet scheme is employed for time integration. Initially, the deformation gradient tensor, density, and particle position are updated to the midpoint of n -th time step as

$$\begin{cases} \mathbb{F}^{n+\frac{1}{2}} = \mathbb{F}^n + \frac{1}{2} \Delta t \dot{\mathbb{F}}^n \\ \rho^{n+\frac{1}{2}} = \rho^0 \frac{1}{J} \\ \mathbf{r}^{n+\frac{1}{2}} = \mathbf{r}^n + \frac{1}{2} \Delta t \dot{\mathbf{u}}^n. \end{cases} \tag{9}$$

Upon calculating the Kirchhoff stress \mathbb{T}^n based on the applied constitutive relation and the artificial damping stress $\mathbb{T}_d^n = \frac{\chi}{2} \left[\dot{\mathbb{F}}^n \mathbb{F}^{n+\frac{1}{2},T} + \mathbb{F}^{n+\frac{1}{2}} \dot{\mathbb{F}}^{n,T} \right]$ and subsequently obtaining particle acceleration using Eq. (4), the velocity is updated through

$$\dot{\mathbf{u}}^{n+1} = \dot{\mathbf{u}}^n + \Delta t \ddot{\mathbf{u}}^{n+1}. \tag{10}$$

After that, the rate of change of the deformation gradient tensor $\dot{\mathbb{F}}^{n+1}$ is computed using Eq. (6). Finally, the deformation gradient tensor and particle positions are updated to a new time step with

$$\begin{cases} \mathbb{F}^{n+1} = \mathbb{F}^{n+\frac{1}{2}} + \frac{1}{2} \Delta t \dot{\mathbb{F}}^{n+1} \\ \rho^{n+1} = \rho^0 \frac{1}{J} \\ \mathbf{r}^{n+1} = \mathbf{r}^{n+\frac{1}{2}} + \frac{1}{2} \Delta t \dot{\mathbf{u}}^{n+1}. \end{cases} \tag{11}$$

Adhering to the Courant-Friedrichs-Lewy (CFL) condition and the limit under external force as referenced in Refs. [49–53], the time step size is given as

$$\Delta t = \text{CFL} \min \left(\frac{h}{C + |\dot{\mathbf{u}}|_{max}}, \sqrt{\frac{h}{|\ddot{\mathbf{u}}|_{max}}} \right), \tag{12}$$

where the CFL number is set to 0.6, as recommended in Refs. [9, 54].

3 Material models

A series of material models, covering elastic, (perfect, linear and non-linear hardening, viscous) plastic, anisotropic with fiber direction, and electrophysiologically induced active stress model, are included here for validating the proposed non-hourglass formulation. Note that the Kirchhoff stress τ used in governing Eqs. (2) and (3) are decomposed into volumetric and deviatoric components for all models.

3.1 Standard elastic material

The Kirchhoff stress τ for the standard elastic material is derived from the strain energy function [55]

$$\mathfrak{W}_e = \mathfrak{W}_v(J) + \mathfrak{W}_s(\bar{b}). \tag{13}$$

Here, the volume-preserving left Cauchy-Green deformation gradient tensor is denoted by $\bar{b} = |b|^{-\frac{1}{d}} b$. For neo-Hookean materials, the volume-dependent strain energy $\mathfrak{W}_v(J)$, with the bulk modulus K , is written as

$$\mathfrak{W}_v(J) = \frac{1}{2}K \left[\frac{1}{2}(J^2 - 1) - \ln J \right]. \tag{14}$$

The shear-dependent strain energy $\mathfrak{W}_s(\bar{b})$ is expressed as [56]

$$\mathfrak{W}_s(\bar{b}) = \frac{1}{2}G (\text{tr}(\bar{b}) - d), \tag{15}$$

where d denotes the dimension, G the shear modulus. Subsequently, the Kirchhoff stress tensor τ is obtained through partial differentiation of the strain energy function with respect to the deformation gradient \mathbb{F} as

$$\tau = \frac{\partial \mathfrak{W}_e}{\partial \mathbb{F}} \mathbb{F}^T = \frac{K}{2} (J^2 - 1) \mathbb{I} + G \text{dev}(\bar{b}), \tag{16}$$

where

$$\text{dev}(\bar{b}) = \bar{b} - \frac{1}{d} \text{tr}(\bar{b}) \mathbb{I} = |b|^{-\frac{1}{d}} \left[b - \frac{1}{d} \text{tr}(b) \mathbb{I} \right] \tag{17}$$

returns the trace-free part of \bar{b} , i.e., $\text{tr}(\text{dev}(\bar{b})) = 0$.

3.2 Plastic material

Four distinct plastic models are considered in this study, encompassing perfect, linear hardening, non-linear hardening, and viscous plastic models. We apply the classical J_2 flow theory [57] to characterize the stress-strain evolution in plasticity. According to this theory, the deformation gradient

tensor \mathbb{F} can be decomposed into its elastic volumetric part \mathbb{F}_e and plastic deviatoric part \mathbb{F}_p as [55]

$$\mathbb{F} = \mathbb{F}_e \mathbb{F}_p. \tag{18}$$

The elastic part of left Cauchy-Green tensor b_e is thus defined as $b = \mathbb{F}_e \mathbb{F}_e^T$. For plasticity analysis, the plastic right Cauchy deformation gradient tensor \mathbb{C}_p is introduced as

$$\mathbb{C}_p = \mathbb{F}_p^T \mathbb{F}_p. \tag{19}$$

The relationship between b_e and \mathbb{C}_p is described as

$$b_e = \mathbb{F} \mathbb{C}_p^{-1} \mathbb{F}^T. \tag{20}$$

The plastic behavior is governed by the deviatoric component of the Kirchhoff stress which is denoted as $\tau_{de} = G \text{dev}(\bar{b})$. To incorporate the plastic behavior, a scalar yield function $f(\tau_{de})$ is introduced. If $f(\tau_{de}) > 0$, indicating the material undergoes plasticity, τ_{de} will be mapped back by a return mapping to the yield surface, a boundary that separates elastic and plastic regions, as τ_{de}^e . The detailed algorithm of the plastic model is presented in Appendix A. It should be emphasized that the updated b_e obtained through the return mapping process can be substituted into Eq. (16) to calculate the stress τ for plastic materials by replacing b .

3.3 Holzapfel-Odgen material

The Holzapfel-Odgen model [58] considers the anisotropic nature of the muscle, such as myocardium. Following Ref [15], the strain energy function is given as

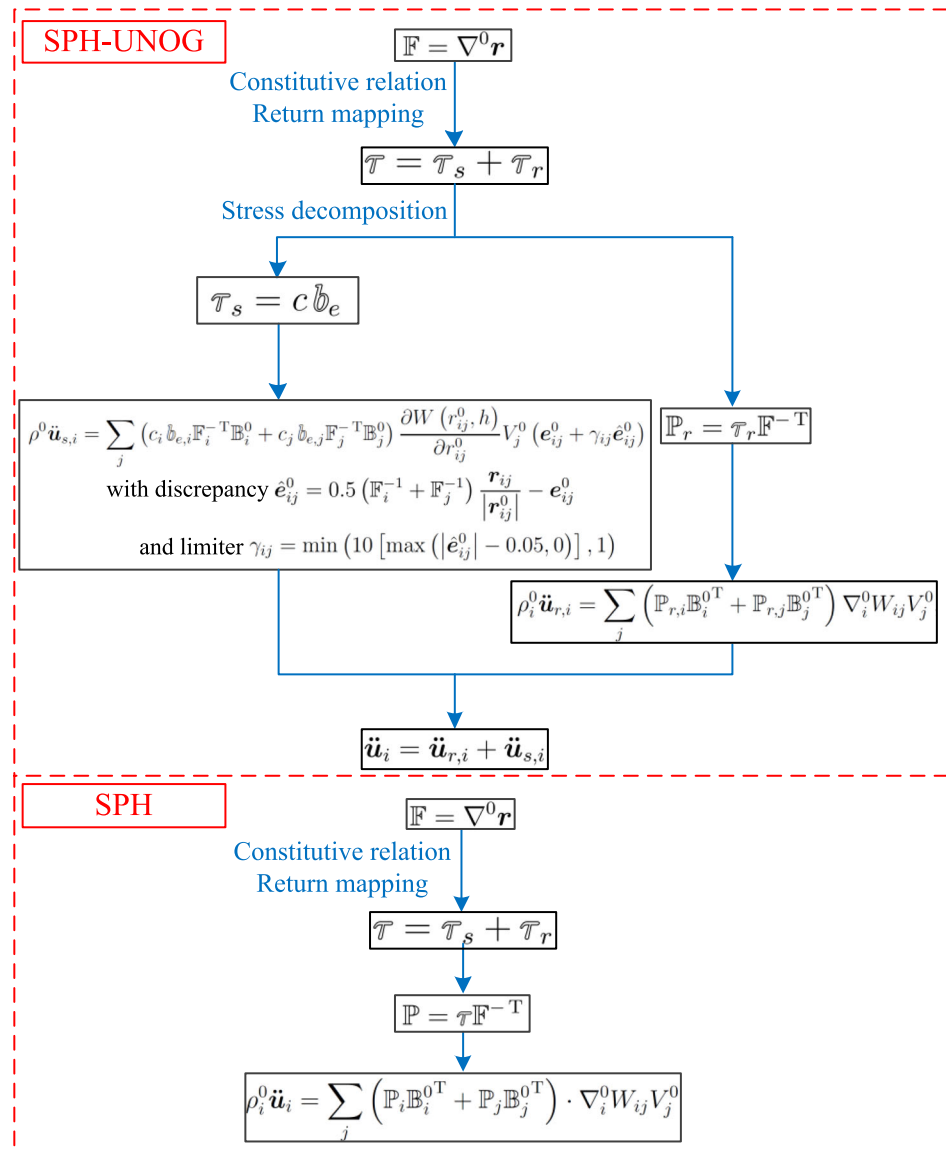
$$\begin{aligned} \mathfrak{W} = & \frac{a}{2b} \exp[b(I_1 - 3)] - a \ln J + \frac{\lambda}{2} (\ln J)^2 \\ & + \sum_{i=f,s} \frac{a_i}{2b_i} \{ \exp[b_i (I_{ii} - 1)^2] - 1 \} \\ & + \frac{a_{fs}}{2b_{fs}} \{ \exp[b_{fs} I_{fs}^2] - 1 \}, \end{aligned} \tag{21}$$

where $a, b, a_f, b_f, a_s, b_s, a_{fs}$ and b_{fs} represent eight positive material constants, and λ is a Lamé parameter. The series of parameters a have units of stress, while b are dimensionless. Here, the principle invariants are defined as

$$I_1 = \text{tr} \mathbb{C}, \quad I_2 = \frac{1}{2} [I_1^2 - \text{tr}(\mathbb{C}^2)], \quad I_3 = \det(\mathbb{C}) = J^2, \tag{22}$$

where the left Cauchy-Green deformation tensor $\mathbb{C} = \mathbb{F}^T \mathbb{F}$, and three other independent invariants associated with directional preferences are given by

Fig. 1 Flowcharts of the original total Lagrangian SPH (denoted as SPH) in Ref. [12] and present (denoted as SPH-UNOG) formulations



$$I_{ff} = \mathbb{C} : \mathbf{f}^0 \otimes \mathbf{f}^0, \quad I_{ss} = \mathbb{C} : \mathbf{s}^0 \otimes \mathbf{s}^0, \quad I_{fs} = \mathbb{C} : \mathbf{f}^0 \otimes \mathbf{s}^0, \quad (23)$$

$$\frac{\partial I_{fs}}{\partial \mathbb{C}} = \mathbf{f}_0 \otimes \mathbf{s}_0 + \mathbf{s}_0 \otimes \mathbf{f}_0, \quad (25)$$

where \mathbf{f}^0 and \mathbf{s}^0 are the undeformed muscle fiber and sheet unit direction, respectively.

The second Piola–Kirchhoff stress \mathbb{S} can be derived by

$$\begin{aligned} \mathbb{S} &= 2 \frac{\partial \mathfrak{W}}{\partial \mathbb{C}} - p \mathbb{C}^{-1} \\ &= 2 \sum_j \frac{\partial \mathfrak{W}}{\partial I_j} \frac{\partial I_j}{\partial \mathbb{C}} - p \mathbb{C}^{-1} \quad j = 1, ff, ss, fs, \end{aligned} \quad (24)$$

where

$$\frac{\partial I_1}{\partial \mathbb{C}} = \mathbb{I}, \quad \frac{\partial I_{ff}}{\partial \mathbb{C}} = \mathbf{f}_0 \otimes \mathbf{f}_0, \quad \frac{\partial I_{ss}}{\partial \mathbb{C}} = \mathbf{s}_0 \otimes \mathbf{s}_0,$$

and $p = \frac{\partial \mathfrak{W}}{\partial J}$ serves as the Lagrange multiplier introduced to enforce incompressibility. Substituting Eqs. (21) and (25) into Eq. (24) and applying $\mathbb{T} = \mathbb{F} \mathbb{S} \mathbb{F}^T$, the Kirchhoff stress \mathbb{T} is obtained as

$$\begin{aligned} \mathbb{T} &= \{\lambda \ln J - a\} \mathbb{I} + a \exp[b(I_1 - 3)] \mathbb{b} \\ &\quad + 2a_f (I_f - 1) \exp[b_f (I_f - 1)^2] \mathbb{F}(\mathbf{f}_0 \otimes \mathbf{f}_0) \mathbb{F}^T \\ &\quad + 2a_s (I_s - 1) \exp[b_s (I_s - 1)^2] \mathbb{F}(\mathbf{s}_0 \otimes \mathbf{s}_0) \mathbb{F}^T \\ &\quad + a_f s I_{fs} \exp[b_{fs} (I_{fs})^2] \mathbb{F}(\mathbf{f}_0 \otimes \mathbf{s}_0 + \mathbf{s}_0 \otimes \mathbf{f}_0) \mathbb{F}^T. \end{aligned} \quad (26)$$

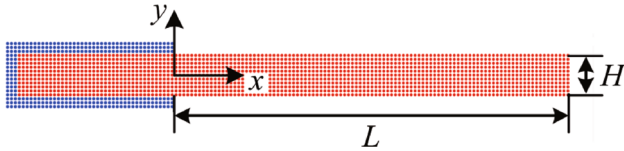


Fig. 2 Oscillating plate: Initial configuration

3.4 Electrophysiologically induced active stress model

Building on the methodology outlined in Refs [15, 59], we incorporate the stress tensor with the transmembrane potential V_m using the active stress approach. This approach decomposes the Kirchhoff stress τ into passive and active components as

$$\tau = \tau_{passive} + \tau_{active}, \tag{27}$$

where the passive component $\tau_{passive}$ describes the stress required to achieve a given passive muscle deformation, which is modeled by the above-mentioned Holzapfel-Odgen material, and the active component τ_{active} denotes the tension activated by the depolarization of the propagating transmembrane potential. Following the active stress approach proposed in Ref. [59], the active component is obtained as

$$\tau_{active} = T_a \mathbb{F} f_0 \otimes f_0 \mathbb{F}^T, \tag{28}$$

where T_a represents the active muscle contraction stress.

4 Unified non-hourglass formulation

Since the hourglass modes exhibit very large local, especially shear, deformation [43], we introduce a correction term in the discretization of shear-stress term to suppress this instability. We first decompose the Kirchhoff stress by considering the material model aforementioned in Sect. 3 as dummy

$$\tau = \tau_s + \tau_r. \tag{29}$$

Here, the first term of the right-hand side $\tau_s = c \mathbb{b}_e$, with $c = |\mathbb{b}_e|^{-\frac{1}{d}} G$ for elastic and plastic materials and $c = a \exp[b(I_1 - 3)]$ for muscle model, contains the main shear stress components, and the second term gives the remaining Kirchhoff stress. For example, $\tau_r = \frac{K}{2} (J^2 - 1) \mathbb{I} - \frac{1}{d} |\mathbb{b}_e|^{-\frac{1}{d}} G \text{tr}(\mathbb{b}_e) \mathbb{I} + \tau_d$ for the elastic and plastic materials applied in this study. Note that $\mathbb{b}_e = \mathbb{b}$ for elastic deformation, including those in the muscle models.

For standard elastic material, the shear part of the first Piola–Kirchhoff stress $\mathbb{P}_s = \tau_s \mathbb{F}^{-T} = c \mathbb{b} \mathbb{F}^{-T}$, and the par-

Table 1 Oscillating plate: Quantitative validation of the oscillation period for $L = 0.2$ m and $H = 0.02$ m with various v_f and ν

v_f	ν	$T_{\text{SPH-UNOG}}$	$T_{\text{Theoretical}}$	Error (%)
0.05	0.22	0.29324	0.27009	8.57
0.1	0.22	0.29223	0.27009	8.20
0.15	0.22	0.29221	0.27009	8.19
0.05	0.30	0.28212	0.26412	6.82
0.1	0.30	0.28096	0.26412	6.38
0.15	0.30	0.28083	0.26412	6.33
0.05	0.40	0.26589	0.25376	4.78
0.1	0.40	0.26483	0.25376	4.36
0.15	0.40	0.26767	0.25376	5.48

Table 2 Oscillating plate: Quantitative validation of the oscillation period for $L = 0.2$ m and $H = 0.01$ m with various v_f and ν

v_f	ν	$T_{\text{SPH-UNOG}}$	$T_{\text{Theoretical}}$	Error (%)
0.05	0.22	0.56959	0.54018	5.44
0.1	0.22	0.56151	0.54018	3.95
0.15	0.22	0.56126	0.54018	3.90
0.05	0.30	0.54541	0.52824	3.25
0.1	0.30	0.53859	0.52824	1.96
0.15	0.30	0.53719	0.52824	1.69
0.05	0.40	0.51230	0.50752	0.94
0.1	0.40	0.50690	0.50752	0.12
0.15	0.40	–	–	–

ticle acceleration induced by the shear stress can be obtained by the standard SPH method as follows

$$\rho_i^0 \ddot{u}_{s,i} = \sum_j (c_i \mathbb{b}_i \mathbb{F}_i^{-T} + c_j \mathbb{b}_j \mathbb{F}_j^{-T}) \frac{\partial W(r_{ij}^0, h)}{\partial r_{ij}^0} V_j^0 \mathbf{e}_{ij}^0, \tag{30}$$

which may suffer from serious hourglass modes. To obtain an essentially non-hourglass formulation as proposed in our previous study [43], the discretization for shear acceleration is instead obtained by applying a non-nested Laplacian formulation with the help of Kirchhoff stress decomposition as

$$\rho_i^0 \ddot{u}_{s,i} = \sum_j (c_i + c_j) \frac{\mathbf{r}_{ij}}{r_{ij}^0} \frac{\partial W(r_{ij}^0, h)}{\partial r_{ij}^0} V_j^0. \tag{31}$$

Note that, although it is proved theoretically in Ref. [43] that Eq. (31) ensures non-increasing of elastic energy, it is essentially a non-dissipative formulation. By using the entity

$\mathbb{F}\mathbb{F}^{-1} = \mathbb{I}$ and $\mathbb{b} = \mathbb{F}\mathbb{F}^T$, one can reformulate Eq. (31) approximately as

$$\rho_i^0 \ddot{u}_{s,i} = \sum_j (c_i \mathbb{b}_i \mathbb{F}_i^{-T} + c_j \mathbb{b}_j \mathbb{F}_j^{-T}) \frac{\partial W(r_{ij}^0, h)}{\partial r_{ij}^0} v_j^0 \left[\frac{1}{2} (\mathbb{F}_i^{-1} + \mathbb{F}_j^{-1}) \frac{\mathbf{r}_{ij}}{r_{ij}^0} \right]. \quad (32)$$

Comparing Eqs. (30) and (32), one can observe that a tracing-back prediction of the initial inter-particle direction

from the current deformation gradient is

$$\mathbf{e}_{ij}^0 \approx \frac{1}{2} (\mathbb{F}_i^{-1} + \mathbb{F}_j^{-1}) \frac{\mathbf{r}_{ij}}{r_{ij}^0}. \quad (33)$$

Such prediction is exact when the deformation is linear, but produces discrepancy for general, especially large deforma-

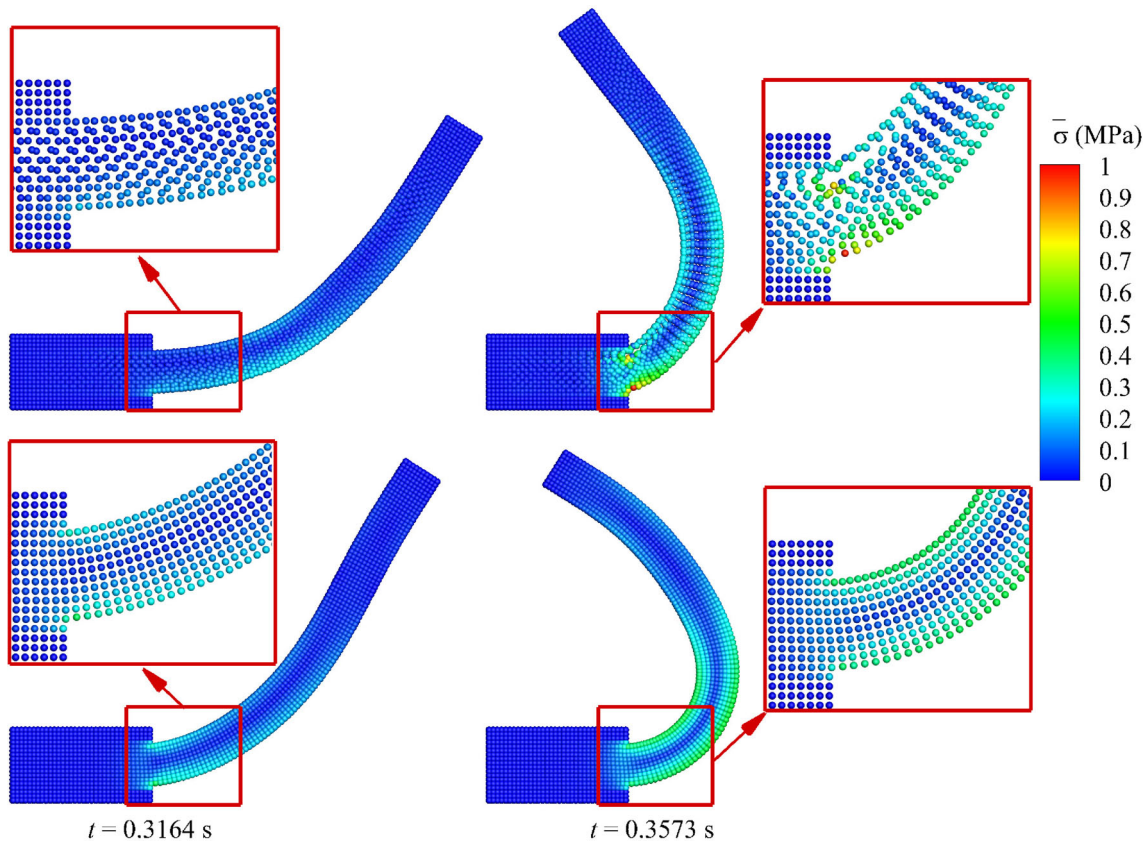
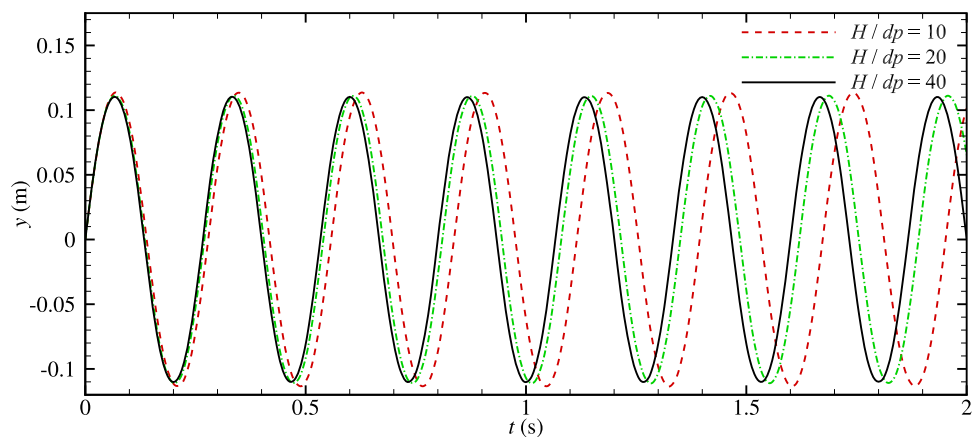


Fig. 3 Oscillating plate: Comparison of the deformed configuration colored by von Mises stress $\bar{\sigma}$ at two time instants obtained by the SPH (top panel) and SPH-UNOG (bottom panel) with the length $L = 0.2$ m,

height $H = 0.02$ m, $v_f = 0.15$, and spatial particle discretization $H/dp = 10$. The material is modeled with density $\rho_0 = 1000.0$ kg/m³, Young's modulus $E = 2.0$ MPa, and Poisson's ratio $\nu = 0.3975$

Fig. 4 Oscillating plate: Time history of the vertical position y observed at the midpoint of the plate strip end obtained by SPH-UNOG in the long term with the length $L = 0.2$ m, height $H = 0.02$ m and $v_f = 0.05$. The material is modeled with density $\rho_0 = 1000.0$ kg/m³, Young's modulus $E = 2.0$ MPa and Poisson's ratio $\nu = 0.3975$. Note that dp is the initial particle spacing. Also note that vanished damping of the oscillation magnitude even for the case with the lowest resolution



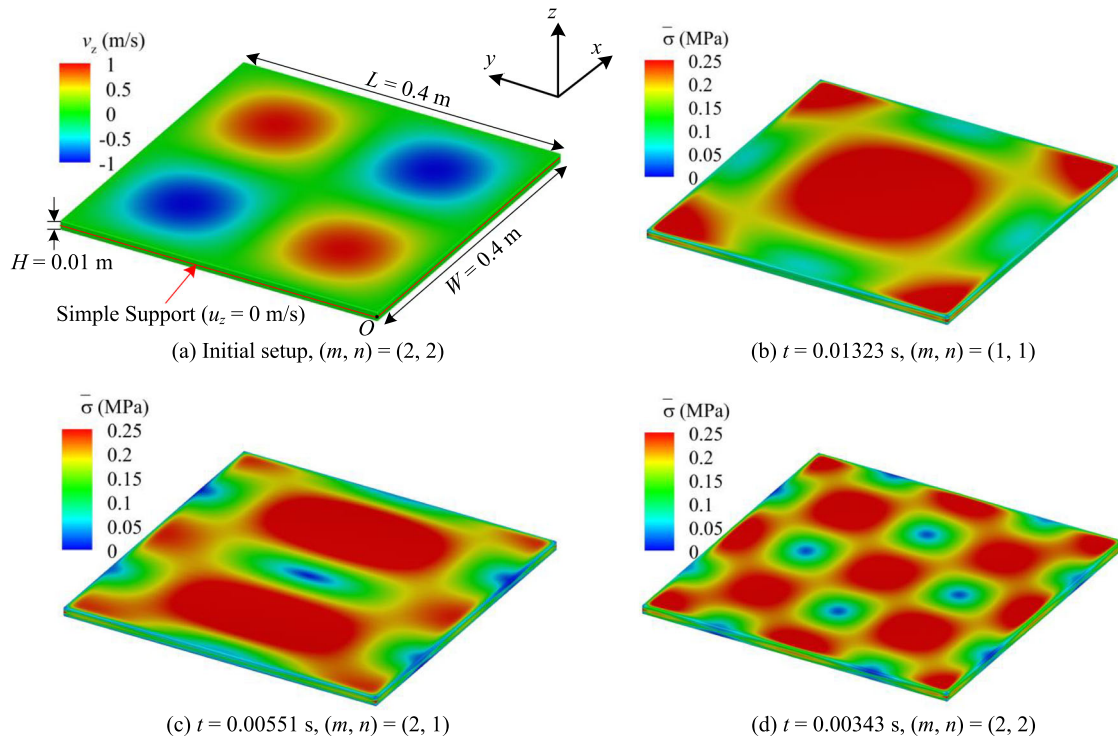


Fig. 5 3D oscillating plate: **a** Schematic of initial setup for the case of $(m, n) = (2, 2)$, **b–d** deformed configuration colored by von Mises stress $\bar{\sigma}$ for the vibration modes of $(m, n) = (1, 1)$, $(2, 1)$ and $(2, 2)$ at the quarter-period time point obtained by the SPH-UNOG with the

length and width $L = W = 0.4$ m, height $H = 0.01$ m, and spatial particle discretization $H/dp = 9$. The material is modeled with density $\rho_0 = 1000.0$ kg/m³, Young’s modulus $E = 100.0$ MPa and Poisson’s ratio $\nu = 0.3$

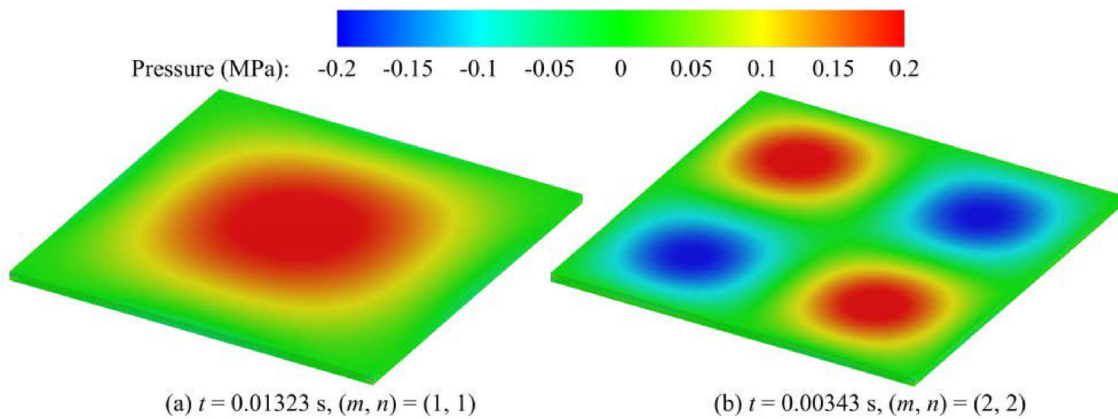


Fig. 6 3D oscillating plate: Deformed configuration colored by pressure for the vibration modes of $(m, n) = (1, 1)$ and $(2, 2)$ at the quarter-period time point obtained by the SPH-UNOG with the spatial particle discretization $H/dp = 9$

tions. Since Eq. (30) is prone to hourglass modes and Eq. (31) essentially free of them, one can incorporate a correction term into Eq. (30) based on the discrepancy as

$$V_j^0 \left(e_{ij}^0 + \gamma_{ij} \hat{e}_{ij}^0 \right), \tag{34}$$

where

$$\rho^0 \ddot{u}_{s,i} = \sum_j \left(c_i b_i \mathbb{F}_i^{-T} + c_j b_j \mathbb{F}_j^{-T} \right) \frac{\partial W \left(r_{ij}^0, h \right)}{\partial r_{ij}^0}$$

$$\hat{e}_{ij}^0 = \frac{1}{2} \left(\mathbb{F}_i^{-1} + \mathbb{F}_j^{-1} \right) \frac{\mathbf{r}_{ij}}{r_{ij}^0} - e_{ij}^0, \tag{35}$$

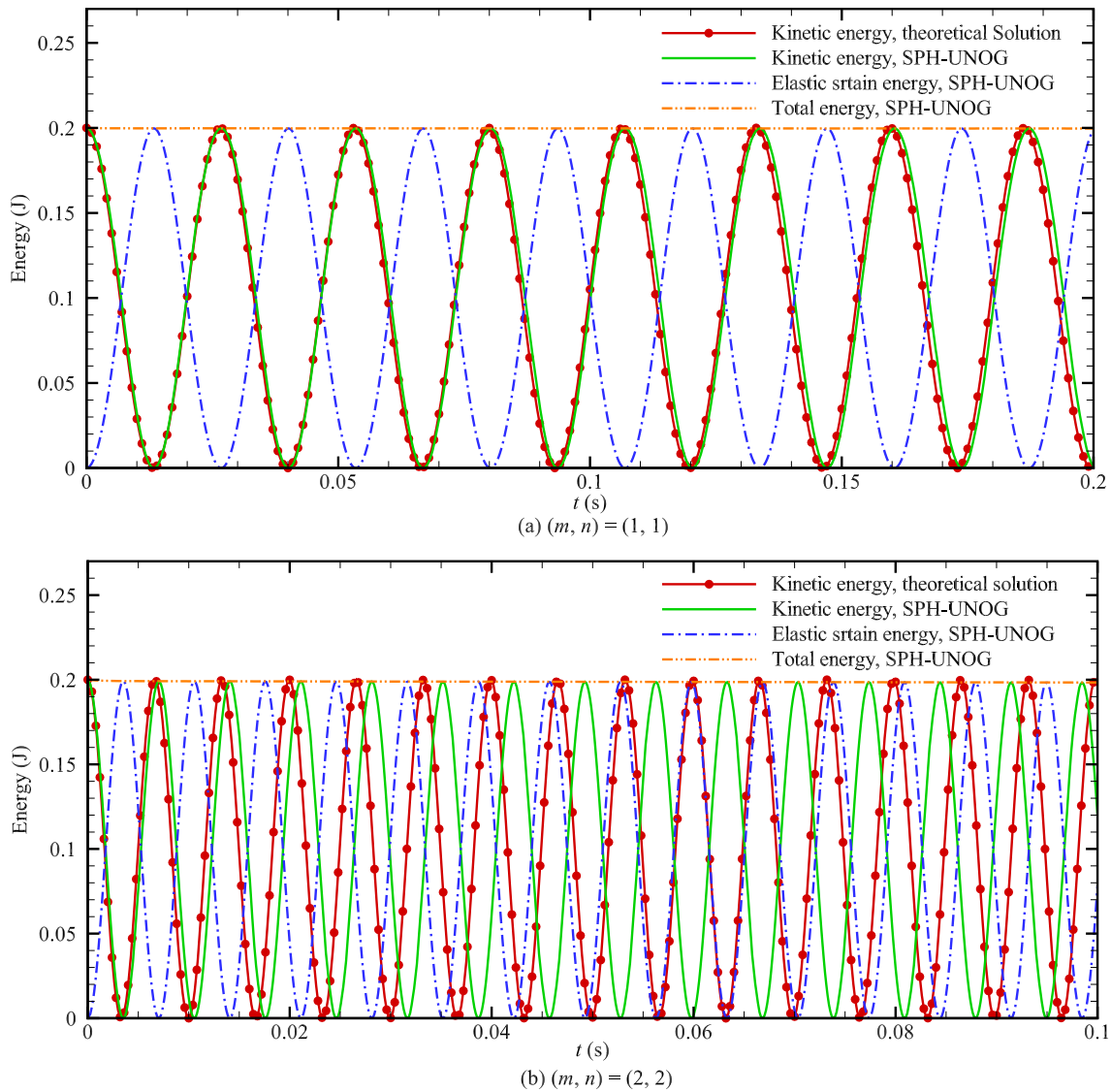


Fig. 7 3D oscillating plate: Time history of the kinetic, elastic strain and total energy for the vibration mode of $(m, n) = (1, 1)$ and $(2, 2)$ obtained by the SPH-UNOG in the long term with the spatial particle

discretization $H/dp = 9$, and the kinetic energy is compared with that of the theoretical solution for both modes and SPH for the mode of $(m, n) = (2, 2)$

and

$$\gamma_{ij} = \min \left(10 \left[\max \left(\left| \hat{e}_{ij}^0 \right| - 0.05, 0 \right) \right], 1 \right). \tag{36}$$

Here, γ_{ij} serves as a magnitude limiter. It is easy to find that Eq. (34) is a reformulation of the weighted average of Eqs. (30) and (32). The formulation is essentially the standard discretization Eq. (30) when the discrepancy $\left| \hat{e}_{ij}^0 \right|$ is less than 0.05 until which the hourglass modes are not noticeable, and then linearly increases the weight of the non-hourglass discretization Eq. (32). When the discrepancy $\left| \hat{e}_{ij}^0 \right|$ reaches 0.15 and beyond, suggesting that the hourglass modes are substantial, the formulation is essentially Eq. (32). Such

weighted-average form conceptually identifies the present formulation from previous FEM, meshless or SPH methods [30–37] as neither Eqs. (30) nor (32) is a dissipative formulation or relevant to extra hourglass-control or viscous stress. As will also be shown in Sections. 5.1 and 5.2, such non-dissipative characteristic also aligns with the second law of thermodynamics, and able to preserve oscillation magnitude and total energy in long-time simulations, even with low resolution.

Note that the correction term is purely numerical, and vanishes as the discrepancy decreases with increasing the resolution of discretization. Also note that the correction term, being dimensionless and purely geometric, is independent of

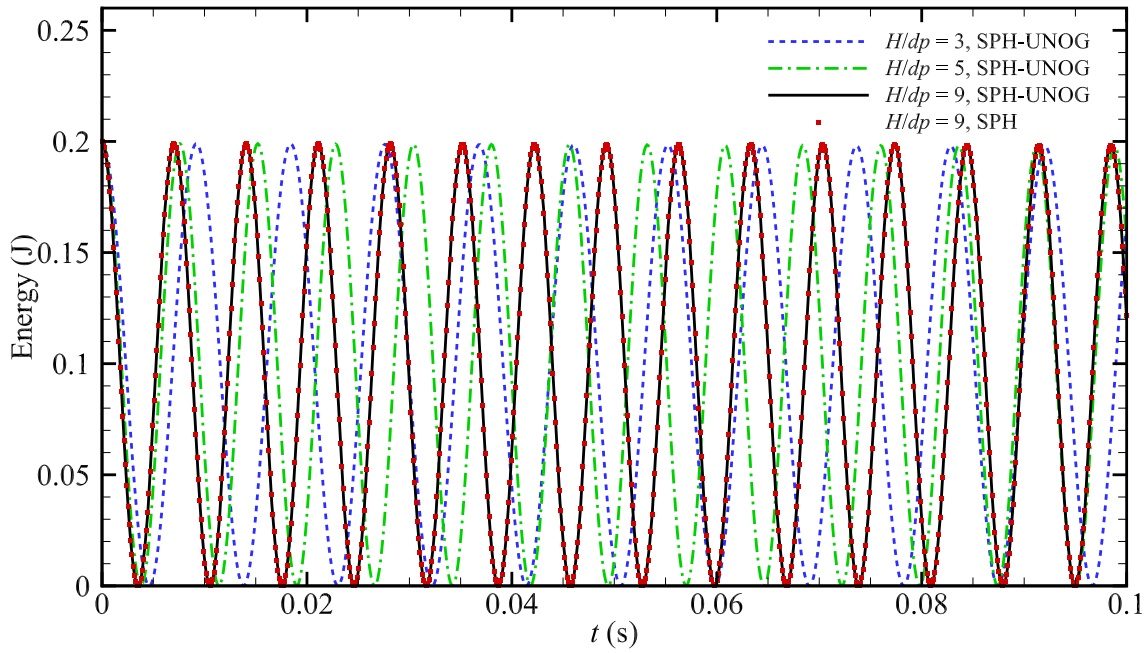


Fig. 8 3D oscillating plate: Time history of the kinetic energy for the vibration mode of $(m, n) = (2, 2)$ obtained by the SPH-UNOG in the long term under three spatial particle resolutions, and its comparison with that obtained by the SPH when $H/dp = 9$

Table 3 3D Oscillating plate: Quantitative validation of the oscillation period for vibration modes of $(m, n) = (1, 1), (2, 1)$ and $(2, 2)$ with three different spatial resolutions

SPH-UNOG	$H/dp = 3$	$H/dp = 5$	$H/dp = 9$	Theoretical
$(m, n) = (1, 1)$	0.0662058	0.0571145	0.0535212	0.0532208
$(m, n) = (2, 1)$	0.0290619	0.0240839	0.0222732	0.0212883
$(m, n) = (2, 2)$	0.0184439	0.0151971	0.0139816	0.0133052

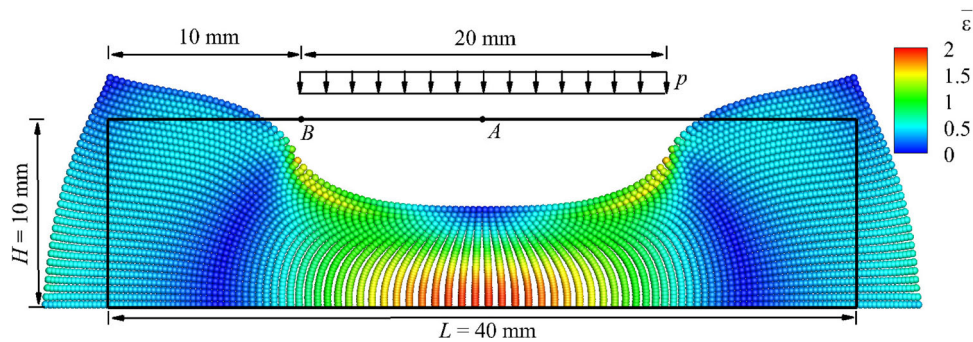


Fig. 9 Punching test: Geometry, loading and deformed configuration colored by von Mises strain $\bar{\epsilon}$ obtained by SPH-UNOG under $p = 400$ N/mm

the material model, which can be implemented in a straightforward way by simply extending \mathbb{b} to \mathbb{b}_e in Eq. (34), enabling seamless handling of complex material models. For example, \mathbb{b}_e can be obtained through return mapping as shown in Algorithm 1 for plastic materials. Therefore, together with the correction matrix \mathbb{B}^0 of Eq. (5) fulfilling the first-order completeness, the unified non-hourglass formulation can be written as

$$\rho^0 \ddot{\mathbf{u}}_{s,i} = \sum_j \left(c_i \mathbb{b}_{e,i} \mathbb{F}_i^{-T} \mathbb{B}_i^0 + c_j \mathbb{b}_{e,j} \mathbb{F}_j^{-T} \mathbb{B}_j^0 \right) \frac{\partial W(r_{ij}^0, h)}{\partial r_{ij}^0} \mathbf{V}_j^0 \left(\mathbf{e}_{ij}^0 + \gamma_{ij} \hat{\mathbf{e}}_{ij}^0 \right). \tag{37}$$

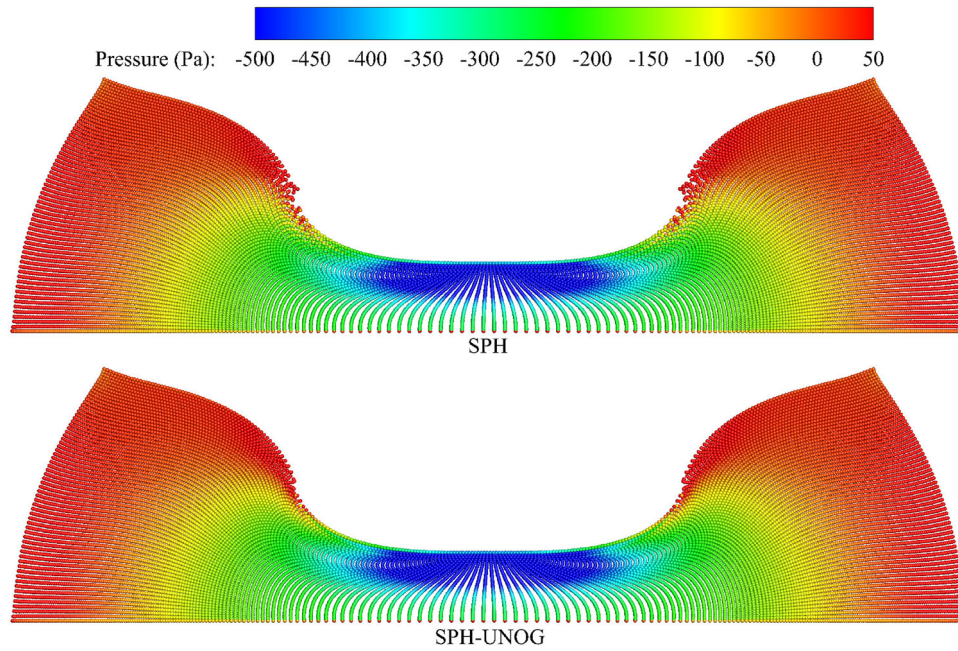


Fig. 10 Punching test: Deformed configuration colored by pressure obtained by the SPH (top panel) and SPH-UNOG (bottom panel) with initial load $p = 800$ N/mm. The spatial particle discretization is $H/dp = 2^6$

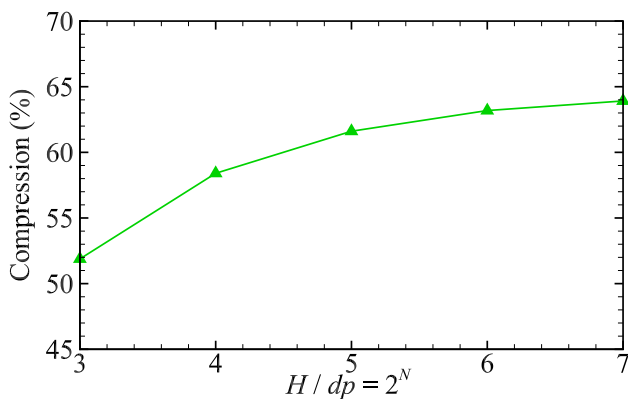


Fig. 11 Punching test: Convergence study of the compression percentage obtained using the present method with particle refinement

With $\mathbb{P}_r = \mathbb{T}_r \mathbb{F}^{-T}$ at hand, the acceleration $\ddot{\mathbf{u}}_{r,i}$ of particle i , resulting from the remaining stress $\mathbb{T}_{r,i}$, is calculated using the Eq. (4) with \mathbb{P}_r substituted for \mathbb{P} . Finally, the acceleration of particle i is expressed as

$$\ddot{\mathbf{u}}_i = \ddot{\mathbf{u}}_{r,i} + \ddot{\mathbf{u}}_{s,i}. \tag{38}$$

For clarity, the flowcharts for the original and present SPH formulations are given, respectively, in Fig. 1.

5 Numerical examples

In this section, we conduct a series of benchmark tests with available analytical or numerical reference data from the lit-

erature to qualitatively and quantitatively assess the accuracy and stability of the proposed unified non-hourglass formulation (denoted as SPH-UNOG). For comparison, we also consider the original standard SPH formulation. Following the validation, we explore the deformation of a complex problem of Oobleck octopus to showcase the potential of the present formulation. The 5th-order Wendland kernel [60], characterized by a smoothing length of $h = 1.15dp$ (where dp denotes the initial particle spacing) and a cut-off radius of $2.3dp$, is employed throughout.

5.1 2D Oscillating plate

First, we examine the oscillation of a thin plate with one edge fixed while the other edges remain free. This classical problem has been extensively explored both theoretically [61] and numerically [43, 62] in the literature. The problem is represented as a plane strain scenario, modeling a 2D plate strip of length $L = 0.2$ m, perpendicular to the fixed edge, with a thickness of $H = 0.02$ m. In accordance with previous studies [43, 62], the plate strip is clamped between several layers of constrained SPH particles, as depicted in Fig. 2. The initial velocity, denoted as v_y and directed perpendicular to the plate strip, is prescribed as follows

$$v_y(x) = v_f c \frac{f(x)}{f(L)}, \tag{39}$$

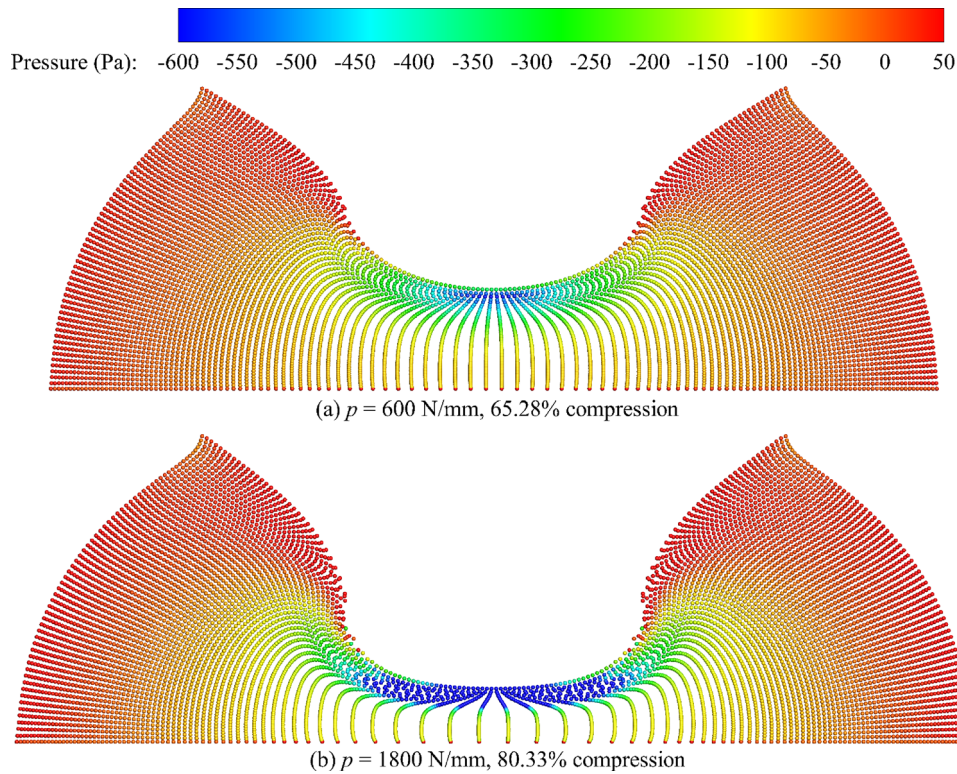


Fig. 12 Punching test: Deformed configuration colored by pressure obtained by the SPH-UNOG with initial load $p = 600$ and 1800 N/mm. The spatial particle discretization is $H/dp = 2^6$

where v_f represents a constant that varies among different cases, and

$$f(x) = (\sin(kL) + \sinh(kL))(\cos(kx) - \cosh(kx)) - (\cos(kL) + \cosh(kL))(\sin(kx) - \sinh(kx)) \quad (40)$$

with k determined by

$$\cos(kL) \cosh(kL) = -1 \quad (41)$$

and $kL = 1.875$. The material properties are defined as follows: density $\rho_0 = 1000.0$ kg/m³, Young’s modulus $E = 2.0$ MPa and Poisson’s ratio ν varies for different cases. The theoretical expression for the frequency ω of the oscillating plate is provided by

$$\omega^2 = \frac{EH^2k^4}{12\rho(1-\nu^2)} \quad (42)$$

Figure 3 depicts the deformed particle configuration, accompanied by the von Mises stress $\bar{\sigma}$ contour, simulated by both SPH and SPH-UNOG under $v_f = 0.15$ and Poisson’s ratio $\nu = 0.3975$. It can be noted that, the SPH results exhibit particle disorder under large deformation, evident in top panel of Fig. 3, especially in the vicinity of maximum stress. As the plate strip undergoes larger deformation, an increasing number of particle pairs adhere together. In contrast, SPH-UNOG mitigates such instability, exhibiting smooth deformation and stress fields.

Table 4 Punching test: The compression percentage for the specimen with dimensions $L = 20$ mm, $H = 10$ mm and spatial particle discretization $H/dp = 2^7$, and its comparison to the results presented in Ref. [66]

p (N/mm)	Compression of SPH-UNOG (%)	Compression [66] (%)	Error (%)
100	22.70045	23.85155	4.83
200	38.10087	39.61885	3.83
300	49.65808	49.84955	0.38
400	56.96744	56.64995	0.56
500	61.77618	61.52457	0.41
600	65.27827	65.13541	0.22

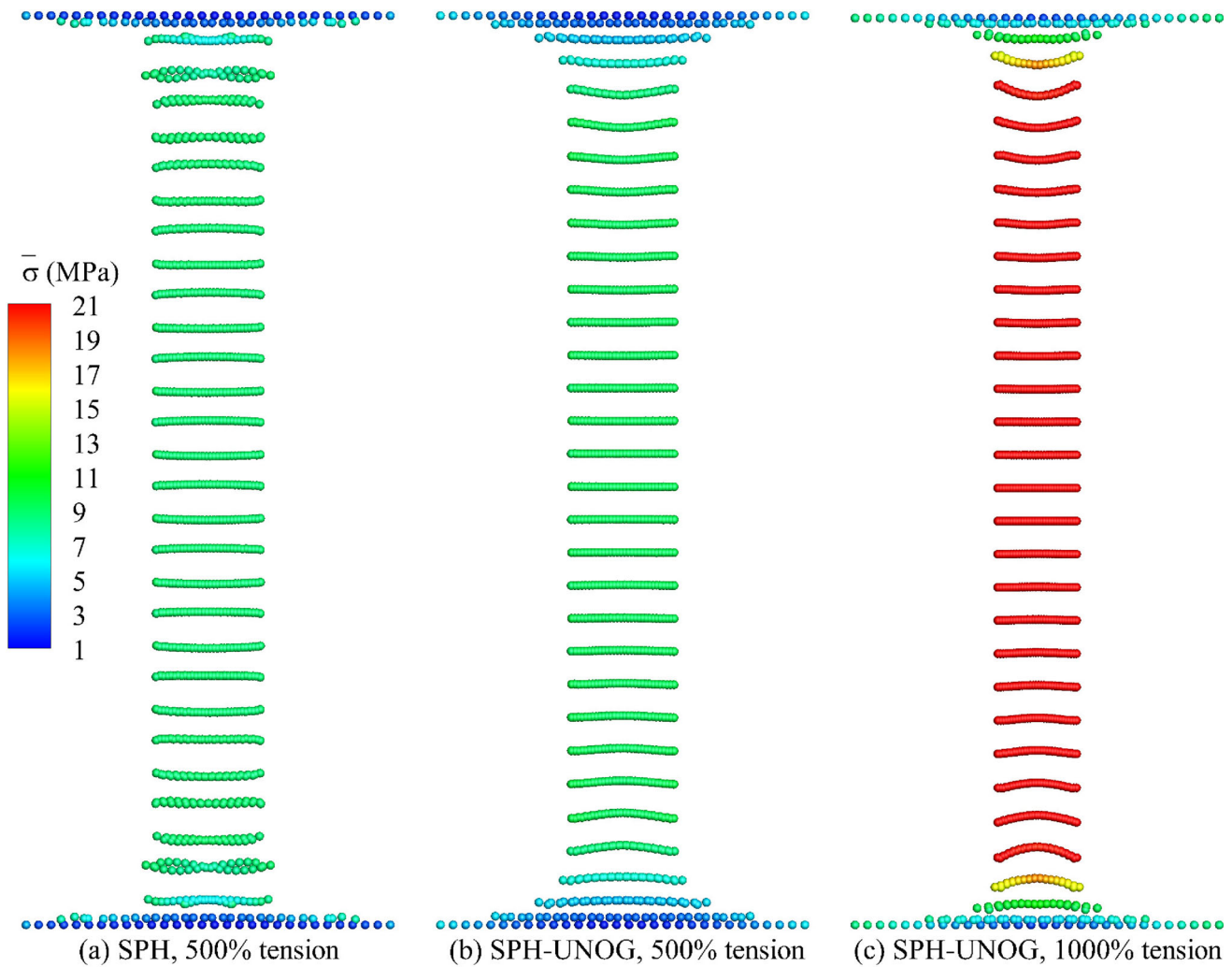
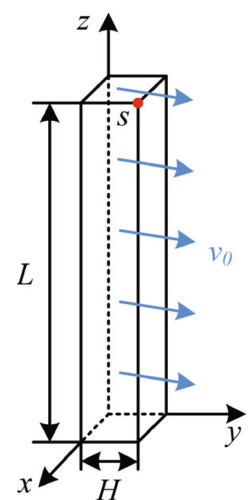


Fig. 13 Pulling test: Deformed configuration plotted with von Mises stress $\bar{\sigma}$ and scaled in the vertical direction for clarity. The material parameters are of density $\rho_0 = 1100 \text{ kg/m}^3$, Young’s modulus $E = 1.0 \text{ GPa}$ and Poisson’s ratio $\nu = 0.45$, and the spatial particle discretization is set as $L/dp = 30$

In order to validate the accuracy of present formulation, a convergence study and comparisons between numerical and theoretical solutions are undertaken. The convergence study involves testing three distinct spatial resolutions: $H/dp = 10$, $H/dp = 20$, and $H/dp = 40$. The time history of vertical position y of the midpoint at the end of the strip, with $v_f = 0.05$, is illustrated in Fig. 4. It can be observed that the discrepancies among various solutions diminish rapidly as the spatial resolution increases. Furthermore, a long-term simulation is conducted herein to underscore the numerical stability of the proposed formulation.

For quantitative validation, oscillation period T obtained by SPH-UNOG with a spatial particle resolution of $H/dp = 40$ are presented in Table 1. A comparison is made with theoretical solutions across a broad range of v_f and ν . The error remains below 9.00% for $\nu = 0.22$ and decreases to approximately 5.00% as the Poisson’s ratio is increased

Fig. 14 Bending column: Initial configuration



to 0.4. Considering the assumption of a very small thickness in the analytical theory, Table 2 presents a comparison

Table 5 Bending column: Parameters for the Holzapfel-Ogden material model. Note that the anisotropic terms are set to zero for the isotropic material

$a = 5.86 \text{ MPa}$	$a_f = ka$	$a_s = 0.0$	$a_{fs} = 0.0$
$b = 1.0$	$b_f = 0.0$	$b_s = 0.0$	$b_{fs} = 0.0$

where the length L remains the same while the thickness H is reduced to half of its previous value. A significantly improved agreement is achieved, with the maximum error decreasing to less than 1.0% for $\nu = 0.4$. Noted that when $\nu_f = 0.15$ and $\nu = 0.4$, the deformation becomes substantial, leading to the plate coming into contact with the constrained base. Consequently, the period of the plate in this scenario is not informative.

5.2 3D oscillating plate

In this section, the oscillation of a 3D thin plate is further explored with a simple support boundary condition applied to all lateral edges. Following the setups in Refs. [63–65], a square plate is modeled with length and width $L = W = 0.4 \text{ m}$ and height $H = 0.01 \text{ m}$, as illustrated in Fig. 5a. The simple support boundary condition is imposed on the center line of the lateral faces, where the corresponding particles are fixed in the z direction. The initial vertical velocity v_z is specified by

$$v_z(x, y) = \sin \frac{m\pi x}{L} \sin \frac{n\pi y}{W}, \tag{43}$$

where m and n are integers controlling the x - and y -directional vibration modes, respectively. The material properties are specified as follows: density $\rho_0 = 1000.0 \text{ kg/m}^3$, Young’s modulus $E = 100.0 \text{ MPa}$, and Poisson’s ratio $\nu = 0.3$. The theoretical vibration period of the plate is determined by

$$T = \frac{2}{\pi} \left[\left(\frac{m}{L} \right)^2 + \left(\frac{n}{W} \right)^2 \right]^{-1} \sqrt{\frac{\rho_0 H}{D}}, \tag{44}$$

where

$$D = \frac{EH^3}{12(1-\nu^2)} \tag{45}$$

denotes the flexural rigidity.

Figure 5b–d displays the deformed particle configuration with von Mises stress contour obtained by the SPH-UNOG for the vibration modes of $(m, n) = (1, 1), (2, 1),$ and $(2, 2)$, with a spatial resolution of $H/dp = 9$. Using the same setup, Fig. 6 illustrates the deformed particle configuration colored by pressure for the vibration modes of $(m, n) = (1, 1)$ and

$(2, 2)$, showcasing similarity with those observed in the literature (refer to Fig. 2 in Ref. [64]), verifying that the current formulation effectively prevents the accumulation of spurious modes.

In all scenarios, the SPH-UNOG method successfully captures smooth deformation and stress fields, demonstrating its numerical stability and robustness. Figure 7 presents the kinetic, elastic strain, and total energy for the vibration modes of $(m, n) = (1, 1)$ and $(2, 2)$. The kinetic energy profiles are compared with the theoretical solutions. Considering that the theoretical solution assumes the plate to be thin enough to neglect shear deformation [63], the numerical periods are estimated with acceptable phase error compared to the theoretical solutions, similar to the findings in Ref.

[64] (see their Fig. 3(b)) and the numerical results of the 2D oscillating plate. Notably, SPH-UNOG accurately estimates the kinetic energy profiles, and exhibits only a 0.18% reduction in oscillation amplitude after 3.5 periods for the case of $(m, n) = (1, 1)$, and a 0.83% reduction after 7 periods for $(m, n) = (2, 2)$. In Fig. 8, the comparison of kinetic energy obtained by SPH-UNOG and SPH is presented. It is evident that SPH-UNOG does not introduce extra numerical dissipation, suggesting that the numerical dissipation primarily arises from the employed numerical damping term, i.e., Eq. 7.

A convergence study and quantitative validation are conducted to demonstrate the accuracy of the present formulation. The convergence study tests three different spatial resolutions, namely $H/dp = 3, H/dp = 5,$ and $H/dp = 9,$ for the vibration modes of $(m, n) = (1, 1), (2, 1),$ and $(2, 2)$. Figure 8 illustrates that the periods of the oscillations converge rapidly, approaching 2nd-order rate, with increasing resolution for $(m, n) = (2, 2)$, while Table 3 summarizes the periods of the oscillations, demonstrating their good agreements with the theoretical values. Given that the present formulation achieves a maximum of second-order accuracy [52], the observed 2nd-order convergence rate confirms this level of accuracy, indicating the applied Kelvin–Voigt type viscous damping does not impact the order of convergence noticeably.

5.3 Punching test

A classical punch test, as referenced in [66, 67], is depicted schematically in Fig. 9. The test involves a rectangular specimen with dimensions $L = 40 \text{ mm}$ in length and $H = 10 \text{ mm}$ in height. This specimen is subjected to a vertically applied load $p \text{ (N/mm)}$ that is uniformly distributed across half of the top edge’s length. The top is constrained horizontally, while the bottom is fixed in the vertical direction. The material considered is an incompressible neo-Hookean type, characterized by the shear modulus $G = 80 \text{ N/mm}^2$ and Poisson’s ratio $\nu = 0.49$.

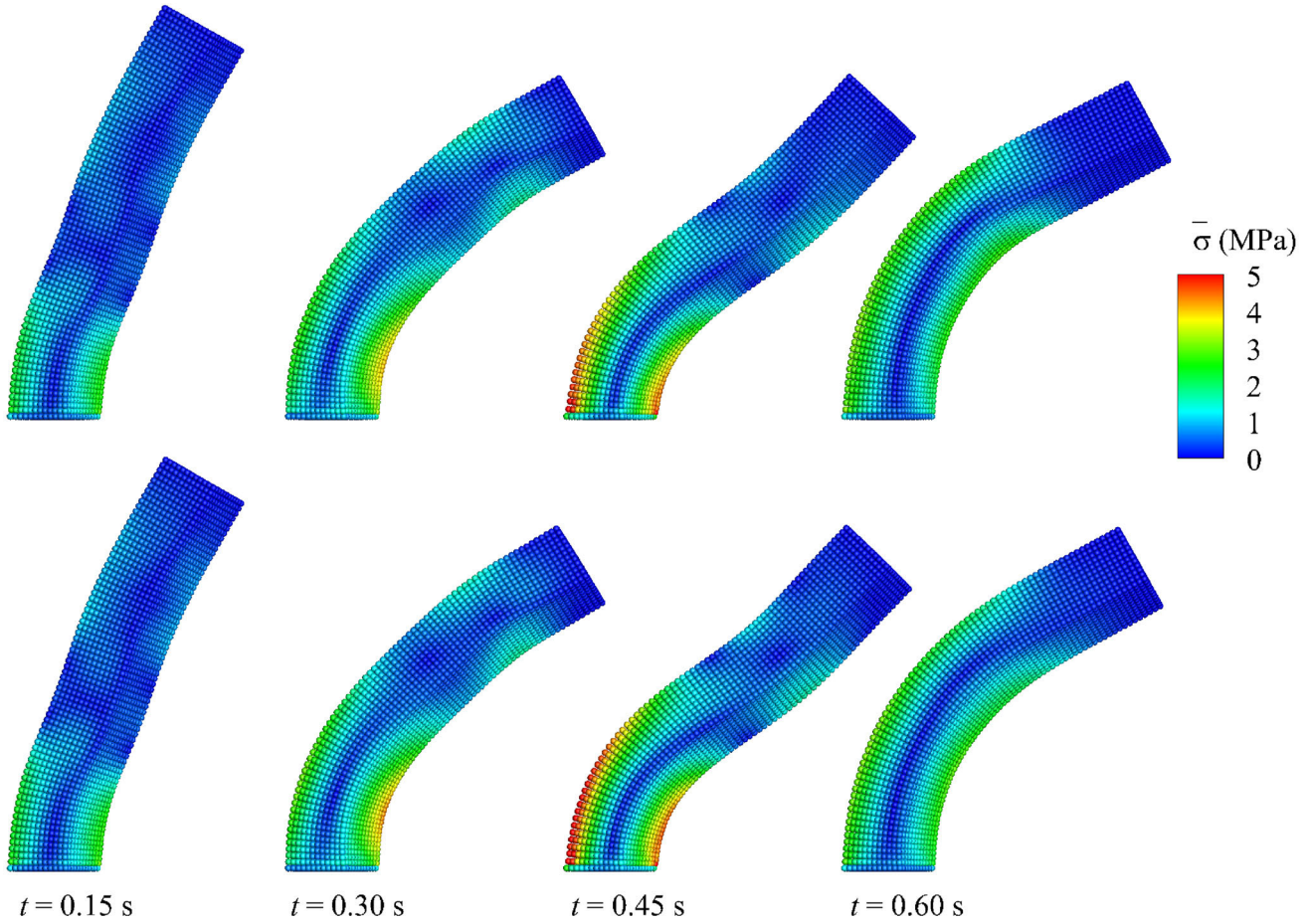


Fig. 15 Bending column: Deformed configuration colored by von Mises stress $\bar{\sigma}$ at serial temporal instants for Neo-Hookean (top panel) and Holzapfel-Ogden (bottom panel) materials obtained by SPH-

UNOG with initial uniform velocity $\mathbf{v}_0 = 10 \left(\frac{\sqrt{3}}{2}, \frac{1}{2}, 0 \right)^T$ m/s. The spatial particle discretization is set as $H/dp = 12$ with H denoting the height of the column and dp the initial particle spacing

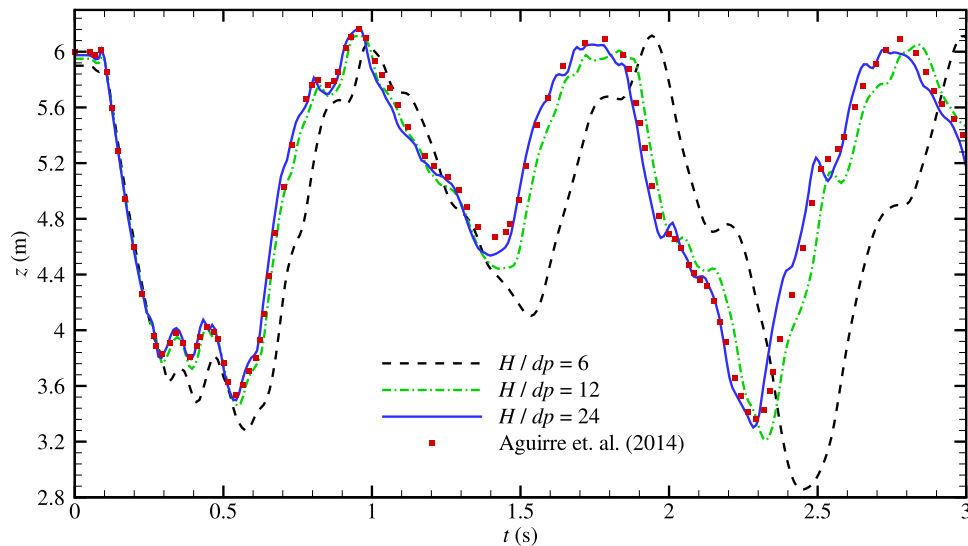


Fig. 16 Bending column: Time history of the vertical position z observed at node S obtained by SPH-UNOG for isotropic Holzapfel-Ogden material with three different spatial resolutions and the initial uniform velocity $\mathbf{v}_0 = 10 \left(\frac{\sqrt{3}}{2}, \frac{1}{2}, 0 \right)^T$ m/s, and its comparison with that of Aguirre et al. [70]

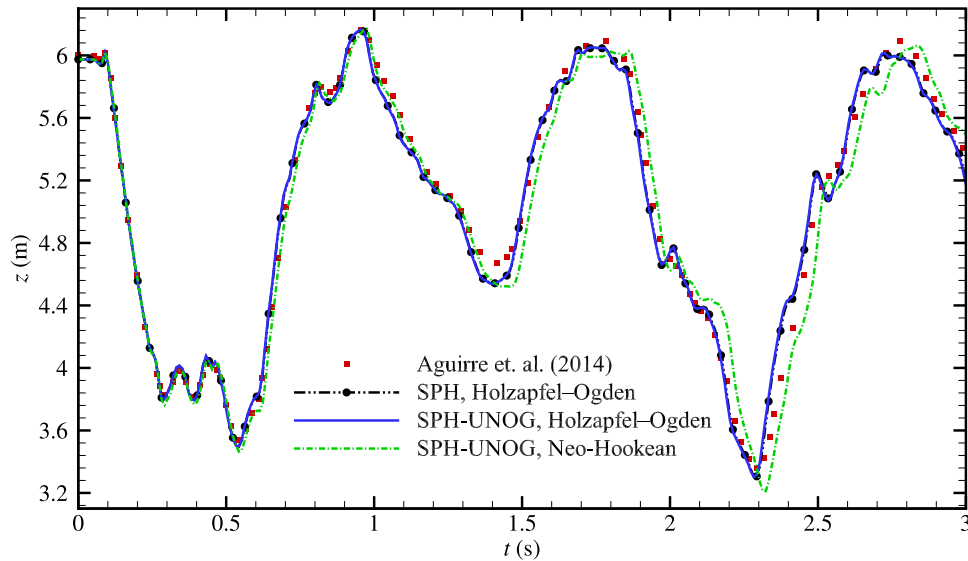


Fig. 17 Bending column: Time history of the vertical position z observed at node S obtained by SPH-UNOG and SPH with initial uniform velocity $\mathbf{v}_0 = 10 \left(\frac{\sqrt{3}}{2}, \frac{1}{2}, 0 \right)^T$ m/s, and its comparison with that of Aguirre et al. [70]. The spatial particle discretization is $H/dp = 24$

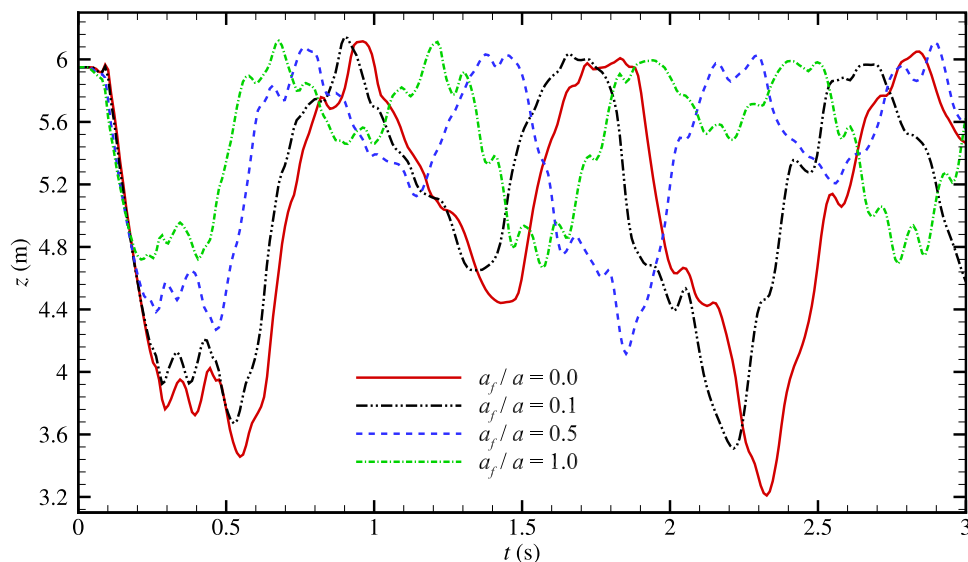


Fig. 18 Bending column: Time history of the vertical position z observed at node S obtained by SPH-UNOG for the Holzapfel-Ogden material model with initial uniform velocity $\mathbf{v}_0 = 10 \left(\frac{\sqrt{3}}{2}, \frac{1}{2}, 0 \right)^T$ m/s. The spatial particle discretization is $H/dp = 12$

Figure 10 illustrates the SPH simulation results under a vertical load of $p = 800$ N/mm, where notable particle disorder and hourglass modes are observed, particularly near the point B (shown in the Fig. 9) of the top edge. In contrast, the SPH-UNOG method demonstrates a highly regular particle arrangement and a smooth pressure distribution, and produce very similar results in terms of deformation and pressure patterns compared with those in the literature (see Fig. 12 in Ref. [67]), highlighting the robustness of the proposed formulation. Additionally, a numerical convergence study is conducted. Figure 11 presents the compression percentage at

point A (from Fig. 9) as a function of the resolution refinement parameter N , where $H/dp = 2^N$. The formulation shows rapid convergence with a compression percentage of 63.915% at $N = 7$, differing by only 0.44% from the 64.2% reported in Ref. [67].

To facilitate a comparison with the results presented in Ref. [66], we adjust the length of the specimen to $L = 20$ mm, and the load p is defined as pressure, while keeping all other parameters unchanged. Table 4 summarizes the comparison when $H/dp = 2^7$, demonstrating a high level of agreement between our results and those reported in Ref.

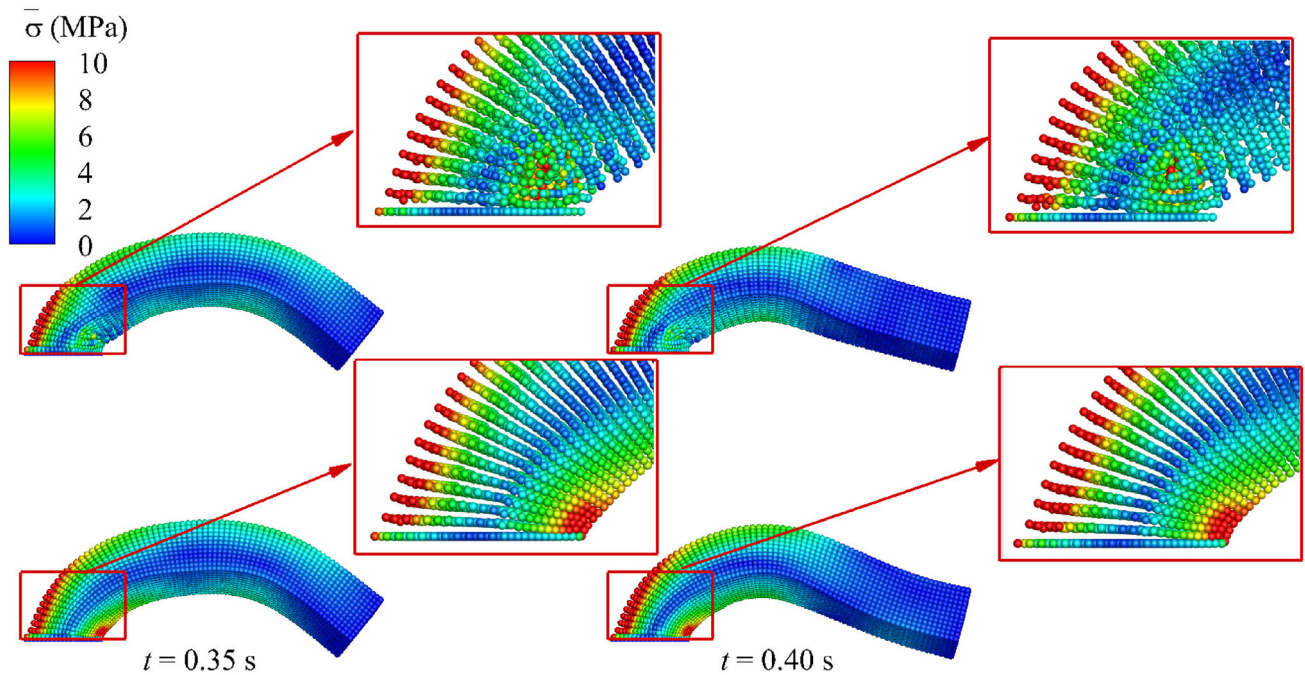


Fig. 19 Bending column: Deformed configuration colored by von Mises stress at two temporal instants obtained by the SPH (top panel) and SPH-UNOG (bottom panel) for isotropic Holzapfel-Ogden mate-

rial model with initial uniform velocity $\mathbf{v}_0 = 20 \left(\frac{\sqrt{3}}{2}, \frac{1}{2}, 0 \right)^T$ m/s. The spatial particle discretization is $H/dp = 12$

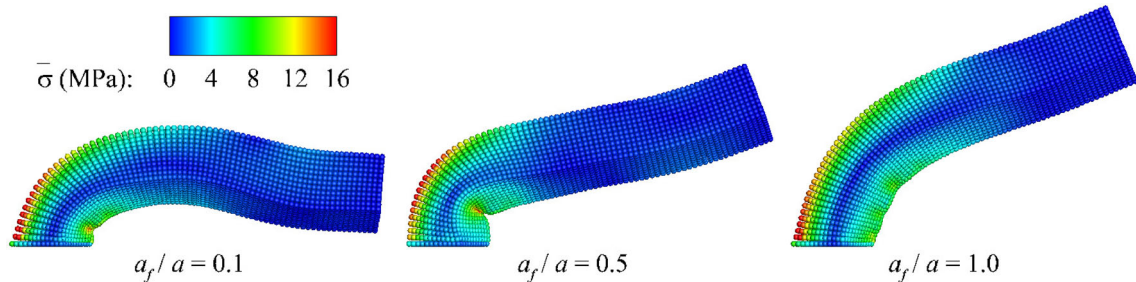


Fig. 20 Bending column: Deformed configuration at 0.4 s colored by von Mises stress obtained by SPH-UNOG for anisotropic Holzapfel-Ogden material model with initial uniform velocity $\mathbf{v}_0 = 20 \left(\frac{\sqrt{3}}{2}, \frac{1}{2}, 0 \right)^T$ m/s. The spatial particle discretization is $H/dp = 12$

[66]. Figure 12a shows the regular particle distribution and a smooth pressure field. To further demonstrate the superior performance of the current formulation, we subject it to a more demanding challenge by increasing the pressure to $p = 1800$ N/mm. As depicted in Fig. 12b, SPH-UNOG continues to exhibit a regular particle distribution and a smooth pressure field, thereby underscoring the robustness of our formulation.

5.4 Pulling test

In this section, the robustness of the proposed formulation is examined through the analysis of a 2D pulling rubber strip [37, 68]. Following the setup in Ref. [37, 68], the rubber

strip is square-shaped with a side length of $L = 2$ mm, and its material properties are characterized by a density $\rho_0 = 1100$ kg/m³, a Young's modulus $E = 1.0$ GPa, and a Poisson's ratio $\nu = 0.45$. The tensile deformation is modeled by applying a velocity of $\mathbf{v} = (0, \pm 0.1$ mm/s) to the top and bottom rows of particles, respectively. The initial particle spacing $dp = L/30$ is utilized to discretize the system, and the splitting random-choice dynamic relaxation method [69] is employed to achieve quasi-static elongation. Figure 13a and b depict the particle configurations along with von Mises stress contours obtained by SPH and SPH-UNOG, respectively, when the material experiences a 500% tension, resulting in an increase in strip length to 12 mm. The SPH method displays instability, evident from parti-

cle disorder within the rows, particularly pronounced near the top and bottom boundaries. In contrast, the current SPH-UNOG formulation successfully predicts the significant tensile deformation in a stable manner, as anticipated. In contrast to the unrealistic outcome reported in Ref. [37] (see their Fig. 8), the resulting deformed configuration in our study exhibits a typical I-shaped cross-section, consistent with the findings of Ref. [68] (see their Fig. 7), although slight discrepancies are observed near the top and bottom boundaries due to the large stress gradient. The robustness of SPH-UNOG is further demonstrated by subjecting the material to an even more challenging condition, with a stretch of 1000% in tension, as illustrated in Fig. 13c.

5.5 Bending column

To further assess the robustness and accuracy of the present formulation, we address a bending-dominated problem with a pre-existing numerical solution available in the literature [70] for quantitative validation. Both neo-Hookean and Holzapfel-Ogden material models are employed in this investigation. Following Ref. [15], a column with a length of $L = 6$ m and a square cross-section (height $H = 1$ m) is clamped at its bottom, oscillating freely under the imposition of an initial uniform velocity $\mathbf{v}_0 = 10 \left(\frac{\sqrt{3}}{2}, \frac{1}{2}, 0 \right)^T$, as depicted in Fig. 14. The neo-Hookean material is modeled with density $\rho_0 = 1100$ kg/m³, Young's modulus $E = 17$ MPa, and Poisson's ratio $\nu = 0.45$. For the Holzapfel-Ogden model, material parameters are detailed in Table 5 with anisotropic terms adjusting accordingly. It is important to note that the Poisson's ratio ν of the Holzapfel-Ogden material is also set as 0.45 and $a = E/2(1 + \nu)$ to facilitate a direct comparison with neo-Hookean in the isotropic scenario.

Figure 15 illustrates the time evolution of the deformed configuration, represented by the von Mises stress contour, as obtained through the present formulation. The results obtained from both material models exhibit remarkable similarity, featuring a well-ordered particle distribution and a smooth stress field. For quantitative validation, the time history of the z -axis position of point S (as marked in Fig. 14) for the isotropic Holzapfel-Ogden material model is presented in Fig. 16. Different spatial resolutions, $H/dp = 6$, $H/dp = 12$, and $H/dp = 24$, are considered, with a comparison to the reference results reported by Aguirre et al. [70]. Notably, robust convergence and a high level of agreement are evident with increasing spatial resolution. As shown in Fig. 17, the outcomes computed by SPH and SPH-UNOG closely align with negligible discrepancies, and the quantitative disparities between the two materials are also minimal.

We further show the versatility of the present formulation by investigating this example incorporating the anisotropic Holzapfel-Ogden material model. In the case of anisotropic

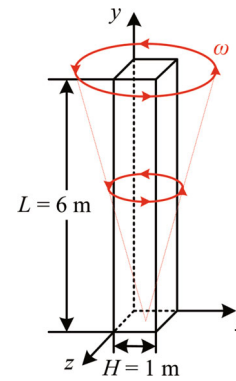


Fig. 21 Twisting column: Initial configuration

material, we set the fiber and sheet directions aligned with z and x coordinates, respectively. We conduct three tests with varying anisotropic ratios: $a_f/a = 0.1$, $a_f/a = 0.5$, and $a_f/a = 1.0$. Figure 18 shows the time history of the vertical displacement of point S . It can be observed that the deformation is reduced as the anisotropic ratio increases.

To showcase the superior performance of the present formulation, we tackle a more challenging problem by elevating the initial velocity to $\mathbf{v}_0 = 20 \left(\frac{\sqrt{3}}{2}, \frac{1}{2}, 0 \right)^T$ m/s for the Holzapfel-Ogden material model. As shown in Fig. 19, the simulation result of the SPH exhibits noticeable particle disorder, especially near the clamped bottom where the maximum von Mises stress exists, while SPH-UNOG captures a highly regular particle distribution and a smooth stress field, underscoring the robustness of the proposed formulation. Furthermore, Fig. 20 presents the deformed configuration colored by von Mises stress for the anisotropic Holzapfel-Ogden material model.

5.6 Twisting column

In this section, we extend the bending column problem to encompass a twisting column, which represents a highly nonlinear scenario, following Refs. [35, 36, 71–74]. As illustrated in Fig. 21, the twisting is initiated with a sinusoidal rotational velocity field given by $\boldsymbol{\omega} = [0, \Omega_0 \sin(\pi y_0/2L), 0]$ with $\Omega_0 = 105$ rad/s. The column, modeled using the Holzapfel-Ogden material, is assumed to exhibit nearly incompressible behavior, with a Poisson's ratio of $\nu = 0.499$. The remaining material parameters remain consistent with those outlined in the previous section. Figure 22 presents the deformed configuration of the isotropic material model at different time instants, accompanied by the von Mises stress contour obtained through SPH-UNOG. The simulation performs well, exhibiting deformation patterns highly consistent with those reported in the literature (see Fig. 28 in Ref. [35]). Addressing a notably more challenging scenario, we increase the initial angular velocity to $\Omega_0 = 330$ rad/s

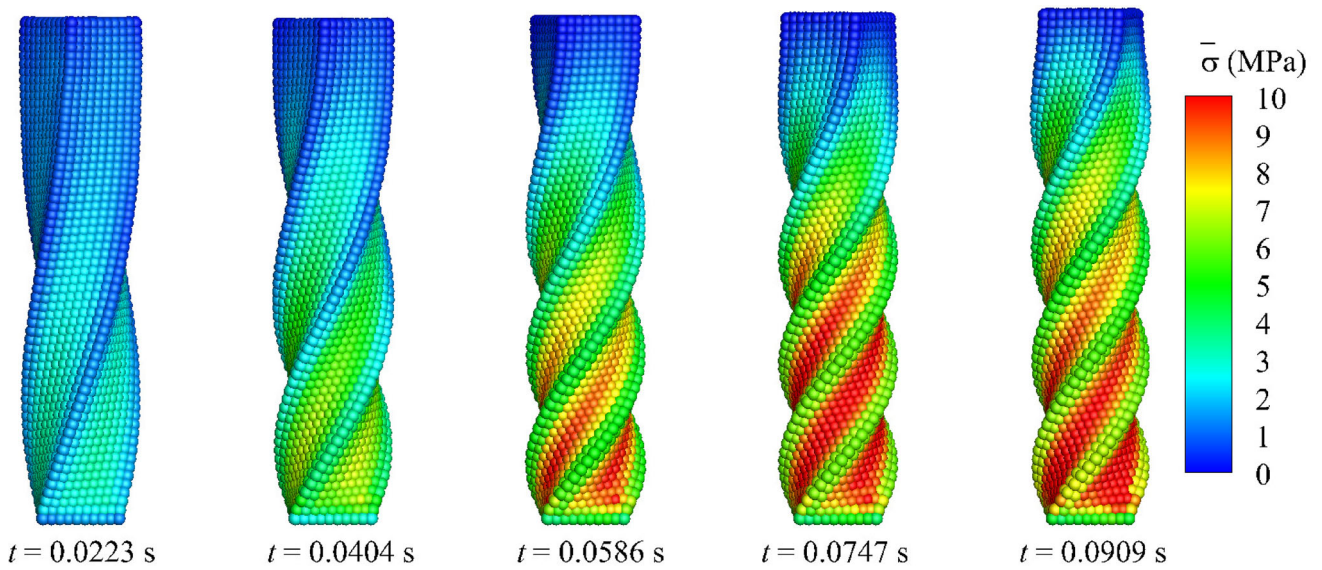


Fig. 22 Twisting column: Deformed configuration colored by von Mises stress at different time instants for the isotropic Holzapfel-Odgen material model obtained by SPH-UNOG. The initial rotational velocity

$\omega = [0, \Omega_0 \sin(\pi y_0/2L), 0]$ with $\Omega_0 = 105$ rad/s. The spatial particle discretization is set as $H/dp = 10$ with H denoting the height of the column and dp the initial particle spacing

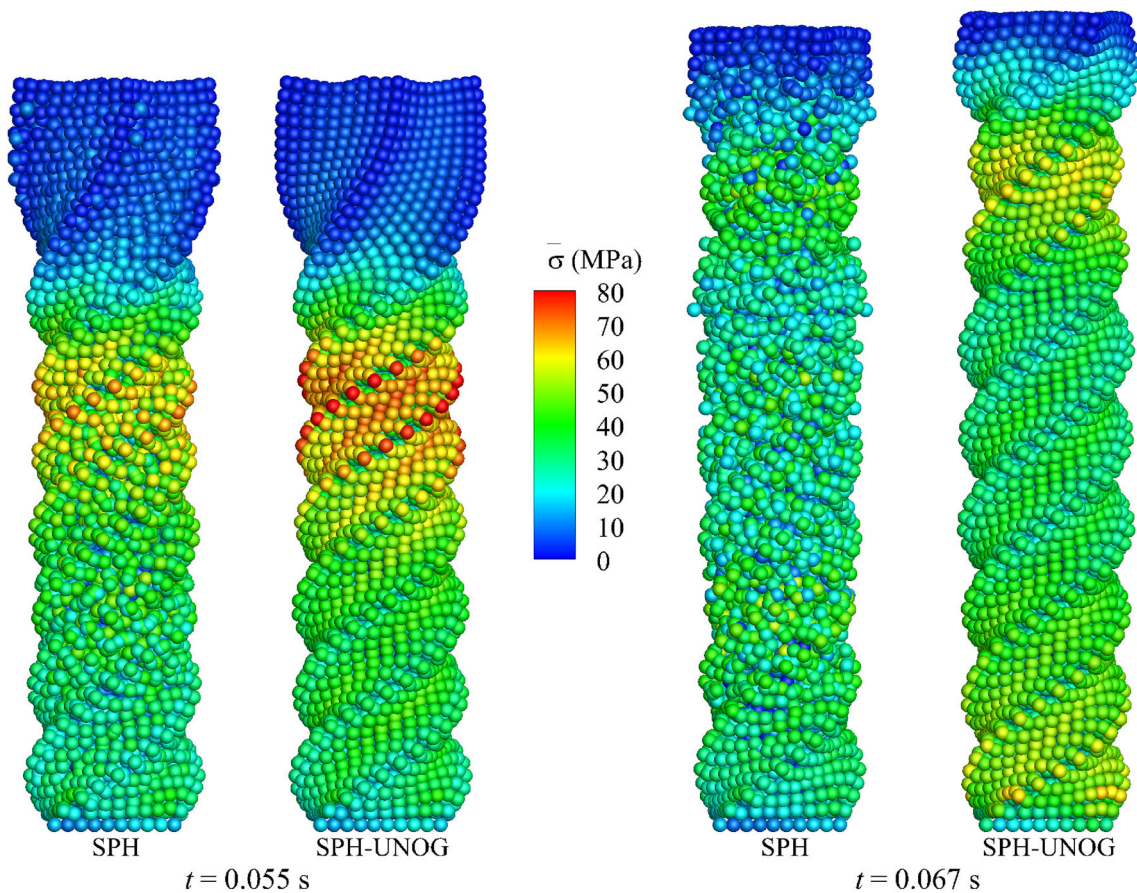


Fig. 23 Twisting column: Deformed configuration colored by von Mises stress at two time instants for the isotropic Holzapfel-Odgen material model obtained by SPH and SPH-UNOG with initial sinusoidal rotational velocity $\Omega_0 = 330$ rad/s. The spatial particle discretization is set as $H/dp = 10$

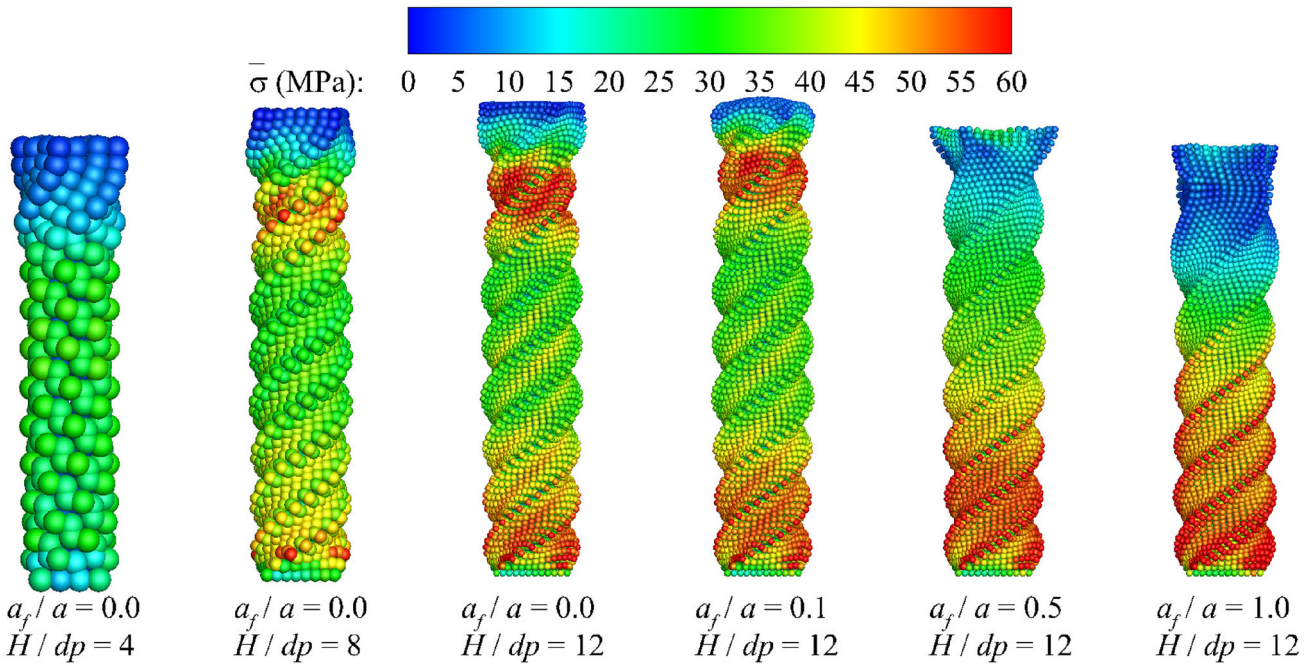


Fig. 24 Twisting column: A sequence of particle refinement and anisotropic ratio increasing analyses using SPH-UNOG with the initial sinusoidal rotational velocity $\Omega_0 = 330$ rad/s

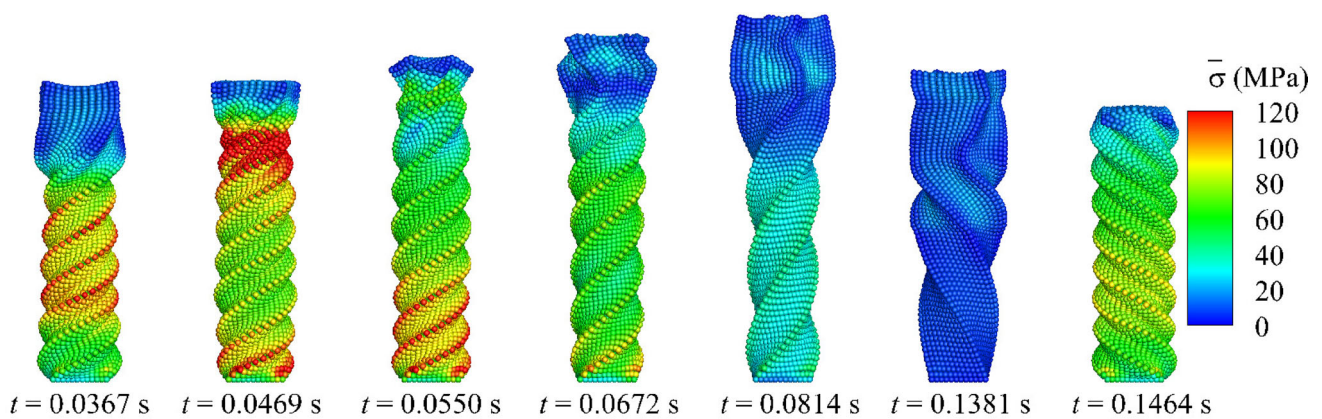


Fig. 25 Twisting column: Deformed configuration plotted with von Mises stress at serial time instants when $a_f/a = 1.0$ obtained by SPH-UNOG with the initial sinusoidal rotational velocity $\Omega_0 = 480$ rad/s. The spatial particle discretization is set as $H/dp = 12$

with a Poisson's ratio of $\nu = 0.49$. It is worth noting that $\Omega_0 = 100$ rad/s and 200 rad/s are already considered challenging, as indicated in Refs. [71, 73]. As shown in Fig. 23, the proposed formulation demonstrates stability, contrasting with the visibly disordered particle results from SPH. Conducting a convergence study involving sequential refinement of spatial resolution from $H/dp = 4$ to $H/dp = 8$ and $H/dp = 12$, and an analysis of anisotropic behavior across varying anisotropic ratios ($a_f/a = 0.1$, $a_f/a = 0.5$, and $a_f/a = 1.0$), Fig. 24 demonstrates robust convergence properties for both deformation and von Mises stress $\bar{\sigma}$, and provides insight into the smooth stress characteristic of the anisotropic Holzapfel-Ogden material.

Table 6 Muscle contraction: Parameters for the Holzapfel-Ogden material model. Note that the anisotropic terms are set to zero for the isotropic analysis

$a = 0.059$ kPa	$a_f = 18.472$ kPa	$a_s = 2.841$ kPa	$a_{fs} = 0.216$ kPa
$b = 8.023$	$b_f = 16.026$	$b_s = 11.12$	$b_{fs} = 11.436$

Finally, to further assess the robustness of the present formulation, we increase the initial angular velocity to $\Omega_0 = 480$ rad/s with $a_f/a = 1.0$. As shown in Fig. 25, the deformed configuration at various time instants is presented. Remarkably, the formulation adeptly captures the extremely large deformations encompassing the entire twisting process,

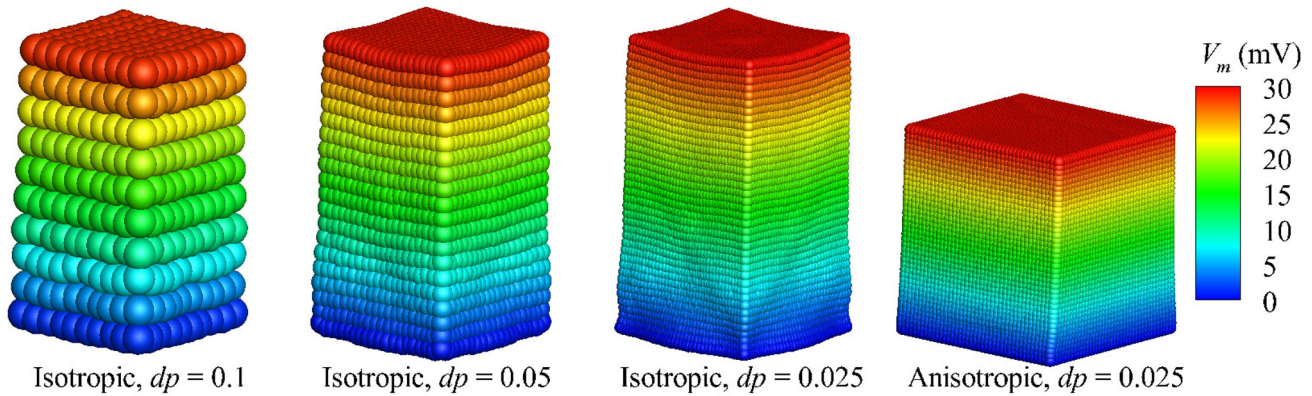


Fig. 26 Muscle contraction: Deformed configuration colored by transmembrane potential V_m obtained by SPH-UNOG when the transmembrane potential of top face $V_m = 30$ mV with three different spatial

resolutions and both isotropic and anisotropic material properties. Note that dp is the initial particle spacing

including the recovery phase and reverse rotation, as anticipated.

5.7 Electrophysiologically induced muscle contraction

Following Refs. [15, 75], we examine a unit cube of muscle characterized by an orthogonal material direction, where the muscle fiber and sheet directions align with the global coordinates. The passive response is described by the Holzapfel-Ogden model, and the material parameters are detailed in Table 6. To initiate the excitation-induced response, a linear distribution of transmembrane potential is applied along the vertical direction, with $V_m = 0$ mV at the bottom face and

Table 7 Muscle contraction: Quantitative validation of the deformation

	$dp = 0.1$	$dp = 0.05$	$dp = 0.025$	Zhang et al. [15]
Displacement	0.4988	0.5248	0.5355	0.535

$V_m = 30$ mV at the top face. For simplicity, we neglect the time variation of the transmembrane potential, and an activation law for active stress is employed by

$$T_a = -0.5V_m. \tag{46}$$

Two distinct tests involving iso- and anisotropic models are conducted in this study.

Figure 26 shows the deformed configuration of the cubic muscle with particle refinement. The results showcase good convergence properties, and qualitative agreement is observed for the isotropic test, aligning well with the findings presented in Ref. [75] (refer to Figure 7 in their work). Moreover, Table 7 indicates that the displacement of the top face at fine particle resolution is 0.5355, demonstrating good agreement with the value of 0.535 reported in Ref. [15]. In the case of the anisotropic test, deformation is reduced owing to the presence of fibers and sheets. The transmembrane potential of top face is increased to $V_m = 300$ mV to further test the robustness of present formulation. As shown in Fig. 27, particle deformation and von Mises strain fields are well captured.

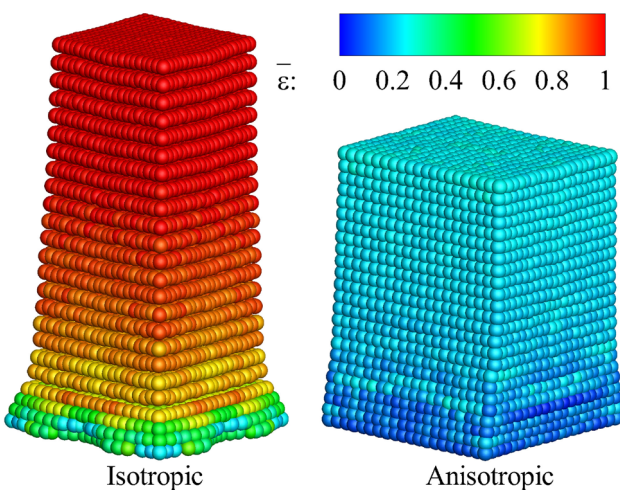


Fig. 27 Muscle contraction: Deformed configuration colored by von Mises strain $\bar{\epsilon}$ obtained by SPH-UNOG when the transmembrane potential of top face is increased to $V_m = 300$ mV with both isotropic and anisotropic material properties. The spatial particle discretization is set as $dp = 0.025$

5.8 Taylor bar

A well-documented Taylor bar example, as explored in Refs [68, 70, 74, 76–85], is utilized to assess the effectiveness of the proposed formulation in high-speed impact scenarios. A 2D copper bar, characterized by an initial length

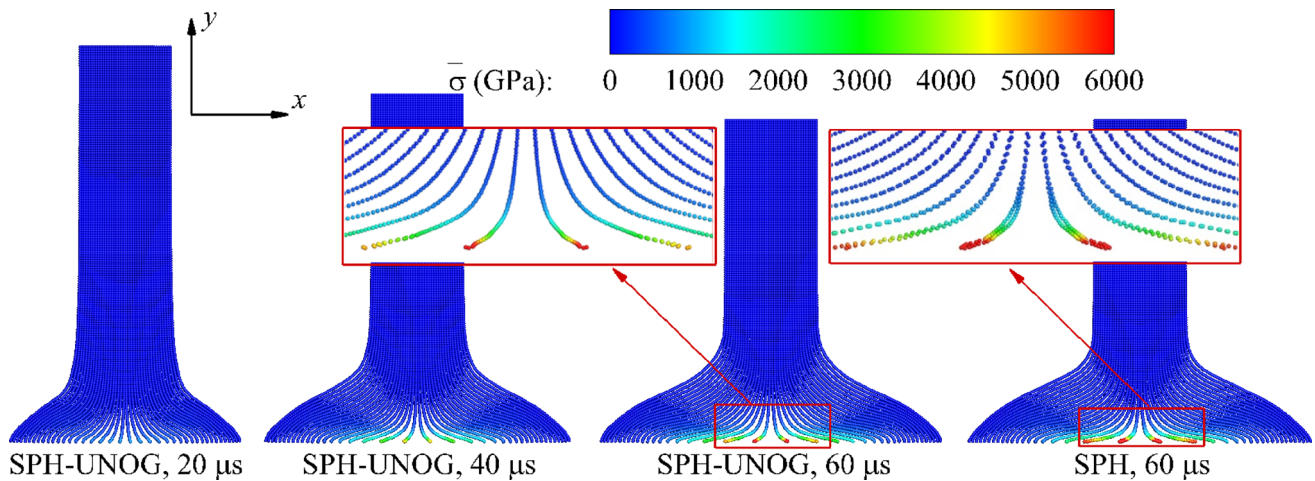


Fig. 28 2D Taylor bar: Deformed configuration colored by von Mises stress $\bar{\sigma}$ at serial temporal instants obtained by SPH-UNOG with initial uniform velocity $\mathbf{v}_0 = (0, -227)^T$ m/s, and its comparison with that of SPH. The material is modeled by isotropic hardening elastic–plasticity with Young’s modulus $E = 117$ GPa, density $\rho^0 = 8.930 \times 10^3$ kg/m³,

Poisson’s ratio $\nu = 0.35$, yield stress $\tau_y = 0.4$ GPa, and hardening modulus $\kappa = 0.1$ GPa. The spatial particle discretization is set as $H/dp = 40$ with H denoting the height of the column and dp the initial particle spacing

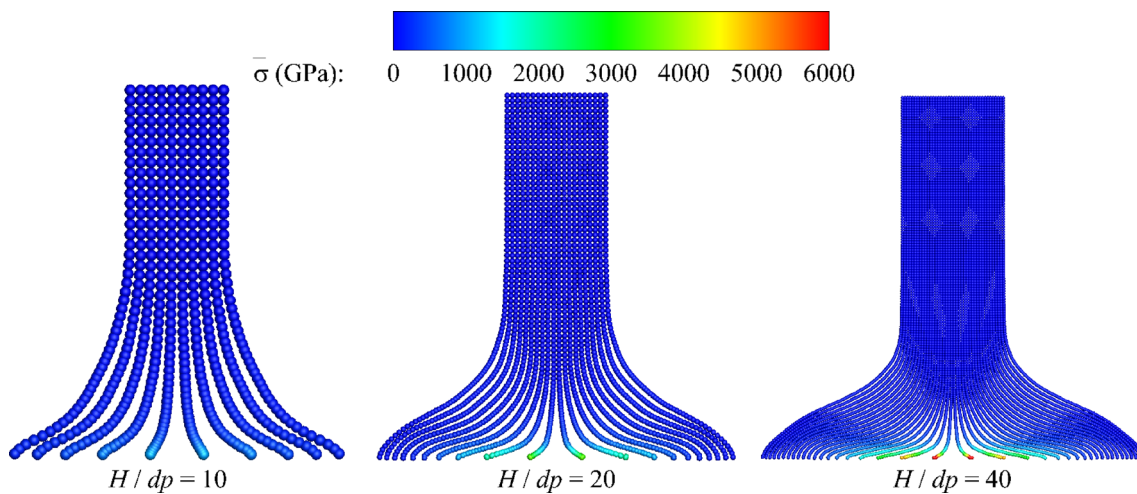


Fig. 29 2D Taylor bar: Deformed configuration colored by von Mises stress $\bar{\sigma}$ obtained by SPH-UNOG with three different spatial resolutions and the initial uniform velocity $\mathbf{v}_0 = (0, -227)^T$ m/s

of $L = 0.03$ m and a height of $H = 0.006$ m, is modeled for plane-strain analysis by undergoing impact against a rigid frictionless wall at time $t = 0$ s with a velocity of $\mathbf{v}_0 = (0, -227)^T$ m/s. To simulate the material response, a hyperelastic–plastic model with linear hardening is employed. The material parameters include Young’s modulus $E = 117$ GPa, density $\rho^0 = 8.930 \times 10^3$ kg/m³, Poisson’s ratio $\nu = 0.35$, yield stress $\tau_y = 0.4$ GPa, and hardening modulus $\kappa = 0.1$ GPa. It should be noted that since the applied artificial damping stress τ_d significantly influences the deformation in high-velocity impact scenar-

ios, τ_d used in the Taylor cases is given as

$$\tau_d = 0.125 \frac{\chi}{2} \frac{db}{dt}, \quad (47)$$

indicating the adoption of a smaller numerical damping compared to other cases. Despite setting the CFL number to 0.1 for instability, which increases the computational overhead, the results converge rapidly even in low-resolution scenarios.

Figure 28 shows the deformed configuration of 2D Taylor bar at different time instants with von Mises stress contour obtained by SPH-UNOG, and its comparison with that simulated by SPH when the time $t = 60 \mu\text{s}$. While both simulations exhibit satisfactory performance and produce

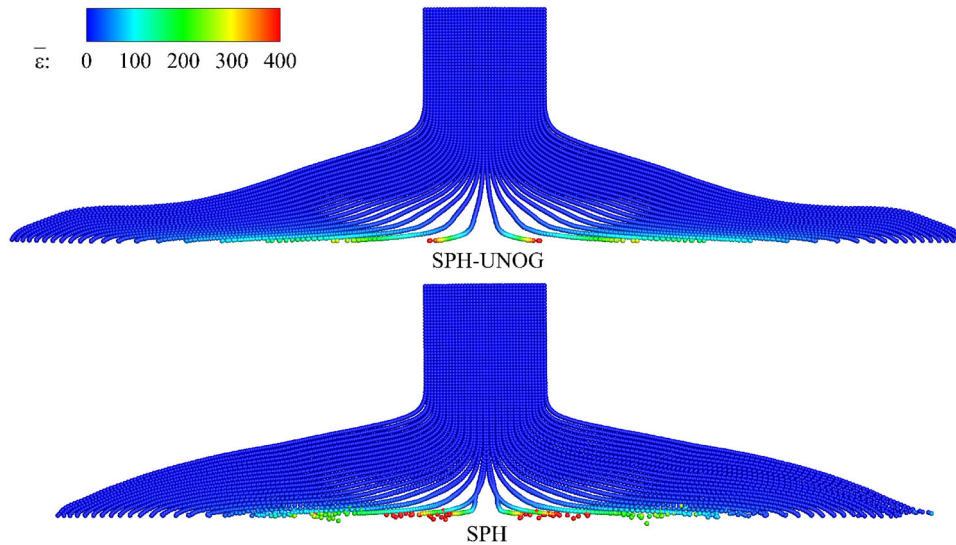


Fig. 30 2D Taylor bar: Deformed configuration colored by von Mises strain $\bar{\epsilon}$ obtained by SPH-UNOG (top panel) and SPH (bottom panel) with initial uniform velocity $\mathbf{v}_0 = (0, -400)^T$ m/s. The spatial particle discretization is set as $H/dp = 40$

comparable results in terms of deformation and stress patterns, SPH-UNOG demonstrates a more uniform particle distribution compared to SPH. In contrast to the nearly 90° contact angles, angles of the left and right lower corners of the deformed bar, shown in Ref. [37] (see their Fig. 9), the resulting deformed configuration in our study displays contact angles of less than 90° , consistent with the observations in Refs. [68] (see their Fig. 10), [79] (see their Fig. 6), and [84] (see their Fig. 9), despite the consideration of a 2D case here. A convergence study is undertaken, incrementally refining the spatial resolution from $H/dp = 10$ to $H/dp = 20$ and $H/dp = 40$. The convergence properties of both deformation and von Mises stress $\bar{\sigma}$ are shown in Fig. 29. A significantly more challenging problem is studied by increasing the initial velocity to

$\mathbf{v}_0 = (0, -400)^T$ m/s. As illustrated in Fig. 30, the unstabilized results from SPH exhibit noticeable particle disorder. Conversely, the outcomes obtained through SPH-UNOG demonstrate an orderly particle distribution and a smooth strain field, even in the presence of significant strain (the maximum von Mises strain exceeds 400).

The 2D Taylor bar is expanded to a 3D analysis, featuring a squared cross-section with dimensions of 0.006×0.006 m, as shown in Fig. 31. Figure 32 illustrates the deformed configuration of the 3D Taylor bar at various time instants, accompanied by von Mises stress contours obtained through SPH-UNOG, and a comparative analysis is presented against the simulation conducted by SPH at $t = 60 \mu\text{s}$. Although both simulations demonstrate good performance and yield comparable results in terms of deformation and stress patterns, SPH-UNOG still exhibits a more uniform particle distribution compared to SPH. A sequence of particle refine-

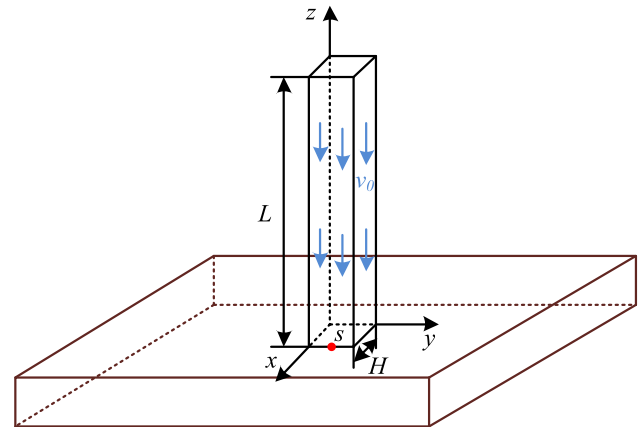


Fig. 31 3D Taylor bar: Problem setup

ment analyzes, from $H/dp = 8$ to $H/dp = 12$, $H/dp = 16$ and $H/dp = 20$, is also conducted. As presented in Fig. 33, the good convergence characteristics of both deformation and the von Mises stress $\bar{\sigma}$ are observed. For further convergence analysis and quantitative validation, Fig. 34 illustrates the temporal evolution of the x -axis position of point S marked in Fig. 31. It is evident from observation that the displacement converges rapidly, approximating a second-order rate, and the x -axis position of the highest resolution is $x = 6.956$ mm, aligning closely with the results in Ref. [83]. A more demanding scenario is investigated by increasing the initial velocity to $\mathbf{v}_0 = (0, 0, -350)^T$ m/s. As depicted in Fig. 35, the results obtained through SPH-UNOG still exhibit an organized particle distribution and a smooth stress field.

Following Refs. [68, 76], we now investigate a round aluminum bar with the initial length $L = 2.346$ cm and radius $R = 0.391$ cm. The material is modeled by perfect plasticity,

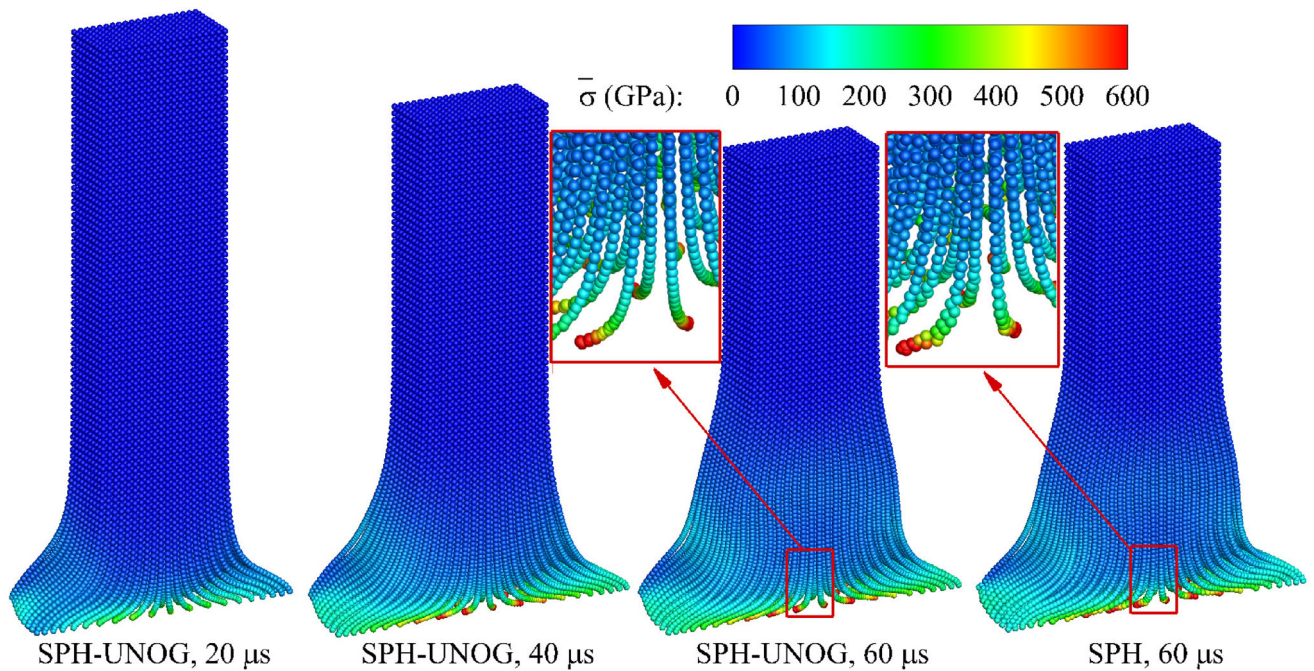


Fig. 32 3D Taylor bar: Deformed configuration colored by von Mises stress $\bar{\sigma}$ at serial temporal instants obtained by SPH-UNOG with initial uniform velocity $\mathbf{v}_0 = (0, 0, -227)^T$ m/s, and its comparison with that of SPH. The material is modeled by isotropic hardening elastic-plasticity with Young's modulus $E = 117$ GPa, density $\rho^0 =$

8.930×10^3 kg/m³, Poisson's ratio $\nu = 0.35$, yield stress $\tau_y = 0.4$ GPa, and hardening modulus $\kappa = 0.1$ GPa. The spatial particle discretization is set as $H/dp = 20$ with H denoting the height of the column and dp the initial particle spacing

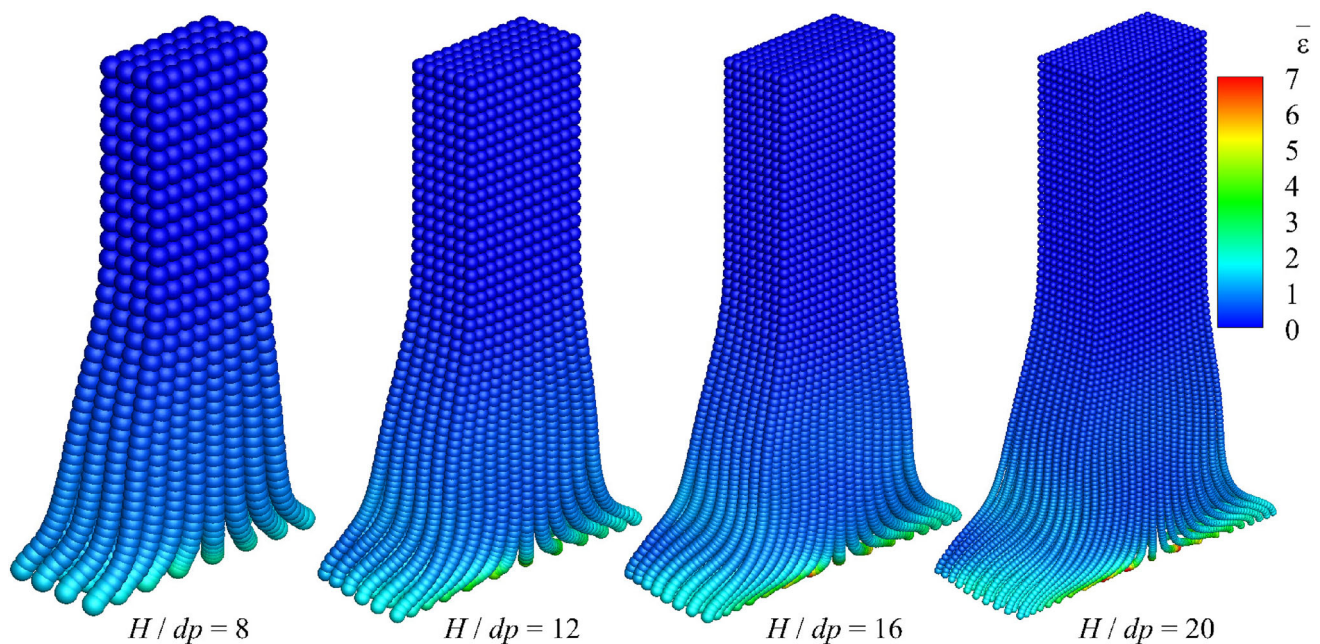


Fig. 33 3D Taylor bar: Deformed configuration colored by von Mises strain $\bar{\epsilon}$ obtained by SPH-UNOG with four different spatial resolutions and the initial uniform velocity $\mathbf{v}_0 = (0, 0, -227)^T$ m/s

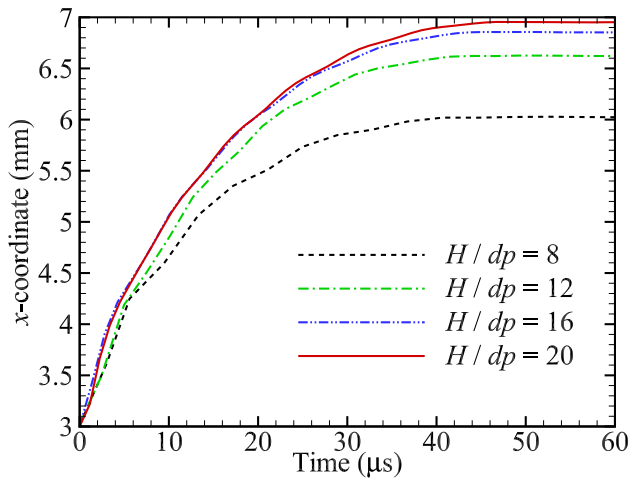


Fig. 34 3D Taylor bar: Time history of the horizontal position x observed at node S obtained by SPH-UNOG with initial uniform velocity $\mathbf{v}_0 = (0, 0, -227)^T$ m/s under four different resolutions

i.e., hardening modulus $\kappa = 0$ Pa, with initial density $\rho_0 = 2700$ kg/m³, Young’s modulus $E = 78.2$ GPa, Poisson’s ratio $\nu = 0.3$, and yield stress $\tau_y = 0.29$ GPa. The initial impact velocity is set as $\mathbf{v}_0 = (0, 0, -373)^T$ m/s. A convergence study is conducted with three resolutions, $R/dp = 8$, $R/dp = 12$ and $R/dp = 16$. As shown in Fig. 36, the good convergence characteristics of both deformation and the von Mises strain $\bar{\epsilon}$ are observed. For quantitative validation, Table 8 summarizes the deformation under various resolutions and compares it with the results from Ref. [68]. Favorable convergence properties and high accuracy are observed.

5.9 Necking bar

In this section, we examine a plane-strain bar undergoing uniform extension, a standard test problem analyzed in Refs. [55, 86, 87]. The bar dimensions are length $L = 53.334$ mm and height $H = 12.826$ mm. To control the location of the necking, the center dimension of the bar is reduced to 0.982 of the side height (1.8% reduction), as shown in Fig. 37. A total displacement of 8 mm is applied on the constrained boundary particles, an additional 4 layers of particles on both sides. The bar exhibits elastic deformation governed by the Neo-Hookean law and the plastic response characterized by the nonlinear isotropic hardening law. Material parameters are detailed in Table 9.

Figure 38 depicts the deformed configuration of the necking bar at different instants, featuring von Mises strain contours, obtained through SPH-UNOG, and a comparative analysis with the simulation performed by SPH under the applied displacement of 6.75 mm. While SPH exhibits noticeable particle disorder, SPH-UNOG presents commendable performance in capturing deformation and strain patterns with a organized particle distribution. It should be noted that, despite the symmetry of this necking bar problem, the strain field exhibits asymmetry owing to the initial asymmetric particle distribution. A series of particle refinement analyses are performed, with the spatial resolution varying from $H/dp = 20$ to $H/dp = 40$ and $H/dp = 60$.

Theresults, depicted in Fig. 39, reveal quite good convergence properties in both deformation and von Mises stress $\bar{\sigma}$, reinforcing the reliability of the simulation outcomes. For a

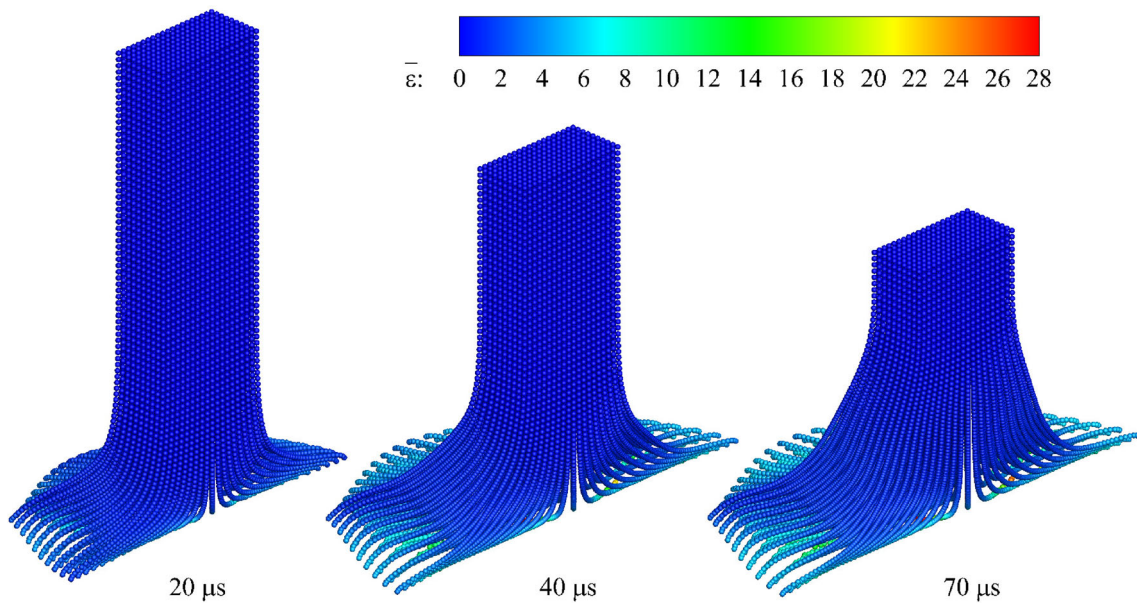


Fig. 35 3D Taylor bar: Deformed configuration colored by von Mises strain $\bar{\epsilon}$ at serial temporal instants obtained by SPH-UNOG with initial uniform velocity $\mathbf{v}_0 = (0, 0, -350)^T$ m/s. The spatial particle discretization is set as $H/dp = 20$

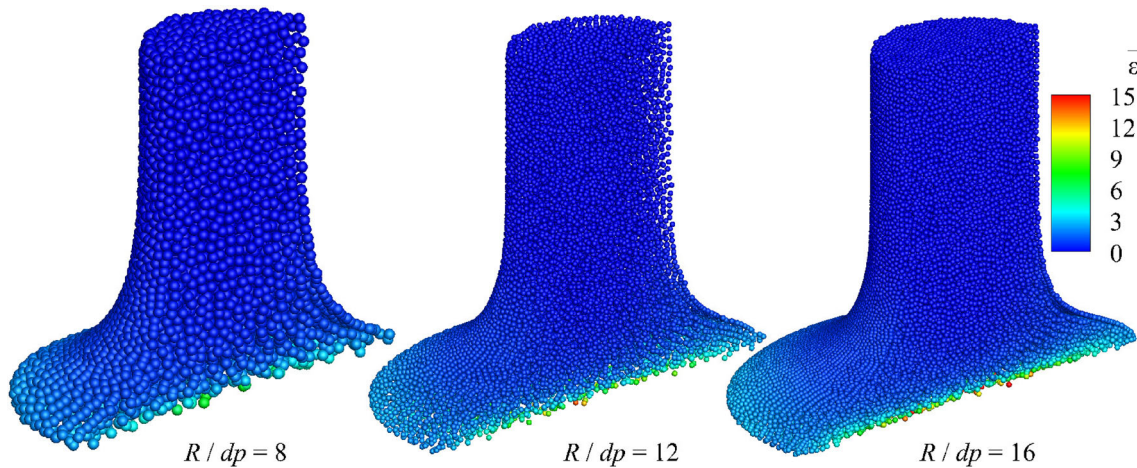


Fig. 36 3D round Taylor bar: Deformed configuration colored by von Mises strain $\bar{\epsilon}$ obtained by SPH-UNOG with three different spatial resolutions and the initial uniform velocity $\mathbf{v}_0 = (0, 0, -373)^T$ m/s. The perfect plastic material is modeled with density $\rho_0 = 2700 \text{ kg/m}^3$,

Young’s modulus $E = 78.2 \text{ GPa}$, Poisson’s ratio $\nu = 0.3$, and yield stress $\tau_y = 0.29 \text{ GPa}$. Note that R is the radius of bar and dp the initial particle spacing

Table 8 3D round Taylor bar: Quantitative validation of deformed geometries for perfect plastic material

	$R/dp = 8$	$R/dp = 12$	$R/dp = 16$	Chen et al. [68]
Length (cm)	1.4816	1.4597	1.4483	1.454
Radius (cm)	0.9120	0.9362	0.9624	1.051

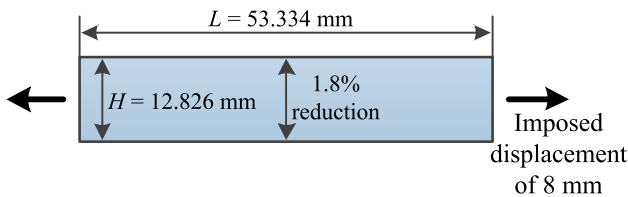


Fig. 37 Necking bar: Problem setup

Table 9 Necking bar: Non-linear hardening elastic–plastic material parameters

Parameters	Value
Shear modulus	80.1938 GPa
Bulk modulus	164.21 GPa
Initial flow stress	450 MPa
Saturation flow stress	715 MPa
Saturation exponent	16.93
Linear hardening coefficient	129.24 MPa

more comprehensive convergence analysis and quantitative validation, Figs. 40 and 41 present the necking displacement of the bar center dimension and the corresponding reaction force exerted by the material in response to the applied tensile load. These results are compared with the highest-order finite element outcomes reported in Ref. [87].

Table 10 Oobleck octopus: Viscoplastic material parameters

Parameters	Value
Density	1000.0 kg/m ³
Shear modulus	11.2 kPa
Bulk modulus	109.0 kPa
Yield stress	0.1 Pa
Viscosity	10
Herschel Bulkley power	2.8

The significant convergence properties and accuracy are noted, reaffirming the reliability of the simulation. And we can observe that after a short elastic response, indicated by the initial linear segment of the reaction force curve, the bar transitions to plastic deformation, marked by a slowly increasing reaction force. Subsequently, the deformation shifts to a mode where plastic effects concentrate in the necking area, leading to a decrease in the reaction force. Figures 42 and 43 present a comparative analysis of displacement and reaction force curves between SPH-UNOG and SPH. Notably, SPH exhibits inaccuracies after a stretching of 1.2 mm due to hourglass modes, while SPH-UNOG maintains accurate performance throughout.

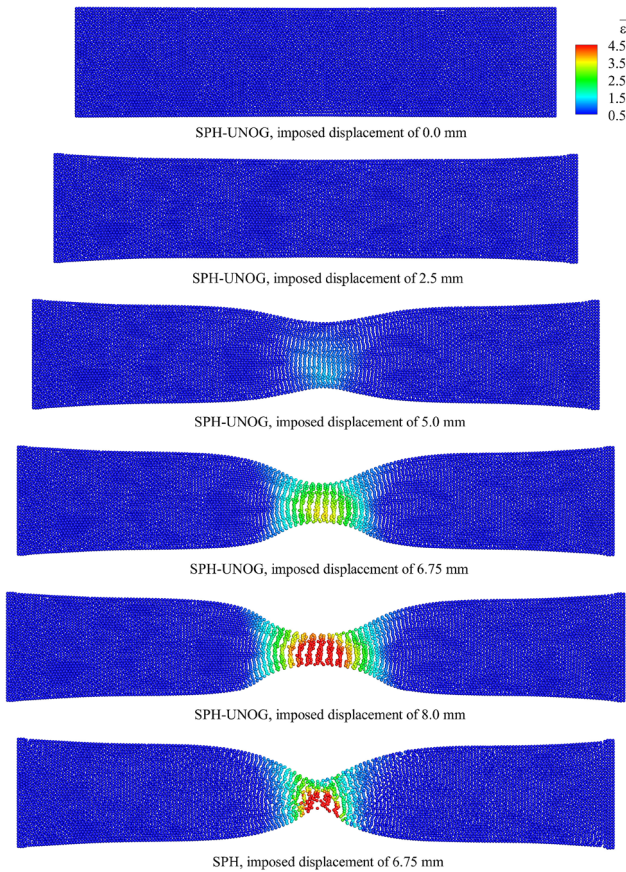


Fig. 38 Necking bar: Deformed configuration colored by von Mises strain $\bar{\epsilon}$ at various instants obtained by SPH-UNOG, and its comparison with that of SPH. The spatial particle discretization is set as $H/dp = 40$ with H denoting the height of bar and dp the initial particle spacing

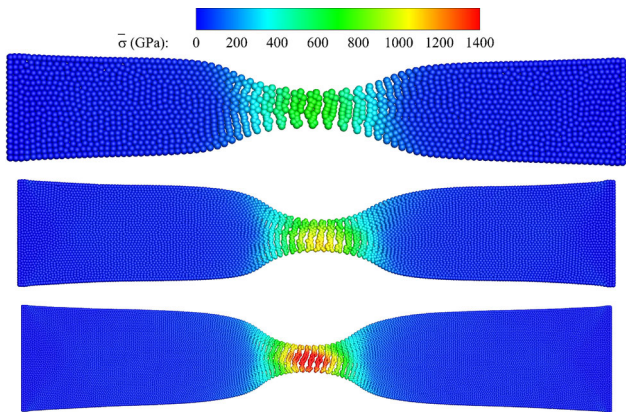


Fig. 39 Necking bar: A sequence of particle refinement analyzes using SPH-UNOG. Three different spatial resolutions, $H/dp = 20$, $H/dp = 40$ and $H/dp = 60$, are applied

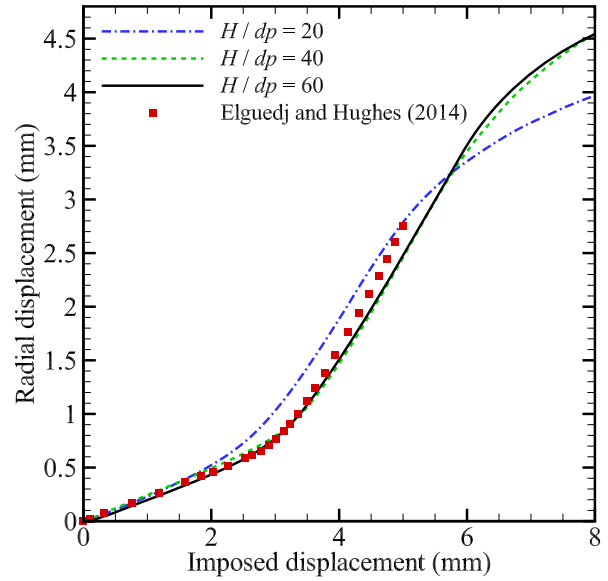


Fig. 40 Necking bar: Necking displacement versus imposed displacement obtained by SPH-UNOG with three different spatial resolutions, and its comparison with that of Elguedj and Hughes [87]

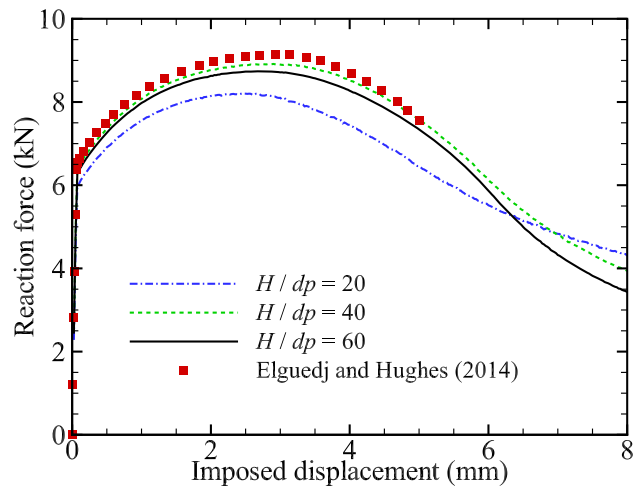


Fig. 41 Necking bar: Reaction force versus imposed displacement obtained by SPH-UNOG with three different spatial resolutions, and its comparison with that of Elguedj and Hughes [87]

5.10 Oobleck octopus

In this section, we analyze mechanical behaviors of an octopus made of shear thickening oobleck, a viscoplastic material. The octopus undergoes deformation under its own gravity and the punch from a half-cylinder, as illustrated in Fig. 44. Note that the half-cylinder stops punching after 0.3 s. The material properties of oobleck are provided in Table 10 [56].

Figure 45 shows the first stage of the octopus deformation, wherein the octopus feet collide with each other at high velocity. Moving on to the second stage, as illustrated in

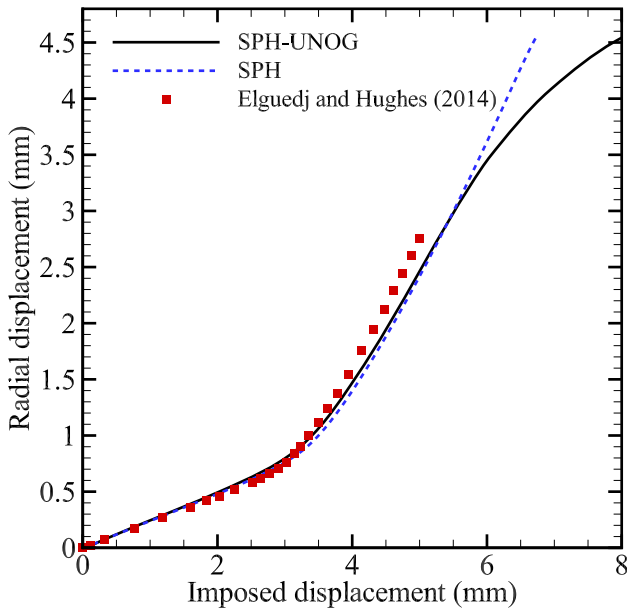


Fig. 42 Necking bar: Necking displacement versus imposed displacement obtained by SPH-UNOG and SPH, and their comparison with that of Elguedj and Hughes [87]. The spatial particle discretization is $H/dp = 40$

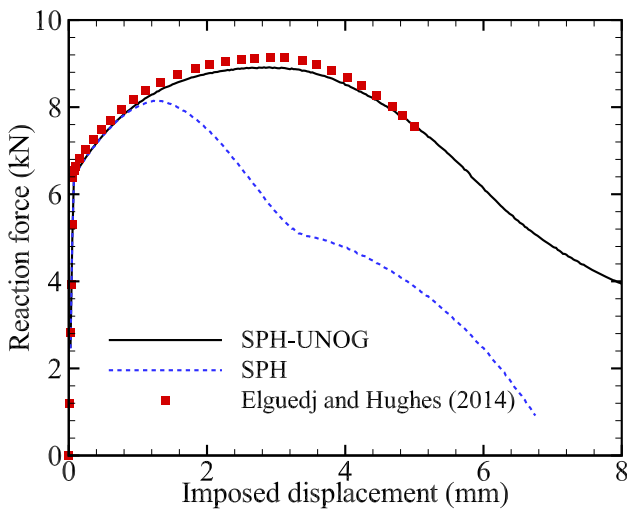


Fig. 43 Necking bar: Reaction force versus imposed displacement obtained by SPH-UNOG and SPH, and their comparison with that of Elguedj and Hughes [87]. The spatial particle discretization is $H/dp = 40$

Fig. 46, significant plastic flow is observed in the octopus. The smooth deformation and huge strain fields highlight the potential of the present formulation for real-world applications.

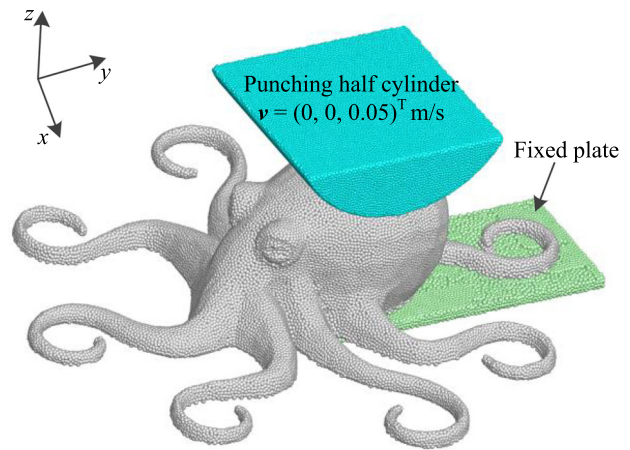


Fig. 44 Oobleck octopus: Initial configuration

6 Concluding remarks

In conclusion, our presented unified non-hourglass formulation addresses a critical gap in TLSPH simulations by offering a comprehensive approach to mitigate hourglass modes, enhancing the reliability and accuracy of simulations across diverse material models and complex scenarios. Through comprehensive validation by benchmark cases, together with a single set of modeling parameters, we show the robustness and accuracy of the present formulation. Furthermore, the successful simulation of the very large deformation of Oobleck serves as a compelling demonstration of the formulation potential in real-world scenarios.

Although the current formulation is designed for TLSPH, it is expected that a similar idea can be applied to updated Lagrangian SPH solid dynamics, as a future work, for situations where latter is preferred. Furthermore, beside hourglass modes, another related numerical stability issue [88], i.e. the non-positivity of the determinant of the deformation gradient under large anisotropic stretch or compression, can be also identified as an area for future research.

Appendix A Plastic algorithm

While specific details regarding the non-linear hardening plastic model are available in our previous work [89] and insights into the viscous plastic model can be found in Ref. [56], we just focus on in-depth elaboration of the perfect and linear hardening plastic models in the following. Note that the primary distinctions among these four plastic models are specifically related to the return mapping which is employed to update the stress and strain states when a material undergoes deformation beyond its elastic limit.

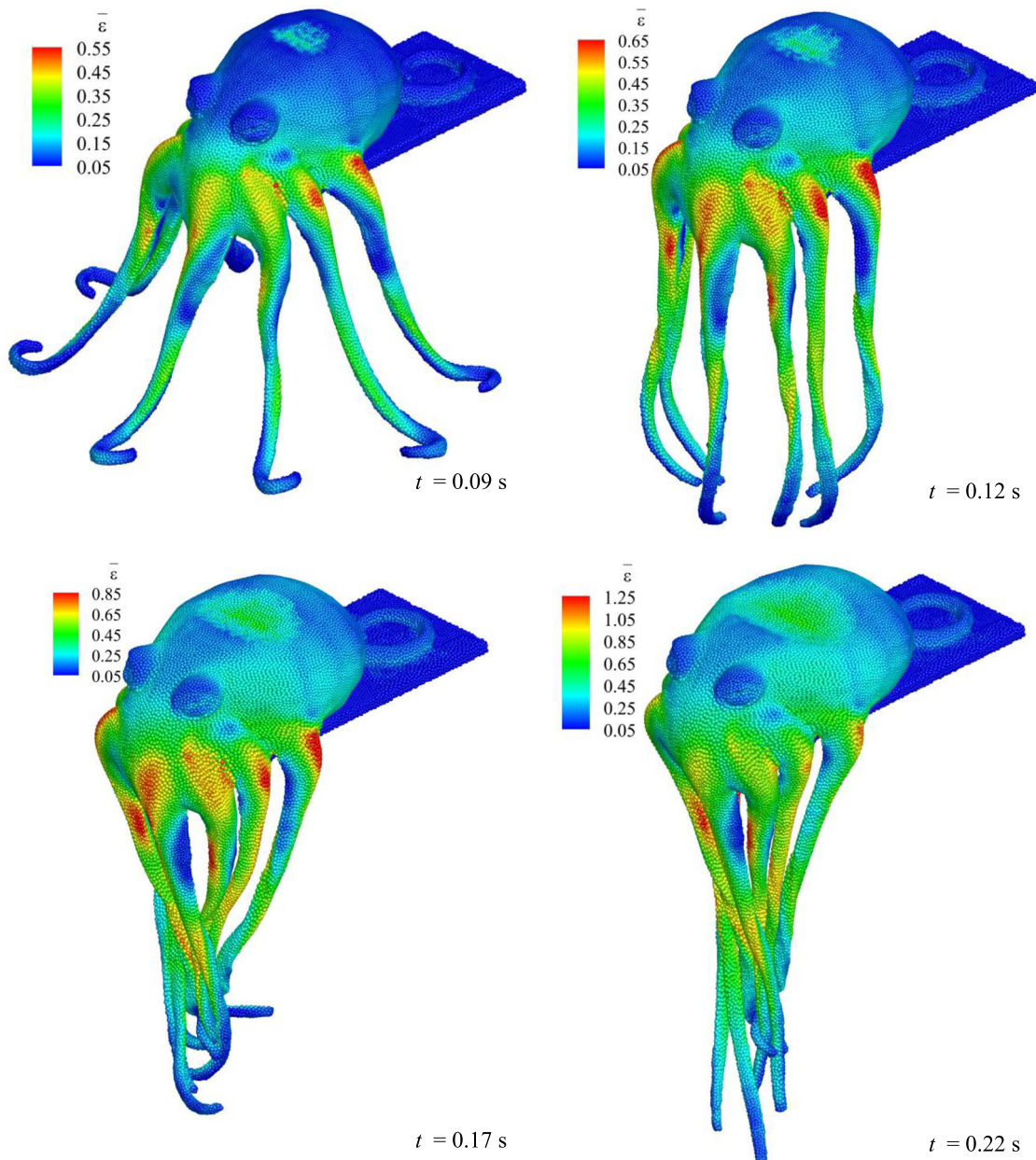


Fig. 45 Oobleck octopus: Deformed configuration of first stage colored by von Mises strain $\bar{\epsilon}$ at serial temporal instants obtained by SPH-UNOG

The scalar yield function $f(\bar{\tau}_{de})$ of the perfect and linear hardening plastic models can be expressed as

$$f(\bar{\tau}_{de}) = \|\bar{\tau}_{de}\|_F - \sqrt{\frac{2}{3}} (\kappa \xi + \tau_y), \tag{A.1}$$

where κ is the hardening modulus, ξ the hardening factor which is 0 for perfect plasticity, and τ_y the initial flow stress, also called yield stress. Note that $\|\cdot\|_F$ denotes a Frobenius norm of a tensor variable. The detailed algorithm of the

linear hardening plastic model from Ref. [55] is presented in Algorithm 1. The superscript $(\cdot)^{trial}$ designates quantities pertaining to a trial elastic state which is assessed to determine whether it exceeds the elastic limit, and the time stepping algorithm is performed in the elastoplastic material description. It is noteworthy that, since a position-based Verlet time-integration scheme [23] is applied in this paper (see also Sec. 2.3), the plastic model algorithm is operated at the mid point of the n -th time step, i.e., the parameter is denoted by $(\cdot)^{n+\frac{1}{2}}$.

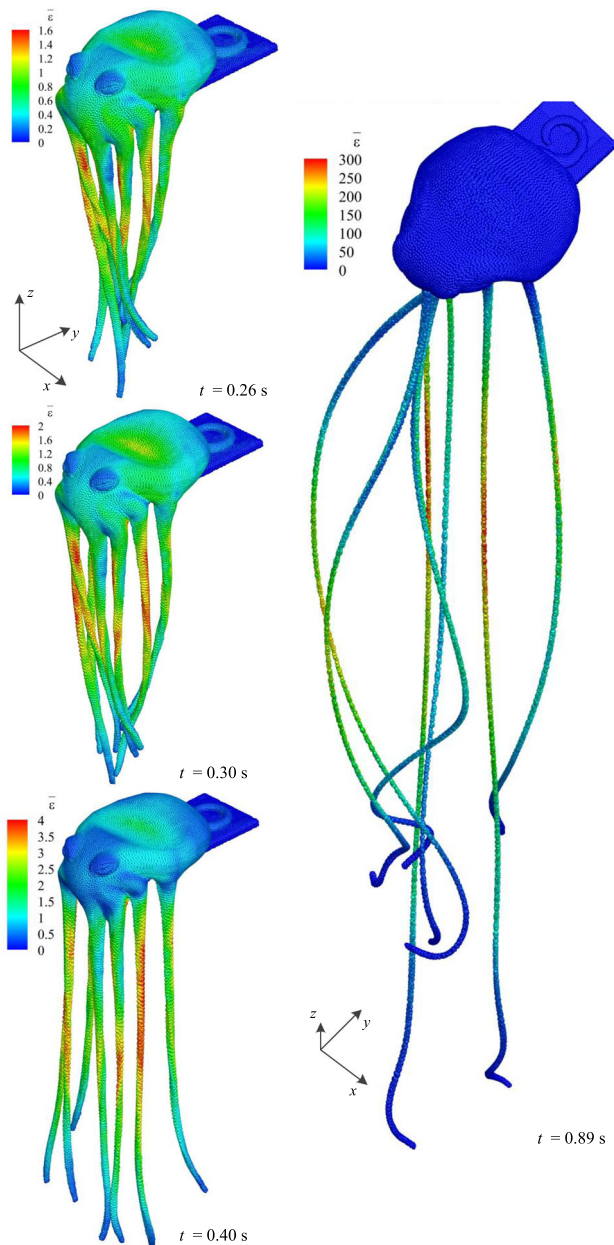


Fig. 46 Oobleck octopus: Deformed configuration of second stage colored by von Mises strain $\bar{\epsilon}$ at serial temporal instants obtained by SPH-UNOG

Algorithm 1: Algorithm for J_2 flow theory with linear isotropic hardening.

- 1 Update deformation tensor $\mathbb{F}^{n+\frac{1}{2}}$
- 2 Compute elastic predictor (Note that $\mathbb{C}_p^0 = \mathbb{I}$)

$$\mathbb{b}_e^{trial,n+\frac{1}{2}} = \mathbb{F}^{n+\frac{1}{2}} \left(\mathbb{C}_p^{n-\frac{1}{2}} \right)^{-1} \left(\mathbb{F}^{n+\frac{1}{2}} \right)^T,$$

$$\mathbb{v}_{de}^{trial,n+\frac{1}{2}} = G \operatorname{dev} \left(\bar{\mathbb{b}}_e^{trial,n+\frac{1}{2}} \right).$$
- 3 Check for plastic loading (Note that $\xi^0 = 0$)

$$f^{trial,n+\frac{1}{2}} = \|\mathbb{v}_{de}^{trial,n+\frac{1}{2}}\|_F - \sqrt{\frac{2}{3}} \left(\kappa \xi^{n-\frac{1}{2}} + \tau_y \right).$$
- 4 **if** $f^{trial,n+\frac{1}{2}} \leq 0$ **then**
- 5 Elastic state, set $(\cdot)^{n+\frac{1}{2}} = (\cdot)^{trial,n+\frac{1}{2}}$, and

$$\left(\mathbb{C}_p^{n+\frac{1}{2}} \right)^{-1} = \left(\mathbb{C}_p^{n-\frac{1}{2}} \right)^{-1}.$$
- 6 **else**
- 7 Plastic state, and perform 9 (the return mapping)
- 8 **end**
- 9 Compute normalized shear modulus

$$\tilde{G} = \frac{1}{d} \operatorname{tr} \left(\bar{\mathbb{b}}_e^{trial,n+\frac{1}{2}} \right) G.$$

Compute increment of hardening factor

$$\xi^{incre,n+\frac{1}{2}} = \frac{0.5 f^{trial,n+\frac{1}{2}}}{\tilde{G} + \kappa/3.0}.$$

Update hardening factor

$$\xi^{n+\frac{1}{2}} = \xi^{n-\frac{1}{2}} + \sqrt{\frac{2}{3}} \xi^{incre,n+\frac{1}{2}}.$$

Update stress and deformation gradient

$$\mathbb{v}_{de}^{n+\frac{1}{2}} = \mathbb{v}_{de}^{trial,n+\frac{1}{2}} - 2\tilde{G}\xi^{incre,n+\frac{1}{2}} \mathbb{v}_{de}^{trial,n+\frac{1}{2}} / \|\mathbb{v}_{de}^{trial,n+\frac{1}{2}}\|_F,$$

$$\mathbb{b}_e^{n+\frac{1}{2}} = \frac{1}{G} \mathbb{v}_{de}^{n+\frac{1}{2}} + \frac{1}{d} \operatorname{tr} \left(\mathbb{b}_e^{trial,n+\frac{1}{2}} \right) \mathbb{I},$$

$$\left(\mathbb{C}_p^{n+\frac{1}{2}} \right)^{-1} = \left(\mathbb{F}^{n+\frac{1}{2}} \right)^{-1} \mathbb{b}_e^{n+\frac{1}{2}} \left(\mathbb{F}^{n+\frac{1}{2}} \right)^{-T}.$$

Acknowledgements D. Wu and X.Y. Hu would like to express their gratitude to the German Research Foundation (DFG) for their sponsorship of this research under grant number DFG HU1527/12-4.

Author contributions D. Wu: Conceptualization, Methodology, Investigation, Visualization, Validation, Formal analysis, Writing—original draft, Writing - review and editing; X.J. Tang: Investigation, Writing—review and editing; S.H. Zhang: Investigation, Writing—review and editing; X.Y. Hu: Supervision, Methodology, Investigation, Writing - review and editing.

Declarations

Conflict of interest The authors declare that they have no known competing financial interests or personal relationships that could have appeared to influence the work reported in this paper.

Open Access This article is licensed under a Creative Commons Attribution 4.0 International License, which permits use, sharing, adaptation, distribution and reproduction in any medium or format, as long as you give appropriate credit to the original author(s) and the source, provide a link to the Creative Commons licence, and indicate if changes were made. The images or other third party material in this article are included in the article's Creative Commons licence, unless indicated otherwise in a credit line to the material. If material is not included in the article's Creative Commons licence and your intended use is not permitted by statutory regulation or exceeds the permitted use, you will need to obtain permission directly from the copyright holder. To view a copy of this licence, visit <http://creativecommons.org/licenses/by/4.0/>.

References

- Randles P, Libersky LD (1996) Smoothed particle hydrodynamics: some recent improvements and applications. *Comput Methods Appl Mech Eng* 139(1–4):375–408
- Luo M, Khayyer A, Lin P (2021) Particle methods in ocean and coastal engineering. *Appl Ocean Res* 114:102734
- Zhang C, Zhu Y-J, Wu D, Adams NA, Hu X (2022) Smoothed particle hydrodynamics: methodology development and recent achievement. *J Hydrodyn* 34(5):767–805
- Xu F, Wang J, Yang Y, Wang L, Dai Z, Han R (2023) On methodology and application of smoothed particle hydrodynamics in fluid, solid and biomechanics. *Acta Mech Sin* 39(2):722185
- Khayyer A, Violeau D, Shao S, Durante D (2023) Preface: latest advances in SPH for fluid mechanics. *Eur J Mech B Fluid* 98:208–210
- Monaghan JJ (2005) Smoothed particle hydrodynamics. *Rep Prog Phys* 68(8):1703
- Liu M, Liu G (2010) Smoothed particle hydrodynamics (SPH): an overview and recent developments. *Arch Comput Methods Eng* 17(1):25–76
- Monaghan JJ (2012) Smoothed particle hydrodynamics and its diverse applications. *Annu Rev Fluid Mech* 44:323–346
- Zhang C, Rezavand M, Zhu Y, Yu Y, Wu D, Zhang W, Wang J, Hu X (2021) SPHinXsys: an open-source multi-physics and multi-resolution library based on smoothed particle hydrodynamics. *Comput Phys Commun* 267:108066
- Sun P-N, Le Touze D, Oger G, Zhang A-M (2021) An accurate FSI-SPH modeling of challenging fluid-structure interaction problems in two and three dimensions. *Ocean Eng* 221:108552
- Antoci C, Gallati M, Sibilla S (2007) Numerical simulation of fluid-structure interaction by SPH. *Comput Struct* 85(11–14):879–890
- Han L, Hu X (2018) SPH modeling of fluid-structure interaction. *J Hydrodyn* 30(1):62–69
- Liu M, Zhang Z (2019) Smoothed particle hydrodynamics (SPH) for modeling fluid-structure interactions. *Sci China Phys Mech Astron* 62(8):1–38
- Pearl JM, Raskin CD, Owen JM (2021) Sph formulation and fluid-solid interface model for the fully compressible interaction of dissimilar materials, Tech. rep., Lawrence Livermore National Lab. (LLNL), Livermore, CA (United States)
- Zhang C, Wang J, Rezavand M, Wu D, Hu X (2021) An integrative smoothed particle hydrodynamics method for modeling cardiac function. *Comput Methods Appl Mech Eng* 381:113847
- Zhang C, Gao H, Hu X (2023) A multi-order smoothed particle hydrodynamics method for cardiac electromechanics with the Purkinje network. *Comput Methods Appl Mech Eng* 407:115885
- Bierwisch C, Mohseni-Mofidi S, Dietemann B, Kraft T, Rudloff J, Lang M (2020) Particle-based simulation, dimensional analysis and experimental validation of laser absorption and thermo-viscous flow during sintering of polymers. *Procedia Cirp* 94:74–79
- Sollich D, Reinheimer E-N, Wagner J, Berger P, Eberhard P (2022) An improved recoil pressure boundary condition for the simulation of deep penetration laser beam welding using the SPH method. *Eur J Mech-B/Fluid* 96:26–38
- Ma G, Bui HH, Lian Y, Tran KM, Nguyen GD (2022) A five-phase approach, SPH framework and applications for predictions of seepage-induced internal erosion and failure in unsaturated/saturated porous media. *Comput Methods Appl Mech Eng* 401:115614
- Lian Y, Bui HH, Nguyen GD, Haque A (2023) An effective and stabilised (u- pl) SPH framework for large deformation and failure analysis of saturated porous media. *Comput Methods Appl Mech Eng* 408:115967
- Feng R, Fourtakas G, Rogers BD, Lombardi D (2024) A general smoothed particle hydrodynamics (SPH) formulation for coupled liquid flow and solid deformation in porous media. *Comput Methods Appl Mech Eng* 419:116581
- Vignjevic R, Campbell J, Libersky L (2000) A treatment of zero-energy modes in the smoothed particle hydrodynamics method. *Comput Methods Appl Mech Eng* 184(1):67–85
- Zhang C, Rezavand M, Hu X (2021) A multi-resolution SPH method for fluid-structure interactions. *J Comput Phys* 429:110028
- Vignjevic R, Campbell J (2009) Review of development of the smooth particle hydrodynamics (SPH) method. In: *Predictive Modeling of Dynamic Processes*, Springer, pp 367–396
- Dyka C, Randles P, Ingel R (1997) Stress points for tension instability in SPH. *Int J Numer Meth Eng* 40(13):2325–2341
- Belytschko T, Guo Y, Kam Liu W, Ping Xiao S (2000) A unified stability analysis of meshless particle methods. *Int J Numer Meth Eng* 48(9):1359–1400
- Randles P, Libersky L (2000) Normalized SPH with stress points. *Int J Numer Meth Eng* 48(10):1445–1462
- Maurel B, Combescure A (2008) An SPH shell formulation for plasticity and fracture analysis in explicit dynamics. *Int J Numer Meth Eng* 76(7):949–971
- Islam MRI, Peng C (2019) A stabilized total-Lagrangian SPH method for large deformation and failure in geomaterials, arXiv preprint [arXiv:1907.06990](https://arxiv.org/abs/1907.06990)
- Beissel S, Belytschko T (1996) Nodal integration of the element-free Galerkin method. *Comput Methods Appl Mech Eng* 139(1–4):49–74
- Kondo M, Suzuki Y, Koshizuka S (2010) Suppressing local particle oscillations in the Hamiltonian particle method for elasticity. *Int J Numer Meth Eng* 81(12):1514–1528
- Belytschko T, Ong JS-J, Liu WK, Kennedy JM (1984) Hourglass control in linear and nonlinear problems. *Comput Methods Appl Mech Eng* 43(3):251–276
- Liu WK, Ong JS-J, Uras RA (1985) Finite element stabilization matrices—a unification approach. *Comput Methods Appl Mech Eng* 53(1):13–46
- Owen JM (2004) A tensor artificial viscosity for SPH. *J Comput Phys* 201(2):601–629
- Lee CH, Gil AJ, Greto G, Kulasegaram S, Bonet J (2016) A new Jameson–Schmidt–Turkel smooth particle hydrodynamics algorithm for large strain explicit fast dynamics. *Comput Methods Appl Mech Eng* 311:71–111
- Zhang C, Zhu Y, Yu Y, Wu D, Rezavand M, Shao S, Hu X (2022) An artificial damping method for total Lagrangian SPH method with application in biomechanics. *Eng Anal Boundary Elem* 143:1–13

37. Ganzenmüller GC (2015) An hourglass control algorithm for Lagrangian smooth particle hydrodynamics. *Comput Methods Appl Mech Eng* 286:87–106
38. Belytschko T (1983) Correction of article by DP Flanagan and T. Belytschko. *Int J Numer Methods Eng* 19(3):467–468
39. Stainier L, Ponthot JP (1994) An improved one-point integration method for large strain elastoplastic analysis. *Comput Methods Appl Mech Eng* 118(1–2):163–177
40. O'Connor J, Rogers BD (2021) A fluid-structure interaction model for free-surface flows and flexible structures using smoothed particle hydrodynamics on a GPU. *J Fluids Struct* 104:103312
41. de Campos PRR, Gil AJ, Lee CH, Giacomini M, Bonet J (2022) A new updated reference Lagrangian smooth particle hydrodynamics algorithm for isothermal elasticity and elasto-plasticity. *Comput Methods Appl Mech Eng* 392:114680
42. Lee CH, de Campos PR Refachinho, Gil AJ, Giacomini M, Bonet J (2023) An entropy-stable updated reference lagrangian smoothed particle hydrodynamics algorithm for thermo-elasticity and thermo-visco-plasticity. *Computat Particle Mech.* 1–39
43. Wu D, Zhang C, Tang X, Hu X (2023) An essentially non-hourglass formulation for total Lagrangian smoothed particle hydrodynamics. *Comput Methods Appl Mech Eng* 407:115915
44. Zhang C, Rezavand M, Zhu Y, Yu Y, Wu D, Zhang W, Zhang S, Wang J, Hu X (2020) SPHinXsys: an open-source meshless, multi-resolution and multi-physics library. *Softw Impacts* 6:100033
45. Bonet J, Lok T-S (1999) Variational and momentum preservation aspects of smooth particle hydrodynamic formulations. *Comput Methods Appl Mech Eng* 180(1–2):97–115
46. Bonet J, Kulasegaram S (2002) A simplified approach to enhance the performance of smooth particle hydrodynamics methods. *Appl Math Comput* 126(2–3):133–155
47. Vignjevic R, Reveles JR, Campbell J (2006) SPH in a total Lagrangian formalism. *CMC-Tech Sci Press-* 4(3):181
48. Westhofen L, Jeske S, Bender J (2023) A comparison of linear consistent correction methods for first-order SPH derivatives. *Proc ACM Comput Graph Interact Tech* 6(3):1–20
49. Hirsch C (1988) Numerical calculation of internal and external flows, vol 1 and 2. Wiley, New York
50. Anderson JD (1995) Computational fluid dynamics: the basics with applications. McGraw-Hill, New York
51. Monaghan JJ (1982) Why particle methods work. *SIAM J Sci Stat Comput* 3(4):422–433
52. Monaghan JJ (1992) Smoothed particle hydrodynamics. *Ann Rev Astron Astrophys* 30:543–574
53. Liu G-R, Liu MB (2003) Smoothed particle hydrodynamics: a meshfree particle method. World Scientific, Singapore
54. Zhang C, Rezavand M, Hu X (2021) A multi-resolution SPH method for fluid-structure interactions. *J Comput Phys* 429:110028
55. Simo JC, Hughes TJ (2006) Computational inelasticity, vol 7. Springer Science & Business Media, Berlin
56. Yue Y, Smith B, Batty C, Zheng C, Grinspun E (2015) Continuum foam: a material point method for shear-dependent flows. *ACM Trans Graph* 34(5):1–20
57. Mises R (1913) *Mechanik der festen Körper im plastisch-deformablen Zustand*. Nachrichten von der Gesellschaft der Wissenschaften zu Göttingen, Mathematisch-Physikalische Klasse 1913:582–592
58. Holzapfel GA, Ogden RW (2009) Constitutive modelling of passive myocardium: a structurally based framework for material characterization. *Philos Trans Royal Soc A: Math Phys Eng Sci* 367(1902):3445–3475
59. Nash MP, Panfilov AV (2004) Electromechanical model of excitable tissue to study reentrant cardiac arrhythmias. *Prog Biophys Mol Biol* 85:501–522
60. Wendland H (1995) Piecewise polynomial, positive definite and compactly supported radial functions of minimal degree. *Adv Comput Math* 4(1):389–396
61. Landau LD, Lifchits EM (1986) *Course of theoretical physics: Theory of elasticity*
62. Zhang C, Hu XY, Adams NA (2017) A generalized transport-velocity formulation for smoothed particle hydrodynamics. *J Comput Phys* 337:216–232
63. Leissa AW (1969) *Vibration of plates*, Vol. 160, Scientific and Technical Information Division, National Aeronautics and Space Administration
64. Khayyer A, Gotoh H, Shimizu Y, Nishijima Y (2021) A 3D Lagrangian meshfree projection-based solver for hydroelastic Fluid-Structure Interactions. *J Fluids Struct* 105:103342
65. Khayyer A, Shimizu Y, Gotoh H, Hattori S (2022) A 3D SPH-based entirely Lagrangian meshfree hydroelastic FSI solver for anisotropic composite structures. *Appl Math Model* 112:560–613
66. Reese S, Küssner M, Reddy BD (1999) A new stabilization technique for finite elements in non-linear elasticity. *Int J Numer Meth Eng* 44(11):1617–1652
67. Wriggers P, De Bellis M, Hudobivnik B (2021) A taylor-hood type virtual element formulations for large incompressible strains. *Comput Methods Appl Mech Eng* 385:114021
68. Chen JS, Pan C, Wu CT, Liu WK (1996) Reproducing kernel particle methods for large deformation analysis of non-linear structures. *Comput Methods Appl Mech Eng* 139(1–4):195–227
69. Zhu Y, Zhang C, Hu X (2022) A dynamic relaxation method with operator splitting and random-choice strategy for SPH. *J Comput Phys* 458:111105
70. Aguirre M, Gil AJ, Bonet J, Carreño AA (2014) A vertex centered finite volume Jameson–Schmidt–Turkel (JST) algorithm for a mixed conservation formulation in solid dynamics. *J Comput Phys* 259:672–699
71. Scovazzi G, Carnes B, Zeng X, Rossi S (2016) A simple, stable, and accurate linear tetrahedral finite element for transient, nearly, and fully incompressible solid dynamics: a dynamic variational multiscale approach. *Int J Numer Meth Eng* 106(10):799–839
72. Rossi S, Abboud N, Scovazzi G (2016) Implicit finite incompressible elastodynamics with linear finite elements: a stabilized method in rate form. *Comput Methods Appl Mech Eng* 311:208–249
73. Lee CH, Gil AJ, Ghavamian A, Bonet J (2019) A total Lagrangian upwind smooth particle hydrodynamics algorithm for large strain explicit solid dynamics. *Comput Methods Appl Mech Eng* 344:209–250
74. Lee CH, Gil AJ, de Campos PRR, Bonet J, Jaugielavičius T, Joshi S, Wood C (2024) A novel Arbitrary Lagrangian Eulerian Smooth Particle Hydrodynamics algorithm for nonlinear solid dynamics. *Comput Methods Appl Mech Eng* 427:117055
75. Garcia-Blanco E, Ortigosa R, Gil AJ, Lee CH, Bonet J (2019) A new computational framework for electro-activation in cardiac mechanics. *Comput Methods Appl Mech Eng* 348:796–845
76. Taylor GI (1948) The use of flat-ended projectiles for determining dynamic yield stress. I. Theoretical considerations. *Proc Royal Soc London Ser A Math Phys Sci* 194(1038):289–299
77. Wilkins ML, Guinan MW (1973) Impact of cylinders on a rigid boundary. *J Appl Phys* 44(3):1200–1206
78. Bonet J, Burton A (1998) A simple average nodal pressure tetrahedral element for incompressible and nearly incompressible dynamic explicit applications. *Commun Numer Methods Eng* 14(5):437–449
79. Li G, Belytschko T (2001) Element-free Galerkin method for contact problems in metal forming analysis. *Eng Comput* 18(1/2):62–78
80. Plunkett B, Cazacu O, Lebensohn R, Barlat F (2007) Elastic-viscoplastic anisotropic modeling of textured metals and validation using the Taylor cylinder impact test. *Int J Plast* 23(6):1001–1021

81. Ma S, Zhang X, Qiu X (2009) Comparison study of MPM and SPH in modeling hypervelocity impact problems. *Int J Impact Eng* 36(2):272–282
82. Lee CH, Gil AJ, Bonet J (2014) Development of a stabilised Petrov–Galerkin formulation for conservation laws in Lagrangian fast solid dynamics. *Comput Methods Appl Mech Eng* 268:40–64
83. Haider J, Lee CH, Gil AJ, Bonet J (2017) A first-order hyperbolic framework for large strain computational solid dynamics: an upwind cell centred total Lagrangian scheme. *Int J Numer Meth Eng* 109(3):407–456
84. Ming L, Pantalé O (2018) An efficient and robust VUMAT implementation of elastoplastic constitutive laws in Abaqus/Explicit finite element code. *Mechanics & Industry* 19(3):308
85. Greto G, Kulasegaram S (2020) An efficient and stabilised SPH method for large strain metal plastic deformations. *Comput Part Mech* 7(3):523–539
86. Taylor R (2011) Isogeometric analysis of nearly incompressible solids. *Int J Numer Meth Eng* 87(1–5):273–288
87. Elguedj T, Hughes TJ (2014) Isogeometric analysis of nearly incompressible large strain plasticity. *Comput Methods Appl Mech Eng* 268:388–416
88. Smith B, Goes FD, Kim T (2018) Stable neo-hookean flesh simulation. *ACM Trans Graph* 37(2):1–15
89. Tang X, Wu D, Wang Z, Haidn O, Hu X (2023) An explicit multi-time stepping algorithm for multi-time scale coupling problems in SPH, arXiv preprint [arXiv:2309.04010](https://arxiv.org/abs/2309.04010)

Publisher's Note Springer Nature remains neutral with regard to jurisdictional claims in published maps and institutional affiliations.

A.3 Paper III

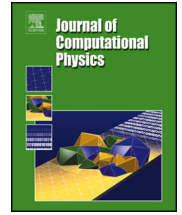
Dong Wu, Chi Zhang, Xiangyu Hu

An SPH formulation for general plate and shell structures with finite deformation and large rotation

In *Journal of Computational Physics*, Volume 510, 2024, p. 113113, DOI: <https://doi.org/10.1016/j.jcp.2024.113113>.

Copyright © 2024 Elsevier. Reprinted with permission.

Contribution: My contribution to this work was the development of the method and the corresponding computer code for its implementation. I performed simulations and analyzed the results, and wrote the manuscript for the publication.



An SPH formulation for general plate and shell structures with finite deformation and large rotation

Dong Wu^a, Chi Zhang^{a,b}, Xiangyu Hu^{a,*}

^a TUM School of Engineering and Design, Technical University of Munich, 85748 Garching, Germany

^b Huawei Technologies Munich Research Center, 80992 Munich, Germany

ARTICLE INFO

Keywords:

Uflyand–Mindlin plate theory
Finite deformations
Geometric non-linearity
Quasi-static and dynamic analyses
Non-isotropic damping
Hourglass modes

ABSTRACT

In this paper, we propose a reduced-dimensional smoothed particle hydrodynamics (SPH) formulation for quasi-static and dynamic analyses of plate and shell structures undergoing finite deformation and large rotation. By exploiting Uflyand–Mindlin plate theory, the present surface-particle formulation is able to resolve the thin structures by using only one layer of particles at the mid-surface. To resolve the geometric non-linearity and capture finite deformation and large rotation, two reduced-dimensional linear-reproducing correction matrices are introduced, and weighted non-singularity conversions between the rotation angle and pseudo normal are formulated. A new non-isotropic Kelvin–Voigt damping is proposed especially for the both thin and moderately thick plate and shell structures to increase the numerical stability. In addition, a shear-scaled momentum-conserving hourglass control algorithm with an adaptive limiter is introduced to suppress the mismatches between the particle position and pseudo normal and those estimated with the deformation gradient. A comprehensive set of test problems, for which the analytical or numerical results from literature or those of the volume-particle SPH model are available for quantitative and qualitative comparison, are examined to demonstrate the accuracy and stability of the present method.

1. Introduction

For computational continuum dynamics, as alternatives to conventional mesh-based methods, e.g. finite element method (FEM) and finite volume method (FVM), meshless methods have flourished in the past decades [1–4]. Smoothed particle hydrodynamics (SPH), initially developed by Lucy [5] and Gingold and Monaghan [6] for astrophysical simulations, is one typical example. In SPH, the continuum is modeled by particles associated with physical properties such as mass and velocity, and the governing equations are discretized in the form of particle interactions using a Gaussian-like kernel function [7,3,8]. Since a significant number of physical system abstractions can be realized through particle interactions, SPH has been used to model multi-physical systems within a unified computational framework [9], which is able to achieve seamless monolithic, strong and conservative coupling [10,11].

To achieve such a unified computational framework, it is crucial to discretize all relevant physics equations using effective and efficient SPH methods. In the case of plate and shell structures which are omnipresent thin structures in scientific and engineering fields such as shipbuilding [12,13], aerospace [14], and medical treatment [15], etc., the traditional full-dimensional or volume-particle SPH method, is not computationally efficient [16]. Since there are well-developed and matured reduced-dimensional theories,

* Corresponding author.

E-mail addresses: dong.wu@tum.de (D. Wu), c.zhang@tum.de (C. Zhang), xiangyu.hu@tum.de (X. Hu).

<https://doi.org/10.1016/j.jcp.2024.113113>

Received 7 September 2023; Received in revised form 10 May 2024; Accepted 13 May 2024

Available online 17 May 2024

0021-9991/© 2024 The Author(s). Published by Elsevier Inc. This is an open access article under the CC BY license (<http://creativecommons.org/licenses/by/4.0/>).

such as Kirchhoff-Love [17] and Uflyand-Mindlin (or Mindlin-Reissner) [18–21], for plate and shell structures based on mid-surface reconstruction, it is expected to develop the computationally much more efficient reduced-dimensional or surface-particle SPH method with a single-layer of particles only.

The early meshless methods for plates and shells were based on Petrov or element-free Galerkin formulation [22–26], or the reproducing kernel particle method [27–29], including plastic deformation and material failure [26]. As for SPH, Maurel and Combescure [30] first developed a surface-particle SPH method for total Lagrangian quasi-static and dynamic analyses of moderately thick plates and shells based on the Uflyand-Mindlin theory and the assumption of small deformation. In their work, besides an artificial viscosity term to alleviate numerical instability issues, a stress point method is applied to temper hourglass or zero-energy modes which exhibit in the traditional SPH method using collocated particles for both deformation and stress. While being effective on preventing zero-energy modes, using stress points may faces several issues, such as how to locate or generate these points for complex geometries, complicated numerical algorithms and the compensation of computational efficiency [31,32]. Nevertheless, this method was later applied in large deformation analyses by Ming et al. [33] and dynamic damage-fracture analyses by Caleyron et al. [34]. Lin et al. [35] developed a similar method for quasi-static analyses, but applied an artificial viscosity term based on membrane and shearing decomposition. Ming et al. [36] first considered finite deformation by taking all strain terms into account with the help of Gauss-Legendre quadrature for more accurately capturing of non-linear stress. Since the introduction of the surface-particle model in SPH, it has succeeded in some engineering applications, such as composite plate and shell structures [37,38], explosion analysis [39], and ship simulations [13].

In this work, we propose a collocated surface-particle SPH formulation for total Lagrangian quasi-static and dynamic analyses of general plate or shell structures, which may be thin or have moderate thickness, involving finite deformation or/and large rotation. First, to better resolve the geometric non-linearity induced by finite deformation and large rotation, two new reduced-dimensional correction matrices for linearly reproducing position and normal direction are introduced, and a weighted conversion algorithm, which achieves non-singularity under large rotation, is proposed. Second, a new non-isotropic Kelvin-Voigt damping base on Ref. [40] is proposed for achieve good numerical stability for both thin and moderately thick plate or shell structures. Third, in order to address hourglass modes using collocated particles only other than introducing extra stress points, drawing the inspiration from Refs. [41,31], a shear-scaled momentum-conserving formulation with an adaptive limiter is developed by mitigating the discrepancy between the actual particle position and pseudo normal and those estimated by the deformation gradient. A set of numerical examples involving quasi-static and dynamic analyses for both thin and moderately thick plate or shell structures are given. The results are compared with analytical, numerical solutions in literature or/and those obtained by the volume-particle SPH method to demonstrate the numerical accuracy and stability of the present method.

The remainder of this manuscript is organized as follows. Section 2 introduces the theoretical model of plates and shells, including the kinematics, constitutive relation, stress correction and conservation equations. The proposed surface-particle SPH formulation, including the reduced-dimensional linear-reproducing correction matrices, weighted conversion algorithm, non-isotropic damping and momentum-conserving hourglass control, is described in Section 3. Numerical examples are presented and discussed in Section 4 and then concluding remarks are given in Section 5. For a better comparison and future opening for in-depth studies, all the computational codes of this work are released in the open-source repository of SPHinXsys [42,9] at <https://github.com/Xiangyu-Hu/SPHinXsys>.

2. Theoretical models

We first introduce the theoretical mode of 3D plate, and then that of 3D shell in which material points may possess different initial normal directions leading to different initial local coordinate systems. After that, we briefly describe the 2D plate and shell models, which resolve the plane strain problem, as a simplification of the 3D counterparts.

2.1. 3D plate model

We consider the Uflyand–Mindlin plate theory [18,19] to account for transverse shear stress which is significant for moderately thick plates. The theory implies that the plate behavior can be represented by one layer of material points at its mid-surface, as shown in Fig. 1.

2.1.1. Kinematics

We introduce $\mathbf{X} = (X, Y, Z)$ to represent the global coordinate system, and $\boldsymbol{\xi} = (\xi, \eta, \zeta)$ and $\mathbf{x} = (x, y, z)$, associated with so-called pseudo-normal vector \mathbf{n} , to denote the initial and current local coordinate systems, respectively. Note that the initial local coordinate system is same with the global one for plate. Each material point possesses five degrees of freedom, viz., three translations $\mathbf{u} = \{u, v, w\}^T$ and two rotations $\boldsymbol{\theta} = \{\theta, \varphi\}^T$ expressed in the global coordinates. Positive values of θ and φ indicate that the plate is rotated anticlockwise around the coordinate axis when the axis points toward the observer and the coordinate system is right-handed. The two rotations are used to update the pseudo-normal $\mathbf{n} = \{n_1, n_2, n_3\}^T$ which is also defined in the global coordinate system and remains straight but is not necessarily perpendicular to the mid-surface, i.e., the pseudo normal may be different with the real normal \mathbf{n}_r , as shown in Fig. 1. Note that $\mathbf{n}^0 = \{0, 0, 1\}^T$ denotes the pseudo-normal in the initial configuration with the superscript $(\bullet)^0$ denoting the initial configuration.

For a 3D plate, the position \mathbf{r} of a material point at a distance χ away from the mid-surface along the pseudo normal \mathbf{n} can be expressed as

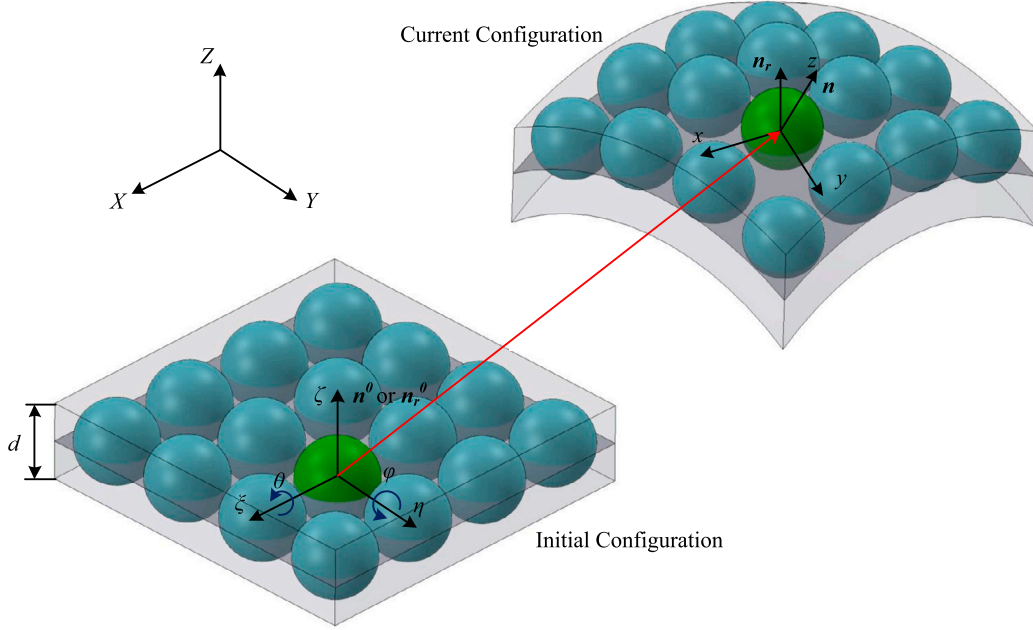


Fig. 1. Schematic of a 3D plate model. Note that, the spherical shape (also in other figures) here does not represent the exact shape of a SPH particle, which is defined by the SPH formulation, but is for schematic illustration.

$$\mathbf{r}(\xi, \eta, \chi, t) = \mathbf{r}_m(\xi, \eta, t) + \chi \mathbf{n}(\xi, \eta, t), \quad \chi \in [-d/2, d/2], \quad (1)$$

where d is the thickness, \mathbf{r}_m the position of the material point at the mid-surface with the subscript $(\bullet)_m$ denoting the mid-surface. Note that since the thickness is assumed to be constant during deformation and the pseudo normal \mathbf{n} represents the plate thickness direction, the distance χ is always between $-d/2$ and $d/2$. Therefore, the displacement \mathbf{u} of the material point can be determined by

$$\mathbf{u}(\xi, \eta, \chi, t) = \mathbf{u}_m(\xi, \eta, t) + \chi \Delta \mathbf{n}(\xi, \eta, t), \quad (2)$$

where $\Delta \mathbf{n} = \mathbf{n} - \mathbf{n}^0$. Then we can define the deformation gradient tensor as

$$\mathbb{F} = \nabla^0 \mathbf{r} = \nabla^0 \mathbf{u} + \mathbb{I} = (\mathbf{a}_1, \mathbf{a}_2, \mathbf{a}_3), \quad (3)$$

where $\nabla^0 \equiv \partial/\partial \xi$ is the gradient operator with respect to the initial configuration, \mathbb{I} the identity matrix, and $\mathbf{a}_1, \mathbf{a}_2, \mathbf{a}_3$ are specified by

$$\begin{cases} \mathbf{a}_1 = \mathbf{r}_{m,\xi} + \chi \mathbf{n}_\xi \\ \mathbf{a}_2 = \mathbf{r}_{m,\eta} + \chi \mathbf{n}_\eta \\ \mathbf{a}_3 = \mathbf{n} \end{cases} \quad (4)$$

with $\nabla^0 \mathbf{r}_m \equiv (\mathbf{r}_{m,\xi}, \mathbf{r}_{m,\eta})^T$ and $\nabla^0 \mathbf{n} \equiv (\mathbf{n}_\xi, \mathbf{n}_\eta)^T$. The deformation gradient tensor can be decomposed into two components as

$$\mathbb{F} = \mathbb{F}_m + \chi \mathbb{F}_n, \quad (5)$$

where $\mathbb{F}_m = (\mathbf{r}_{m,\xi}^T, \mathbf{r}_{m,\eta}^T, \mathbf{n}^T)$ and $\mathbb{F}_n = (\mathbf{n}_\xi^T, \mathbf{n}_\eta^T, 0)$. The change rate of this deformation gradient is expressed as

$$\dot{\mathbb{F}} = \nabla^0 \dot{\mathbf{u}} = \nabla^0 \dot{\mathbf{u}}_m + \chi \nabla^0 \dot{\mathbf{n}}, \quad (6)$$

where $\dot{\mathbf{u}}_m$ and $\dot{\mathbf{n}}$ denote the velocity and change rate of pseudo-normal, respectively. Furthermore, the real normal \mathbf{n}_r is given as

$$\mathbf{n}_r = \frac{\mathbf{r}_{m,\xi} \times \mathbf{r}_{m,\eta}}{|\mathbf{r}_{m,\xi} \times \mathbf{r}_{m,\eta}|}. \quad (7)$$

2.1.2. Constitutive relation

With the deformation gradient tensor \mathbb{F} , the Green-Lagrangian strain tensor \mathbb{E} can be obtained as

$$\mathbb{E} = \frac{1}{2} (\mathbb{F}^T \mathbb{F} - \mathbb{I}) = \frac{1}{2} (\mathbb{C} - \mathbb{I}), \quad (8)$$

where \mathbb{C} is the right Cauchy deformation gradient tensor. The Eulerian Almansi strain \mathbb{e} can be converted from \mathbb{E} as

$$\mathcal{E} = \mathbb{F}^{-T} \cdot \mathbb{E} \cdot \mathbb{F}^{-1} = \frac{1}{2} (\mathbb{I} - \mathbb{F}^{-T} \mathbb{F}^{-1}). \quad (9)$$

When the material is linear and isotropic, the Cauchy stress \mathcal{G} reads

$$\begin{aligned} \mathcal{G} &= K \operatorname{tr}(\mathcal{E}) \mathbb{I} + 2G \left(\mathcal{E} - \frac{1}{3} \operatorname{tr}(\mathcal{E}) \mathbb{I} \right) \\ &= \lambda \operatorname{tr}(\mathcal{E}) \mathbb{I} + 2\mu \mathcal{E}, \end{aligned} \quad (10)$$

where λ and μ are the Lamé constants, $K = \lambda + 2\mu/3$ the bulk modulus and $G = \mu$ the shear modulus. The relationship between the two moduli is given by

$$E = 2G(1 + \nu) = 3K(1 - 2\nu), \quad (11)$$

where E denotes the Young's modulus and ν the Poisson's ratio.

2.1.3. Stress correction

As the thickness is significantly less than the length and width of plate, the following boundary conditions hold when the plate is free from external forces on its surfaces where $\chi = \pm \frac{d}{2}$ or $z = \pm \frac{d}{2}$

$$\sigma_{xz}^l \Big|_{z=\pm \frac{d}{2}} = 0, \quad \sigma_{yz}^l \Big|_{z=\pm \frac{d}{2}} = 0, \quad (12)$$

$$\sigma_{zz}^l \Big|_{z \in [-\frac{d}{2}, \frac{d}{2}]} = 0, \quad (13)$$

with the superscript $(\bullet)^l$ denoting the current local coordinates. Taking the boundary condition Eq. (13) and constitutive Eq. (10) into account, the following relation of strains holds [27]

$$\bar{\epsilon}_{zz}^l = \frac{-\nu (\epsilon_{xx}^l + \epsilon_{yy}^l)}{1 - \nu}, \quad (14)$$

where the current local strain \mathcal{E}^l is obtained by

$$\mathcal{E}^l = \mathbb{Q} \mathcal{E} \mathbb{Q}^T. \quad (15)$$

Here, \mathbb{Q} is the orthogonal transformation matrix from the global to current local coordinates. Following Batoz and Dhatt [43], \mathbb{Q} can be given as

$$\mathbb{Q} = \begin{bmatrix} n_3 + \frac{(n_2)^2}{1+n_3} & -\frac{n_1 n_2}{1+n_3} & -n_1 \\ -\frac{n_1 n_2}{1+n_3} & n_3 + \frac{(n_1)^2}{1+n_3} & -n_2 \\ n_1 & n_2 & n_3 \end{bmatrix}. \quad (16)$$

To satisfy the boundary conditions of Eq. (12), the transverse shear stress should be corrected as [44]

$$\bar{\sigma}_{xz}^l = \bar{\sigma}_{zx}^l = \kappa \sigma_{xz}^l, \quad \bar{\sigma}_{yz}^l = \bar{\sigma}_{zy}^l = \kappa \sigma_{yz}^l, \quad (17)$$

where κ denotes the shear correction factor which is typically set to 5/6 for the rectangular section of the isotropic plate. Taking the corrected strain $\bar{\mathcal{E}}^l$ into constitutive Eq. (10) and then applying Eq. (17), the corrected current local Cauchy stress $\bar{\mathcal{G}}^l$ is obtained.

2.1.4. Conservation equations

The mass conservation equation can be written as

$$\rho = J_m^{-1} \rho^0, \quad (18)$$

where $J_m = \det(\mathbb{F}_m)$, ρ^0 and ρ represent the initial and current densities, respectively. The momentum conservation equation is

$$\rho \ddot{\mathbf{u}}^l = \nabla \cdot (\bar{\mathcal{G}}^l)^T \quad (19)$$

or

$$\rho \begin{bmatrix} \ddot{u}^l \\ \ddot{v}^l \\ \ddot{w}^l \end{bmatrix} = \begin{bmatrix} \frac{\partial \bar{\sigma}_{xx}^l}{\partial x} + \frac{\partial \bar{\sigma}_{xy}^l}{\partial y} + \frac{\partial \bar{\sigma}_{xz}^l}{\partial z} \\ \frac{\partial \bar{\sigma}_{yx}^l}{\partial x} + \frac{\partial \bar{\sigma}_{yy}^l}{\partial y} + \frac{\partial \bar{\sigma}_{yz}^l}{\partial z} \\ \frac{\partial \bar{\sigma}_{zx}^l}{\partial x} + \frac{\partial \bar{\sigma}_{zy}^l}{\partial y} + \frac{\partial \bar{\sigma}_{zz}^l}{\partial z} \end{bmatrix}. \quad (20)$$

With Eqs. (12) and (13), we can integrate Eq. (20) along χ or $z \in [-d/2, d/2]$ as

$$d\rho \begin{bmatrix} \ddot{u}_m^l \\ \ddot{v}_m^l \\ \ddot{w}_m^l \end{bmatrix} = \begin{bmatrix} \frac{\partial N_{xx}^l}{\partial x} + \frac{\partial N_{xy}^l}{\partial y} \\ \frac{\partial N_{yx}^l}{\partial x} + \frac{\partial N_{yy}^l}{\partial y} \\ \frac{\partial N_{zx}^l}{\partial x} + \frac{\partial N_{zy}^l}{\partial y} \end{bmatrix}, \quad (21)$$

where the stress resultant \mathbb{N}^l is calculated by the Gauss–Legendre quadrature rule as

$$\mathbb{N}^l = \int_{-d/2}^{d/2} \bar{\sigma}^l(z) dz = \sum_{ip=1}^N \bar{\sigma}^l(z_{ip}) A_{ip}. \quad (22)$$

Here, z_{ip} is the integral point, A_{ip} the weight, and N the number of the integral point. Since the quadrature rule is conducted to yield an exact result for polynomials of degree $2N - 1$ or lower [45], N is determined by the applied constitutive relation.

By multiplying both sides of Eq. (19) by z and integrating along $z \in [-d/2, d/2]$, the angular momentum conservation equation can be obtained as

$$\frac{d^3}{12} \rho \begin{bmatrix} \ddot{n}_1^l \\ \ddot{n}_2^l \\ \ddot{n}_3^l \end{bmatrix} = \begin{bmatrix} \frac{\partial M_{xx}^l}{\partial x} + \frac{\partial M_{xy}^l}{\partial y} \\ \frac{\partial M_{yx}^l}{\partial x} + \frac{\partial M_{yy}^l}{\partial y} \\ \frac{\partial M_{zx}^l}{\partial x} + \frac{\partial M_{zy}^l}{\partial y} \end{bmatrix} + \begin{bmatrix} -N_{xz}^l \\ -N_{yz}^l \\ 0 \end{bmatrix}, \quad (23)$$

where the moment resultant \mathbb{M}^l is calculated as

$$\mathbb{M}^l = \int_{-d/2}^{d/2} z \bar{\sigma}^l(z) dz = \sum_{ip=1}^N z_{ip} \bar{\sigma}^l(z_{ip}) A_{ip}. \quad (24)$$

Note that

$$\int_{-d/2}^{d/2} z \frac{\partial \bar{\sigma}_{xz}^l}{\partial z} dz = \left[z \bar{\sigma}_{xz}^l \right]_{-d/2}^{d/2} - \int_{-d/2}^{d/2} \bar{\sigma}_{xz}^l dz = -N_{xz}^l. \quad (25)$$

Therefore, the two governing equations, including the evolution of mid-surface displacement and pseudo normal, respectively, for the 3D plate can be described as

$$\begin{cases} d\rho \ddot{\mathbf{u}}_m^l = \nabla^l \cdot (\mathbb{N}^l)^T \\ \frac{d^3}{12} \rho \ddot{\mathbf{n}}^l = \nabla^l \cdot (\mathbb{M}^l)^T + \mathbf{Q}^l, \end{cases} \quad (26)$$

where

$$\mathbb{N}^l = \begin{bmatrix} N_{xx}^l & N_{xy}^l & 0 \\ N_{yx}^l & N_{yy}^l & 0 \\ N_{zx}^l & N_{zy}^l & 0 \end{bmatrix}, \mathbb{M}^l = \begin{bmatrix} M_{xx}^l & M_{xy}^l & 0 \\ M_{yx}^l & M_{yy}^l & 0 \\ M_{zx}^l & M_{zy}^l & 0 \end{bmatrix}, \mathbf{Q}^l = \begin{bmatrix} -N_{xz}^l \\ -N_{yz}^l \\ 0 \end{bmatrix}. \quad (27)$$

In total Lagrangian formulation, the conservation equations above are converted into

$$\begin{cases} d\rho^0 \ddot{\mathbf{u}}_m = (\mathbb{F}_m)^{-T} \nabla^0 \cdot (\mathbf{J}_m \mathbb{N}^T) \\ \frac{d^3}{12} \rho^0 \ddot{\mathbf{n}} = (\mathbb{F}_m)^{-T} \nabla^0 \cdot (\mathbf{J}_m \mathbb{M}^T) + \mathbf{J}_m \mathbf{Q}^T \mathbf{Q}^l, \end{cases} \quad (28)$$

where $\mathbb{N} = \mathbf{Q}^T \mathbb{N}^l \mathbf{Q}$ and $\mathbb{M} = \mathbf{Q}^T \mathbb{M}^l \mathbf{Q}$ are the stress and moment resultants, respectively, in global coordinates.

2.2. 3D shell model

Based on the 3D plate model, the 3D shell model is obtained by introducing the initial local coordinate system and the transformation matrix from the global to initial local coordinate system. As the transformation matrix is a unit matrix for plates, both plates and shells can be constructed in their initial local coordinates, allowing for a unified model for both structures.

2.2.1. Kinematics

The kinematics of shell can be constructed in the initial local coordinates denoted with the superscript $(\bullet)^L$. Each material point possesses five degrees of freedom, viz., three translations $\mathbf{u}^L = \{u^L, v^L, w^L\}^T$ and two rotations $\boldsymbol{\theta}^L = \{\theta^L, \varphi^L\}^T$ as shown in Fig. 2. The pseudo-normal vector is also presented in initial local coordinates by $\mathbf{n}^L = \{n_1^L, n_2^L, n_3^L\}^T$, especially denoted by $\mathbf{n}^{0,L} = \{0, 0, 1\}^T$ in the initial local configuration. The local position \mathbf{r}^L of a material point can be expressed as

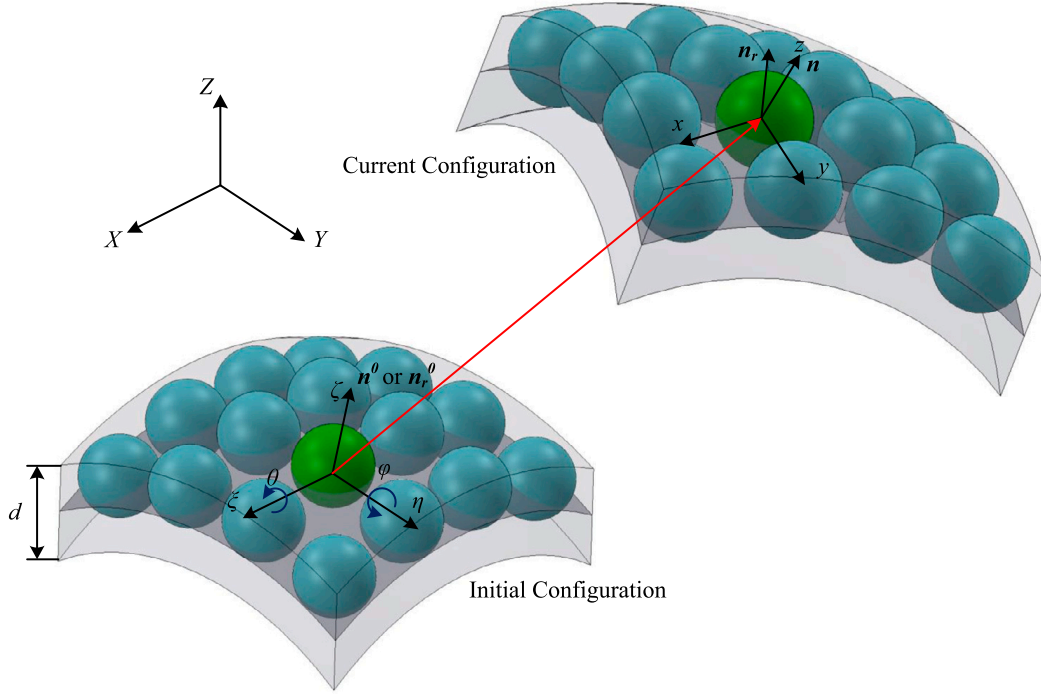


Fig. 2. Schematic of a 3D shell model.

$$\mathbf{r}^L(\xi, \eta, \chi, t) = \mathbf{r}_m^L(\xi, \eta, t) + \chi \mathbf{n}^L(\xi, \eta, t), \quad \chi \in [-d/2, d/2]. \quad (29)$$

The local displacement \mathbf{u}^L can thus be obtained by

$$\mathbf{u}^L(\xi, \eta, \chi, t) = \mathbf{u}_m^L(\xi, \eta, t) + \chi \Delta \mathbf{n}^L(\xi, \eta, t), \quad (30)$$

where $\Delta \mathbf{n}^L = \mathbf{n}^L - \mathbf{n}^{0,L}$. Similar to 3D plates, the local deformation gradient tensor of 3D shells can be defined as

$$\mathbb{F}^L = \nabla^{0,L} \mathbf{r}^L + \nabla^{0,L} \mathbf{n}^L - \nabla^{0,L} \mathbf{n}^{0,L} = (\mathbf{a}_1^L, \mathbf{a}_2^L, \mathbf{a}_3^L), \quad (31)$$

where $\nabla^{0,L} \equiv \partial/\partial \xi$ is the gradient operators defined in the initial local configuration, and $\mathbf{a}_1^L, \mathbf{a}_2^L, \mathbf{a}_3^L$ are detailed by

$$\begin{cases} \mathbf{a}_1^L = \mathbf{r}_{m,\xi}^L + \chi \mathbf{n}_{\xi}^L - \chi \mathbf{n}_{\xi}^{0,L} \\ \mathbf{a}_2^L = \mathbf{r}_{m,\eta}^L + \chi \mathbf{n}_{\eta}^L - \chi \mathbf{n}_{\eta}^{0,L} \\ \mathbf{a}_3^L = \mathbf{n}^L. \end{cases} \quad (32)$$

2.2.2. Stress correction and conservation equation

With the local deformation gradient tensor \mathbb{F}^L , the local Eulerian Almansi strain \mathcal{E}^L can be calculated by the Eq. (9). After that, the current local \mathcal{E}^l is obtained according to the coordinate transformation as

$$\mathcal{E}^l = \mathbb{Q}(\mathbb{Q}^0)^T \mathcal{E}^L \mathbb{Q}^0 \mathbb{Q}^T, \quad (33)$$

where \mathbb{Q}^0 , the orthogonal transformation matrix from the global to initial local coordinates, is calculated from Eq. (16) while the current pseudo normal \mathbf{n} is replaced by the initial one \mathbf{n}^0 . And then the corrected strain $\bar{\mathcal{E}}^l$ is estimated by applying Eq. (14). After getting the current local Cauchy stress \mathcal{S}^l by Eq. (10), the corrected one $\bar{\mathcal{S}}^l$ is obtained by Eq. (17).

Note that the total Lagrangian conservation equations of a 3D shell has the same form as Eqs. (28) with $\mathbb{F}_m = (\mathbb{Q}^0)^T \mathbb{F}_m^L \mathbb{Q}^0$.

2.3. 2D plate/shell model

If a plate/shell is assumed to be a strip that is very long and has a finite width, and the transverse load is assumed to be uniform along the length, the analysis can be simplified at any cross section as a plane strain problem [46].

The kinematics of 2D plate and shell can also be built in initial local coordinates. The 2D model is in the global X - Z plane, and each material point possesses three degrees of freedom, viz., two translations $\mathbf{u}^L = \{u^L, w^L\}^T$ and one rotation $\theta^L = \{\varphi^L\}^T$ expressed in the initial local coordinates. The pseudo-normal vector is presented in the initial local coordinates by $\mathbf{n}^L = \{n_1^L, n_3^L\}^T$, especially denoted by $\mathbf{n}^{0,L} = \{0, 1\}^T$ in the initial local configuration. Similar to 3D model, the local position \mathbf{r}^L of a material point can be expressed as

$$\mathbf{r}^L(\xi, \chi, t) = \mathbf{r}_m^L(\xi, t) + \chi \mathbf{n}^L(\xi, t), \quad \chi \in [-d/2, d/2], \quad (34)$$

the local displacement \mathbf{u}^L can be evaluated as

$$\mathbf{u}^L(\xi, \chi, t) = \mathbf{u}_m^L(\xi, t) + \chi \Delta \mathbf{n}^L(\xi, t), \quad (35)$$

and the local deformation gradient tensor is written as

$$\mathbb{F}^L = \nabla^{0,L} \mathbf{r}^L + \nabla^{0,L} \mathbf{n}^L - \nabla^{0,L} \mathbf{n}^{0,L} = (\mathbf{a}_1^L, \mathbf{a}_3^L), \quad (36)$$

where \mathbf{a}_1^L and \mathbf{a}_3^L are given by

$$\begin{cases} \mathbf{a}_1^L = \mathbf{r}_{m,\xi}^L + \zeta \mathbf{n}_\xi^L - \zeta \mathbf{n}_\xi^{0,L} \\ \mathbf{a}_3^L = \mathbf{n}^L. \end{cases} \quad (37)$$

The coordinate transformation matrix \mathbb{Q} from global to current local coordinates is simplified from Eqs. (16) as

$$\mathbb{Q} = \begin{bmatrix} n_3 & -n_1 \\ n_1 & n_3 \end{bmatrix}, \quad (38)$$

and the 2D transformation matrix \mathbb{Q}^0 from global to initial local coordinates can also be calculated by Eq. (38) while the current pseudo normal \mathbf{n} is replaced by the initial one \mathbf{n}^0 . The corrected relation of strains is simplified from Eq. (14) as

$$\bar{\epsilon}_{zz}^l = \frac{-v\epsilon_{xx}^l}{1-v}. \quad (39)$$

Finally, the 2D conservation equation is identical to 3D Eq. (28) with

$$\mathbb{N}^l = \begin{bmatrix} N_{xx}^l & 0 \\ N_{zx}^l & 0 \end{bmatrix}, \mathbb{M}^l = \begin{bmatrix} M_{xx}^l & 0 \\ M_{zx}^l & 0 \end{bmatrix}, \mathbf{Q}^l = \begin{bmatrix} -N_{xz}^l \\ 0 \end{bmatrix}. \quad (40)$$

3. SPH method for plate and shell structures

In this section, we first introduce the reduced-dimensional SPH method, and detail the proposed formulations for plate and shell structures, including the discretization of conservation equations, non-singular conversion algorithm for the kinematics between rotation angles and pseudo normal, and the algorithms to increase numerical stability and alleviate hourglass modes. After that, the time-integration schemes are presented.

3.1. Reduced-dimensional SPH method

In full-dimensional SPH method, the smoothed field $f(\mathbf{r})$ is obtained as

$$f(\mathbf{r}) = \int_{\Omega} f(\mathbf{r}') W(\mathbf{r} - \mathbf{r}', h) d\mathbf{r}', \quad (41)$$

where $f(\mathbf{r}')$ is the original continuous field before smoothing, Ω the entire space and $W(\mathbf{r} - \mathbf{r}', h)$ a Gaussian-like kernel function with smoothing length h denoting the compact support. By carrying out the integration of Eq. (41) along the thickness of the plate/shell structure, we can obtain the reduced-dimensional smoothed field by

$$f(\mathbf{r}) \approx \int_{\hat{\Omega}} f(\mathbf{r}') \widehat{W}(\mathbf{r} - \mathbf{r}', h) d\mathbf{r}', \quad (42)$$

where $\hat{\Omega}$ denotes the reduced space and $\widehat{W}(\mathbf{r} - \mathbf{r}', h)$ the reduced kernel function. Note that Eqs. (41) and (42) have identical forms of formulation. A reduced-dimensional fifth-order Wendland kernel [47] reads

$$\widehat{W}(q, h) = \alpha \begin{cases} (1 + 2q)(1 - q/2)^4 & \text{if } 0 \leq q \leq 2 \\ 0 & \text{otherwise} \end{cases}, \quad (43)$$

where $q = |\mathbf{r} - \mathbf{r}'|/h$ and the constant α is equal to $\frac{3}{4h}$ and $\frac{7}{4\pi h^2}$ for 2D and 3D problems, respectively. Also note that the reduced kernel function has identical form with the full-dimensional counterpart except different dimensional normalizing constant parameter, allowing the integration of unit can be satisfied in the reduced space. Due to the almost identical forms, in present work from here, we do not identify the full- and reduced-dimensional formulations unless explicitly mentioned.

In the reduced-dimensional SPH method, similarly to the full-dimensional counterpart [7], the gradient of the variable field $f(\mathbf{r})$ at a surface particle i can be approximated as

$$\begin{aligned}\nabla f_i &= \int_{\Omega} \nabla f(\mathbf{r}) W(\mathbf{r}_i - \mathbf{r}, h) d\mathbf{r} \\ &= - \int_{\Omega} f(\mathbf{r}) \nabla W(\mathbf{r}_i - \mathbf{r}, h) d\mathbf{r} \approx - \sum_j f_j \nabla W_{ij} V_j,\end{aligned}\quad (44)$$

where V is the reduced particle volume, i.e. length and area for 2D and 3D problems, respectively. Here, the summation is conducted over all the neighboring particles j located at the support domain of the particle i , and $\nabla W_{ij} = -\frac{\partial W(\mathbf{r}_{ij}, h)}{\partial \mathbf{r}_{ij}} \mathbf{e}_{ij}$ is the gradient of the kernel function with $\mathbf{r}_{ij} = \mathbf{r}_i - \mathbf{r}_j$ and $\mathbf{e}_{ij} = \mathbf{r}_{ij}/|\mathbf{r}_{ij}|$ denoting the unit vector pointing from particle j to i . Equation (44) can be modified into a strong form as

$$\nabla f_i = \nabla f_i - f_i \nabla 1 \approx \sum_j f_{ij} \nabla W_{ij} V_j, \quad (45)$$

where $f_{ij} = f_i - f_j$ is the interparticle difference value. This strong-form derivative operator can be used to determine the local structure of a field, such as the deformation gradient tensor. And Eq. (44) can also be modified into a weak form as

$$\nabla f_i = f_i \nabla 1 + \nabla f_i \approx - \sum_j (f_i + f_j) \nabla W_{ij} V_j. \quad (46)$$

This weak-form derivative operator is applied here for solving the conservation equations. Thanks to its anti-symmetric feature, i.e., $\nabla W_{ij} = -\nabla W_{ji}$, the momentum conservation of the particle system is ensured [7].

Note that the fundamental theory of the reduced-dimensional SPH method is generally outlined above without specifying whether the initial or update formulation is used. In the present work, this SPH method is applied for total Lagrangian formulation [48], as also illustrated in conversion Eq. (28). Therefore, the smoothing kernel function and its derivatives are only evaluated once, also denoted with superscript $(\bullet)^0$ at the initial configuration, and kept unchanged during the simulation.

3.2. First-order consistency corrections

For the full-dimensional SPH in total Lagrangian formulation, in order to remedy the 1st-order inconsistency which is caused by incomplete kernel support at domain boundary or with irregular particle distribution, the symmetric correction matrix \mathbb{B}_i^0 for each particle [49,3] is introduced for each particle to satisfy the linear-reproducing condition

$$\left(\sum_j \mathbf{r}_{ij}^0 \otimes \nabla^0 W_{ij} V_j^0 \right) \mathbb{B}_i^0 = \mathbb{I}. \quad (47)$$

Then the strong-form approximations of gradient Eq. (45) is modified as

$$\nabla^0 f_i \approx \left(\sum_j f_{ij} \nabla^0 W_{ij} V_j^0 \right) \mathbb{B}_i^0, \quad (48)$$

and the weak-form approximations of divergence Eq. (46) as

$$\nabla^0 \cdot f_i \approx - \sum_j (f_i \mathbb{B}_i^0 + f_j \mathbb{B}_j^0) \nabla^0 W_{ij} V_j^0. \quad (49)$$

In the reduced-dimensional SPH, we generalize the linear-reproducing condition as

$$\left[\mathbb{G}^T \mathbb{Q}_i^0 \left(\sum_j \mathbf{q}_{ij}^0 \otimes \nabla^0 W_{ij} V_j^0 \right) (\mathbb{Q}_i^0)^T \mathbb{G} \right] \mathbb{B}_i^{0,L} = \mathbb{K}_i, \quad (50)$$

where \mathbf{q}_{ij}^0 is the initial inter-particle difference of a linear vector, \mathbb{Q}_i^0 is the transformation matrix from the global to initial local coordinates, and \mathbb{G} is a reducing matrix, i.e.,

$$\mathbb{G} = \begin{bmatrix} 1 \\ 0 \end{bmatrix} \quad \text{and} \quad \begin{bmatrix} 1 & 0 \\ 0 & 1 \\ 0 & 0 \end{bmatrix} \quad (51)$$

for 2D and 3D problems, respectively. It ensures that the corrections are carried out within the local reduced space. Similarly, the strong-form approximations of gradient Eq. (45) is modified as

$$\nabla^0 f_i \approx \left(\sum_j f_{ij} \nabla^0 W_{ij} V_j^0 \right) \tilde{\mathbb{B}}_i^0, \quad (52)$$

where $\tilde{\mathbb{B}}_i^0 = (\mathbb{Q}_i^0)^T \mathbb{G} \mathbb{B}_i^{0,L} \mathbb{G}^T \mathbb{Q}_i^0$ and the weak-form approximations of divergence Eq. (46) as

$$\nabla^0 \cdot f_i \approx - \sum_j \left(f_i \tilde{\mathbb{B}}_i^0 + f_j \tilde{\mathbb{B}}_j^0 \right) \nabla^0 W_{ij} V_j^0. \quad (53)$$

Here, we introduce the correction matrix $\tilde{\mathbb{B}}_i^0 = \tilde{\mathbb{B}}_i^{0,r}$, $\mathbf{q}_{ij}^0 = \mathbf{r}_{ij}^0$ and \mathbb{K}_i is the reduced identity matrix denoted as

$$\mathbb{K}_i = \mathbb{K}^r = [1] \quad \text{and} \quad \begin{bmatrix} 1 & 0 \\ 0 & 1 \end{bmatrix} \quad (54)$$

for 2D and 3D problems, respectively, to correct the position-based quantities. Similarly, we introduce the correction matrix $\tilde{\mathbb{B}}_i^0 = \tilde{\mathbb{B}}_i^{0,n}$, $\mathbf{q}_{ij}^0 = \mathbf{n}_{ij}^0$ and

$$\mathbb{K}_i = \mathbb{K}_i^n = [1/R_i^L] \quad \text{and} \quad \begin{bmatrix} 1/R_{1,i}^L & 0 \\ 0 & 1/R_{2,i}^L \end{bmatrix}, \quad (55)$$

where R_i^L , $R_{1,i}^L$ and $R_{2,i}^L$ are the curvature radii of particle i for 2D and 3D problems, respectively, to correct rotation-based quantities. Note that, as SPH is nearly of 2nd order accuracy for evenly distributed particles [50], ensuring 1st-order completeness for the gradient is adequate.

3.3. Discretization of conservation equations

With two correction matrices obtained from Eq. (50) and following Eq. (53), the momentum equations (28) are discretized as

$$d\rho_i^0 \ddot{\mathbf{u}}_{m,i} = \sum_j \left(J_{m,i} \mathbb{N}_i (\mathbb{F}_{m,i})^{-T} \tilde{\mathbb{B}}_i^{0,r} + J_{m,j} \mathbb{N}_j (\mathbb{F}_{m,j})^{-T} \tilde{\mathbb{B}}_j^{0,r} \right) \nabla^0 W_{ij} V_j^0, \quad (56)$$

and

$$\begin{aligned} \frac{d^3}{12} \rho_i^0 \ddot{\mathbf{n}}_i &= \sum_j \left(J_{m,i} \mathbb{M}_i (\mathbb{F}_{m,i})^{-T} \tilde{\mathbb{B}}_i^{0,n} + J_{m,j} \mathbb{M}_j (\mathbb{F}_{m,j})^{-T} \tilde{\mathbb{B}}_j^{0,n} \right) \nabla^0 W_{ij} V_j^0 \\ &+ J_{m,i} (\mathbb{Q}_i^0)^T \mathbf{Q}_i^l. \end{aligned} \quad (57)$$

Note that, as collocated particles are used in the present formulation, both the deformation gradient $\mathbb{F}_{m,i}$, stress and moment resultants, i.e. \mathbb{N}_i and \mathbb{M}_i , are computed at the same particles.

3.4. Kelvin–Voigt type damping

Following Ref. [40], when calculating the current local Cauchy stress by using the constitutive Eq. (10), an artificial damping stress \mathcal{D}_d^l based on the Kelvin–Voigt type damper is introduced here as

$$\mathcal{D}_d^l = J_m^{-1} \mathbb{Q} (\mathbb{Q}^0)^T \mathbb{F}^L \dot{\mathbb{E}}^L \gamma (\mathbb{F}^L)^T \mathbb{Q}^0 \mathbb{Q}^T, \quad (58)$$

where the numerical viscosity matrix

$$\gamma = \begin{bmatrix} \rho c h / 2 & 0 \\ 0 & \rho c s / 2 \end{bmatrix} \quad \text{and} \quad \begin{bmatrix} \rho c h / 2 & 0 & 0 \\ 0 & \rho c h / 2 & 0 \\ 0 & 0 & \rho c s / 2 \end{bmatrix} \quad (59)$$

where $c = \sqrt{K/\rho}$ and $s = \min(h, d)$, for 2D and 3D problems, respectively. Note that, different from Ref. [40], where an isotropic numerical damping is applied, the present damping leads to a smaller out-of-plane contribution when $d < h$, which makes it suitable for both thin and moderately thick plate and shell structures. The change rate of the Green–Lagrangian strain tensor is given as

$$\dot{\mathbb{E}}^L = \frac{1}{2} \left[(\dot{\mathbb{F}}^L)^T \mathbb{F}^L + (\mathbb{F}^L)^T \dot{\mathbb{F}}^L \right]. \quad (60)$$

Here, the change rate of the deformation gradient tensor of particle i is

$$\dot{\mathbb{F}}_i^L = \nabla^0 \cdot \mathbf{u}_i^L = \nabla^0 \cdot \dot{\mathbf{u}}_{m,i}^L + \chi \nabla^0 \cdot \dot{\mathbf{n}}_i^L, \quad (61)$$

where

$$\begin{cases} \nabla^0 \dot{\mathbf{u}}_{m,i}^L = \mathbb{Q}_i^0 \left(\sum_j \dot{\mathbf{u}}_{m,ij} \otimes \nabla^0 W_{ij} V_j^0 \right) \tilde{\mathbb{B}}_i^{0,r} (\mathbb{Q}_i^0)^T \\ \nabla^0 \dot{\mathbf{n}}_i^L = \mathbb{Q}_i^0 \left(\sum_j \dot{\mathbf{n}}_{ij} \otimes \nabla^0 W_{ij} V_j^0 \right) \tilde{\mathbb{B}}_i^{0,n} (\mathbb{Q}_i^0)^T \end{cases} \quad (62)$$

are obtained following the consistency condition Eq. (50) and the strong-form correction Eq. (52).

3.5. Hourglass control

Inspired from Refs. [41,31] in full-dimensional SPH for total Lagrangian solid dynamics, we introduce a hourglass control algorithm here to alleviate the hourglass modes in the dynamics of plate and shell structures.

First, we estimate the position of the inter-particle middle point linearly using the deformation gradient tensor from particles i and j , respectively, as

$$\mathbf{r}_{i+\frac{1}{2}} = \mathbf{r}_{m,i} - \frac{1}{2} \mathbb{F}_{m,i} \mathbf{r}_{m,ij}^0, \quad \mathbf{r}_{j-\frac{1}{2}} = \mathbf{r}_{m,j} + \frac{1}{2} \mathbb{F}_{m,j} \mathbf{r}_{m,ij}^0. \quad (63)$$

One can find that the inconsistency beyond linear estimation $\hat{\mathbf{r}}_{ij} = \mathbf{r}_{i+\frac{1}{2}} - \mathbf{r}_{j-\frac{1}{2}}$ is

$$\hat{\mathbf{r}}_{ij} = \mathbf{r}_{m,ij} - \frac{1}{2} (\mathbb{F}_{m,i} + \mathbb{F}_{m,j}) \mathbf{r}_{m,ij}^0. \quad (64)$$

To suppress the position inconsistency $\hat{\mathbf{r}}_{ij}$, we introduce an extra correction term to the discrete momentum conservation Eq. (56) as

$$d\rho_i^0 \ddot{\mathbf{u}}_{m,i}^{cor} = \sum_j \alpha G \beta_{ij} \gamma_{ij}^r D \hat{\mathbf{r}}_{ij} \frac{\partial W(\mathbf{r}_{ij}^0, h)}{\partial \mathbf{r}_{ij}^0} V_j^0 \quad (65)$$

where $\beta_{ij} = W_{ij}^0 / W_0$ leads to less correction to further neighbors, $\gamma_{ij}^r = \min(2|\hat{\mathbf{r}}_{ij}| / |\mathbf{r}_{m,ij}|, 1)$ is an adaptive limiter for less correction on the domain where the inconsistency is less pronounced, D the dimension, and parameter $\alpha = 0.002$ according to the numerical experiment and remains constant throughout this work. Note that, since the inconsistency decreases with decreasing particle spacing, different from Refs. [31], the present correction is purely numerical and vanishes with increasing resolution. Similarly, for the predicted pseudo normal, the difference of the intermediate point can be described as

$$\hat{\mathbf{n}}_{ij} = \mathbf{n}_{ij} - \mathbf{n}_{ij}^0 - \frac{1}{2} (\mathbb{F}_{n,i} + \mathbb{F}_{n,j}) \mathbf{r}_{ij}^0. \quad (66)$$

Similar with Eq. (65), the extra correction term added to the discrete angular momentum conservation Eq. (57) is

$$\frac{d^3}{12} \rho_i^0 \ddot{\mathbf{n}}_i^{cor} = \sum_j \alpha G d^2 \beta_{ij} \gamma_{ij}^n D \hat{\mathbf{n}}_{ij} \frac{\partial W(\mathbf{r}_{ij}^0, h)}{\partial \mathbf{r}_{ij}^0} V_j^0, \quad (67)$$

where the adaptive limiter is $\gamma_{ij}^n = \min(2|\hat{\mathbf{n}}_{ij}| / |\mathbf{n}_{ij} - \mathbf{n}_{ij}^0|, 1)$. Note that, different with Refs. [41,31], the present correction force is introduced in particle pairwise pattern, implying momentum conservation [7]. Also note that, the correction force is scaled to the shear, rather than Young's, modulus, due to the fact that the hourglass modes are characterized by shear deformation [32].

3.6. Conversion between rotations and pseudo normal

Different from the mid-surface displacement, which can be numerically integrated directly from its evolution equation, the pseudo normal is not suitable for direct numerical integration since its unit magnitude may not be maintained strictly. In the present work, different from using Rodrigues formula [51,35], we update the pseudo normal \mathbf{n}^L with a more straightforward formulation base on Euler angles [51,44]

$$\mathbf{n}^L = \mathbb{R}_\eta^L \mathbb{R}_\xi^L \mathbf{n}^{0,L}, \quad (68)$$

where $\mathbb{R}_\xi^L \equiv \mathbb{R}_\xi(\theta^L)$ and $\mathbb{R}_\eta^L \equiv \mathbb{R}_\eta(\varphi^L)$ are the local rotation matrices respected to the axes ξ and η , respectively, or, equivalently, with the change rate

$$\dot{\mathbf{n}}^L = \dot{\mathbb{R}}_\eta^L \mathbb{R}_\xi^L \mathbf{n}^{0,L}, \quad (69)$$

where $\dot{\mathbb{R}}_\xi^L \equiv \mathbb{R}_\xi(\theta^L, \dot{\theta}^L)$ and $\dot{\mathbb{R}}_\eta^L \equiv \mathbb{R}_\eta(\varphi^L, \dot{\varphi}^L)$. Here, the rotations and their change rates are numerically integrated directly with the help of conversion relations.

Specifically, for a 2D problem, \mathbb{R}_ξ^L is a unit matrix, and \mathbb{R}_η^L can be described as

$$\mathbb{R}_\eta^L = \begin{bmatrix} \cos \varphi^L & \sin \varphi^L \\ -\sin \varphi^L & \cos \varphi^L \end{bmatrix}. \quad (70)$$

Then, one has the relation as

$$\mathbf{n}^L = (\sin \varphi^L, \cos \varphi^L)^T, \quad (71)$$

its 1st-order time derivative corresponding Eq. (69)

$$\dot{\mathbf{n}}^L = (\cos \varphi^L \cdot \dot{\varphi}^L, -\sin \varphi^L \cdot \dot{\varphi}^L)^T, \quad (72)$$

and 2nd-order derivative

$$\ddot{\mathbf{n}}^L = (-\sin \varphi^L \cdot (\dot{\varphi}^L)^2 + \cos \varphi^L \cdot \ddot{\varphi}^L, -\cos \varphi^L \cdot (\dot{\varphi}^L)^2 - \sin \varphi^L \cdot \ddot{\varphi}^L)^T. \quad (73)$$

Note that Eq. (73) suggests two theoretically equivalent conversion relations

$$\dot{\varphi}^L = \frac{\ddot{n}_1^L + \sin \varphi^L \cdot (\dot{\varphi}^L)^2}{\cos \varphi^L} \quad \text{and} \quad \ddot{\varphi}^L = \frac{\ddot{n}_2^L + \cos \varphi^L \cdot (\dot{\varphi}^L)^2}{-\sin \varphi^L}. \quad (74)$$

Although each of them can be used to obtain the rotation angle φ^L and its change rate with direct numerical integration and hence the pseudo normal with Eq. (68), there are singularities at large rotation angles $\varphi^L = 0.5\pi + k\pi$ (1st relation) or $\varphi^L = k\pi$ (2nd relation) with $k = 0, 1, 2, 3, \dots$ [52,51,53]. In order to eliminate the singularities, we propose to use both relations with a weighted average as

$$\begin{aligned} \dot{\varphi}^L &= (\cos \varphi^L)^2 \frac{\ddot{n}_1^L + \sin \varphi^L \cdot (\dot{\varphi}^L)^2}{\cos \varphi^L} + (\sin \varphi^L)^2 \frac{\ddot{n}_2^L + \cos \varphi^L \cdot (\dot{\varphi}^L)^2}{-\sin \varphi^L} \\ &= \cos \varphi^L \left(\ddot{n}_1^L + \sin \varphi^L \cdot (\dot{\varphi}^L)^2 \right) - \sin \varphi^L \left(\ddot{n}_2^L + \cos \varphi^L \cdot (\dot{\varphi}^L)^2 \right), \end{aligned} \quad (75)$$

which cancels both denominators.

As for 3D problems, the rotation matrices \mathbb{R}_ξ^L and \mathbb{R}_η^L are

$$\mathbb{R}_\xi^L = \begin{bmatrix} 1 & 0 & 0 \\ 0 & \cos \theta^L & -\sin \theta^L \\ 0 & \sin \theta^L & \cos \theta^L \end{bmatrix}, \quad (76)$$

and

$$\mathbb{R}_\eta^L = \begin{bmatrix} \cos \varphi^L & 0 & \sin \varphi^L \\ 0 & 1 & 0 \\ -\sin \varphi^L & 0 & \cos \varphi^L \end{bmatrix}. \quad (77)$$

Similarly, one has the relation between rotations and pseudo normal [54]

$$\mathbf{n}^L = (\cos \theta^L \sin \varphi^L, -\sin \theta^L, \cos \theta^L \cos \varphi^L)^T, \quad (78)$$

its 1st-order time derivatives corresponding Eq. (69)

$$\begin{cases} \dot{n}_1^L = -\sin \theta^L \sin \varphi^L \dot{\theta}^L + \cos \theta^L \cos \varphi^L \dot{\varphi}^L \\ \dot{n}_2^L = -\cos \theta^L \dot{\theta}^L \\ \dot{n}_3^L = -\sin \theta^L \cos \varphi^L \dot{\theta}^L - \cos \theta^L \sin \varphi^L \dot{\varphi}^L, \end{cases} \quad (79)$$

and 2nd-order derivatives

$$\begin{cases} \ddot{n}_1^L = -\sin \theta^L \sin \varphi^L \ddot{\theta}^L - \cos \theta^L \sin \varphi^L (\dot{\theta}^L)^2 - 2 \sin \theta^L \cos \varphi^L \dot{\theta}^L \dot{\varphi}^L \\ \quad - \cos \theta^L \sin \varphi^L (\dot{\varphi}^L)^2 + \cos \theta^L \cos \varphi^L \ddot{\varphi}^L \\ \ddot{n}_2^L = \sin \theta^L (\dot{\theta}^L)^2 - \cos \theta^L \ddot{\theta}^L \\ \ddot{n}_3^L = -\sin \theta^L \cos \varphi^L \ddot{\theta}^L - \cos \theta^L \cos \varphi^L (\dot{\theta}^L)^2 + 2 \sin \theta^L \cos \varphi^L \dot{\theta}^L \dot{\varphi}^L \\ \quad - \cos \theta^L \cos \varphi^L (\dot{\varphi}^L)^2 - \cos \theta^L \sin \varphi^L \ddot{\varphi}^L. \end{cases} \quad (80)$$

Note that, one can obtain 3 theoretically equivalent conversion relations, respectively, by 1st and 3rd expressions of Eq. (80) as

$$\begin{cases} \ddot{\theta}^L = -\left(\ddot{n}_3^L \cos \varphi^L + \ddot{n}_1^L \sin \varphi^L + (\dot{\varphi}^L)^2 \cos \theta^L + (\dot{\theta}^L)^2 \cos \theta^L \right) / \sin \theta^L \\ \ddot{\varphi}^L = \left(\ddot{n}_1^L \cos \varphi^L - \ddot{n}_3^L \sin \varphi^L + 2 \dot{\varphi}^L \dot{\theta}^L \sin \theta^L \right) / \cos \theta^L, \end{cases} \quad (81)$$

1st and 2nd expressions

$$\begin{cases} \ddot{\theta}^L = \left(\sin \theta^L (\dot{\theta}^L)^2 - \ddot{n}_2^L \right) / \cos \theta^L \\ \ddot{\varphi}^L = \left(\ddot{n}_1^L \cos \theta^L + (\dot{\varphi}^L)^2 \cos^2 \theta^L \sin \varphi^L + (\dot{\theta}^L)^2 \sin \varphi^L - \ddot{n}_2^L \sin \varphi^L \sin \theta^L \right. \\ \quad \left. + 2 \dot{\varphi}^L \dot{\theta}^L \cos \varphi^L \cos \theta^L \sin \theta^L \right) / \cos \varphi^L \cos^2 \theta^L, \end{cases} \quad (82)$$

and 2nd and 3rd expressions

$$\begin{cases} \ddot{\theta}^L = (\sin \theta^L (\dot{\theta}^L)^2 - \ddot{n}_2^L) / \cos \theta^L \\ \ddot{\varphi}^L = -(\ddot{n}_3^L \cos \theta^L + (\dot{\varphi}^L)^2 \cos \varphi^L \cos^2 \theta^L + (\dot{\theta}^L)^2 \cos \varphi^L - \ddot{n}_2^L \cos \varphi^L \sin \theta^L \\ \quad - 2\dot{\varphi}^L \dot{\theta}^L \cos \theta^L \sin \varphi^L \sin \theta^L) / \sin \varphi^L \cos^2 \theta^L. \end{cases} \quad (83)$$

Again, each of these conversion relations suffers singularities at large rotations similar to that of 2D formulations. To eliminate the singularities, we first apply the weighted average to the conversion between $\ddot{\theta}^L$ and \ddot{n}^L with Eqs. (81) and (82) as

$$\begin{aligned} \ddot{\theta}^L = & -\left(\ddot{n}_3^L \cos \varphi^L + \ddot{n}_1^L \sin \varphi^L + (\dot{\varphi}^L)^2 \cos \theta^L + (\dot{\theta}^L)^2 \cos \theta^L\right) \sin \theta^L \\ & + \left(\sin \theta^L (\dot{\theta}^L)^2 - \ddot{n}_2^L\right) \cos \theta^L. \end{aligned} \quad (84)$$

Then, for the conversion relation between $\ddot{\varphi}^L$ and \ddot{n}^L , according to Eq. (81), we can rewrite the relation as

$$\cos \theta^L = B / \ddot{\varphi}^L, \quad (85)$$

where B denotes the numerator of the 2nd expression in Eq. (81). We further denote the numerators of the 2nd expressions in Eqs. (82) and (83), respectively, as B_1 and B_2 . Inserting Eq. (85) into Eqs. (82) and (83), we have

$$\begin{cases} \ddot{\varphi}^L = (B^2 \cos \varphi^L) / B_1 \\ \ddot{\varphi}^L = (B^2 \sin \varphi^L) / B_2, \end{cases} \quad (86)$$

and obtain the weighted average of the conversion relation as

$$\ddot{\varphi}^L = \frac{B_1 B^2 \cos \varphi^L + B_2 B^2 \sin \varphi^L}{B_1^2 + B_2^2}. \quad (87)$$

3.7. Time stepping

For the time integration of plate and shell dynamics, we use the position-based Verlet scheme [55,56]. At the beginning of each time step, the deformation gradient, particle position, rotation angles and pseudo normal are updated to the midpoint of the n -th time step as

$$\begin{cases} \mathbb{F}^{L,n+\frac{1}{2}} = \mathbb{F}^{L,n} + \frac{1}{2} \Delta t \dot{\mathbb{F}}^{L,n} \\ \mathbf{r}_m^{n+\frac{1}{2}} = \mathbf{r}_m^n + \frac{1}{2} \Delta t \dot{\mathbf{u}}_m^n \\ \boldsymbol{\theta}^{L,n+\frac{1}{2}} = \boldsymbol{\theta}^{L,n} + \frac{1}{2} \Delta t \dot{\boldsymbol{\theta}}^{L,n} \\ \mathbf{n}^{L,n+\frac{1}{2}} = \mathbf{n}^{L,n} + \frac{1}{2} \Delta t \dot{\mathbf{n}}^{L,n}. \end{cases} \quad (88)$$

With updated $\mathbb{F}^{L,n+\frac{1}{2}}$ in hand, the corrected Almansi strain $\mathbb{E}^{L,n+\frac{1}{2}}$ is obtained by Eqs. (9) and (14) or (39). Then the corrected Cauchy stress $\mathbb{S}^{L,n+\frac{1}{2}}$ is calculated by applying constitutive relation Eq. (10) and correction Eq. (17). After getting the resultant $\mathbb{N}^{L,n+\frac{1}{2}}$, $\mathbb{M}^{L,n+\frac{1}{2}}$ and $\mathbb{Q}^{L,n+\frac{1}{2}}$ by the Gauss-Legendre quadrature Eqs. (22) and (24), the conservation equations are solved to obtain the $\dot{\mathbf{u}}_m^{n+1}$ and $\dot{\mathbf{n}}^{n+1}$. After transforming $\dot{\mathbf{n}}^{n+1}$ to $\dot{\mathbf{n}}^{L,n+1}$, $\dot{\boldsymbol{\theta}}^{L,n+1}$ is obtained through the conversion relation between the pseudo normal and rotation angle, i.e., Eq. (75) for 2D problems and Eqs. (84) and (87) for 3D problems. At this point, the velocity and angular velocity are updated by

$$\begin{cases} \dot{\mathbf{u}}_m^{n+1} = \dot{\mathbf{u}}_m^n + \Delta t \ddot{\mathbf{u}}_m^{n+1} \\ \dot{\boldsymbol{\theta}}^{L,n+1} = \dot{\boldsymbol{\theta}}^{L,n} + \Delta t \ddot{\boldsymbol{\theta}}^{L,n+1}, \end{cases} \quad (89)$$

and the change rate of pseudo normal $\dot{\mathbf{n}}$ is updated by Eq. (72) or (79). Finally, the change rate of the deformation gradient $\dot{\mathbb{F}}^{L,n+1}$ is estimated by Eq. (61), and then the deformation gradient, density, particle position, rotation angles and pseudo normal are updated to the new time step with

$$\begin{cases} \mathbb{F}^{L,n+1} = \mathbb{F}^{L,n+\frac{1}{2}} + \frac{1}{2} \Delta t \dot{\mathbb{F}}^{L,n+1} \\ \rho^{n+1} = (\mathbf{J}_m^{n+1})^{-1} \rho^0 \\ \mathbf{r}_m^{n+1} = \mathbf{r}_m^{n+\frac{1}{2}} + \frac{1}{2} \Delta t \dot{\mathbf{u}}_m^{n+1} \\ \boldsymbol{\theta}^{L,n+1} = \boldsymbol{\theta}^{L,n+\frac{1}{2}} + \frac{1}{2} \Delta t \dot{\boldsymbol{\theta}}^{L,n+1} \\ \mathbf{n}^{L,n+1} = \mathbf{n}^{L,n+\frac{1}{2}} + \frac{1}{2} \Delta t \dot{\mathbf{n}}^{L,n+1}. \end{cases} \quad (90)$$

For the numerical stability, the time-step size Δt is given by

$$\Delta t = \text{CFL} \min(\Delta t_1, \Delta t_2, \Delta t_3), \quad (91)$$

where

$$\begin{cases} \Delta t_1 = \min\left(\frac{h}{c_v + |\dot{\mathbf{u}}_m|_{\max}}, \sqrt{\frac{h}{|\dot{\mathbf{u}}_m|_{\max}}}\right) \\ \Delta t_2 = \min\left(\frac{1}{c_v + |\dot{\boldsymbol{\theta}}^L|_{\max}}, \sqrt{\frac{1}{|\dot{\boldsymbol{\theta}}^L|_{\max}}}\right) \\ \Delta t_3 = h \left(\frac{\rho(1-\nu^2)/E}{2+(\pi^2/12)(1-\nu)[1+1.5(h/d)^2]} \right)^{1/2}. \end{cases} \quad (92)$$

Note that the time-step size Δt_3 follows the Refs. [57,35] and depends on the thickness and material properties, and the present Courant-Friedrichs-Lewy (CFL) number is set as 0.6 [58,9]. An overview of the complete solution procedure is presented in Algorithm 1.

Algorithm 1: The present SPH method for plate/shell structures.

- 1 Setup parameters and initialize the simulation;
 - 2 Construct the particle-neighbor list and compute the kernel values;
 - 3 Compute the correction matrices $\tilde{\mathbb{B}}^{0,r}$ and $\tilde{\mathbb{B}}^{0,n}$ for each particle (Section 3.2);
 - 4 **while** *simulation is not finished* **do**
 - 5 Compute the time-step size Δt using Eq. (91);
 - 6 Update the deformation gradient tensor \mathbb{F}^L , particle position \mathbf{r}_m , rotation angle $\boldsymbol{\theta}^L$ and pseudo normal \mathbf{n} for half time step $\Delta t/2$;
 - 7 Compute and correct the Cauchy stress $\boldsymbol{\sigma}^l$ (Sections 2.1.2 and 2.1.3);
 - 8 Compute the resultants \mathbb{N}^l and \mathbb{M}^l , and shear force \mathbf{Q}^l (Eq. (27));
 - 9 Compute the acceleration $\ddot{\mathbf{u}}_m$ (Eqs. (56) and (65)) and $\ddot{\mathbf{n}}$ (Eqs. (57) and (67));
 - 10 Compute the angular acceleration $\ddot{\boldsymbol{\theta}}^L$ (Eq. (75) for 2D problems, and Eqs. (84) and (87) for 3D problems);
 - 11 Update the velocity $\dot{\mathbf{u}}_m$ and angular velocity $\dot{\boldsymbol{\theta}}^L$ for a time step Δt ;
 - 12 Compute the change rate of pseudo normal $\dot{\mathbf{n}}^L$ using Eq. (72) or (79);
 - 13 Compute the change rate of the deformation gradient tensor $\partial\mathbb{F}^L/\partial t$ (Eq. (61));
 - 14 Update the deformation gradient tensor \mathbb{F}^L , density ρ , particle position \mathbf{r}_m , rotation angle $\boldsymbol{\theta}^L$ and pseudo normal \mathbf{n} for another half time step $\Delta t/2$;
 - 15 **end**
 - 16 Terminate the simulation.
-

Furthermore, it is important to highlight that achieving full incremental objectivity is facilitated by employing the finite deformation formulation [59,60] and adopting the local particle material model [61]. Additionally, reference-validated time step sizes further ensure the elimination of objectivity concerns [59]. The absence of objectivity issues is also demonstrated through convergence analysis and comparison of results with references in the following numerical examples.

4. Numerical examples

To demonstrate the accuracy and stability of the proposed surface-particle SPH method (denoted as shell method), this section investigates a series of benchmark tests where analytical or numerical reference data from the literature or/and volume-particle SPH method (denoted as volume method) are available for qualitative and quantitative comparison. Following Refs. [62], the smoothing length $h = 1.15dp$, where dp denotes the initial particle spacing, and a cut-off radius of $2.3dp$ is employed in all the following simulations, to maintain acceptable accuracy while minimizing computational efforts with small number of neighboring particles. Note that a splitting random-choice dynamic relaxation method, as outlined in [63], is applied to quickly acquire the quasi-static solutions for steady analysis.

4.1. 2D oscillating plate strip

The first example involves a plate strip with initial uniform transverse velocity along the length with one edge fixed and the others free, which has previously been theoretically [64] and numerically [65,66,32] investigated in the literature. As shown in Fig. 3(a), this plate strip is assumed to be infinitely long along the y -axis with a finite width $a = 0.2$ m along the x -axis. To demonstrate that both thin and moderately thick structures can be simulated, this plate strip is modeled with the thicknesses $d = 0.01$ m and 0.001 m. The material properties are set as follows: density $\rho_0 = 1000.0$ kg/m³, Young's modulus $E = 2.0$ MPa, and Poisson's ratio ν varies for different cases. Fig. 3(b) shows the discrete model of the chosen cross-section with clamped edges at $x = 0$. The transverse velocity v_z is applied to the plate strip as

$$v_z(x) = v_f c \frac{f(x)}{f(a)}, \quad (93)$$

where v_f is a constant that varies with different cases, and

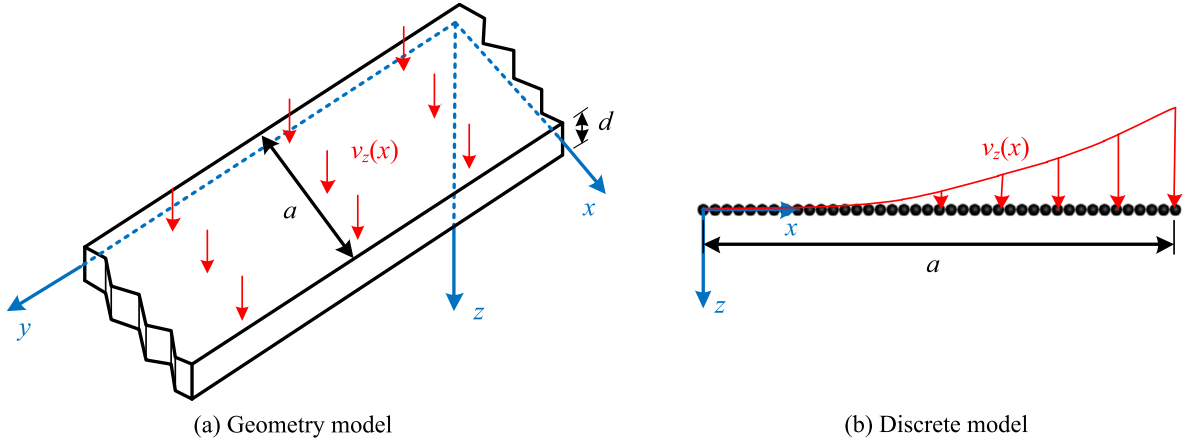


Fig. 3. 2D oscillating plate strip: Initial configuration with width $a = 0.2$ m.

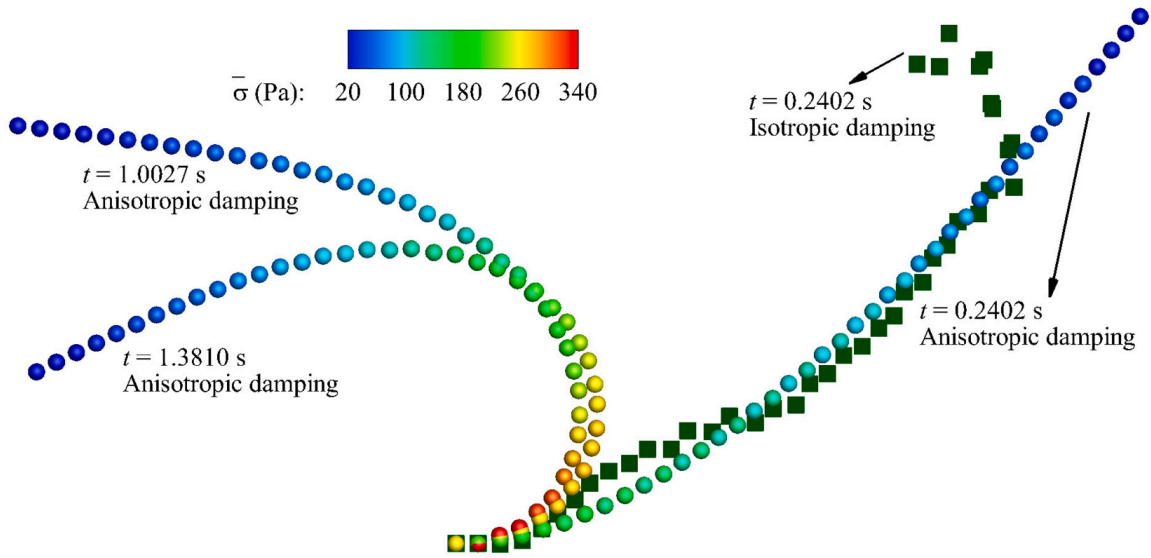


Fig. 4. 2D oscillating plate strip: Deformed particle configuration colored by von Mises stress $\bar{\sigma}$ of the mid-surface at serial time instants with the width $a = 0.2$ m, thickness $d = 0.001$ m, $v_f = 0.01$, and spatial particle resolution $a/dp = 40$, and the comparison of particle distribution obtained by using iso- and anisotropic Kelvin-Voigt damping. The material is modeled with density $\rho_0 = 1000.0$ kg/m³, Young's modulus $E = 2.0$ MPa, and Poisson's ratio $\nu = 0.4$. (For interpretation of the colors in the figure(s), the reader is referred to the web version of this article.)

$$f(x) = (\sin(ka) + \sinh(ka))(\cos(kx) - \cosh(kx)) - (\cos(ka) + \cosh(ka))(\sin(kx) - \sinh(kx)) \quad (94)$$

with k determined by

$$\cos(ka) \cosh(ka) = -1 \quad (95)$$

and $ka = 1.875$. The frequency ω of the oscillating plate strip is theoretically given by

$$\omega^2 = \frac{Ed^2k^4}{12\rho(1-\nu^2)}. \quad (96)$$

Fig. 4 shows the particles with von Mises stress $\bar{\sigma}$ contour for the case of $d = 0.001$ m, $v_f = 0.01$, $\nu = 0.4$, with an initial particle spacing of $dp = a/40 = 0.005$ m. Additionally, it showcases the comparison of particle distribution obtained by employing iso- and anisotropic Kelvin-Voigt damping, highlighting the effectiveness of the anisotropic damping, and illustrating how excessive damping in the thickness direction contaminates the numerical results when isotropic damping is applied. It should be noted that the present method predicts smooth deformation and stress fields without singularities for large rotations (more than π). Three different spatial resolutions, $a/dp = 40$, $a/dp = 80$, and $a/dp = 160$, are tested in the convergence study. Fig. 5 shows the time history of vertical position z of the strip endpoint with $d = 0.01$ m, $v_f = 0.025$ and $\nu = 0.4$. It can be observed that typical 2nd-order convergence has been achieved. In addition, a long-term simulation is performed herein to demonstrate the numerical stability of the proposed formulation. For quantitative validation, Tables 1 and 2 detail the oscillation period T for a wide range of v_f and ν , obtained by the present method with the spatial particle resolution $a/dp = 160$, when thickness $d = 0.01$ m and 0.001 m, respectively, and the

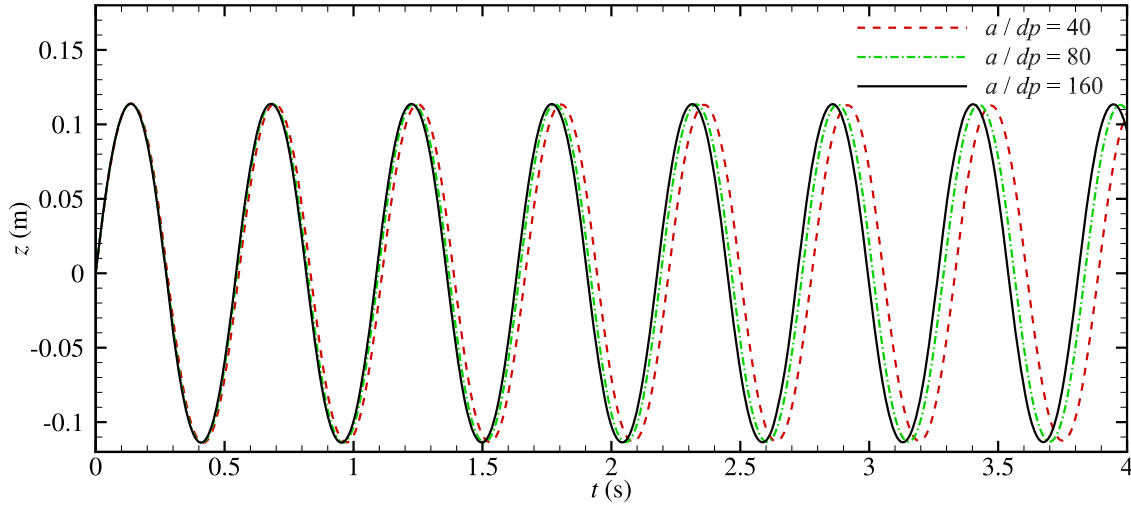


Fig. 5. 2D oscillating plate strip: Time history of the vertical position z observed at the plate strip endpoint in the long term when $d = 0.01$ m, $v_f = 0.025$ and $\nu = 0.4$.

Table 1

2D oscillating plate strip: Quantitative validation of the oscillation period for $a = 0.2$ m and $d = 0.01$ m with various v_f and ν .

v_f	ν	$T_{\text{Shell model}}$	$T_{\text{Theoretical}}$	Error
0.025	0.22	0.58137	0.54018	7.63%
0.05	0.22	0.57715	0.54018	6.92%
0.1	0.22	0.56801	0.54018	5.15%
0.025	0.30	0.56804	0.52824	7.53%
0.05	0.30	0.56308	0.52824	6.60%
0.1	0.30	0.55481	0.52824	5.03%
0.025	0.40	0.54447	0.50752	7.28%
0.05	0.40	0.53683	0.50752	5.78%
0.1	0.40	0.53252	0.50752	4.93%

Table 2

2D oscillating plate strip: Quantitative validation of the oscillation period for $a = 0.2$ m and $d = 0.001$ m with various v_f and ν .

v_f	ν	$T_{\text{Shell model}}$	$T_{\text{Theoretical}}$	Error
0.0025	0.22	5.80249	5.40182	7.42%
0.005	0.22	5.75544	5.40182	6.55%
0.01	0.22	5.64181	5.40182	4.44%
0.0025	0.30	5.66756	5.28243	7.29%
0.005	0.30	5.61006	5.28243	6.20%
0.01	0.30	5.49156	5.28243	3.96%
0.0025	0.40	5.42826	5.07519	6.96%
0.005	0.40	5.34224	5.07519	5.26%
0.01	0.40	5.27522	5.07519	3.94%

comparison to theoretical solution obtained from small perturbation analysis. The differences, which are less than 8.00% for $\nu = 0.22$ and decrease to about 5.00% when the Poisson's ratio is increased to 0.4, are acceptable.

4.2. 3D square plate

In this section, a 3D square plate under different types of boundary conditions is considered for quasi-steady analyses, as shown in Fig. 6. With side length $a = b = 254$ mm and thickness $d = 25.4$ mm, the plate material is defined with density $\rho_0 = 1600$ kg/m³, Young's modulus $E = 53.7791$ GPa and Poisson's ratio $\nu = 0.3$. Three types of boundary conditions denoted as SS0, SS1 and SS3 following Refs. [46,35] are implemented as

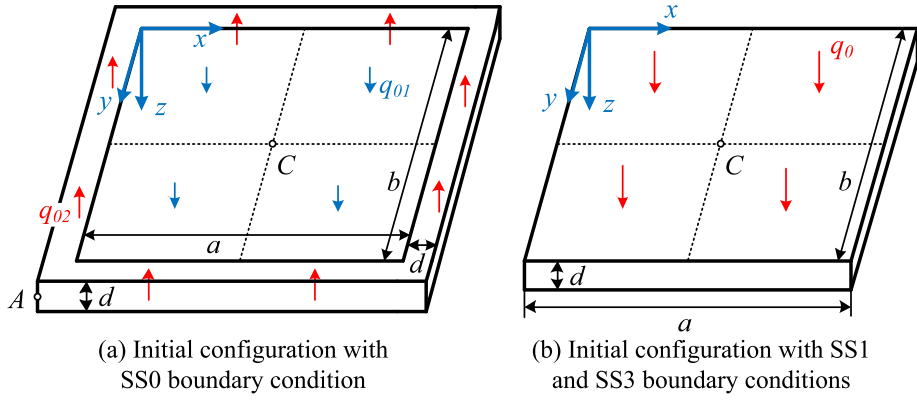


Fig. 6. 3D square plate: Problem setup with $a = b = 254$ mm and thickness $d = 25.4$ mm.

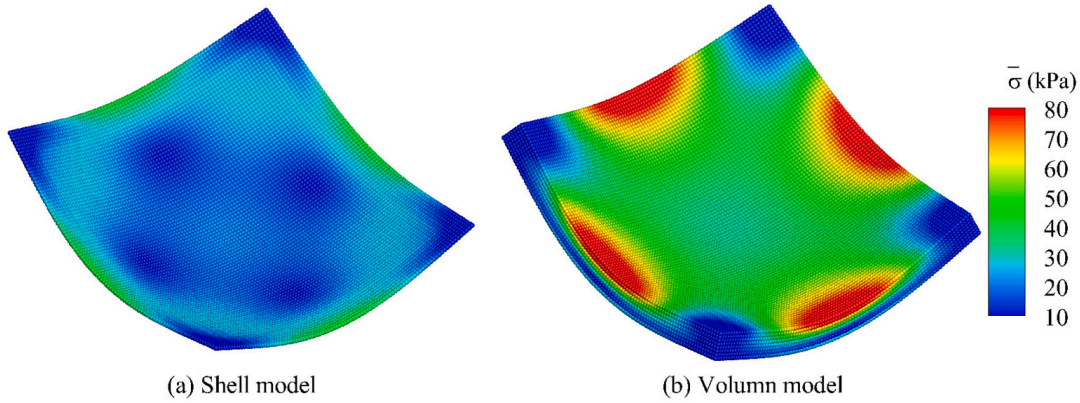


Fig. 7. 3D square plate: Particles colored by von Mises stress $\bar{\sigma}$ of tests with SS0 obtained by the present shell (left) and volume (right) methods under the loading factor $\bar{P}_1 = 25$. Note that the left panel shows the stress $\bar{\sigma}$ of the plate mid-surface. The material is modeled with the density $\rho_0 = 1600$ kg/m³, Young's modulus $E = 53.7791$ GPa and Poisson's ratio $\nu = 0.3$. The spatial particle resolution is set as $d/dp = 8$.

- SS0: constrained mass center without constrained boundaries;
- SS1: $u = w = \varphi = 0$ on edges parallel to x -axis and $v = \theta = 0$ on edges parallel to y -axis;
- SS3: $u = v = w = 0$ on all edges.

Note that, for the case of SS0, the outer square ring with width d is imposed with negative pressure q_{02} . The uniformly distributed loads are parameterized by the loading factors \bar{P} and \bar{P}_1 as $q_0 = \bar{P}E(d/a)^4$, $q_{01} = \bar{P}_1E(d/a)^4$ and $q_{02}(2ad + 2bd + 4d^2) = q_{01}ab$, so that the applied negative force along the z -axis prevents the center of mass from moving.

For comprehensive validation, a convergence study of tests with SS0 is conducted, and the results are compared with those obtained by the volume method released in the SPHinXsys repository [9]. Fig. 7 shows the particle distribution and stress fields under the loading factor $\bar{P}_1 = 25$ with the spatial discretization $d/dp = 8$. Fig. 8 shows the non-dimensional deflection $\bar{w}_C = w_C/d$ and $\bar{w}_A = w_A/d$ probed at the central point C and corner point A , respectively, obtained by both SPH shell and volume methods. It should be emphasized that there are only quite small differences between the results of the present reduced-dimensional and full-dimensional models.

The particles colored by von Mises stress $\bar{\sigma}$ at the mid-surface for three spatial discretizations, $a/dp = 20$, $a/dp = 40$ and $a/dp = 80$, with the SS1 and SS3 boundary conditions under $\bar{P} = 200$ are shown in Fig. 9. It can be observed that the regular particle distribution and smooth stress field are obtained. Also, both the deformation and von Mises stress $\bar{\sigma}$ exhibit good convergence properties with particle refinement. In order to demonstrate the accuracy of the present method, the non-dimensional deflections \bar{w}_C for tests with SS1 and SS3 under various spatial resolutions are compared to those of the Ref. [46]. As shown in Figs. 10, the numerical results quickly converge to the reference solutions obtained by the finite element method (FEM) with increasing resolution.

4.3. Dynamic response of a 3D square plate

Following Ref. [67], the 3D square plate studied in Section 4.2 is considered herein with the thickness $d = 12.7$ mm and Young's modulus $E = 68.94$ GPa. The SS0 and SS3 boundary conditions are applied for dynamic analyses under a step loading of uniform normal pressure $q_{01} = q_0 = 2.068427$ MPa. For convergence study, three different spatial discretizations, i.e., $d/dp = 2$, $d/dp = 4$ and $d/dp = 8$, are considered.

For quantitative validation, Fig. 11 shows the time history of the deflections w_C probed at the central point C and w_A at the corner point A with SS0 boundary condition and its comparison to the results obtained by the volume method. Also, Fig. 12 shows

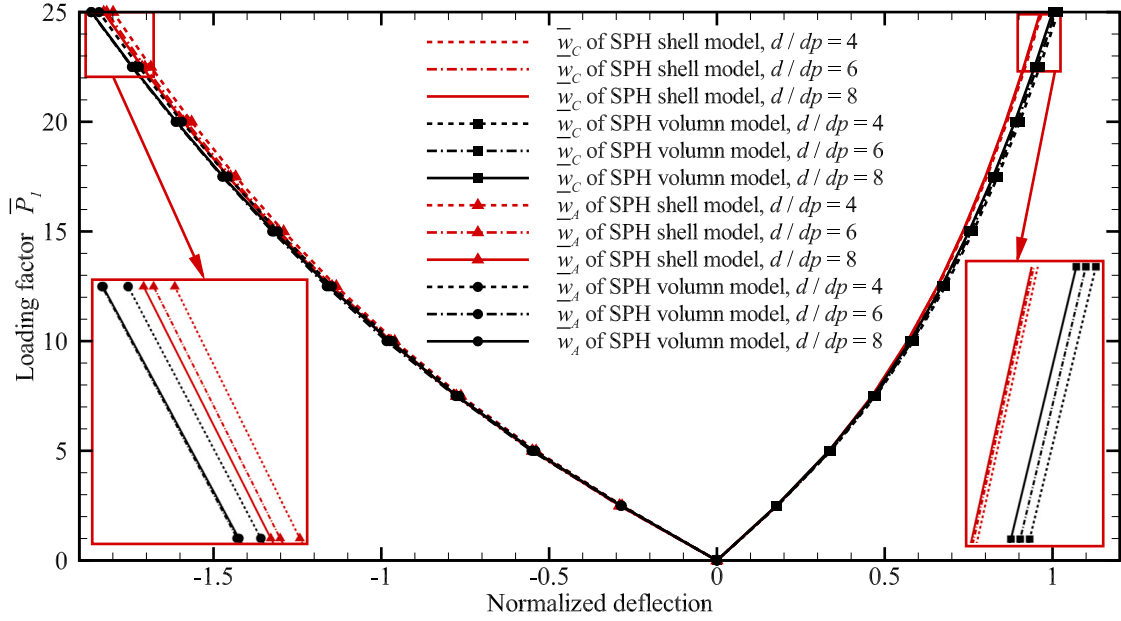


Fig. 8. 3D square plate: Load-deflection curves of tests with SS0 under three different spatial resolutions, and their comparison with those of the volume method [9].

the time history of the deflection w_C with the SS3 boundary condition and its comparison with that of Ref. [67]. In general, the present results are in good agreements with those obtained by the volume method and of Ref. [67]. Note that a long-term simulation is conducted, when the SS3 boundary condition is applied, to demonstrate the numerical stability of the proposed formulation, and only exhibits a 0.86% reduction in oscillation amplitude after 7 periods.

4.4. 3D cantilevered plate

Following Refs [68–70], the static response of a 3D cantilevered plate subjected to a distributed end shear load f_0 is considered. As shown in Fig. 13, the plate with length $a = 10$ m, width $b = 1$ m and thickness $d = 0.1$ m is clamped at $y = 0$, and has material parameters of density $\rho_0 = 1100$ kg/m³, Young's modulus $E = 1.2$ MPa and Poisson's ratio $\nu = 0.0$. The shear load is parameterized by a loading factor \bar{F} as $f_0 = \bar{F}EI/a^2$ with the inertia moment $I = bd^3/12$. Three different resolutions, i.e., $b/dp = 5$, $b/dp = 7$ and $b/dp = 9$, are considered for convergence study.

Fig. 14 shows the particles colored by the vertical displacement under different loading factor \bar{F} at the spatial resolution $b/dp = 9$. A regular particle distribution and smooth vertical displacement field are noted. Fig. 15 gives the displacement u_c and w_c of the point C, defined in Fig. 13, as a function of the loading factor \bar{F} and the initial particle spacing dp , and their comparison with those in Ref. [70]. It can be noted that the displacement is converging rapidly, again at about 2nd-order, with increasing resolution, demonstrating the accuracy of the present method.

4.5. Scordelis-Lo roof

As shown in Fig. 16, the Scordelis-Lo roof with length $a = 50$ m, radius $r = 25$ m, thickness $d = 0.25$ m and $\beta = 40^\circ$ is considered herein, and the material properties are density $\rho_0 = 36$ kg/m³, Young's modulus $E = 432$ MPa and zero Poisson's ratio. The roof is supported at its ends by fixed diaphragms, i.e. the translations in x and z directions are constrained, and subjected to a gravity loading of $g = 10$ m/s².

The FEM solution of the vertical displacement w at the midpoint of the side edge converges to 0.3024 m as reported in Refs. [71,72]. A sequentially refined resolutions of $b/dp = 15, 20, 25, 30$ and 40 with $b = 2r\beta$ denoting the arc length of the roof end are considered to assess the convergence property of the present method. Fig. 17 shows the particles colored with the von Mises stress $\bar{\sigma}$ of the mid-surface obtained at different resolutions. The regular particle distribution and smooth stress fields are noted. With increasing resolution, a clear convergence is exhibited. The profile of normalized displacement $\bar{w} = \frac{w}{0.3024 \text{ m}}$ with varying spatial resolution obtained by the present method is depicted in Fig. 18. It can be noted that the result converges rapidly to $w = 0.2991$ m when $dp = b/40 = 0.8727$ m with 1.09% error compared to the solution of Refs. [71,72]. Note that since $dp > w$, i.e., the size of a particle is considerably larger than the displacement, the present method struggles to accurately capture such small displacements. Another possible reason for the small discrepancy is the not-strictly imposed traction-free boundary condition as SPH does not have explicit definition of material surface.

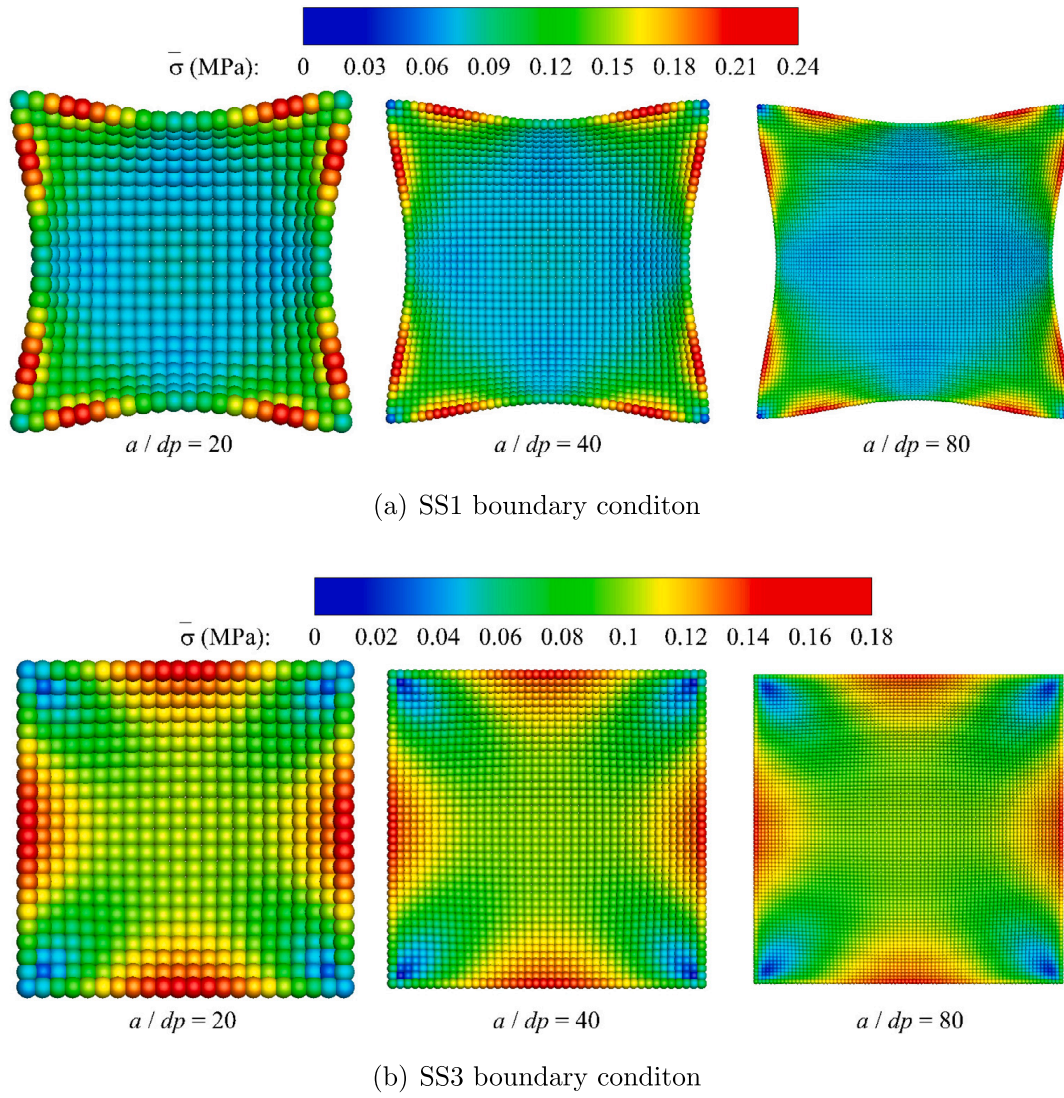


Fig. 9. 3D square plate: Particles colored by von Mises stress $\bar{\sigma}$ of the mid-surface with particle refinement under the loading factor $\bar{P} = 200$ and SS1 and SS3 boundary conditions. The plate material has parameters of the density $\rho_0 = 1600 \text{ kg/m}^3$, Young's modulus $E = 53.7791 \text{ GPa}$ and Poisson's ratio $\nu = 0.3$.

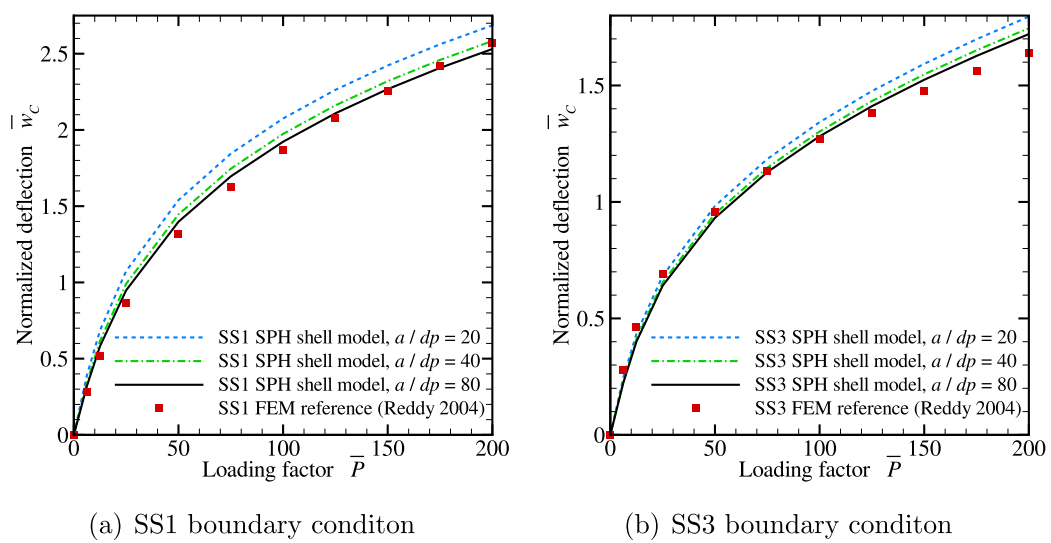


Fig. 10. 3D square plate: Load-deflection curves of tests with SS1 and SS3 under three different spatial resolutions, and their comparison with that of Reddy [46].

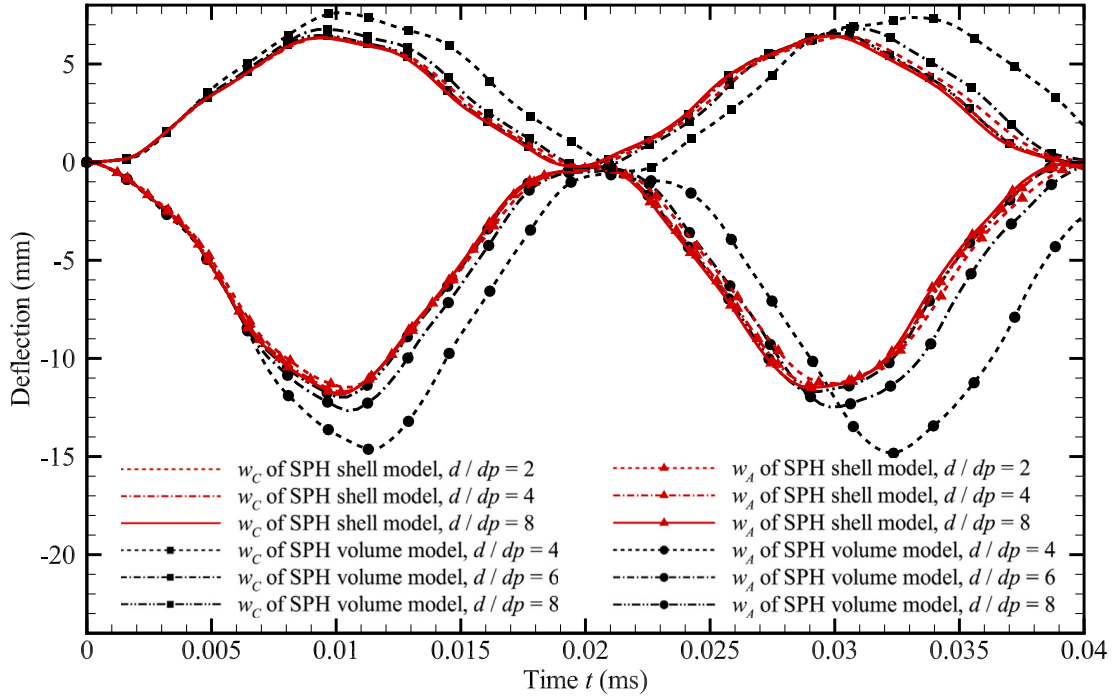


Fig. 11. 3D square plate with dynamic response: Time history of the deflection w_C and w_A probed at the central point C and corner point A, respectively, with SS0 boundary condition. The material is modeled with the density $\rho_0 = 1600 \text{ kg/m}^3$, Young's modulus $E = 68.94 \text{ GPa}$ and Poisson's ratio $\nu = 0.3$.

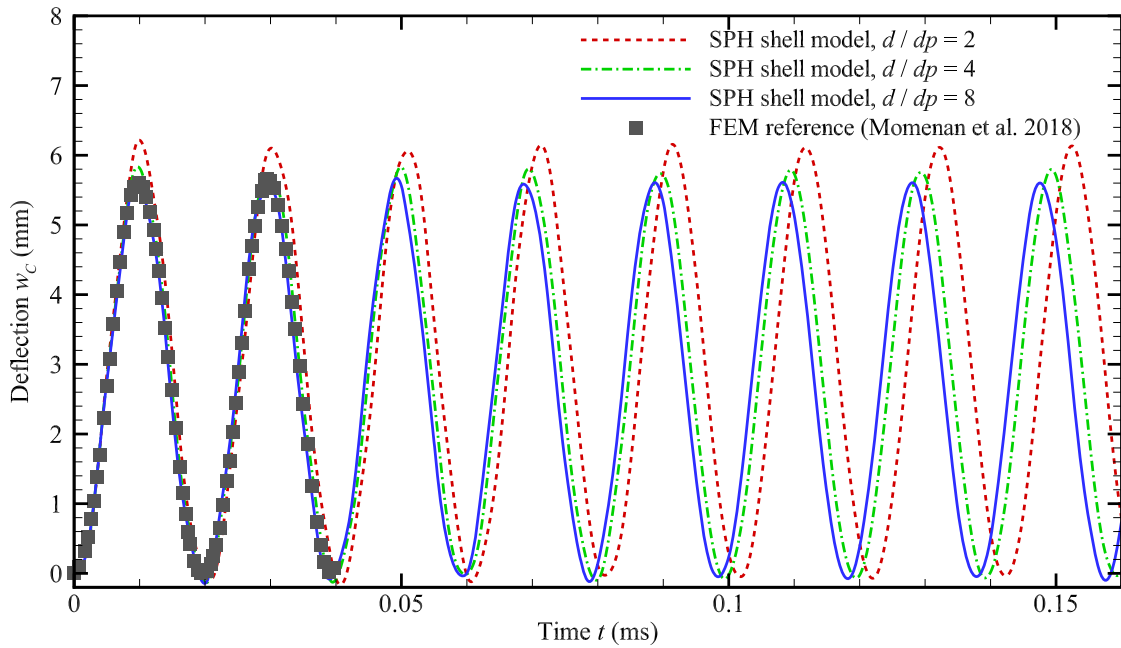


Fig. 12. 3D square plate with dynamic response: Time history of the deflection w_C observed at the central point C with SS3 boundary condition in the long term.

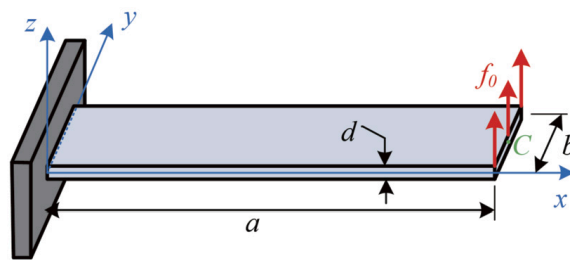


Fig. 13. 3D cantilevered plate: Initial configuration with the length $a = 10 \text{ m}$, width $b = 1 \text{ m}$ and thickness $d = 0.1 \text{ m}$.

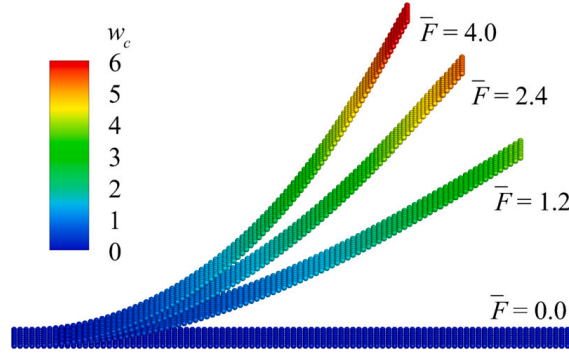


Fig. 14. 3D cantilevered plate: Particles colored by the vertical displacement w_c under the various loading factor \bar{F} at spatial resolution $b/dp = 9$. The material is set as the density $\rho_0 = 1100 \text{ kg/m}^3$, Young's modulus $E = 1.2 \text{ MPa}$ and Poisson's ratio $\nu = 0.0$.

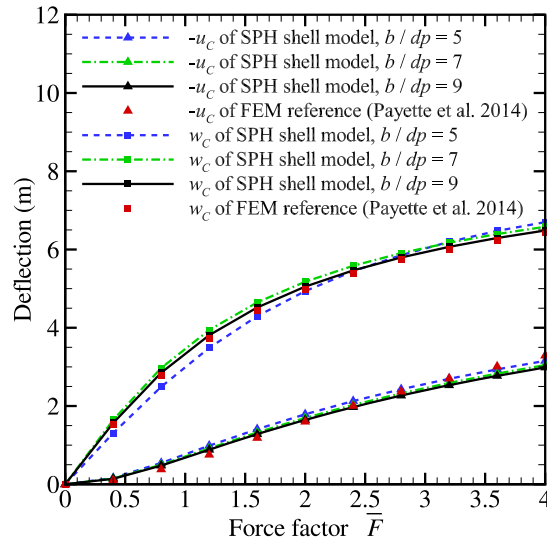


Fig. 15. 3D cantilevered plate: Load-deflection curves with three various spatial discretizations, and their comparison with that of Payette et al. [70].

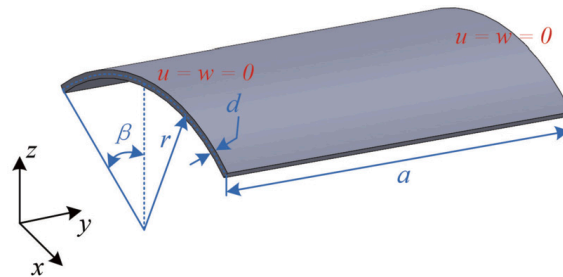


Fig. 16. Scordelis-Lo roof: Initial configuration with the length $a = 50 \text{ m}$, radius $r = 25 \text{ m}$, thickness $d = 0.25 \text{ m}$ and $\beta = 40^\circ$.

4.6. Pinched hemispherical shell

We now consider a pinched hemispherical shell with an 18° circular cutout at its pole following Refs. [73–75,69,70]. As shown in Fig. 19(a), the hemispherical shell with the radius $r = 10.0 \text{ m}$ and thickness $d = 0.04 \text{ m}$ is loaded by four alternating radial point forces F , prescribed along the equator at 90° intervals. A linear elastic material with the density $\rho_0 = 1100 \text{ kg/m}^3$, Young's modulus $E = 68.25 \text{ MPa}$ and Poisson's ratio $\nu = 0.3$ is applied.

Fig. 19(b-d) shows the distribution of von Mises stress $\bar{\sigma}$ at the mid-surface under varying magnitude of the point force F . The regular particle distribution is observed, although slight stress fluctuation, i.e., the hourglass modes, is exhibited particularly under high force magnitudes. Although we emphasize that the parameter α of hourglass control algorithm remains constant throughout this work, we have also explored adjustments to α in pursuit of improved results without hourglass modes. As shown in Fig. 20, the smooth stress fields are observed. Considering that α is not universally applicable, a more robust hourglass control method may be required. For quantitative analysis and convergence study, the radial deflections w_A and w_B of monitoring points A and B as a function of the point force magnitude and resolution are compared with those of Ref. [69]. Three different spatial discretizations,

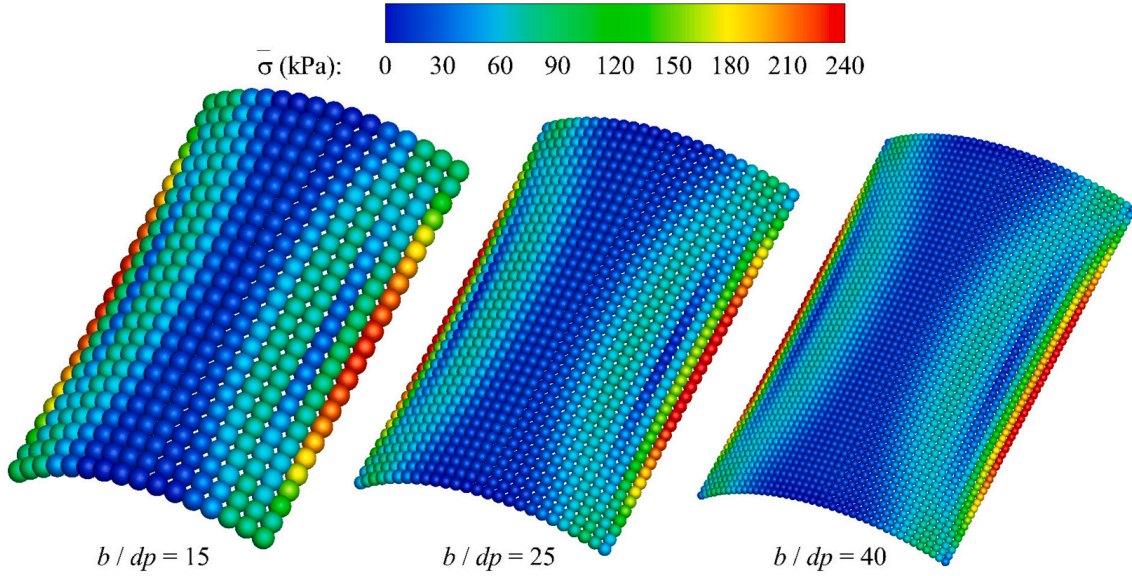


Fig. 17. Scordelis-Lo roof: Particles colored by the von Mises stress $\bar{\sigma}$ of the mid-surface obtained by the present method with particle refinement. The material is set as the density $\rho_0 = 36 \text{ kg/m}^3$, Young's modulus $E = 432 \text{ MPa}$ and Poisson's ratio $\nu = 0.0$.

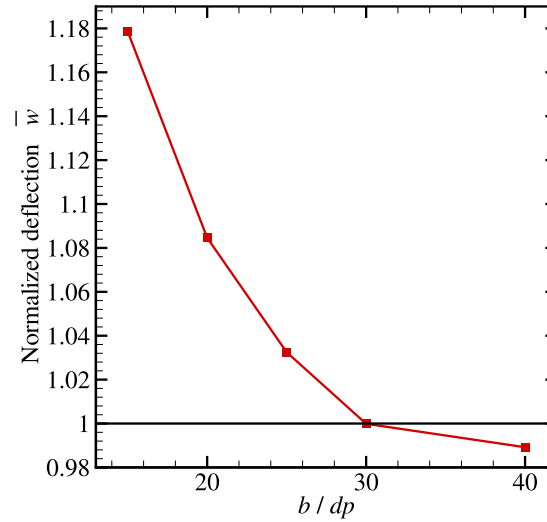


Fig. 18. Scordelis-Lo roof: Convergence study of the displacement, normalized by a reference result of 0.3024 m [71,72], obtained using the present method with particle refinement.

i.e., $2\pi r/dp = 80, 160$ and 240 , are considered for convergence study. As shown in Fig. 21, the results of present SPH shell model is quickly converging to those of Ref. [69].

4.7. Pulled-out cylindrical shell

A more challenging benchmark test with large displacements is considered in this section following Refs. [30,76]. As shown in Fig. 22, a cylindrical shell with the radius $r = 5.0 \text{ m}$, length $a = 10.35 \text{ m}$ and thickness $d = 0.094 \text{ m}$ is subjected to a pair of point forces F which are equal in magnitude and opposite in direction. A linear elastic material with the density $\rho_0 = 1100 \text{ kg/m}^3$, Young's modulus $E = 10.5 \text{ MPa}$ and Poisson's ratio $\nu = 0.3125$ is applied.

Fig. 23 shows the distribution of von Mises stress $\bar{\sigma}$ at the mid-surface under varying magnitude of the point force F . While the result, obtained without the hourglass control algorithm applied when $F = 50 \text{ kN}$, exhibits particle disorder, particularly near the location of the applied point forces, the application of hourglass control ensures a regular particle distribution and smooth stress fields. For quantitative analysis and convergence study, the radial displacements w_A , w_B and w_C of monitoring points A , B and C as a function of the point force magnitude and resolution are compared with those of Ref. [30,76]. Three different spatial discretizations, i.e., $b/dp = 80, 160$ and 240 with $b = 2\pi r$ denoting the circumference length of the end, are considered for convergence study. As shown in Fig. 24, the bifurcation point of the curve is accurately predicted, suggesting good accuracy and robustness of the present method.

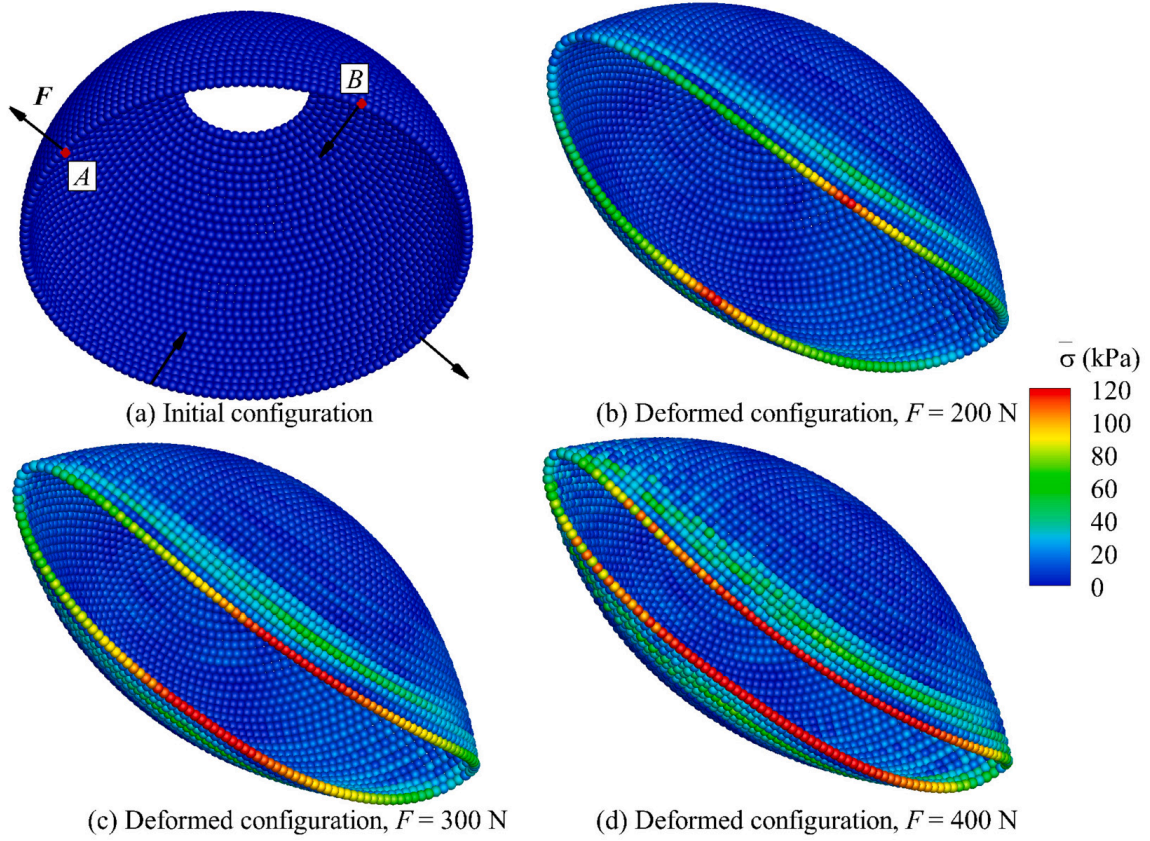


Fig. 19. Pinched hemispherical shell: (a) Initial configuration with the radius of the mid-surface $r = 10.0$ m and thickness $d = 0.04$ m, (b-d) particles colored by the von Mises stress $\bar{\sigma}$ of the mid-surface under 3 point force magnitudes at spatial discretization $2\pi r/dp = 160$. The material parameters are set as the density $\rho_0 = 1100$ kg/m³, Young's modulus $E = 68.25$ MPa and Poisson's ratio $\nu = 0.3$.

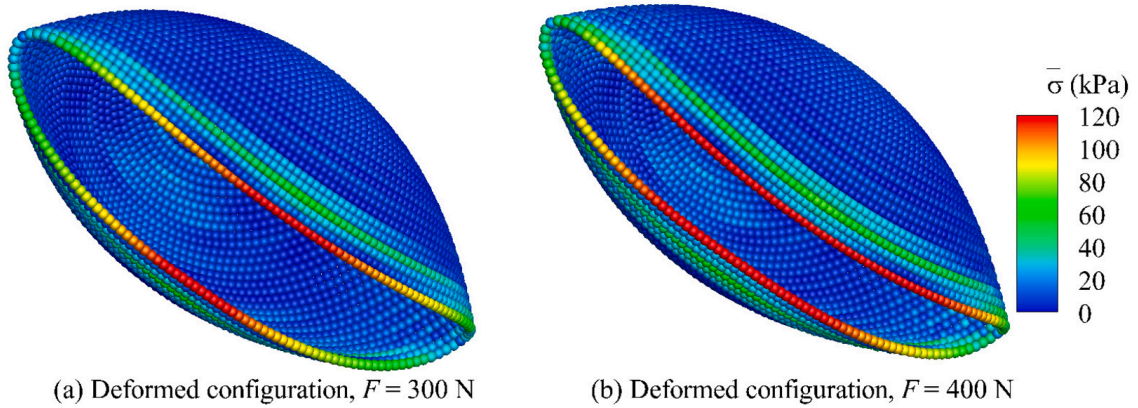


Fig. 20. Pinched hemispherical shell: Particles colored by the von Mises stress $\bar{\sigma}$ of the mid-surface under 2 point force magnitudes at spatial discretization $2\pi r/dp = 160$.

4.8. Pinched semi-cylindrical shell

We further consider a pinched semi-cylindrical shell with finite deformation and rotation following Refs. [77,78,69,79]. As shown in Fig. 25(a), the semi-cylindrical shell with the radius $r = 1.016$ m, length $a = 3.048$ m and thickness $d = 0.03$ m is completely clamped at a circumferential periphery and experiences a pinching force at the center of free-hanging periphery. Along its longitudinal edges, the vertical direction and the rotation about the y -axis are constrained. The elastic material properties are density $\rho_0 = 1100$ kg/m³, Young's modulus $E = 20.685$ MPa and Poisson's ratio $\nu = 0.3$.

Fig. 25(b-d) shows the distribution of von Mises stress $\bar{\sigma}$ at the mid-surface under varying magnitude of the point force F . Noted that the present method features regular particle distribution and smooth stress fields, even close to the constrained edges and place where the point force is applied, without singularities for finite rotations (more than 0.5π). For quantitative analysis and convergence study, the downward deflection w_A of monitoring point A as a function of the point force magnitude and resolution is compared with that of Ref. [69]. Three different spatial discretizations, i.e., $\pi r/dp = 20, 40$ and 80 , are considered for convergence study. As

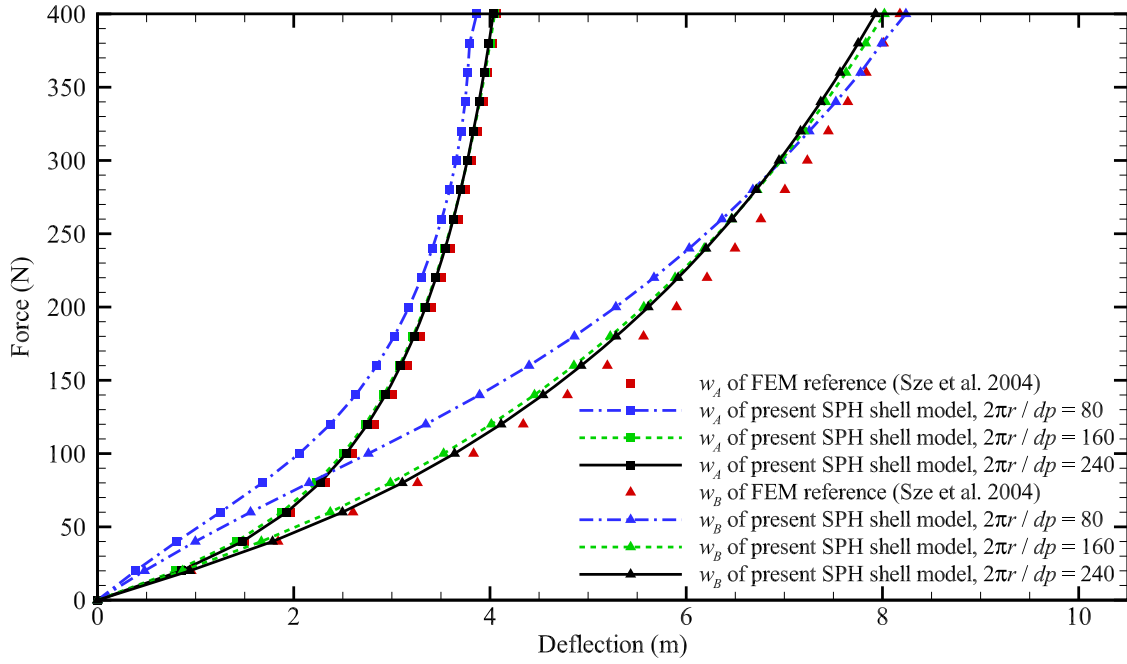


Fig. 21. Pinched hemispherical shell: Curves of radical displacements of points *A* and *B* as a function of the point force magnitude and spatial resolution, and their comparison with those of Sze et al. [69].

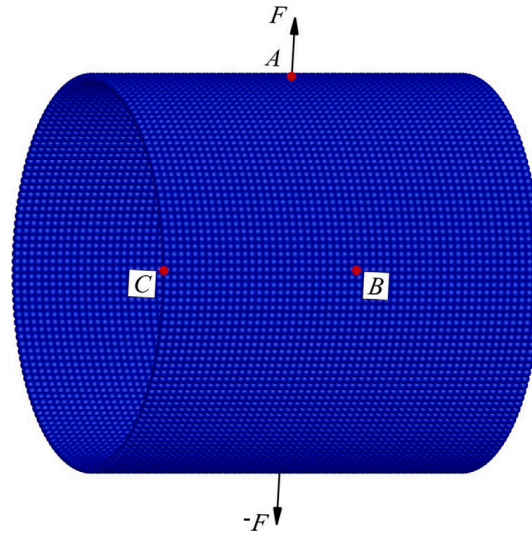


Fig. 22. Pulled-out cylindrical shell: Initial configuration with the radius of the mid-surface $r = 5.0$ m, length $a = 10.35$ m and thickness $d = 0.094$ m.

shown in Fig. 26, the result difference obtained by the present SPH shell method between different resolution rapidly decreases as the spatial refinement, and the results agree well with those of Ref. [69].

5. Concluding remarks

In this paper, we present a reduced-dimensional SPH method for quasi-static and dynamic analyses of both thin and moderately thick plate and shell structures. By introducing two reduced-dimensional linear-reproducing correction matrices, the method reproduces linear gradients of the position and pseudo-normal. The finite deformation is taken into account by considering all terms of strain with the help of Gauss-Legendre quadrature along the thickness. To cope with large rotations, the method introduces weighted non-singularity conversion relation between the rotation angles and pseudo normal. A non-isotropic Kelvin-Voigt damping and a momentum-conserving hourglass control algorithm with a limiter are also proposed to increase numerical stability and to suppress hourglass modes. An extensive set of numerical examples have been investigated to demonstrate the accuracy and robustness of the present method.

This study assumes plate and shell structures behave as continuous media, represented by a smooth distribution of particles, while also maintaining constant thickness, straight pseudo-normal, and particles with two rotation degrees of freedom. Furthermore, the

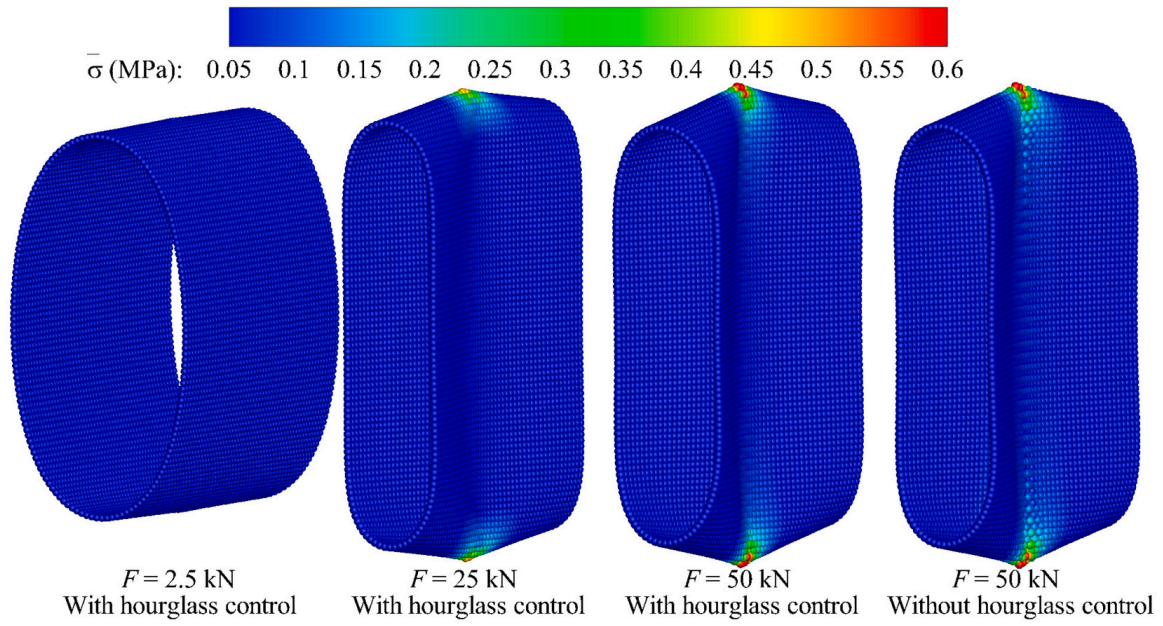


Fig. 23. Pulled-out cylindrical shell: Particles colored by the von Mises stress $\bar{\sigma}$ of the mid-surface under 3 point force magnitudes at spatial resolution of $b/dp = 160$, and its comparison with the results obtained without hourglass control applied. The material parameters are set as the density $\rho_0 = 1100 \text{ kg/m}^3$, Young's modulus $E = 10.5 \text{ MPa}$ and Poisson's ratio $\nu = 0.3125$.

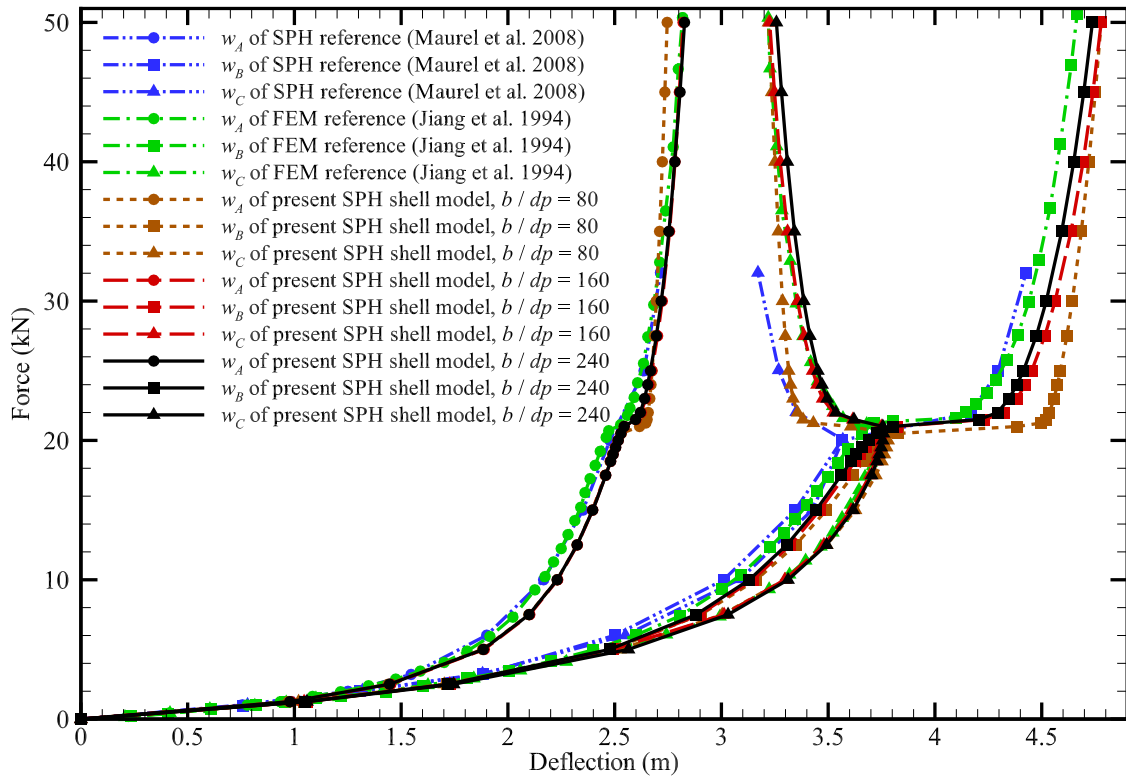


Fig. 24. Pulled-out cylindrical shell: Curves of radical displacements of points A, B and C as a function of the point force magnitude and spatial resolution, and their comparison with those of Maurel and Combescure [30] and Jiang et al. [76].

proposed method only employs an isotropic and linear elastic material model, and is restricted to simulations of a whole piece of thin structure. The extensions of this method are to explore variations like changing thickness, considering additional drilling rotation, and applying nonlinear elastic, plastic, anisotropic, and fracture material models. Another outlook is to simulate complex structures, such as I-beams, which are combined by several pieces of thin structures. A comprehensive stability analysis concerning spatial and temporal discretization is also part of our future work. The simulation results for the pinched hemispherical shell still exhibit hourglass modes. Developing a modified or new hourglass-control algorithm is planned for future work. One potential direction is to explore methods similar to those used in traditional mesh-based approaches, where the concentration of particle stress is mitigated

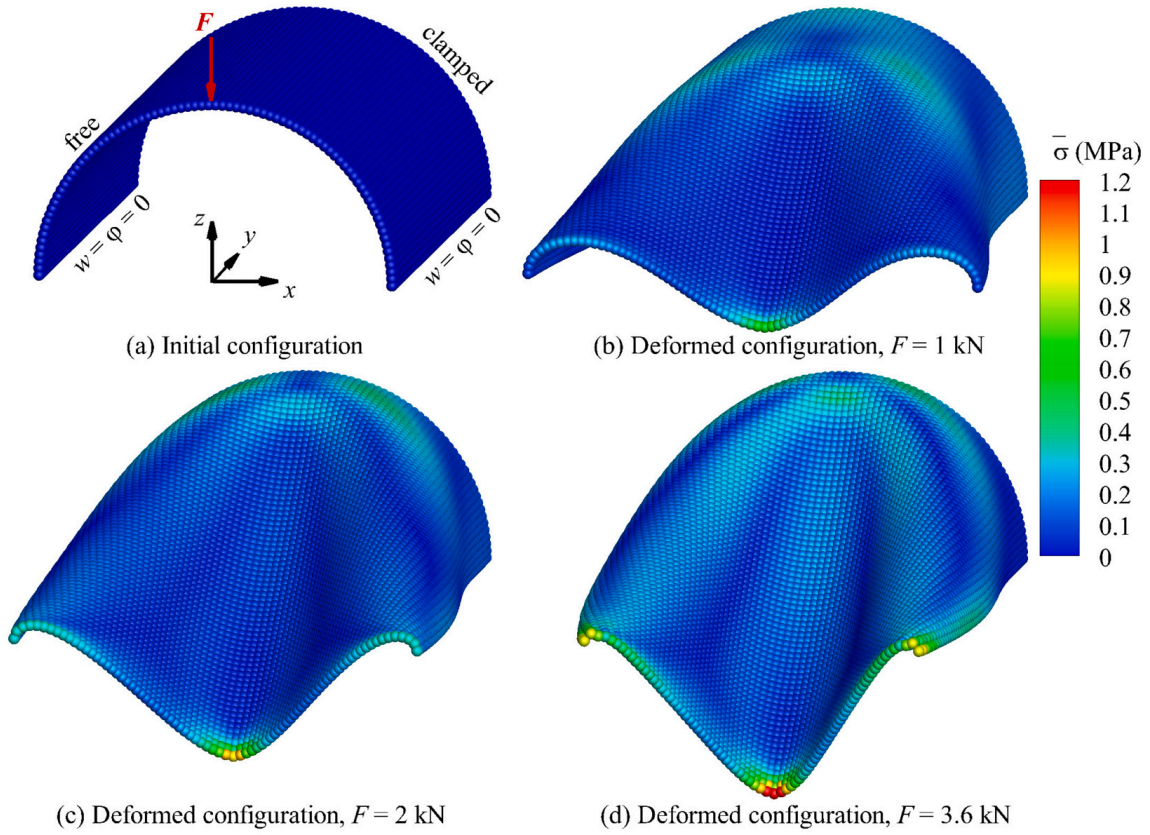


Fig. 25. Pinched semi-cylindrical shell: (a) Initial configuration with the radius $r = 1.016$ m, length $a = 3.048$ m and thickness $d = 0.03$ m, (b-d) particles colored by the von Mises stress $\bar{\sigma}$ of the mid-surface under 3 point force magnitudes at spatial resolution $b/d\rho = 80$. The material parameters are set as the density $\rho_0 = 1100$ kg/m³, Young's modulus $E = 20.685$ MPa and Poisson's ratio $\nu = 0.3$.

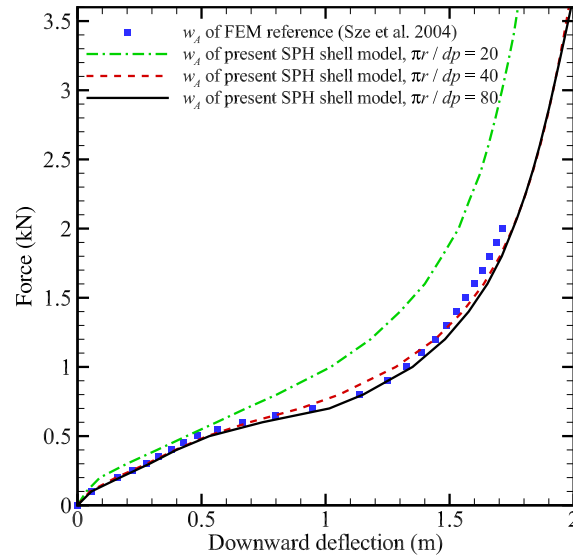


Fig. 26. Pinched semi-cylindrical shell: Curves of radical displacements of point A as a function of the point force magnitude and spatial resolution, and their comparison with those of Sze et al. [69].

by redistributing it to surrounding particles using a specific distribution function. And we also aim to apply the essentially non-hourglass formulation proposed in our previous work [32] to handle the hourglass issues by calculating the acceleration induced by shear stress through a Laplacian operator. We also notice that the traction-free boundary condition is not strictly imposed in our study, suggesting a future work to improve. Note that the current method, initially designed for plate and shell structures with moderate to high moduli, can be extended to soft thin structures like membranes. Additionally, future work, along with the multi-physical modeling within unified computational framework, may also involve developing SPH methods for interactions between fluid and thin structures.

List of symbols

The next list describes the symbols that are used within the body of the document.

- $\mathbf{n} = \{n_1, n_2, n_3\}^T$ pseudo normal
 $\mathbf{u} = \{u, v, w\}^T$ displacements
 $\boldsymbol{\theta} = \{\theta, \varphi\}^T$ rotations
 $\boldsymbol{\xi} = (\xi, \eta, \zeta)$ initial local coordinate system
 $\mathbf{X} = (X, Y, Z)$ global coordinate system
 $\mathbf{x} = (x, y, z)$ current local coordinate system
 $(\bullet)^0$ indicating the parameter (\bullet) is defined at the initial configuration and global coordinate system
 $(\bullet)^I$ indicating the parameter (\bullet) is defined at the current configuration and current local coordinate system
 $(\bullet)^{0,L}$ indicating the parameter (\bullet) is defined at the initial configuration and initial local coordinate system
 $(\bullet)_m$ representing the mid-surface parameter

CRedit authorship contribution statement

Dong Wu: Writing – original draft, Visualization, Validation, Methodology, Investigation, Formal analysis, Conceptualization. **Chi Zhang:** Writing – review & editing, Investigation. **Xiangyu Hu:** Writing – review & editing, Supervision, Methodology, Investigation, Conceptualization.

Declaration of competing interest

The authors declare that they have no known competing financial interests or personal relationships that could have appeared to influence the work reported in this paper.

Data availability

The code is open source.

Acknowledgement

D. Wu is partially supported by the China Scholarship Council (No. 201906130189). D. Wu, C. Zhang and X.Y. Hu would like to express their gratitude to the German Research Foundation (DFG) for its sponsorship of this research under grant number DFG HU1527/12-4.

References

- [1] T. Belytschko, Y. Krongauz, D. Organ, M. Fleming, P. Krysl, Meshless methods: an overview and recent developments, *Comput. Methods Appl. Mech. Eng.* 139 (1–4) (1996) 3–47.
- [2] G.R. Liu, Y.T. Gu, *An Introduction to Meshfree Methods and Their Programming*, Springer Science & Business Media, 2005.
- [3] M. Liu, G. Liu, Smoothed particle hydrodynamics (SPH): an overview and recent developments, *Arch. Comput. Methods Eng.* 17 (1) (2010) 25–76.
- [4] C. Zhang, Y.-j. Zhu, D. Wu, N.A. Adams, X. Hu, Smoothed particle hydrodynamics: methodology development and recent achievement, *J. Hydrodyn.* 34 (5) (2022) 767–805.
- [5] L.B. Lucy, A numerical approach to the testing of the fission hypothesis, *Astron. J.* 82 (1977) 1013–1024.
- [6] R.A. Gingold, J.J. Monaghan, Smoothed particle hydrodynamics: theory and application to non-spherical stars, *Mon. Not. R. Astron. Soc.* 181 (3) (1977) 375–389.
- [7] J.J. Monaghan, Smoothed particle hydrodynamics, *Rep. Prog. Phys.* 68 (8) (2005) 1703.
- [8] J.J. Monaghan, Smoothed particle hydrodynamics and its diverse applications, *Annu. Rev. Fluid Mech.* 44 (2012) 323–346.
- [9] C. Zhang, M. Rezavand, Y. Zhu, Y. Yu, D. Wu, W. Zhang, J. Wang, X. Hu, SPHinXsys: an open-source multi-physics and multi-resolution library based on smoothed particle hydrodynamics, *Comput. Phys. Commun.* (2021) 108066.
- [10] H.G. Matthies, J. Steindorf, Partitioned strong coupling algorithms for fluid–structure interaction, *Comput. Struct.* 81 (8–11) (2003) 805–812.
- [11] H.G. Matthies, R. Niekamp, J. Steindorf, Algorithms for strong coupling procedures, *Comput. Methods Appl. Mech. Eng.* 195 (17–18) (2006) 2028–2049.
- [12] B.C. Cerik, K. Lee, S.-J. Park, J. Choung, Simulation of ship collision and grounding damage using Hosford-Coulomb fracture model for shell elements, *Ocean Eng.* 173 (2019) 415–432.
- [13] Y.-X. Peng, A.-M. Zhang, F.-R. Ming, S.-P. Wang, A meshfree framework for the numerical simulation of elasto-plasticity deformation of ship structure, *Ocean Eng.* 192 (2019) 106507.
- [14] G. Totaro, Z. Gürdal, Optimal design of composite lattice shell structures for aerospace applications, *Aerosp. Sci. Technol.* 13 (4–5) (2009) 157–164.
- [15] J.D. Laubrie, J.S. Mousavi, S. Avril, A new finite-element shell model for arterial growth and remodeling after stent implantation, *Int. J. Numer. Methods Biomed. Eng.* 36 (1) (2020) e3282.
- [16] P.W. Cleary, Modelling confined multi-material heat and mass flows using SPH, *Appl. Math. Model.* 22 (12) (1998) 981–993.
- [17] A.E.H. Love, The small free vibrations and deformation of a thin elastic shell, in: *Proceedings of the Royal Society of London Series I*, vol. 43, 1887, pp. 352–353.
- [18] Y.S. Uflyand, Wave propagation by transverse vibrations of beams and plates, *PMM: J. Appl. Math. Mech.* 12 (1948) 287–300.
- [19] R. Mindlin, Influence of rotary inertia and shear on flexural motions of isotropic, elastic plates, *J. Appl. Mech.* 18 (1951) 31–38.
- [20] I. Elishakoff, F. Hache, N. Challamel, Vibrations of asymptotically and variationally based Uflyand–Mindlin plate models, *Int. J. Eng. Sci.* 116 (2017) 58–73.
- [21] I. Elishakoff, *Handbook on Timoshenko-Ehrenfest Beam and Uflyand-Mindlin Plate Theories*, World Scientific, 2020.
- [22] P. Krysl, T. Belytschko, Analysis of thin shells by the element-free Galerkin method, *Int. J. Solids Struct.* 33 (20–22) (1996) 3057–3080.

- [23] S. Li, W. Hao, W.K. Liu, Numerical simulations of large deformation of thin shell structures using meshfree methods, *Comput. Mech.* 25 (2000) 102–116.
- [24] T. Rabczuk, P. Areias, T. Belytschko, A meshfree thin shell method for non-linear dynamic fracture, *Int. J. Numer. Methods Eng.* 72 (5) (2007) 524–548.
- [25] D. Li, Z. Lin, S. Li, Numerical analysis of Mindlin shell by meshless local Petrov-Galerkin method, *Acta Mech. Solida Sin.* 21 (2) (2008) 160–169.
- [26] T. Rabczuk, R. Gracie, J.-H. Song, T. Belytschko, Immersed particle method for fluid–structure interaction, *Int. J. Numer. Methods Eng.* 81 (1) (2010) 48–71.
- [27] B.M. Donning, W.K. Liu, Meshless methods for shear-deformable beams and plates, *Comput. Methods Appl. Mech. Eng.* 152 (1–2) (1998) 47–71.
- [28] J.-S. Chen, D. Wang, A constrained reproducing kernel particle formulation for shear deformable shell in Cartesian coordinates, *Int. J. Numer. Methods Eng.* 68 (2) (2006) 151–172.
- [29] Y. Peng, A. Zhang, F. Ming, A thick shell model based on reproducing kernel particle method and its application in geometrically nonlinear analysis, *Comput. Mech.* 62 (2018) 309–321.
- [30] B. Maurel, A. Combescure, An SPH shell formulation for plasticity and fracture analysis in explicit dynamics, *Int. J. Numer. Methods Eng.* 76 (7) (2008) 949–971.
- [31] G.C. Ganzenmüller, An hourglass control algorithm for Lagrangian smooth particle hydrodynamics, *Comput. Methods Appl. Mech. Eng.* 286 (2015) 87–106.
- [32] D. Wu, C. Zhang, X. Tang, X. Hu, An essentially non-hourglass formulation for total Lagrangian smoothed particle hydrodynamics, *Comput. Methods Appl. Mech. Eng.* 407 (2023) 115915.
- [33] F.-R. Ming, A.-M. Zhang, X.-Y. Cao, A robust shell element in meshfree SPH method, *Acta Mech. Sin.* 29 (2) (2013) 241–255.
- [34] F. Caleyron, A. Combescure, V. Faucher, S. Potapov, Dynamic simulation of damage-fracture transition in smoothed particles hydrodynamics shells, *Int. J. Numer. Methods Eng.* 90 (6) (2012) 707–738.
- [35] J. Lin, H. Naceur, D. Coutellier, A. Laksimi, Efficient meshless SPH method for the numerical modeling of thick shell structures undergoing large deformations, *Int. J. Non-Linear Mech.* 65 (2014) 1–13.
- [36] F. Ming, A. Zhang, S. Wang, Smoothed particle hydrodynamics for the linear and nonlinear analyses of elastoplastic damage and fracture of shell, *Int. J. Appl. Mech.* 7 (02) (2015) 1550032.
- [37] J. Lin, H. Naceur, A. Laksimi, D. Coutellier, On the implementation of a nonlinear shell-based SPH method for thin multilayered structures, *Compos. Struct.* 108 (2014) 905–914.
- [38] J. Lin, H. Naceur, D. Coutellier, S. Abrate, Numerical modeling of the low-velocity impact of composite plates using a shell-based SPH method, *Meccanica* 50 (10) (2015) 2649–2660.
- [39] Y.-X. Peng, A.-M. Zhang, F.-R. Ming, Numerical simulation of structural damage subjected to the near-field underwater explosion based on sph and rkpm, *Ocean Eng.* 222 (2021) 108576.
- [40] C. Zhang, Y. Zhu, Y. Yu, D. Wu, M. Rezavand, S. Shao, X. Hu, An artificial damping method for total Lagrangian SPH method with application in biomechanics, *Eng. Anal. Bound. Elem.* 143 (2022) 1–13.
- [41] M. Kondo, Y. Suzuki, S. Koshizuka, Suppressing local particle oscillations in the Hamiltonian particle method for elasticity, *Int. J. Numer. Methods Eng.* 81 (12) (2010) 1514–1528.
- [42] C. Zhang, M. Rezavand, Y. Zhu, Y. Yu, D. Wu, W. Zhang, S. Zhang, J. Wang, X. Hu, SPHinXsys: an open-source meshless, multi-resolution and multi-physics library, *Softw. Impacts* 6 (2020) 100033.
- [43] J.-L. Batoz, G. Dhaut, Modélisation des structures par éléments finis: Solides élastiques, Presses Université, Laval, 1990.
- [44] K. Wisniewski, Finite Rotation Shells: Basic Equations and Finite Elements for Reissner Kinematics, CIMNE-Springer, 2010.
- [45] A. Gil, J. Segura, N.M. Temme, Numerical Methods for Special Functions, SIAM, 2007.
- [46] J.N. Reddy, Theory and Analysis of Elastic Plates and Shells, CRC Press, 2006.
- [47] H. Wendland, Piecewise polynomial, positive definite and compactly supported radial functions of minimal degree, *Adv. Comput. Math.* 4 (1) (1995) 389–396.
- [48] P. Randles, L.D. Libersky, Smoothed particle hydrodynamics: some recent improvements and applications, *Comput. Methods Appl. Mech. Eng.* 139 (1–4) (1996) 375–408.
- [49] R. Vignjevic, J.R. Reveles, J. Campbell, SPH in a total Lagrangian formalism, *CMC-Tech. Sci. Press* 4 (3) (2006) 181.
- [50] M.-B. Liu, S.-m. Li, On the modeling of viscous incompressible flows with smoothed particle hydro-dynamics, *J. Hydrodyn.* 28 (5) (2016) 731–745.
- [51] P. Betsch, A. Menzel, E. Stein, On the parametrization of finite rotations in computational mechanics: a classification of concepts with application to smooth shells, *Comput. Methods Appl. Mech. Eng.* 155 (3–4) (1998) 273–305.
- [52] J.C. Simo, D.D. Fox, M.S. Rifai, On a stress resultant geometrically exact shell model. Part III: Computational aspects of the nonlinear theory, *Comput. Methods Appl. Mech. Eng.* 79 (1) (1990) 21–70.
- [53] P. Singla, D. Mortari, J.L. Junkins, How to avoid singularity for Euler angle set, in: Proceedings of the AAS Space Flight Mechanics Conference, Hawaii, 2004, pp. AAS04–190.
- [54] T.J. Hughes, K.S. Pister, Consistent linearization in mechanics of solids and structures, *Comput. Struct.* 8 (3–4) (1978) 391–397.
- [55] L. Verlet, Computer “experiments” on classical fluids. I. Thermodynamical properties of Lennard-Jones molecules, *Phys. Rev.* 159 (1) (1967) 98.
- [56] C. Zhang, M. Rezavand, X. Hu, A multi-resolution SPH method for fluid-structure interactions, *J. Comput. Phys.* 429 (2021) 110028.
- [57] T.Y. Tsui, P. Tong, Stability of transient solution of moderately thick plate by finite-difference method, *AIAA J.* 9 (10) (1971) 2062–2063.
- [58] C. Zhang, M. Rezavand, X. Hu, A multi-resolution SPH method for fluid-structure interactions, *J. Comput. Phys.* 429 (2021) 110028.
- [59] H.H. Bui, R. Fukagawa, K. Sako, S. Ohno, Lagrangian meshfree particles method (SPH) for large deformation and failure flows of geomaterial using elastic–plastic soil constitutive model, *Int. J. Numer. Anal. Methods Geomech.* 32 (12) (2008) 1537–1570.
- [60] C. Peng, S. Wang, W. Wu, H.-s. Yu, C. Wang, J.-y. Chen, LOQUAT: an open-source GPU-accelerated SPH solver for geotechnical modeling, *Acta Geotech.* 14 (2019) 1269–1287.
- [61] H. Fan, S. Li, A peridynamics-SPH modeling and simulation of blast fragmentation of soil under buried explosive loads, *Comput. Methods Appl. Mech. Eng.* 318 (2017) 349–381.
- [62] C. Zhang, J. Wang, M. Rezavand, D. Wu, X. Hu, An integrative smoothed particle hydrodynamics method for modeling cardiac function, *Comput. Methods Appl. Mech. Eng.* 381 (2021) 113847.
- [63] Y. Zhu, C. Zhang, X. Hu, A dynamic relaxation method with operator splitting and random-choice strategy for sph, *J. Comput. Phys.* (2022) 111105.
- [64] L.D. Landau, E.M. Lifchits, Course of Theoretical Physics: Theory of Elasticity, 1986.
- [65] J.P. Gray, J.J. Monaghan, R. Swift, SPH elastic dynamics, *Comput. Methods Appl. Mech. Eng.* 190 (49–50) (2001) 6641–6662.
- [66] C. Zhang, X.Y. Hu, N.A. Adams, A generalized transport-velocity formulation for smoothed particle hydrodynamics, *J. Comput. Phys.* 337 (2017) 216–232.
- [67] B. Momenan, M.R. Labrosse, A new continuum-based thick shell finite element for soft biological tissues in dynamics: part 1-preliminary benchmarking using classic verification experiments, arXiv preprint, arXiv:1801.04029, 2018.
- [68] K. Sze, S.-J. Zheng, A stabilized hybrid-stress solid element for geometrically nonlinear homogeneous and laminated shell analyses, *Comput. Methods Appl. Mech. Eng.* 191 (17–18) (2002) 1945–1966.
- [69] K. Sze, X. Liu, S. Lo, Popular benchmark problems for geometric nonlinear analysis of shells, *Finite Elem. Anal. Des.* 40 (11) (2004) 1551–1569.
- [70] G. Payette, J. Reddy, A seven-parameter spectral/hp finite element formulation for isotropic, laminated composite and functionally graded shell structures, *Comput. Methods Appl. Mech. Eng.* 278 (2014) 664–704.
- [71] T. Belytschko, H. Stolarski, W.K. Liu, N. Carpenter, J.S. Ong, Stress projection for membrane and shear locking in shell finite elements, *Comput. Methods Appl. Mech. Eng.* 51 (1–3) (1985) 221–258.
- [72] J. Simo, D. Fox, M. Rifai, On a stress resultant geometrically exact shell model. Part II: The linear theory; computational aspects, *Comput. Methods Appl. Mech. Eng.* 73 (1) (1989) 53–92.

- [73] J. Simo, M. Rifai, D. Fox, On a stress resultant geometrically exact shell model. Part IV: Variable thickness shells with through-the-thickness stretching, *Comput. Methods Appl. Mech. Eng.* 81 (1) (1990) 91–126.
- [74] N. Buechter, E. Ramm, Shell theory versus degeneration—a comparison in large rotation finite element analysis, *Int. J. Numer. Methods Eng.* 34 (1) (1992) 39–59.
- [75] L. Jiang, M. Chernuka, A simple four-noded corotational shell element for arbitrarily large rotations, *Comput. Struct.* 53 (5) (1994) 1123–1132.
- [76] L. Jiang, M.W. Chernuka, N.G. Pegg, A co-rotational, updated Lagrangian formulation for geometrically nonlinear finite element analysis of shell structures, *Finite Elem. Anal. Des.* 18 (1–3) (1994) 129–140.
- [77] N. Stander, A. Matzenmiller, E. Ramm, An assessment of assumed strain methods in finite rotation shell analysis, *Eng. Comput.* 6 (1) (1989) 58–66.
- [78] B. Brank, F. Damjanić, D. Perić, On implementation of a nonlinear four node shell finite element for thin multilayered elastic shells, *Comput. Mech.* 16 (5) (1995) 341–359.
- [79] R. Arciniega, J. Reddy, Tensor-based finite element formulation for geometrically nonlinear analysis of shell structures, *Comput. Methods Appl. Mech. Eng.* 196 (4–6) (2007) 1048–1073.